

Activation, Reactivity and Dynamics of Manganese Pincer Complexes in Hydrogenation Catalysis

Yang, W.

DOI

[10.4233/uuid:c40b1935-c5f1-4887-9185-d514ef408d6f](https://doi.org/10.4233/uuid:c40b1935-c5f1-4887-9185-d514ef408d6f)

Publication date

2022

Document Version

Final published version

Citation (APA)

Yang, W. (2022). *Activation, Reactivity and Dynamics of Manganese Pincer Complexes in Hydrogenation Catalysis*. [Dissertation (TU Delft), Delft University of Technology]. <https://doi.org/10.4233/uuid:c40b1935-c5f1-4887-9185-d514ef408d6f>

Important note

To cite this publication, please use the final published version (if applicable). Please check the document version above.

Copyright

Other than for strictly personal use, it is not permitted to download, forward or distribute the text or part of it, without the consent of the author(s) and/or copyright holder(s), unless the work is under an open content license such as Creative Commons.

Takedown policy

Please contact us and provide details if you believe this document breaches copyrights. We will remove access to the work immediately and investigate your claim.

Activation, Reactivity and Dynamics of Manganese Pincer Complexes in Hydrogenation Catalysis

Dissertation

for the purpose of obtaining the degree of doctor

at Delft University of Technology

by the authority of the Rector Magnificus, Prof.dr.ir. T.H.J.J. van der Hagen,

chair of the Board of Doctorates

to be defended publicly on

by

Wenjun YANG (杨文军)

Master of Science in Chemistry,

China Agricultural University, China

Born in Shangrao, China

This dissertation has been approved by the promotor.

Promotor: Prof. dr. E. A. Pidko

Co-promotor: dr. G. A. Filonenko

Composition of the doctoral committee:

Rector Magnificus	Chairperson
Prof. dr. Evgeny A. Pidko	Delft University of Technology, promotor
Dr. Georgy A. Filonenko	Delft University of Technology, copromotor

Independent members:

Prof. dr. Frank Hollmann	Delft University of Technology
Prof. dr. Rhett Kempe,	University of Bayreuth, Germany
Prof. dr. Edwin Otten	University of Groningen, Netherland
Dr. Caroline T. Saouma	University of Utah, USA
Dr. Danny Broere	Utrecht University, Netherland
Prof. dr. Atsushi. Urakawa	Delft University of Technology (reserve member)

The work described in this dissertation was carried out in the Inorganic Systems Engineering (ISE) group, Department of Chemical Engineering, Faculty of Applied Science, Delft University of Technology. The research was funded by the European Research Council under the European Union's Horizon 2020 Research and Innovation Program (Grant Agreement No. 725686).



European Research Council
Established by the European Commission

Printed by: Proefschrift specialist

Copyright © 2022 by W. Yang

ISBN 978-94-6366-615-2

An electronic version of the dissertation is available at TU Delft library

Contents

Chapter I	Introduction: Rethinking the Performance of Hydrogenation Catalysts	1
Chapter II	Countering Deactivation and Accelerating Activation: the Approach to a Robust and Efficient Mn(I) Carbonyl Hydrogenation Catalyst	35
Chapter III	Switching Between Carbonyl Hydrogenation and Olefin Transposition Catalysis via Controlling Ligand Dynamics in Mn(I) complexes	61
Chapter IV	Composition Dynamics of Reaction Environment in Homogeneous Ester Hydrogenation	85
Chapter V	Utilizing Design of Experiments Approach to Assess Kinetic Parameters for a Mn Homogeneous Hydrogenation Catalyst	113
Appendix		
Summary		
Samenvatting		
Acknowledgements		
Curriculum Vitae		
List of Publications		

Introduction: Rethinking the Performance of Hydrogenation Catalysts

Abstract

Effective assessment of catalytic performance is the foundation for the rational design and development of new catalysts with superior performance. The ubiquitous screening/optimization studies take reaction yield as the sole performance metric in an approach that often neglects the complexity of catalytic system and intrinsic reactivities of the catalysts. Using an example of hydrogenation catalysis, we examine the transient behavior of molecular catalysts often encountered in activation, deactivation and catalytic turnover processes. Each of these processes and the reaction environment in which they take place are gradually shown to determine the real-time catalyst speciation and the resulting kinetics of the overall catalytic reaction. As a result, the performance of hydrogenation catalyst appears to be a complex and time-dependent metric defined by multiple descriptors apart from reaction yield. In this chapter we review these catalytically relevant descriptors to arrive at the comprehensive description of catalytic performance.

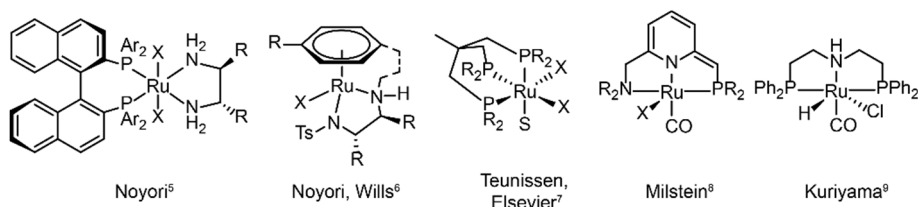
1.1 Molecular catalysis for reductive transformations

Reduction reactions, and those of carbonyl compounds specifically, are essential chemical transformations with far-reaching applications in industry for producing pharmaceuticals, fragrances, flavours, and other fine-chemical intermediates.¹ This field has progressed from stoichiometric reductions to modern hydrogenation catalysis, which circumvents the generation of considerable amounts of waste.² Heterogeneous catalysts are the work-horse of the industrial hydrogenation.³ Despite the harsh conditions commonly required for the operation, they are widely employed for the production of bulk chemicals where selectivity is not a primary concern. Molecularly-defined homogeneous transition metal-based catalysts take a role of a complementary tool for lower-temperature and more “specialized” catalytic reductions in synthetic applications requiring high selectivities and/or high tolerance of functional groups, commonly encountered in fine- and pharmaceutical chemistry industries.⁴

The 2001 Nobel Prize in Chemistry awarded to Noyori for his work on asymmetric hydrogenation catalysts: $[(P^{\wedge}P)RuX_2(N^{\wedge}N)]$ highlights the prominent role that hydrogenation techniques acquired in modern industry (**Figure 1.1 A**).⁵ Other seminal landmarks include the powerful $[(N^{\wedge}N)Ru(arene)]$ catalyst by Noyori and Wills for the efficient asymmetric carbonyl transfer hydrogenation,⁶ the robust Ru(Triphos) catalyst by Teunissen and Elsevier that turn out to be effective for the hydrogenation of challenging carboxylic acid substrates,⁷ the lutidine-based Ru(PNN) complex by Milstein,⁸ and the Ru-MACHO family of complexes by Kuriyama⁹ as the inspiration of the bifunctional ester hydrogenation catalysts.

The vast majority of efficient carbonyl hydrogenation catalysts have been bifunctional complexes featuring an acidic moiety in the ligand backbones (**Figure 1.1 B**).¹⁰ This reactive site can be deprotonated with an external base to

A) Pioneering catalysts of homogeneous carbonyl hydrogenation



B) Metal-ligand cooperative (MLC) complexes

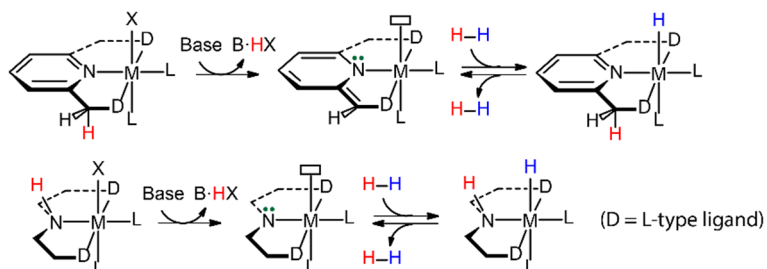


Figure 1. 1. Landmarks of homogeneous hydrogenation (A) and the activation mode of metal-ligand cooperative (MLC) complexes via protonation and deprotonation (B).

generate the reactive molecular system comprised of a highly basic site on the ligand and the coordinately unsaturated metal center. This acid-base pair is able to split H_2 heterolytically, leading to the formation of metal hydride that can reduce carbonyl compounds via a concerted/cooperative hydride transfer and protonation. The whole process represents a typical metal-ligand cooperation (MLC) mechanism based on protonation/deprotonation. While the degree to which the MLC is involved in catalysis remains debated,¹¹ the introduction of ligand platforms with cooperative sites has been confirmed as a versatile way to induce hydrogenation reactivity in transition metal catalysts.¹²

Significant progress has been made in this field mainly by noble metal complexes based on ruthenium, iridium, rhodium, and osmium.¹³ The requirements for more sustainable processes recently also initiated an intensive investigation of alternative catalysts based on earth-abundant, inexpensive 3d metals (Fe, Co, and Mn).^{12b, 14} Taking this idea a step further, the transition metal-free catalytic hydrogenation was achieved in past decade by ‘frustrated Lewis pair’ catalysts but

is still in its infancy.¹⁵ Despite the great amount of hydrogenation catalysts that have been developed, understanding the fundamental laws of hydrogenation catalysis that would allow for designing new catalytic systems rationally, remains a central subject in modern catalysis research.

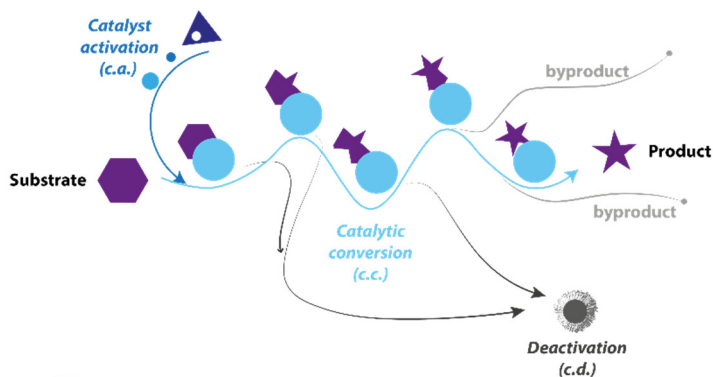
Dealing with diversity of available catalysts and their designs one inevitably faces a question of how to find good catalysts for a desired transformation, i.e. ones with superior performance - a common metric for the evaluation of homogeneous catalysts that is not strictly defined. The typical approach for finding an active catalyst relies on trail and error. Specifically, the modern high-throughput catalyst screening begins with the formulation of massive libraries of transition-metal/ligand combinations. These catalyst combinations are then rapidly screened for a model chemical conversion under pre-defined conditions

A) Catalytic performance with the focus on reaction yields (P_A).



$$P_A = Y_{\text{yield}} = F(I_{\text{ligand}}, I_{\text{metal}}, I_{\text{geometry}} \dots)_{\text{catalyst}} + F(E_T, E_P, E_{\text{soln}}, E_{\text{additive}} \dots)_{\text{conditions}}$$

B) Catalytic performance with the focus on reaction kinetics (P_B).



$$P_B = \frac{dY}{dt} = F(I_1, I_2, E_1, E_2, \dots)_{c.a.} + F(I_a, I_b, E_a, E_b, \dots)_{c.c.} + F(I_d, I_{ii}, E_d, E_{ii}, \dots)_{c.d.}$$

Figure 1. 2. Two different views of catalysis system and corresponding describing methodologies of catalytic performance (P) with catalyst structural parameters (I) and reaction condition parameters (E).

to pick out the best performing candidates, of which the operation conditions will be further optimized. In this framework, catalysis is treated as an organic reaction, and the final yield becomes the primary descriptor of catalytic performance (*Figure 1. 2 A*). However, catalysis as phenomenon is centred around the acceleration of chemical transformation, i.e. improvements in kinetic behaviour, not the yield itself. While most screening studies aim at enhancing the final yield by varying catalyst structure and reaction environment, they fall short of providing kinetic data that describes catalysis in universal terms.

In addition to the mismatch between yield terms used in conventional optimization and the kinetic nature of catalysis, the complexity of catalytic systems can also pose a significant challenge for studying intrinsic reactivities of the catalysts. A rapid development of advanced experimental techniques has allowed unprecedented insights into the molecular behaviour of catalyst as it undergoes distinct stages of catalyst activation, deactivation, and catalytic turnover. These processes comprise the complex catalytic reactivity network that define the time-dependent catalyst speciation and the resulting kinetics under specified conditions (*Figure 1. 2 B*). Growing evidence in the literature, as well as this thesis, reveals that apart from the catalytic turnover, other processes can also significantly steer the kinetics and outcomes of the system. This complexity can conceal the intrinsic reactivity of catalysts, making it elusive and challenging to study.

In this chapter we summarize the effects that precatalyst activation, catalyst deactivation and the environment are known to have on hydrogenation catalysis. By linking the catalytic performance to the transient behavior of catalyst in these processes, we can reveal its highly dynamic, time- and condition-dependent nature that is far too complex to rely on final yield as the single descriptor. New descriptors for each catalytic stage will be discussed together with their role in establishing more comprehensive description of catalytic systems.

1.2 The effect of precatalyst activation

The extreme sensitivity of active catalyst species renders their isolation and direct use in catalysis arguably complicated, if not impossible. Because of this, chemists often make use of precatalysts that require specific activation process to reach the active state (*Figure 1. 2 B*). While the precatalyst activation is conducted at the initial stage of the reaction and not involved in catalytic cycle, it can still be an important factor that affects catalyst performance. As with every chemical transformation, catalyst activation can proceed with varying rate and selectivity, both being capable of affecting the outcome of the catalytic reaction as a whole. Below we examine these factors in more detail.

1.2.1 The rate of precatalyst activation

In general, the rate of precatalyst activation defines how quickly the active species or their precursors are supplied to the catalytic cycle. Depending on the activation chemistry, this supply can either be instant or slow in time. Apart from base-induced dehydrohalogenation (*Figure 1. 1 B*), known as rapid, nearly instantaneous process, bifunctional hydrogenation precatalysts may require further transformations during activation, e.g. dissociation of an ancillary ligand to open the coordination site for hosting substrate molecules. Such process widely occurs with transition-metal catalysts, and can be the rate-determining step for activation. For example, the Mn-CNP catalyst (**1-1**) described in Chapter 2 is a cationic complex and readily offers a coordinately-saturated amido complex (**1-2**) under basic condition (*Figure 1. 3 A*).¹⁶ One of the three carbonyl groups in **1-2** need to be detached before the splitting of H₂ can take place and the catalytic turnover begins. This process is very sluggish, evidenced by the slow replacement of CO with hydride in stoichiometric experiment of **1-2** as well as the long induction period in both of the hydrogen reactions catalyzed by **1-1** and **1-2** (*Figure 1. 3 A*, top and B, left). Alternatively, the treatment of precatalyst **1-1** with

KBHET₃ can furnish **1-3** via the Mn hydride **1-4** featuring a free phosphine arm (**Figure 1.3 A**, bottom). The reattachment of strong P donor largely facilitated the CO dissociation, leading to the faster formation of **1-3** and thus a higher overall catalytic performance. This is evident from the rate profile in **Figure 1.3 B** showing that adequate activation protocol allows to achieve 2.5-fold higher reaction rates with the same amount of catalyst. Thus the sluggish catalyst activation can hamper the overall catalytic performance, obscuring the part of the intrinsic reactivity of the examined catalyst.

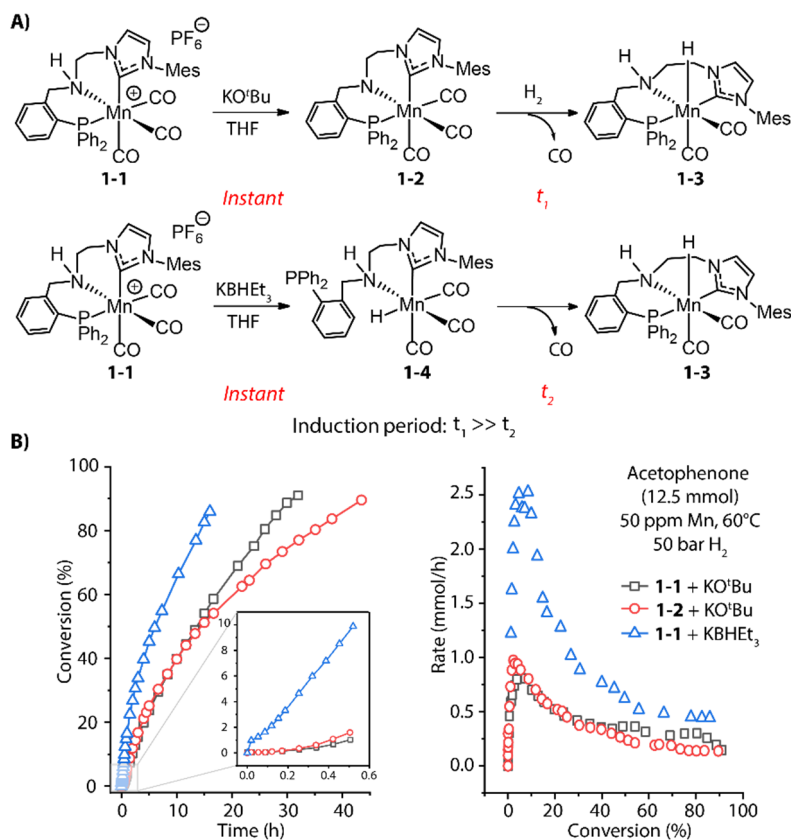


Figure 1.3. Activation of MnCNP precatalyst and corresponding catalytic performance. (A) Generation of active Mn hydride **1-3** through CO dissociation with two different activation protocols: alkoxide base KO^tBu and hydride donor KBHET₃; (B) The conversion and rate profiles for the hydrogenations of acetophenone with **1-1** and **1-2** in the presence of 1 mol% KO^tBu or 1 mol% KBHET₃ promoters at 60 °C, 50 bar H₂ and 50 ppm Mn loading. Adapted with permission from ref (16).

Similarly, the removal of a CO ligand is the key step for the activation of Knölker-type iron complexes (**1-5**, **Figure 1. 4**). While these complexes were first reported in 1953,¹⁷ their catalytic applications for hydrogenations remained unknown until the conversion of a CO ligand in these complexes to hydride was efficiently achieved via a Hieber reaction (**Figure 1. 4**, path a).¹⁸ In principle, the iron hydride is also accessible via the direct thermal dissociation of CO ligand under H₂, which however can be kinetically challenging. This pathway was later enabled by powerful oxidative cleavage with Me₃NO or UV irradiation (**Figure 1. 4**, paths b and c).¹⁹ The resulting intermediate **IntA** can effectively activate H₂ via an MLC mechanism to yield the Fe hydride species **1-6**. Due to the high sensitivity of **1-6**, **1-5** is generally utilized as the precatalyst for hydrogenation and requires an *in-situ* activation.²⁰ The rate of catalyst activation via a particular approach can determine the performance of **1-5**. However, systematic kinetic studies on different activation protocols or the catalysis initiated via them are very rarely carried out,²¹ as is also the case for these systems. Protocols (b) and (c) are presumably much faster, resulting in the generally better catalytic results of the reactions that utilize them.²² The activation protocol with Me₃NO, however, is more widely used in hydrogenations because of its higher compatibility with pressurized reactors. Based on the understanding of activation process, more-labile nitrile ligand was introduced to replace one of the CO ligand in **1-5**, furnishing the new precatalyst that can achieve the activation-free transfer hydrogenation of aldehydes and ketones.²³

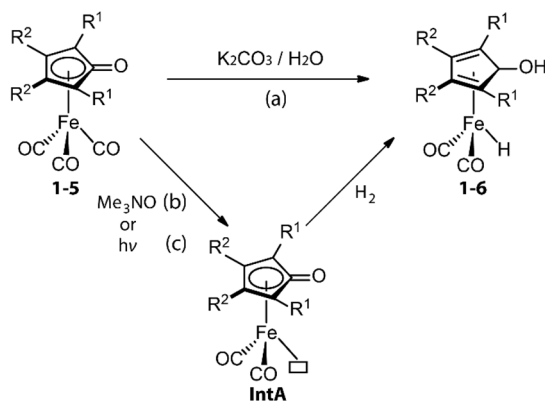


Figure 1. 4. Removal of CO ligand in the activations of (cyclopentadienone)iron carbonyl complexes. (a) Conversion of Fe-CO to Fe-hydride via a Hieber reaction; (b, c) Generation of vacant coordination sites via UV-induced CO dissociation or oxidative cleavage of CO with Me₃NO followed by the activation of H₂.

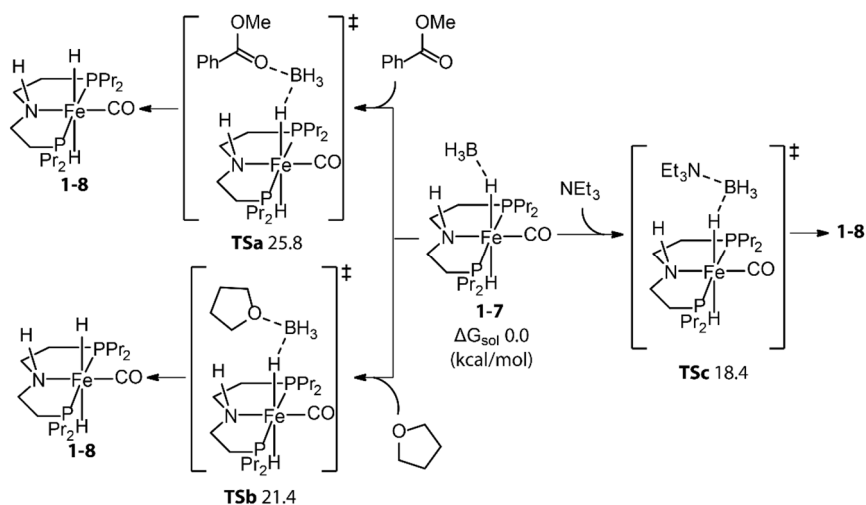


Figure 1. 5. Trapping BH₃ from Fe-PNP precatalyst. The energetics for the generation of active catalyst species 1-8 via the removal of BH₃ with different Lewis bases: ester substrates, tetrahydrofuran solvents, and trimethylamine additives. Adapted with permission from ref (27). Copyright (2014) American Chemical Society.

Even metal hydride species may require an additional activation before catalysis. For example, the hydride in Fe-PNP complex 1-7 (**Figure 1. 5**) was found to be a BH₃ adduct by Hazari and Schneider.²⁴ Subsequently Beller²⁵ and Guan²⁶

independently developed the efficient base-free ester hydrogenation with this well-defined pincer complex. Relevant mechanistic studies disclosed that dihydride species **1-8** was the actual active species, and the dissociation of BH_3 is essential for the initiation of precatalyst **1-7**. The utilization of a Lewis base is a straightforward way to trap the Lewis acid, BH_3 . To study how **1-8** was generated under catalytic conditions, Guan calculated the energetics for the BH_3 trapping process with different Lewis bases, such as the ester substrate, the tetrahydrofuran solvent, or the trimethylamine additive (**Figure 1. 5**).²⁷ DFT calculations showed that the activation of **1-7** with the strong Lewis base Et_3N was the fastest process with the lowest energy barrier (18.4 kcal/mol). Indeed, this rapid induction resulted in a near doubling of the rate in the ester hydrogenation with Et_3N compared to the control experiment without additives.

The control of catalyst-activation process is also crucial for alkene hydrogenation catalysts. A classic example is the Wilkinson's catalyst $(\text{PPh}_3)_3\text{RhCl}$ (**1-9**), of which the performance was limited by the slow dissociation of two phosphine ligands (**Figure 1. 6 A**).²⁸ Ancillary diene ligands that can be hydrogenated, and weakly coordinating anions that will stay in the second coordination sphere were then applied to the evolution of this complex, which could accelerate the generation of adequate open sites (**Figure 1. 6 B**). The resulting Schrock-Osborn catalyst $(\text{PPh}_3)_2\text{Rh}(\text{diene})[\text{PF}_6^-]$ (**1-10**) gave around 6-fold higher turnover frequency in the hydrogenation of terminal alkenes compared to the classical catalyst **1-9**.²⁹ The hydride transfer to olefins is more challenging for Mn(I) catalysts that are coordinately saturated with high-field ligands. An ancillary CO ligand must be removed from the neutral Mn(I) complex to furnish a vacant site for the coordination of an olefin molecule next to the active Mn-hydride, which can be kinetically unfavorable. Kirchner and coworkers found that a Mn-alkyl complex readily furnished $16e^-$ Mn hydride species **1-11-H** via the migratory insertion of a CO ligand into the Mn-alkyl bond followed by hydrogenolysis

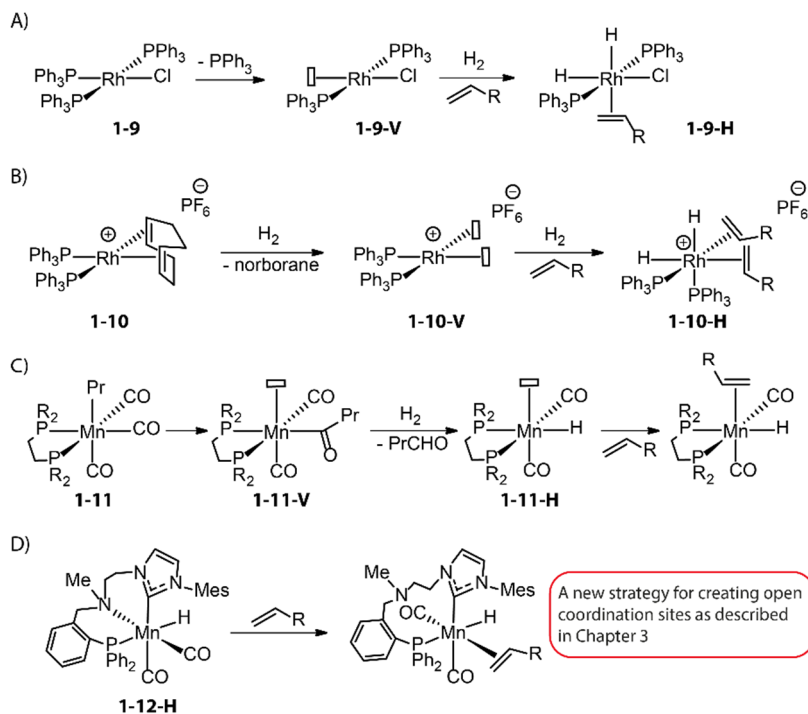


Figure 1. 6. Different strategies for generating vacant sites in the activations of alkene hydrogenation/transposition catalysts. A) Direct dissociations of phosphine ligands in Wilkinson's catalyst **1-9**; B) Reduction of diene ligands followed by the rapid dissociation in Schrock-Osborn catalyst **1-10**; C) Consumption of CO ligand via its migratory insertion to Mn-alkyl followed by hydrogenolysis in Mn alkyl catalyst **1-11**; D) The temporary dissociation of dynamic ligand in N-alkylated Mn-CNP catalyst **1-12-H**.

(**Figure 1. 6 C**).³⁰ This coordinately unsaturated Mn-H enabled the first Mn-catalyzed hydrogenation of alkenes. Alternatively, ligand dynamics can be utilized to temporarily create free space and initiate the catalytic turnover as disclosed in Chapter 3. The alkylation of N-H group within Mn-CNP complex (**1-1**) could elevate the steric hindrance of N donor and facilitate its reversible dissociation (**Figure 1. 6 D**).³¹ This strategy led to the new catalyst **1-12-H** for effective transposition as well as hydrogenation of olefins.

The examples described above point out that the performance of catalysts in operation can be highly dependent on the rates of their activation protocols. For some hydrogenation systems, the dissociation of ancillary ligands from the

precatalysts, commonly treated as a simple process, can not only limit the rate of the catalyst activation, but also determine the apparent performance of the catalytic system. Induction period observed in reaction kinetics is a strong indicator of slow activation. Further mechanistic and kinetic analysis of catalyst activation is also crucial, based on which one can accelerate the precatalyst activation and significantly improve the catalytic results.

1.2.2 The selectivity of precatalyst activation

The majority of chemical reactions do not proceed with quantitative yields and selectivities, and those accompanying catalyst activation are no exception. Reactions with organic or inorganic bases, generally required for activating bifunctional hydrogenation precatalysts, despite their formal simplicity can often lead to catalytically inert or less reactive side-products, causing partial catalyst degradation.

For example, Mn complexes with typical aliphatic PNP pincer ligands show multitude of reactions upon base activation. The reactions of such Mn bifunctional catalysts with strong base are known to readily result in the active dicarbonyl amido complex **1-14** (*Figure 1. 7 A*).³² However, the repulsive force between the metal-ligand bonding electrons within Mn complex is stronger compared to noble-metal ones due to the smaller ionic radius of the Mn center. As a result, Mn complexes should have low constraints of the coordination geometry and can collapse to the structures with lower coordination numbers.³³ The covalent nature of Mn-N bond in Mn species **1-14** could further enhance the ring strain of the complex as evidenced by its bipyramidal rather than square pyramidal geometry, leading to the dissociation of the side arm of the pincer ligand. In Chapter 4 our group investigated the direct activations of various Mn-MACHO (Et₂, ⁱPr₂) with alkoxide bases and observed that in addition to the desired **1-14**, small amounts of deprotonated Mn-PN complexes **1-15** featuring a

dissociated P-donor was also generated (**Figure 1. 7 A**). The deprotonated Fe-PNP complexes, analogous to Mn-PNP, were prone to fully collapse, giving only free pincer ligand and metal deposits, as reported by Hazari and Schneider.³⁴ As for the late-transition-metal hydrogenation catalysts, the base-activated species are geometrically stable. However the presence of the vacant site in the square pyramidal activated complex would favor the complex aggregation and formation of dimers. When tracking the activation of widely used Ru-MACHO (**1-16**), Schaub and co-workers observed the generation of Ru dimer complexes **1-18**, **1-19**, and a tripodal Ru(0) **1-20** apart from the target amido complex **1-17** (**Figure 1. 7 B**).³⁵ Apparently, the dimerization was the main degradation pathway of the catalyst. The bidentate PN in **1-19** and tetradentate NP₃ in **1-20** also indicated the occurrence of disproportionation of PNP ligand.

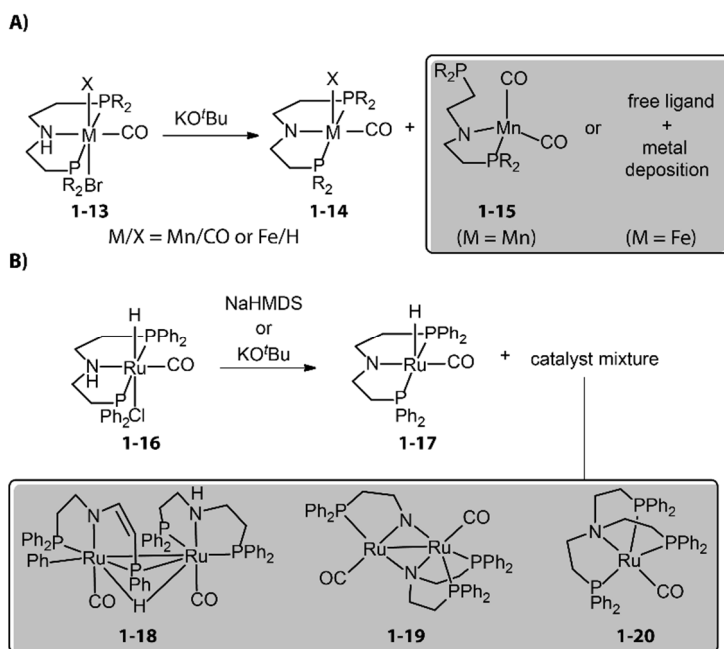


Figure 1. 7. The degradation of hydrogenation precatalysts during activation stage. A) The reactions of catalysts based on first-row transition metals (Mn and Fe) with strong base can lead to the partial or full dissociations of ligands. B) The base-activated Ru complex tends to form Ru dimmers.

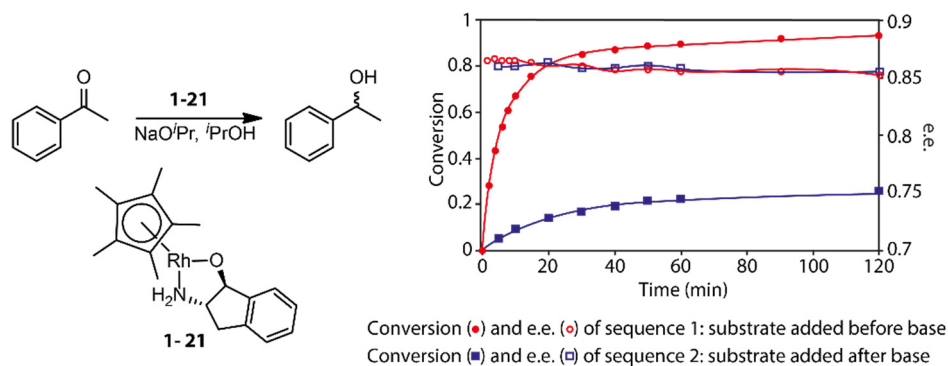


Figure 1. 8. The effect of precatalyst degradation on reaction kinetics and the stabilizing effect of carbonyl substrates on precatalyst activation. (Left) The transfer hydrogenation of acetophenones catalyzed by an Rh bifunctional catalyst **1-21**. (Right) The conversion and enantiomeric excess (e.e.) kinetics for the transfer hydrogenation operated in two different procedures: sequence 1, ketone substrates were added before the activation of the precatalyst initialized by NaOⁱPr; sequence 2, ketone substrates were added after the activation of precatalyst **1-21**. Adapted with permission from ref (36). Copy right (2004) American Chemical Society.

The loss of active catalyst species during the activation stage typically leads to the permanent decrease of the catalytic activity before the actual catalysis. A thorough characterization of the side-products formed during the activation is typically required to spot it. A common way to promote the selective supply of active catalysts is introducing donor that can stabilize the coordinately unsaturated intermediate prior to the activation process. The substrates with carbonyl groups in hydrogenation catalysis are the candidates of such donors.

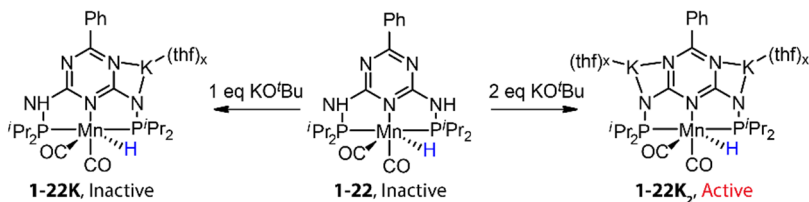
As discussed by Gavriilidis and co-workers, the addition of substrate before base activation can largely enhance the performance for the asymmetric transfer hydrogenation of ketone catalyzed by bifunctional Rh/aminoindanol **1-21** (**Figure 1. 8**).³⁶ The observed much lower rate from the onset of reaction as well as the identical enantioselectivity in sequence 2 compared to sequence 1 confirmed the presence of a profound precatalyst degradation during the activation step. Apparently the weak oxygen donor acetophenone can suppress such unfavorable effect. For highly labile activated species, strong donors may be required for their stabilization. Monodentate phosphine ligands were reported as

efficient additives for improving the selectivity of hydrogenation precatalysts activation.³⁷ Schaub and co-workers observed an improved performance in Ru-MACHO-catalyzed dehydrogenative coupling of hexanol with the addition of phosphine.^{37d} It was possible that the improved reactivity of Ru-MACHO stemmed from the electron-donating ability of phosphine additive. A relevant quantum-chemical study showed that catalytic pathway with phosphine dissociation is energetically much more favorable, suggesting the main role of the phosphine additive is to stabilize the active catalyst.

As discussed above, activation of hydrogenation precatalysts with a strong base can lead to their partial degradation. As a consequence, the observed catalytic performance does not correspond to the intrinsic activity of catalyst, but rather to that of remaining amount of active species after the activation. Care need to be taken regarding the activation sequence, activation time as well as the loading of the reactive compounds. Addition of stabilizers can be beneficial for highly sensitive catalysts. However not every side reaction during activation process leads to degradation: on occasion, some ligand rearrangements and metal dimerization events are advantageous for catalysis, as discovered by for example Chianese^{37b} and Gusev³⁸.

Besides the partial degradation, divergently generating new catalytic species by varying the types or loadings of the activators can achieve different performance with the same precatalyst. Kempe and coworkers investigated the hydride transfer step between a hydrogenation catalyst and the imine substrates, and surprisingly found that the neutral Mn hydride species **1-22** with protonated amine groups in the ligand backbone was inactive for this transformation (*Figure 1. 9 A*).³⁹ However, further deprotonation of **1-22** with KO^tBu can enhance the activity of the Mn hydride

A) Activated catalyst species for hydride transfer to imine.



B) Activated catalyst species for H₂ splitting.

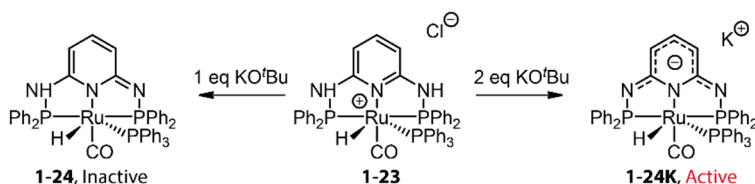


Figure 1. 9. Divergent activation of hydrogenation precatalysts and the resulting catalytic species with different activities. A) The activation of Mn hydride **1-22** with different base loadings can result in bimetallic species (Mn-K) and trimetallic species (Mn-K₂). **1-22K₂** is the most active hydride species that can reduce imines. B) Treating Ru complex **1-23** with different loadings of KO^tBu can give rise to **1-24** or **1-24K** with only the latter one being active enough to split hydrogen molecule.

with only the double-deprotonated species **1-22K₂** being active enough to reduce imines. A similar activity trend was also observed by our group in H₂ splitting with a RuPN₃P complex (**Figure 1. 9 B**).⁴⁰ While the mono-deprotonated complex of **1-23** was inert under H₂ atmosphere, ionic species **1-24K** obtained by adding two equivalent of KO^tBu readily dissociated molecular hydrogen, and could further reduce CO₂. The multiplicity of the precatalyst activation render their performance quite dynamic.

1.3 Composition dynamics of reaction environments

Multiple components comprise catalytic systems. Apart from being reactants, stoichiometric reagents or catalyst species that are directly relevant for catalysis, the components of the reaction mixture contribute to defining the reaction environment indirectly. In principle, the efficiency of any given catalytic process is dependent on the reaction environment. Since catalysis progresses with the

consumption of starting materials and the formation of new molecules, the reactivity of catalyst in the course of reaction would not be constant due to the change of reaction mixture composition. In the case of carbonyl hydrogenation, reaction environment changes from aprotic to highly protic and polar one throughout the reaction. Such changes in conditions can affect the performance of the catalytic system.

For example, our group computed the *operando* free energy diagrams for the homogeneous ester hydrogenation with Mn-PN catalyst (**1-25**) in THF and neat condition.⁴¹ Specifically, the energetics of individual states in the catalytic cycle were calculated at varied concentrations of the ester substrate and alcohol product via COSMO-RS solvent model⁴² to mimic the composition evolution in

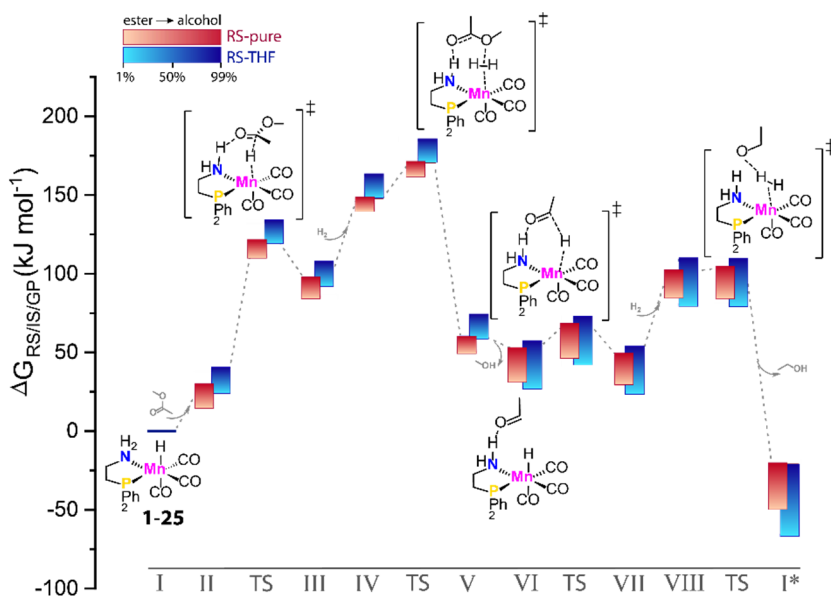


Figure 1. 10. The dynamic energetics of catalysis in the course of reaction. RS-computed The *operando* free energy diagrams of Mn-PN-catalyzed ester hydrogenation along the reaction coordinate. Here only the hydrogen-shuttle catalytic pathways in THF (RS-THF) or neat condition (RS-pure) are shown. Adapted with permission from ref (41). © Licensed under a [CC BY-NC-ND 4.0 license](https://creativecommons.org/licenses/by-nc-nd/4.0/)

the course of reaction. We found that the free energy surface of catalysis via the hydrogen shuttle mechanism was highly dynamic and conversion-dependent (**Figure 1. 10**). The energies of each state increased to a different degree as reaction progresses. Catalysis under neat condition showed more pronounced perturbation in the course of reaction compared to the reaction in THF. In general, these changes caused the decrease of overall reaction favorability, i.e. thermodynamics, as the reaction proceeds. For some elementary steps, we observed highly nonlinear behavior of their kinetic and thermodynamic parameters with the progress of the reaction. This gave rise to the non-monotonous trends in the kinetic profile predicted by microkinetic modeling.

The catalyst speciation can also be dynamic in the course of reaction. In Chapter 4, we showed this by the example of Mn-CNC-catalyzed ester hydrogenation system where the alcohol product could further bind to the activated amido species **1-26** and form Mn alkoxide (Mn-OR) **1-27** (**Figure 1. 11 A**).⁴³ Monitoring the hydrogenation with operando-IR spectroscopy showed that state **1-26** comprised over 90% proportion of catalyst at the beginning and was probably the resting state in catalysis. However, along with the production of alcohol, the proportion of **1-26** continuously decreased with **1-27** becoming the dominant species eventually (**Figure 1. 11 B**). A control experiment with the addition of extra alcohol prior to catalysis displayed large proportion of Mn alkoxide and much lower catalytic rate from the onset of reaction, confirming the inhibitory effect of the product. Therefore the accumulation of alcohol product continuously consumed **1-26**, leading to the severe drop of the steady state concentration of active catalyst species. As a result, the catalytic efficiency of ester hydrogenation was substantially inhibited. Given the numerous reports on the formation of stable metal alkoxides, we envision the product inhibition effects should be common in carbonyl hydrogenation systems and decrease the catalytic efficiency to a different degree based on the thermodynamic stability of the inhibited state.⁴⁴

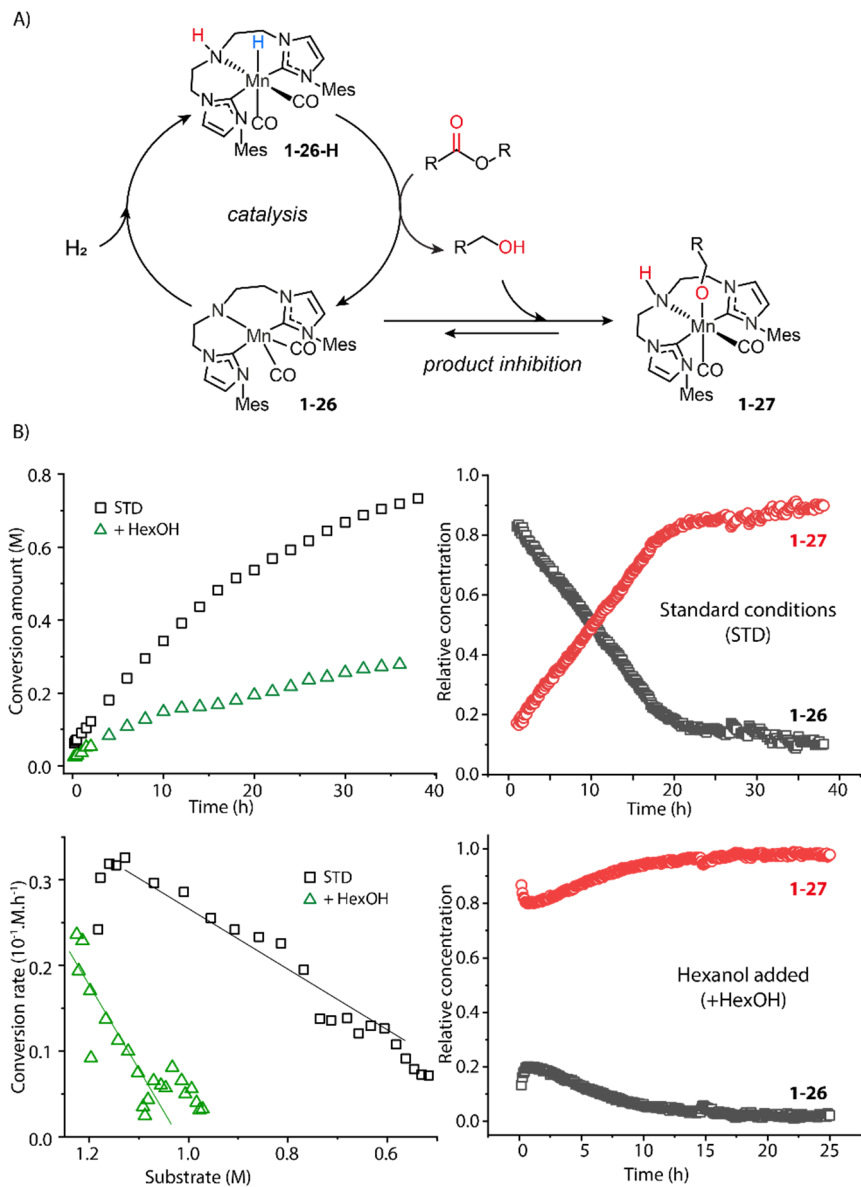


Figure 1. 11. The impact of dynamic reaction environment on the performance of an ester hydrogenation catalytic system. A) The catalytic cycle of the Mn-CNC-catalyzed ester reduction. The alcohol product can bind to **1-26** and form inhibited species **1-27**; B) The kinetics and reaction rate plots (left) as well as the real-time concentration of catalyst species (right) for the hydrogenations of hexyl hexanoates catalyzed by Mn-CNC. The catalyst evolution was traced by operando IR spectroscopy. Conditions - standard: hexyl hexanoate (1.25 M), catalyst (0.1 mol%), KO^tBu (10 mol%) in THF (8.2 mL), 70°C, 40 bar H₂; hexanol added: extra alcohol added at 1.25 M. Adapted with permission from ref (43). © Licensed under a [CC BY 4.0 license](https://creativecommons.org/licenses/by/4.0/).

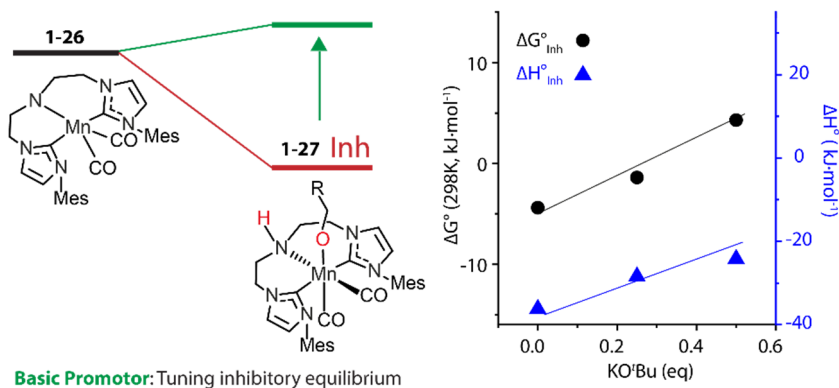


Figure 1. 12. The dependence of the free energy surface for inhibitory equilibrium on base concentration. The Gibbs free energy changes and enthalpy changes of the equilibrium **1-26-1-27** at different concentration of KO^tBu in THF. Adapted with permission from ref (43). © Licensed under a [CC BY 4.0 license](https://creativecommons.org/licenses/by/4.0/).

As shown above, the effects of product formation on catalysis can only be extracted from reaction kinetics. Coupling this with the in-situ tracking of catalyst state with spectroscopies can further help determining which catalytic process is primarily perturbed, leading to the rational tuning of the system.

The most straightforward way to suppress the inhibitory effect of the reaction product is to remove it during the catalysis, apart from varying the ligand structure and the nature of the catalyst.⁴² As reported by Hansen and Rosner, the *in situ* derivatization of amine product with the addition of di-tert-butyl dicarbonate ((Boc)₂O) resulted in ca. 16-fold higher hydrogenation rate compared to the control experiment.⁴⁵ In addition, one can also tune the free energy surface of inhibitory process. The studies from our group on Mn-catalyzed ester reduction pointed to the ability of alkoxide base additives for favoring the product elimination from the Mn-OR adducts.⁴⁶ For Mn-CNC system (**Figure 1. 11**) we disclosed that the increase of KO^tBu concentration significantly elevated the standard Gibbs free energy of alkoxide formation (**1-26—1-27**) from negative to positive and rendered this transformation unfavorable (**Figure 1. 12**, see Chapter 4). Accordingly the lifetime of active catalyst in high-base-loading

experiment are prolonged, leading to the substantial enhancement of the efficiency of ester reduction. The dependence of the free energy surface of such equilibrium on base concentration remained solid when extended to other Mn hydrogenation catalysts (see Chapter 4). Since the base promotor is formally not chemically involved in the reaction, it can be viewed as a component of reaction medium that perturbs the reaction environment for inhibitory process. This was the first indication unknown to us, that formally a reaction component can alter the intrinsic thermodynamics of elementary steps of catalysis and make the catalytic action highly condition-dependent and tunable.

By the same token, the promotional effect of additives, that do not cause chemical changes, may stem from their perturbation to the reaction environment. For example, Lewis acids are widely used to promote the performance of CO₂ hydrogenations.⁴⁷ In the kinetics and mechanism studies conducted by Hazari and coworkers, the rate constant of the rate-determining step of an Ir-PNP-catalyzed system, hydride transfer from **1-28** to CO₂, was found to be linearly dependent on the concentration of LiPF₆ (**Figure 1. 13**).⁴⁸ The Lewis acid in the catalysis medium lowered the activation energy of the hydride transfer and accelerated the overall reaction rate.

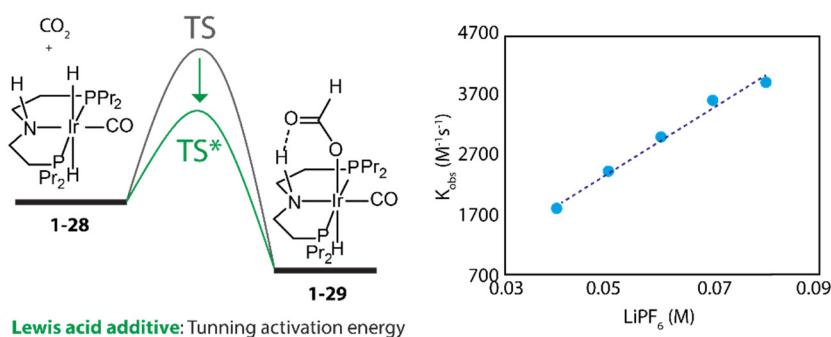


Figure 1. 13. The dependency of the energy barrier for hydride transfer process on Lewis acid concentration. The rate constants of the transformation **1-28-1-29** at different concentration of LiPF₆ in THF. Adapted with permission from ref (48). © Licensed under a [CC BY-NC 4.0 license](https://creativecommons.org/licenses/by-nc/4.0/).

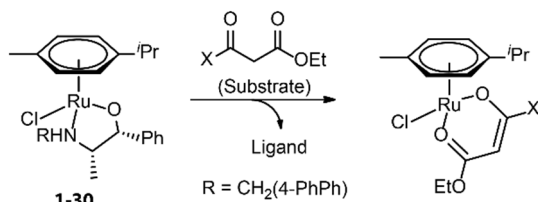
The change of reaction compositions can alter the reaction environment and redefine the kinetic and thermodynamic parameters of catalysis. Furthermore, the degrees of these intrinsic perturbations seem to be dependent on the concentration of the interferer component. This crucial feature readily distinguishes environmental effects from direct molecular involvement.

1.4 The effect of catalyst deactivation in catalysis

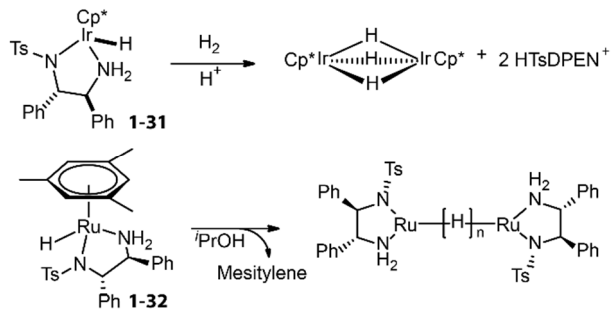
Catalyst deactivation in the course of the catalytic process leads to the loss of the active species and the decrease of the catalytic performance.⁴⁹ Due to the low concentration of catalyst and the co-occurrence of multiple deactivation pathways, mechanistic studies of deactivation in catalysis are challenging. However, understanding this process is still crucial for enhancing the stability of catalysts.

Although stabilized by substrate, hydrogen gas and other donors in the catalytic system, hydrogenation catalysts can still degrade under the reaction conditions. For example, Beller's group monitored the reaction mixture for the Fe-^{iPr}MACHO-catalyzed methanol dehydrogenation by NMR, and found that the catalyst slowly decomposed by ligand dissociation similarly to the degradation pathway described for base activation process (**Figure 1. 7 A**).⁵⁰ Apart from those described in catalyst activation process, new deactivation pathways occurring during catalysis have also been reported. As described by Carpentier and coworkers, the β -oxo ester substrate could act as a bidentate donor and replace the ligand backbone of asymmetric transfer hydrogenation catalyst (β -amino alcohol)(arene)Ru (**Figure 1. 14 A**).⁵¹ Inactive hydride-bridged metal dimers formed after the acid-induced or thermal dissociation of ligand from Ru or Ir center (**Figure 1. 14 B**).⁵² The bifunctional Ir complex with DPEN framework proved to degrade into iridacycles via C-H cleavage at the phenyl group of ligand

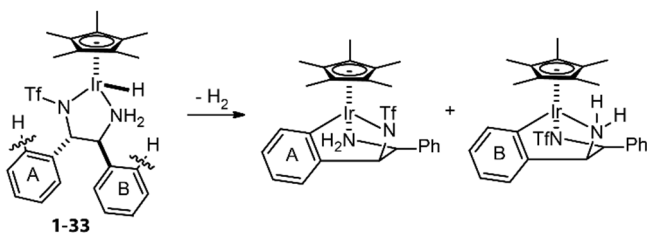
A) Replacement of ligand with substrate



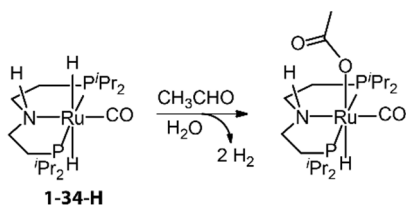
B) Formation of hydride-bridged dimer



C) C-H cleavage at phenyl group of ligand



D) Water trace-induced formation of acetato complex



E) Protonation-induced CO transfer between two complexes

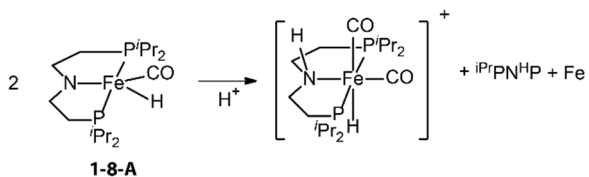


Figure 1. 14. Deactivation pathways of hydrogenation catalysts.

backbone (**Figure 1. 14 C**).⁵³ The traces of water in reaction medium could lead to the formation of inactive acetate Ru species from Ru-^{iPr}MACHO in the dehydrogenative coupling catalysis (**Figure 1. 14 D**).⁵⁴ When amido Fe-^{iPr}PNP was protonated by a bulky Brønsted acid, the resulting cationic complex could capture carbonyl from another complex and enter the inhibited state.⁵⁵ Meanwhile the other catalyst that provided the ancillary CO ligand would fully decompose to free ligand and iron nanoparticles (**Figure 1. 14 E**).

A common protocol to confirm the presence of catalyst deactivation is to check if a reaction gives non-quantitative conversion in prolonged reaction time. This is however not a robust indicator. Catalyst deactivation is not an instant process, and the remaining active catalyst species would promote the reaction before fully degrading. For a certain hydrogenation reaction, the negative effect of the catalyst deactivation on the final catalytic results can be compensated by increasing the initial catalyst concentration (**Figure 1. 15**). In general, full conversion of a catalytic reaction can be achieved as long as adequate amounts of the catalyst are added, which is not applicable when the deactivation rate of the catalyst is extremely high. For a good catalyst, its deactivation side-reactions feature high energy barrier and progress with relatively sluggish rate compared to catalytic turnover. Therefore, the deactivation can be easily overlooked and is significantly more noticeable at low catalyst loading. For instance, the transfer hydrogenation of acetophenone with 25 ppm Mn-CN catalyst **1-35** at 70 °C rapidly halted at around 1 h with 8% yield, while the catalysis with 50 and 75 ppm catalyst did not show signs of imminent termination (**Figure 1. 16**).⁵⁶ The high energy barrier of the deactivation process can also render it extremely sensitive to temperature change. Namely, the rate of deactivation increases faster than that of catalysis when the temperature increases. In the same transfer hydrogenation system, the reaction at 70°C was faster initially but was surpassed by the reaction performed

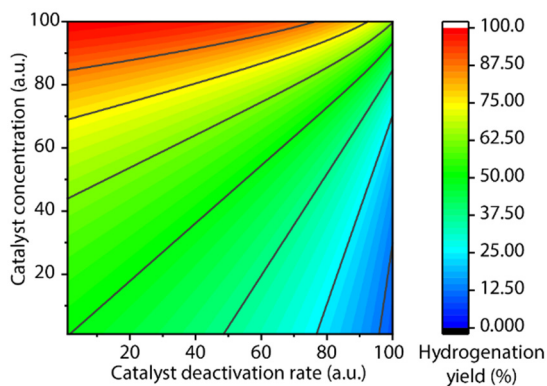


Figure 1.15. The competitive effects of initial catalyst concentration and catalyst deactivation rate on final reaction yield. The kinetic model of a catalytic ester hydrogenation reaction was used to predict the final conversions (the conversion at very long reaction time) at variable initial catalyst concentration and catalyst deactivation rates (assumed as a first-order deactivation).

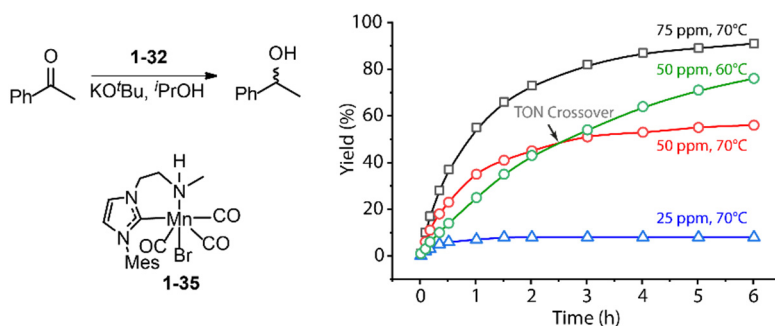


Figure 1.16. More noticeable catalyst deactivation at low catalyst loadings and high reaction temperatures. (Left) The transfer hydrogenation of acetophenone catalyzed by Mn-CN **1-35**. (Right) The kinetic profile of the left catalysis at catalyst loadings of 25, 50 and 75 ppm and reaction temperatures of 60 and 70 °C. Adapted with permission from ref (56). © Licensed under a [CC BY-NC 4.0 license](https://creativecommons.org/licenses/by-nc/4.0/).

at 60 °C with same amount of **1-35** (50 ppm). This difference occurred due to the faster deactivation at 70°C, evident from the typical TON crossover point where a low temperature reaction begins being more beneficial in terms of number of turnovers compared to the high temperature reaction.

Although catalyst deactivation is ultimately inevitable, the catalytic performance can still be improved by tuning the balance between deactivation and productive

conversion. In case of Ir catalyst **1-33**, the removal of the phenyl group responsible for metallacycle formation (*Figure 1. 14 C*) offered a new catalyst that achieved 2-time higher TON in the H₂ evolution from formic acid for 125 min. For catalyst that suffer from reaction with water, e.g. **1-34-H**, the addition of molecular sieves or alkoxide base would allow maintaining sustained catalytic activity. In addition, moving to pincer ligands from mono- or bidentate ones has been demonstrated as an effective strategy to counter the catalyst deactivation. Indeed, for example, extending the bidentate 'CN' ligand of **1-35** with additional phosphine donor led to a robust catalyst (Mn-CNP **1-1**, *Figure 1. 3 A*) that could tolerate high temperature up to 120 °C (see Chapter 2). While the reduction rates with Mn-CNP were inferior to those with **1-35** at low temperatures, the improvement of thermal stability opened a broader temperature window for catalysis operation, among which enhanced catalytic performance was eventually achieved. This catalyst gave rise to an unprecedented turnover number (up to 200 000) in the hydrogenation of ketones at 120 °C.

1.5 Summary and outlook

We hopefully demonstrate that the catalyst performance is defined by a complex reaction network comprised of multiple stages of catalyst operation. The rate and selectivity of precatalyst activation, the compositional effects imposed by reaction environment and the catalyst deactivation dynamics all play a role in determining the outcomes of catalytic hydrogenations. Studying these crucial parameters can provide direct instructions for improving catalytic systems. It can also help us comprehensively describe the complex reactivity networks so that the work put in catalyst optimization would progressively rely on more and more existing knowledge.

In Chapter 2 we discuss a multitude of reactivity pathways and new unexpected properties that Mn pincer complexes can exhibit in catalysis and during

activation (**Figure 1. 3**). Chapter 4 provides an example of the importance of mechanistic analysis for interpreting catalytic phenomena. Here we examined the deactivation of Mn ester hydrogenation pincer catalysts and found that important reaction parameters like catalyst speciation and reaction thermodynamics not only are dynamic and change through the course of reaction, but are also subject to external control by reaction promoters (**Figure 1. 11** and **Figure 1. 12**). Finally in Chapter 3 we argue that the type of reaction under study also falls in the category of dynamic variables in catalysis. In this Chapter, we show how suppression of target reactivity for which the catalyst is originally optimized, can produce new types of catalyst with unknown reactivity patterns (**Figure 1. 6**).

Acknowledging the challenge of extracting such chemical information from the optimization studies with yield as the only metric of catalytic performance, we suggest that more data of kinetic and mechanistic nature need to be examined. While collecting massive kinetic datasets is burdensome and time-consuming on its own, data-driven approach based on statistic modelling can be highly informative. A representative case of such analysis is described in this thesis in Chapter 5, which proved the possibility for extracting kinetic information from high-throughput screening/optimization experiments.⁵⁷

1.6 References

1. Rylander, P. N., *Catalytic Hydrogenation in Organic Syntheses: Paul Rylander*. Academic Press: New York, 1979.
2. Carruthers, J.; Carruthers, W.; Coldham, I., *Modern methods of organic synthesis*. Cambridge University Press: 2004.
3. (a) Weissermel, K.; Arpe, H.-J., *Industrial organic chemistry*. John Wiley & Sons: 2008; (b) Pritchard, J.; Filonenko, G. A.; Van Putten, R.; Hensen, E. J.; Pidko, E. A., Heterogeneous and homogeneous catalysis for the hydrogenation of carboxylic acid derivatives: history, advances and future directions. *Chem. Soc. Rev.* **2015**, *44*, 3808-3833.
4. Vries, J. G. d., *The handbook of homogeneous hydrogenation*. Wiley-Vch: Weinheim, 2007.

5. (a) Ault, A., The Nobel prize in chemistry for 2001. *J. Chem. Educ.* **2002**, *79*, 572; (b) Noyori, R., Centenary Lecture. Chemical multiplication of chirality: Science and applications. *Chem. Soc. Rev.* **1989**, *18*, 187-208; (c) Noyori, R., Chiral metal complexes as discriminating molecular catalysts. *Science* **1990**, *248*, 1194-1199; (d) Noyori, R.; Takaya, H., BINAP: an efficient chiral element for asymmetric catalysis. *Acc. Chem. Res.* **1990**, *23*, 345-350.
6. (a) Hashiguchi, S.; Fujii, A.; Takehara, J.; Ikariya, T.; Noyori, R., Asymmetric transfer hydrogenation of aromatic ketones catalyzed by chiral ruthenium (II) complexes. *J. Am. Chem. Soc.* **1995**, *117*, 7562-7563; (b) Fujii, A.; Hashiguchi, S.; Uematsu, N.; Ikariya, T.; Noyori, R., Ruthenium (II)-catalyzed asymmetric transfer hydrogenation of ketones using a formic acid– triethylamine mixture. *J. Am. Chem. Soc.* **1996**, *118*, 2521-2522; (c) Takehara, J.; Hashiguchi, S.; Fujii, A.; Inoue, S.-i.; Ikariya, T.; Noyori, R., Amino alcohol effects on the ruthenium (II)-catalysed asymmetric transfer hydrogenation of ketones in propan-2-ol. *Chem. Commun.* **1996**, 233-234; (d) Haack, K. J.; Hashiguchi, S.; Fujii, A.; Ikariya, T.; Noyori, R., The Catalyst Precursor, Catalyst, and Intermediate in the RuII-Promoted Asymmetric Hydrogen Transfer between Alcohols and Ketones. *Angew. Chem. Int. Ed. Engl.* **1997**, *36*, 285-288; (e) Matsumura, K.; Hashiguchi, S.; Ikariya, T.; Noyori, R., Asymmetric transfer hydrogenation of α , β -acetylenic ketones. *J. Am. Chem. Soc.* **1997**, *119*, 8738-8739; (f) Murata, K.; Okano, K.; Miyagi, M.; Iwane, H.; Noyori, R.; Ikariya, T., A practical stereoselective synthesis of chiral hydrobenzoin via asymmetric transfer hydrogenation of benzils. *Org. Lett.* **1999**, *1*, 1119-1121; (g) Yamakawa, M.; Ito, H.; Noyori, R., The metal– ligand bifunctional catalysis: A theoretical study on the ruthenium (II)-catalyzed hydrogen transfer between alcohols and carbonyl compounds. *J. Am. Chem. Soc.* **2000**, *122*, 1466-1478; (h) Noyori, R.; Yamakawa, M.; Hashiguchi, S., Metal– ligand bifunctional catalysis: a nonclassical mechanism for asymmetric hydrogen transfer between alcohols and carbonyl compounds. *J. Org. Chem.* **2001**, *24*, 7931-7944; (i) Yamakawa, M.; Yamada, I.; Noyori, R., CH/ π Attraction: The Origin of Enantioselectivity in Transfer Hydrogenation of Aromatic Carbonyl Compounds Catalyzed by Chiral η^6 -Arene-Ruthenium (ii) Complexes. *Angew. Chem. Int. Ed.* **2001**, *40*, 2881-2821; (j) Hayes, A. M.; Morris, D. J.; Clarkson, G. J.; Wills, M., A class of ruthenium (II) catalyst for asymmetric transfer hydrogenations of ketones. *J. Am. Chem. Soc.* **2005**, *127*, 7318-7319.
7. (a) Teunissen, H. T.; Elsevier, C. J., Ruthenium catalysed hydrogenation of dimethyl oxalate to ethyleneglycol. *Chem. Commun.* **1997**, 667-668; (b) Teunissen, H., Homogeneous ruthenium catalyzed hydrogenation of esters to alcohols. *Chem. Commun.* **1998**, 1367-1368; (c) van Engelen, M. C.; Teunissen, H. T.; de Vries, J. G.; Elsevier, C. J., Suitable ligands for homogeneous ruthenium-catalyzed hydrogenolysis of esters. *J. Mol. Catal. A: Chem.* **2003**, *206*, 185-192; (d) Rosi, L.; Frediani, M.; Frediani, P., Isotopomeric diols by “one-pot” Ru-catalyzed homogeneous hydrogenation of dicarboxylic acids. *J. Organomet Chem* **2010**, *695*, 1314-1322; (e) Hanton, M. J.; Tin, S.; Boardman, B. J.; Miller,

P., Ruthenium-catalysed hydrogenation of esters using tripodal phosphine ligands. *J. Mol. Catal. A: Chem.* **2011**, *346*, 70-78.

8. Zhang, J.; Leitus, G.; Ben-David, Y.; Milstein, D., Efficient homogeneous catalytic hydrogenation of esters to alcohols. *Angew. Chem. Int. Ed.* **2006**, *45*, 1113-1115.

9. Kuriyama, W.; Matsumoto, T.; Ogata, O.; Ino, Y.; Aoki, K.; Tanaka, S.; Ishida, K.; Kobayashi, T.; Sayo, N.; Saito, T., Catalytic hydrogenation of esters. Development of an efficient catalyst and processes for synthesising (R)-1, 2-propanediol and 2-(1-menthoxy) ethanol. *Org. Process Res. Dev.* **2012**, *16*, 166-171.

10. Khusnutdinova, J. R.; Milstein, D., Metal–ligand cooperation. *Angew. Chem. Int. Ed.* **2015**, *54*, 12236-12273.

11. (a) Dub, P. A.; Scott, B. L.; Gordon, J. C., Why does alkylation of the N–H functionality within M/NH bifunctional Noyori-type catalysts lead to turnover? *J. Am. Chem. Soc.* **2017**, *139*, 1245-1260; (b) Dub, P. A.; Gordon, J. C., The role of the metal-bound N–H functionality in Noyori-type molecular catalysts. *Nat. Rev. Chem.* **2018**, *2*, 396-408.

12. (a) Werkmeister, S.; Neumann, J.; Junge, K.; Beller, M., Pincer-Type Complexes for Catalytic (De) Hydrogenation and Transfer (De) Hydrogenation Reactions: Recent Progress. *Chem. Eur. J.* **2015**, *21*, 12226-12250; (b) Alig, L.; Fritz, M.; Schneider, S., First-row transition metal (de) hydrogenation catalysis based on functional pincer ligands. *Chem. Rev.* **2018**, *119*, 2681-2751.

13. (a) McQuillin, F. J., *Homogeneous hydrogenation in organic chemistry*. Springer Science & Business Media: 2012; Vol. 1; (b) Chaloner, P. A.; Esteruelas, M. A.; Joó, F.; Oro, L. A., *Homogeneous hydrogenation*. Springer Science & Business Media: 2013; Vol. 15; (c) Etayo, P.; Vidal-Ferran, A., Rhodium-catalysed asymmetric hydrogenation as a valuable synthetic tool for the preparation of chiral drugs. *Chem. Soc. Rev.* **2013**, *42*, 728-754; (d) Gunanathan, C.; Milstein, D., Bond activation and catalysis by ruthenium pincer complexes. *Chem. Rev.* **2014**, *114*, 12024-12087.

14. (a) Filonenko, G. A.; van Putten, R.; Hensen, E. J.; Pidko, E. A., Catalytic (de) hydrogenation promoted by non-precious metals–Co, Fe and Mn: recent advances in an emerging field. *Chem. Soc. Rev.* **2018**, *47*, 1459-1483; (b) Gorgas, N.; Kirchner, K., Isoelectronic manganese and iron hydrogenation/dehydrogenation catalysts: Similarities and divergences. *Acc. Chem. Res.* **2018**, *51*, 1558-1569; (c) Kallmeier, F.; Kempe, R., Manganese Complexes for (De) Hydrogenation Catalysis: A Comparison to Cobalt and Iron Catalysts. *Angew. Chem. Int. Ed.* **2018**, *57*, 46-60; (d) Mukherjee, A.; Milstein, D., Homogeneous catalysis by cobalt and manganese pincer complexes. *ACS Catal.* **2018**, *8*, 11435-11469; (e) Wang, Y.; Wang, M.; Li, Y.; Liu, Q., Homogeneous manganese-catalyzed hydrogenation and dehydrogenation reactions. *Chem* **2020**, *7*, 1180-1223; (f) Azouzi, K.;

Valyaev, D. A.; Bastin, S.; Sortais, J.-B., Manganese—new prominent actor in transfer hydrogenation catalysis. *Curr. Opin. Green Sust.* **2021**, *31*, 100511; (g) Clarke, M. L.; Widegren, M. B., Hydrogenation reactions using Group III to Group VII transition metals. *Homogeneous Hydrogenation with Non-Precious Catalysts* **2019**, 111-140.

15. (a) Stephan, D. W., Frustrated Lewis pairs: from concept to catalysis. *Acc. Chem. Res.* **2015**, *48*, 306-316; (b) Stephan, D. W., Frustrated Lewis pairs. *J. Am. Chem. Soc.* **2015**, *137*, 10018-10032; (c) Stephan, D. W.; Erker, G., Frustrated Lewis pair chemistry: development and perspectives. *Angew. Chem. Int. Ed.* **2015**, *54*, 6400-6441; (d) Stephan, D. W., The broadening reach of frustrated Lewis pair chemistry. *Science* **2016**, *354*, aaf7229; (e) Scott, D. J.; Fuchter, M. J.; Ashley, A. E., Designing effective 'frustrated Lewis pair' hydrogenation catalysts. *Chem. Soc. Rev.* **2017**, *46*, 5689-5700; (f) Jupp, A. R.; Stephan, D. W., New directions for frustrated Lewis pair chemistry. *Trends in Chemistry* **2019**, *1*, 35-48; (g) Lam, J.; Szkop, K. M.; Mosaferi, E.; Stephan, D. W., FLP catalysis: main group hydrogenations of organic unsaturated substrates. *Chem. Soc. Rev.* **2019**, *48*, 3592-3612; (h) Feng, X.; Meng, W.; Du, H., Frustrated Lewis Pair Catalyzed Asymmetric Reactions. In *Frustrated Lewis Pairs*, Springer: 2021; pp 29-86.

16. Yang, W.; Chernyshov, I. Y.; van Schendel, R. K.; Weber, M.; Müller, C.; Filonenko, G. A.; Pidko, E. A., Robust and efficient hydrogenation of carbonyl compounds catalysed by mixed donor Mn (I) pincer complexes. *Nat. Commun.* **2021**, *12*, 1-8.

17. (a) Reppe, W.; Vetter, H., Carbonylierung VI. Synthesen mit metallcarbonylwasserstoffen. *Justus Liebig's Annalen der Chemie* **1953**, *582*, 133-161; (b) Knölker, H.-J.; Heber, J.; Mahler, C. H., Transition metal-diene complexes in organic synthesis. XIV: Regioselective iron-mediated [2+ 2+ 1] cycloadditions of alkynes and carbon monoxide: synthesis of substituted cyclopentadienones. *Synlett* **1992**, 1002-1004; (c) Knölker, H.-J.; Heber, J., Transition metal-diene complexes in organic synthesis. XVIII: Iron-mediated [2+ 2+ 1] cycloadditions of diynes and carbon monoxide: selective demetalation reactions. *Synlett* **1993**, 924-926; (d) Knölker, H.-J.; Baum, E.; Heber, J., Transition Metal-Diene Complexes in Organic Synthesis, Part 25.1 Cycloadditions of Annulated 2, 5-Bis (trimethylsilyl) cyclopentadienones. *Tetrahedron Lett.* **1995**, *36*, 7647-7650.

18. (a) Casey, C. P.; Guan, H., An efficient and chemoselective iron catalyst for the hydrogenation of ketones. *J. Am. Chem. Soc.* **2007**, *129*, 5816-5817; (b) Knölker, H. J.; Baum, E.; Goesmann, H.; Klauss, R., Demetalation of Tricarbonyl (cyclopentadienone) iron Complexes Initiated by a Ligand Exchange Reaction with NaOH—X-Ray Analysis of a Complex with Nearly Square-Planar Coordinated Sodium. *Angew. Chem. Int. Ed.* **1999**, *38*, 2064-2066.

19. Berkessel, A.; Reichau, S.; von der Höh, A.; Leconte, N.; Neudörfl, J. r.-M., Light-Induced Enantioselective Hydrogenation Using Chiral Derivatives of Casey's Iron-Cyclopentadienone Catalyst. *Organometallics* **2011**, *30*, 3880-3887.
20. (a) Pagnoux-Ozherelyeva, A.; Pannetier, N.; Mbaye, M. D.; Gaillard, S.; Renaud, J. L., Knölker's iron complex: an efficient in situ generated catalyst for reductive amination of alkyl aldehydes and amines. *Angew. Chem. Int. Ed.* **2012**, *51*, 4976-4980; (b) Fleischer, S.; Zhou, S.; Junge, K.; Beller, M., General and highly efficient iron-catalyzed hydrogenation of aldehydes, ketones, and α , β -unsaturated aldehydes. *Angew. Chem. Int. Ed.* **2013**, *52*, 5120-5124; (c) Moulin, S.; Dentel, H.; Pagnoux-Ozherelyeva, A.; Gaillard, S.; Poater, A.; Cavallo, L.; Lohier, J. F.; Renaud, J. L., Bifunctional (cyclopentadienone) iron-tricarbonyl complexes: synthesis, computational studies and application in reductive amination. *Chem. Eur. J.* **2013**, *19*, 17881-17890; (d) Yan, T.; Feringa, B. L.; Barta, K., Iron catalysed direct alkylation of amines with alcohols. *Nat. Commun.* **2014**, *5*, 1-7; (e) Rosas-Hernández, A.; Alsabeh, P. G.; Barsch, E.; Junge, H.; Ludwig, R.; Beller, M., Highly active and selective photochemical reduction of CO₂ to CO using molecular-defined cyclopentadienone iron complexes. *Chem. Commun.* **2016**, *52*, 8393-8396; (f) Yan, T.; Feringa, B. L.; Barta, K., Benzylamines via iron-catalyzed direct amination of benzyl alcohols. *ACS Catal.* **2016**, *6*, 381-388.
21. (a) Sanford, M. S.; Love, J. A.; Grubbs, R. H., Mechanism and Activity of Ruthenium Olefin Metathesis Catalysts. *J. Am. Chem. Soc.* **2001**, *123*, 6543-6554; (b) Biscoe, M. R.; Fors, B. P.; Buchwald, S. L., A New Class of Easily Activated Palladium Precatalysts for Facile C–N Cross-Coupling Reactions and the Low Temperature Oxidative Addition of Aryl Chlorides. *J. Am. Chem. Soc.* **2008**, *130*, 6686-6687; (c) Melvin, P. R.; Balcells, D.; Hazari, N.; Nova, A., Understanding Precatalyst Activation in Cross-Coupling Reactions: Alcohol Facilitated Reduction from Pd(II) to Pd(0) in Precatalysts of the Type (η^3 -allyl)Pd(L)(Cl) and (η^3 -indenyl)Pd(L)(Cl). *ACS Catal.* **2015**, *5*, 5596-5606.
22. (a) Vailati Facchini, S.; Neudörfl, J. M.; Pignataro, L.; Cettolin, M.; Gennari, C.; Berkessel, A.; Piarulli, U., Synthesis of [Bis (hexamethylene) cyclopentadienone] iron Tricarbonyl and its Application to the Catalytic Reduction of C=O Bonds. *ChemCatChem* **2017**, *9*, 1461-1468; (b) Del Grosso, A.; Chamberlain, A. E.; Clarkson, G. J.; Wills, M., Synthesis and applications to catalysis of novel cyclopentadienone iron tricarbonyl complexes. *Dalton Transactions* **2018**, *47*, 1451-1470.
23. Plank, T. N.; Drake, J. L.; Kim, D. K.; Funk, T. W., Air-Stable, Nitrile-Ligated (Cyclopentadienone) iron Dicarbonyl Compounds as Transfer Reduction and Oxidation Catalysts. *Adv. Synth. Catal.* **2012**, *354*, 597-601.
24. Koehne, I.; Schmeier, T. J.; Bielinski, E. A.; Pan, C. J.; Lagaditis, P. O.; Bernskoetter, W. H.; Takase, M. K.; Würtele, C.; Hazari, N.; Schneider, S., Synthesis and

structure of six-coordinate iron borohydride complexes supported by PNP ligands. *Inorg. Chem.* **2014**, *53*, 2133-2143.

25. Werkmeister, S.; Junge, K.; Wendt, B.; Alberico, E.; Jiao, H.; Baumann, W.; Junge, H.; Gallou, F.; Beller, M., Hydrogenation of esters to alcohols with a well-defined iron complex. *Angew. Chem. Int. Ed.* **2014**, *53*, 8722-8726.

26. Chakraborty, S.; Dai, H.; Bhattacharya, P.; Fairweather, N. T.; Gibson, M. S.; Krause, J. A.; Guan, H., Iron-based catalysts for the hydrogenation of esters to alcohols. *J. Am. Chem. Soc.* **2014**, *136*, 7869-7872.

27. Qu, S.; Dai, H.; Dang, Y.; Song, C.; Wang, Z.-X.; Guan, H., Computational mechanistic study of Fe-catalyzed hydrogenation of esters to alcohols: improving catalysis by accelerating precatalyst activation with a Lewis base. *ACS Catal.* **2014**, *4*, 4377-4388.

28. Osborn, J. A.; Jardine, F. H.; Young, J. F.; Wilkinson, G., The preparation and properties of tris (triphenylphosphine) halogenorhodium (I) and some reactions thereof including catalytic homogeneous hydrogenation of olefins and acetylenes and their derivatives. *Journal of the Chemical Society A: Inorganic, Physical, Theoretical* **1966**, 1711-1732.

29. (a) Schrock, R. R.; Osborn, J. A., Catalytic hydrogenation using cationic rhodium complexes. I. Evolution of the catalytic system and the hydrogenation of olefins. *J. Am. Chem. Soc.* **1976**, *98*, 2134-2143; (b) Crabtree, R., Iridium compounds in catalysis. *Acc. Chem. Res.* **1979**, *12*, 331-337.

30. Weber, S.; Stöger, B.; Veiros, L. F.; Kirchner, K., Rethinking Basic Concepts—Hydrogenation of Alkenes Catalyzed by Bench-Stable Alkyl Mn (I) Complexes. *ACS Catal.* **2019**, *9*, 9715-9720.

31. Yang, W.; Chernyshov, I. Y.; Weber, M.; Pidko, E. A.; Filonenko, G. A., Switching between Hydrogenation and Olefin Transposition Catalysis via Silencing NH Cooperativity in Mn(I) Pincer Complexes. *ACS Catal.* **2022**, *17*, 10818-10825.

32. Elangovan, S.; Topf, C.; Fischer, S.; Jiao, H.; Spannenberg, A.; Baumann, W.; Ludwig, R.; Junge, K.; Beller, M., Selective catalytic hydrogenations of nitriles, ketones, and aldehydes by well-defined manganese pincer complexes. *J. Am. Chem. Soc.* **2016**, *138*, 8809-8814.

33. Zell, T.; Langer, R., From Ruthenium to Iron and Manganese—A Mechanistic View on Challenges and Design Principles of Base-Metal Hydrogenation Catalysts. *ChemCatChem* **2018**, *10*, 1930-1940.

34. Bielinski, E. A.; Lagaditis, P. O.; Zhang, Y.; Mercado, B. Q.; Würtele, C.; Bernskoetter, W. H.; Hazari, N.; Schneider, S., Lewis acid-assisted formic acid

dehydrogenation using a pincer-supported iron catalyst. *J. Am. Chem. Soc.* **2014**, *136*, 10234-10237.

35. Anaby, A.; Schelwies, M.; Schwaben, J.; Rominger, F.; Hashmi, A. S. K.; Schaub, T., Study of precatalyst degradation leading to the discovery of a new Ru⁰ precatalyst for hydrogenation and dehydrogenation. *Organometallics* **2018**, *37*, 2193-2201.

36. Sun, X.; Manos, G.; Blacker, J.; Martin, J.; Gavriilidis, A., Asymmetric Transfer Hydrogenation of Acetophenone with 1 R, 2 S-Aminoindanol/Pentamethylcyclopentadienylrhodium Catalyst. *Org. Process Res. Dev.* **2004**, *8*, 909-914.

37. (a) Sun, Y.; Koehler, C.; Tan, R.; Annibale, V. T.; Song, D., Ester hydrogenation catalyzed by Ru-CNN pincer complexes. *Chem. Commun.* **2011**, *47*, 8349-8351; (b) He, T.; Buttner, J. C.; Reynolds, E. F.; Pham, J.; Malek, J. C.; Keith, J. M.; Chianese, A. R., Dehydroalkylative activation of CNN-and PNN-pincer ruthenium catalysts for ester hydrogenation. *J. Am. Chem. Soc.* **2019**, *141*, 17404-17413; (c) Le, L.; Liu, J.; He, T.; Malek, J. C.; Cervarich, T. N.; Buttner, J. C.; Pham, J.; Keith, J. M.; Chianese, A. R., Unexpected CNN-to-CC Ligand Rearrangement in Pincer-Ruthenium Precatalysts Leads to a Base-Free Catalyst for Ester Hydrogenation. *Organometallics* **2019**, *38*, 3311-3321; (d) Tindall, D. J.; Menche, M.; Schelwies, M.; Paciello, R. A.; Schäfer, A.; Comba, P.; Rominger, F.; Hashmi, A. S. K.; Schaub, T., Ru⁰ or Ru^{II}: A Study on Stabilizing the “Activated” Form of Ru-PNP Complexes with Additional Phosphine Ligands in Alcohol Dehydrogenation and Ester Hydrogenation. *Inorg. Chem.* **2020**, *59*, 5099-5115.

38. Spasyuk, D.; Smith, S.; Gusev, D. G., From esters to alcohols and back with ruthenium and osmium catalysts. *Angew. Chem. Int. Ed.* **2012**, *51*, 2772-2775.

39. Freitag, F.; Irrgang, T.; Kempe, R., Mechanistic Studies of Hydride Transfer to Imines from a Highly Active and Chemoselective Manganate Catalyst. *J. Am. Chem. Soc.* **2019**, *141*, 11677-11685.

40. Tossaint, A. S.; Rebreyend, C.; Sinha, V.; Weber, M.; Canossa, S.; Pidko, E. A.; Filonenko, G. A., Two step activation of Ru-PN3P pincer catalysts for CO₂ hydrogenation. *Catal. Sci. Technol.* **2022**, *12*, 2972-2977.

41. Krieger, A. M.; Kuliaev, P.; Armstrong Hall, F. Q.; Sun, D.; Pidko, E. A., Composition-and Condition-Dependent Kinetics of Homogeneous Ester Hydrogenation by a Mn-Based Catalyst. *J. Phys. Chem. C* **2020**, *124*, 26990-26998.

42. Klamt, A., The COSMO and COSMO-RS solvation models. *Wiley Interdisciplinary Reviews: Computational Molecular Science* **2011**, *1*, 699-709.

43. Yang, W.; Kalavalapalli, T. Y.; Krieger, A. M.; Khvorost, T. A.; Chernyshov, I. Y.; Weber, M.; Uslamin, E. A.; Pidko, E. A.; Filonenko, G. A., Basic Promotors Impact

Thermodynamics and Catalyst Speciation in Homogeneous Carbonyl Hydrogenation. *J. Am. Chem. Soc.* **2022**, *144*, 8129-8137.

44. Krieger, A. M.; Sinha, V.; Kalikadien, A. V.; Pidko, E. A., Metal-ligand cooperative activation of HX (X= H, Br, OR) bond on Mn based pincer complexes. *Z. Anorg. Allg. Chem.* **2021**, *647*, 1486-1494.

45. Hansen, K. B.; Rosner, T.; Kubryk, M.; Dormer, P. G.; Armstrong, J. D., Detection and elimination of product inhibition from the asymmetric catalytic hydrogenation of enamines. *Org. Lett.* **2005**, *7*, 4935-4938.

46. Van Putten, R.; Uslamin, E. A.; Garbe, M.; Liu, C.; Gonzalez-de-Castro, A.; Lutz, M.; Junge, K.; Hensen, E. J.; Beller, M.; Lefort, L.; Pidko, E. A., Non-Pincer-Type Manganese Complexes as Efficient Catalysts for the Hydrogenation of Esters. *Angew. Chem. Int. Ed.* **2017**, *56*, 7531-7534.

47. Bernskoetter, W. H.; Hazari, N., Reversible hydrogenation of carbon dioxide to formic acid and methanol: Lewis acid enhancement of base metal catalysts. *Acc. Chem. Res.* **2017**, *50*, 1049-1058.

48. Heimann, J. E.; Bernskoetter, W. H.; Hazari, N.; Mayer, J. M., Acceleration of CO₂ insertion into metal hydrides: ligand, Lewis acid, and solvent effects on reaction kinetics. *Chem. Sci.* **2018**, *9*, 6629-6638.

49. Crabtree, R. H., Deactivation in homogeneous transition metal catalysis: causes, avoidance, and cure. *Chem. Rev.* **2015**, *115*, 127-150.

50. Alberico, E.; Sponholz, P.; Cordes, C.; Nielsen, M.; Drexler, H. J.; Baumann, W.; Junge, H.; Beller, M., Selective hydrogen production from methanol with a defined iron pincer catalyst under mild conditions. *Angew. Chem. Int. Ed.* **2013**, *52*, 14162-14166.

51. (a) Everaere, K.; Mortreux, A.; Bulliard, M.; Brussee, J.; van der Gen, A.; Nowogrocki, G.; Carpentier, J. F., (β -Amino alcohol)(arene) ruthenium (II)-Catalyzed Asymmetric Transfer Hydrogenation of Functionalized Ketones– Scope, Isolation of the Catalytic Intermediates, and Deactivation Processes. *Eur. J. Org. Chem.* **2001**, *2001*, 275-291; (b) Everaere, K.; Mortreux, A.; Carpentier, J. F., Ruthenium (II)-Catalyzed Asymmetric Transfer Hydrogenation of Carbonyl Compounds with 2-Propanol and Ephedrine-Type Ligands. *Adv. Synth. Catal.* **2003**, *345*, 67-77.

52. (a) Letko, C. S.; Heiden, Z. M.; Rauchfuss, T. B., Activation and deactivation of Cp* Ir (TsDPEN) hydrogenation catalysts in water. Wiley Online Library: 2009; (b) Hall, A. M.; Dong, P.; Codina, A.; Lowe, J. P.; Hintermair, U., Kinetics of Asymmetric Transfer Hydrogenation, Catalyst Deactivation, and Inhibition with Noyori Complexes As Revealed by Real-Time High-Resolution FlowNMR Spectroscopy. *ACS Catal.* **2019**, *9*, 2079-2090.

53. Matsunami, A.; Kuwata, S.; Kayaki, Y., A bifunctional iridium catalyst modified for persistent hydrogen generation from formic acid: Understanding deactivation via cyclometalation of a 1, 2-Diphenylethylenediamine motif. *ACS Catal.* **2017**, *7*, 4479-4484.
54. Nguyen, D. H.; Trivelli, X.; Capet, F.; Swesi, Y.; Favre-Réguillon, A.; Vanoye, L.; Dumeignil, F.; Gauvin, R. M., Deeper mechanistic insight into Ru pincer-mediated acceptorless dehydrogenative coupling of alcohols: exchanges, intermediates, and deactivation species. *ACS Catal.* **2018**, *8*, 4719-4734.
55. Curley, J. B.; Smith, N. E.; Bernskoetter, W. H.; Ertem, M. Z.; Hazari, N.; Mercado, B. Q.; Townsend, T. M.; Wang, X., Understanding the Reactivity and Decomposition of a Highly Active Iron Pincer Catalyst for Hydrogenation and Dehydrogenation Reactions. *ACS Catal.* **2021**, *11*, 10631-10646.
56. van Putten, R.; Benschop, J.; de Munck, V. J.; Weber, M.; Müller, C.; Filonenko, G. A.; Pidko, E. A., Efficient and Practical Transfer Hydrogenation of Ketones Catalyzed by a Simple Bidentate Mn– NHC Complex. *ChemCatChem* **2019**, *11*, 5232-5235.
57. van Schendel, R. K.; Yang, W.; Uslamin, E. A.; Pidko, E. A., Utilizing Design of Experiments Approach to Assess Kinetic Parameters for a Mn Homogeneous Hydrogenation Catalyst. *ChemCatChem* **2021**, *13*, 4886-4896.

**Countering Deactivation and Accelerating
Activation: the Approach to a Robust and
Efficient Mn(I) Carbonyl Hydrogenation
Catalyst**

Abstract

While representing a more sustainable alternative to conventional noble metal-based systems, manganese hydrogenation catalysts are prone to degradation under catalytic conditions once operation temperatures are high, leading to the significant decrease of their catalytic performance. Herein, we upgraded a Mn(I)-NHC catalyst by extending its bidentate ligand to pincer type ones. The resulting Mn-CNP catalyst showed enhanced thermal stability and could tolerate high reaction temperatures up to 120 °C. Higher turnover numbers for the hydrogenation of acetophenones were obtained with this new catalyst. Furthermore, our reactivity and kinetic analysis pointed to the crucial role of the catalyst activation step for the catalytic performance. While conventional activation employing alkoxide bases can ultimately provide catalytically competent species under hydrogen atmosphere, activation of Mn(I) precatalyst with hydride donor promoters, e.g. KHBET_3 , dramatically improves catalytic performance of the system and eliminates induction times associated with slow catalyst activation. With the improved activation method, the Mn-CNP gives rise to the excellent productivity (TOF up to $41\,000\text{ h}^{-1}$) and stability (TON up to 200 000) in hydrogenation catalysis. This system enables near-quantitative hydrogenation of ketones, imines, aldehydes and formate esters at the catalyst loadings as low as 5-200 ppm.

This chapter has been published as:

Wenjun Yang, Ivan Yu Chernyshov, Robin KA van Schendel, Manuela Weber, Christian Müller, Georgy A Filonenko, Evgeny A Pidko, *Nat. Commun.* **2021**, *12*, 1

Contributions: W.Y. designed, conducted the experiments, and analyzed the data; I.Y.C. performed the DFT calculation; R.K.A.S. conducted part of kinetics studies; M.W. and C.M. performed crystal structure determination and analysis; G.A.F. and E.A.P. supervised the research.

2.1 Introduction

Catalytic hydrogenation of carbonyl derivatives with molecular hydrogen is an essential technique for the production of bulk and fine chemicals.¹ The state of the art in hydrogenation catalysis to this date is laid down by well-defined noble metal complexes based on ruthenium, iridium, and rhodium.² However, the requirements for more sustainable hydrogenation processes recently initiated a search for earth-abundant, inexpensive 3d metals that can replace their noble counterparts.³ In this search, the catalysts based on highly biocompatible and abundant Mn metal became particularly prominent.⁴

Manganese-based hydrogenation catalysis has become a subject of intense research since 2016, largely set off by the pioneering work of Beller and co-workers.⁵ A Mn pincer complex **A** (**Figure 2. 1**) promoted hydrogenation of ketones, aldehydes and nitriles operating at 1-3 mol% loading at 60-120 °C and 10-50 bar H₂ pressure. Following the initial reports, the field of hydrogenation with Mn was extended to several prominent ligand platforms.^{4d, 4e, 6} Specifically, in addition to aminopincer ligands, the diamino triazine-based pincers **B** and lutidine-derived PNN pincer **C** ligands were introduced to Mn-catalyzed hydrogenations by the groups of Kempe⁷ and Milstein⁸, and saw further improvement in recent years.^{6k}

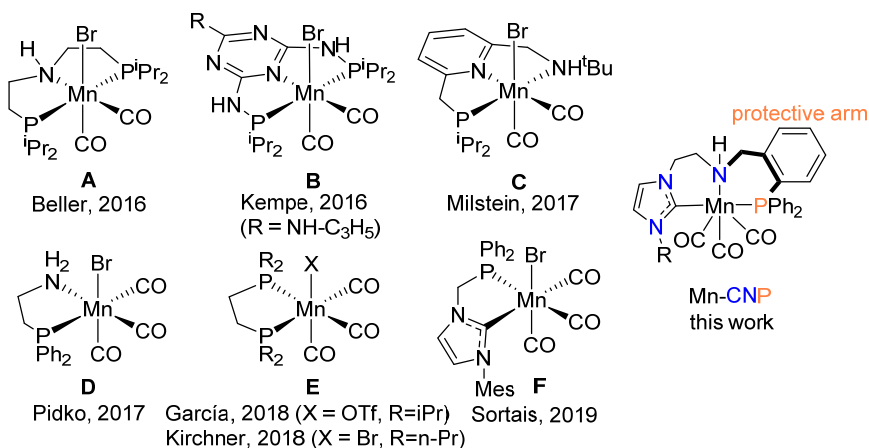


Figure 2. 1. Selected examples of Mn hydrogenation catalysts and the complex used in this work.

In addition to pincer ligands, several bidentate ligands have been employed in Mn catalysis. These include PN aminophosphines developed by our group (**D**, Figure 1),⁹ diphosphines **E** reported by the groups of Kirchner¹⁰ and García¹¹. The most recent addition to this set was reported by Sortais and co-workers who described catalyst **F** (Figure 2. 1) based on a bidentate ligand containing phosphine and N-heterocyclic carbene (NHC) donors. Together with catalyst **B**, complex **F** is one of the most potent Mn ketone hydrogenation catalysts requiring ca. 0.1 mol% catalyst loading for operation.¹²

The activity of Mn catalysts is generally lower than that of noble metal catalysts with majority of Mn-catalyzed hydrogenations requiring relatively high catalyst loadings of 0.1 - 5 mol% - a feature that strongly limits their practical utility. We recently demonstrated that reliance on such high metal loadings in Mn catalysis might stem from the limited stability of Mn pre-catalysts, most noticeable when Mn loadings are low.¹³ Namely, we noted that Mn(I)-NHC complexes featuring aminocarbene “CN” bidentate ligands were highly competent hydride transfer catalysts at low reaction temperatures, but a rapid catalyst degradation took place upon even marginal increase of reaction temperatures or reduction of catalyst loading below 100 ppm with respect to reduction substrate.¹³ Catalyst deactivation in the course of catalysis leads to the loss of the active catalyst species and the decay of catalytic performance. To counter this effect, we employed a pincer ligand platform (Figure 2. 1) in this work and developed an active and highly stable Mn(I) catalyst that can promote hydrogenation reactions at catalyst loadings as low as 5 parts per million.

2.2 Synthesis and hydrogenation activity of complex 3.

Our initial synthetic effort was targeted at addressing the stability of manganese catalysts utilizing bidentate “CN” ligands (**1**, Figure 2. 2) by extending the ligand with additional phosphine donor arm. This extension of CN ligand **1** was done via a straightforward reductive amination producing the air-stable **L1** in 81% yield (Figure 2. 2). The **L1** can undergo complexation to form **3** by a one-pot reaction involving pre-coordination to Mn(CO)₅Br followed by the base-assisted formation of the NHC complex (Figure 2. 2). Analytically pure MnCNP complex **3** was isolated in 51% yield with its identity confirmed by NMR and IR spectroscopy and elemental analysis (see section 2.6.1).

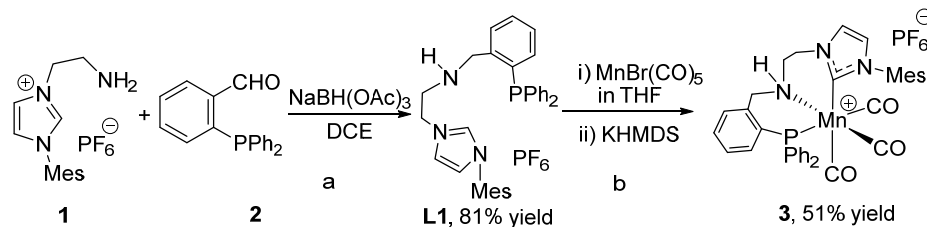
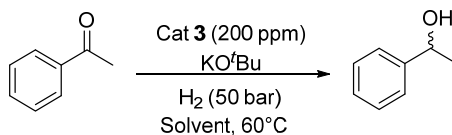


Figure 2. 2. Synthesis of Mn(I) complex **3**. **a.** Conditions: **1** (8 mmol), **2** (1 eq.), NaBH(OAc)₃ (2.5 eq.), DCE (20 mL), rt, 12 h. **b.** Conditions: i) **L1** (0.5 mmol), MnBr(CO)₅ (1 eq.), THF (5 mL), 50 °C - rt, 12 h; ii) KHMDS (1.1 eq.), rt, 3 h.

The IR spectrum of **3** features three strong bands at 2021, 1943, 1919 cm⁻¹ consistent with the presence of three carbonyl ligands in a *facial* arrangement within the cationic complex.¹⁵ The characteristic ³¹P resonances in NMR spectrum of **3** appear at δ = 37.53 (s), -144.4 (hep, ¹J_{FP} 712.8 Hz) ppm confirming the coordination of the phosphine donor arm and the presence of the hexafluorophosphate anion in **3**. Finally, the ¹³C NMR revealed resonances at 217.7, 215.5, 213.9, 187.0 ppm confirming the presence of three inequivalent carbonyl ligands and a Mn-bound NHC ligand.

Complex **3** is a potent and thermally stable pre-catalyst for ketone hydrogenation. We screened its performance in hydrogenation of acetophenone benchmark substrate in various solvents and found dioxane, diethyl ether, isopropanol, and methyl *tert*-butyl ether solvent to be optimal for performance (**Table 2. 1**, entries 1-8). In the screening experiments we determined the approximate reaction time by H₂ consumption traces. Namely, the reaction was stopped after the pressure of catalytic system stopped decreasing. According to this parameter, we identified that the activity of complex **3** in THF solvent was not high due to the long reaction time (23 h) for achieving full conversion (entry 7). Polar solvents, such as acetonitrile and methanol, were shown to be detrimental to the catalysis and led to the trace conversion of acetophenone (entries 7-8). The effect of different base loadings was subsequently investigated with 0.02-1 mol% KO^tBu (entries 9-15). Our results showed that about 2.5 eq. KO^tBu with respect to catalyst, that was at the same level of the base amounts required for precatalyst activation, was adequate to achieve the high activity of catalyst **3**. This result suggested that the primary role of base is to activate the precatalyst.

Table 2. 1. Screening of solvent and base amount for acetophenone hydrogenation with **3**.^a

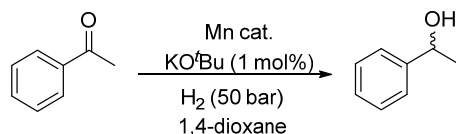
Entry	solvent	KO ^t Bu (mol%)	t (h) ^b	Y _{alc} (%) ^c
1	Dioxane	1	8	99
2	Diethyl ether	1	4	99
3	IPA	1	8	99
4	Toluene	1	23	45
5	MeCN	1	20	0
6	MeOH	1	20	13
7	THF	1	23	99
8	MTBE	1	8	99
9	Dioxane	1	6	99
10	Dioxane	0.5	6	99
11	Dioxane	0.1	6	99
12	Dioxane	0.05	6	99
13	Dioxane	0.04	7	5
14	Dioxane	0.03	7	3
15	Dioxane	0.02	7	TRACE

^a Reactions were conducted with acetophenone (5 mmol), Mn catalyst **3** (200 ppm), KO^tBu (1 mol%) in solvent (3 mL) at 60°C under 50 bar H₂. ^b Total reaction time and that of GC analysis. ^c Yield determined by GC with dodecane (0.25 mmol) as internal standard.

Although the preliminary screening results suggest diethyl ether as the optimal solvent, conducting high-temperature reaction in such volatile medium can be challenging in regard of maintaining the same substrate/catalyst concentration in parallel experiments. Therefore dioxane solvent and 1 mol% KO^tBu were further used to test the hydrogenation reactions with low-loading catalyst, which could potentially give high turnover numbers. The results listed in **Table 2. 2** indicate that the quantitative hydrogenation of

acetophenone to the corresponding alcohol can be obtained with catalyst loadings as low as 50 ppm at 60°C (entries 1-3). Importantly, catalyst **3** tolerates elevated reaction temperatures of 80 and 100 °C, that marks a significant improvement of thermal stability over the parent CN bidentate that rapidly degraded as the temperatures were elevated over 70°C.¹³ Even at 100 °C hydrogenations with **3** led to quantitative yields requiring only 50 ppm catalyst loading (Entries 5, 6). At low catalyst loading conditions, the activity of **3** compares favourably with a related MnPNP system **A**⁵ (Entries 4 and 5). The hydrogenation with **3** at 200 ppm loading at 80°C is complete within 3 hours, whereas catalyst **A** (**Table 2. 2**, entry 4) provides 67% conversion in 24 hours under identical conditions.

Table 2. 2 Manganese-catalyzed hydrogenation of acetophenone. ^a



Entry	Cat. (mol%/ppm)	T (°C)	t (h) ^b	Yield (%) ^c
1	3 (0.02/200)	60	16	99
2	3 (0.01/100)	60	16	99
3	3 (0.005/50)	60	46	99
4	A (0.02/200)	80	24	67
5	3 (0.02/200)	80	3	99
6	3 (0.02/200)	100	1	99
7	3 (0.01/100)	100	3	99
8	3 (0.005/50)	100	28	99
9	3 (0.0025/25)	100	28	87

^a Conditions: acetophenone (5 mmol), Mn catalyst **3**, KO^tBu (1 mol%), 1,4-dioxane (3 mL), P = 50 bar H₂. ^b Total reaction time and that of GC analysis, for H₂ uptake traces see **Figure 2. 3**. ^c Yield determined by GC with dodecane as internal standard.

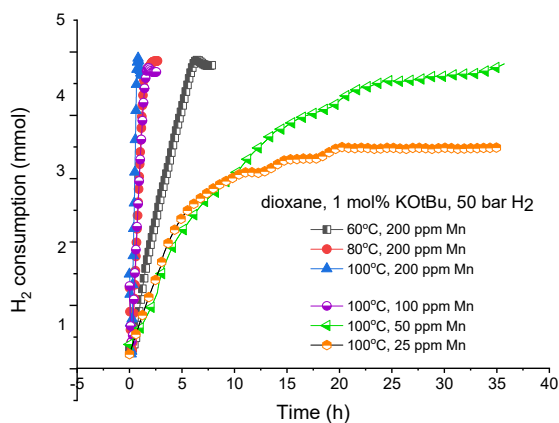


Figure 2. 3. H₂ consumption traces of acetophenone hydrogenation with **3** at different temperatures (right) for experiments listed in **Table 2. 2** entries 3, 5-9.

The analysis of reaction progress using the H₂ uptake measurements (**Figure 2. 3**) reveals that catalyst deactivation at elevated temperatures is only pronounced at very low catalyst loadings. Namely, for the reaction at 100 °C (entries 6-9, **Table 2. 2**), full ketone conversion can be reached with 50 ppm of **3**, whereas at 25 ppm the reaction does not proceed beyond 87 % conversion level regardless of the reaction times employed (**Figure 2. 3**). Having observed that the introduction of a protective phosphine arm in complex **3** has markedly increased the catalyst thermal stability, we sought to improve the performance of **3** further. Apart from stability per se, we aimed at improving catalyst activation protocol that is an integral parameter to any catalytic system.

2.3 Mechanistic analysis.

Catalyst activation, at large, is the reactivity pattern resulting in the generation of the active catalyst species. Similar to most bifunctional hydrogenation catalysts, our initial approach to catalyst activation involved the reaction of **3** with excess strong KO^tBu alkoxide base followed by H₂ to form the catalytically active Mn-H moiety (**Figure 2. 4**, a). Tracking this transformation with the IR spectroscopy we observed a rapid and clean conversion of **3** upon reaction with KO^tBu (**Figure 2. 4**, b) into the amido complex **4**. Notably, all three CO ligands were retained within **4** as follows from the presence of new bands at 1989, 1901, 1885 cm⁻¹. The resonance of phosphine donor in **4** was slightly shifted upfield to $\delta = 31.7$ ppm in ³¹P NMR compared to the initial cationic complex **3**

($\delta = 37.7$ ppm, see section 2.6.1). At the same time complex **4** as well as its parent complex **3** exhibited restricted mesityl group rotation dynamics evidenced by the loss of equivalency between ortho-methyl substituents of the mesityl group on the NMR timescales – a typical feature of Mn(I) NHC complexes.³⁵

Complex **4** was stable in THF for up to 24 hours and could be isolated as microcrystalline solid in 70% yield. The analysis of solid-state crystal structure of **4** confirmed the *facial* configuration of the tridentate CNP ligand implied by the NMR and IR spectral data (**Figure 2. 4**, c). Remarkably, the single crystal X-ray diffraction results revealed a highly unusual P-donor binding geometry in **4** with N-Mn-P angle of mere 67.4° . For comparison, the corresponding valent angles in related Mn-PNP pincer complexes are

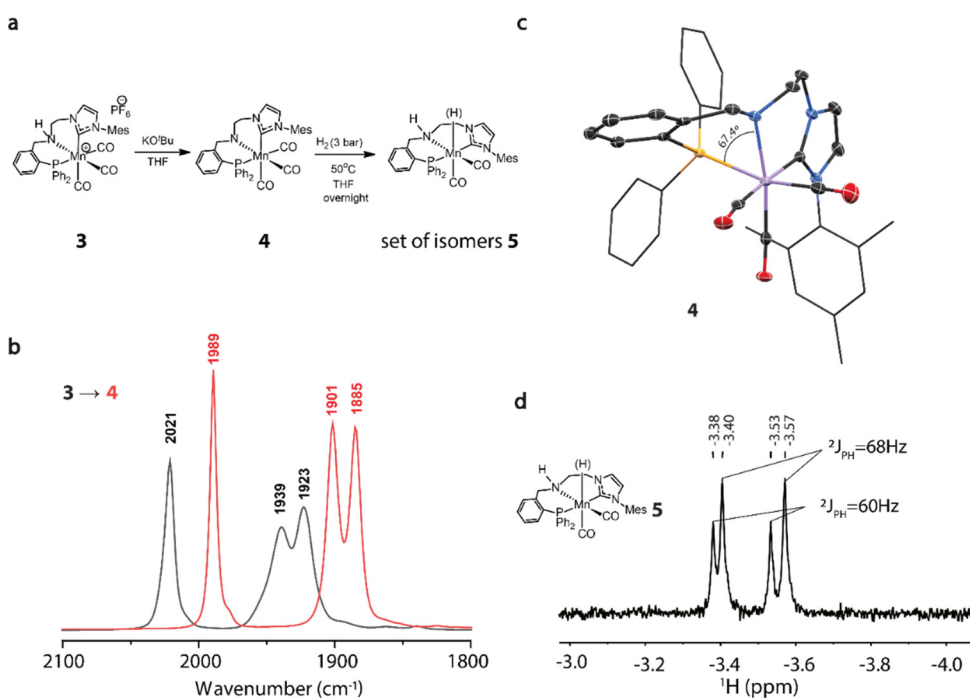


Figure 2. 4. Activation and reactivity of complex **3**. **a** Generation of complex **5** upon reaction with H_2 (3 bar). **b** IR spectra of complex **3** (black) and *in situ* generated complex **4** (red) recorded in THF at $25^\circ C$. **c** Molecular structure of complex **4** in the crystal with thermal ellipsoids drawn at 50 % probability. **d** Hydride region of 1H NMR (THF- d_8) spectra of *in situ* generated isomers of complex **5**.

$> 80^\circ$,¹⁴ indicating a significant coordination strain in complex **4** featuring the *fac*-bound CNP ligand.

Complex **4** reacted with H₂ gas upon heating, resulting in a loss of one of the CO ligands and the formation of isomers of a manganese hydride pincer complex **5** (**Figure 2. 4**). However, this reaction was particularly slow and proceeded to ca. 24% conversion of the starting complex **4** at 50 °C over 12 h under 3 bar H₂ pressure. The reaction gives rise to two new doublet resonances in ¹H NMR spectrum at -3.46 and -3.49 ppm with ²J_{PH} = 60.0 Hz and 68.0 Hz, respectively (**Figure 2. 4**, d), corresponding to two isomers of dicarbonyl Mn-H species **5** with phosphine arm bound to Mn centre.

While the direct isolation and characterization of these Mn hydride species was challenging, we tried to assign their structures via DFT calculations. A series isomers of complex **5** with *fac*- and *mer*- geometries were proposed and optimized, of which the generating IR frequencies of CO ligands and ¹H-NMR shifts of Mn-H can be used to assess the possible structures by the comparison with the experimental results. As shown in **Figure 2. 5** and **Figure 2. 6**, all analyzed isomers feature similar CO ligand vibration frequencies. But for calculated *fac* isomers of **5** we observed significantly high field shifted hydride resonance values varying from -7.8 to -18.8 ppm that allowed us to rule out the formation of hydride species with *fac*-bound CNP ligand (**Figure 2. 5**). Indeed the placement of the hydride ligand for *fac*-isomers is in the *trans* configuration to donor groups of the CNP ligand, which can significantly results in its high-field shifts in NMR that were not experimentally observed. In contrast, the calculated *mer*-isomers (**P1-P2**, **Figure 2. 6**) gave hydride resonances (-1.50, -3.38 ppm) that were more similar to those observed in experiments (-3.46, -3.49 ppm). Therefore our DFT analysis suggested that the isomers of complex **5** could be distinguished by the respective positions of the axial carbonyl and hydride ligands relative to the meridionally bound CNP pincer.

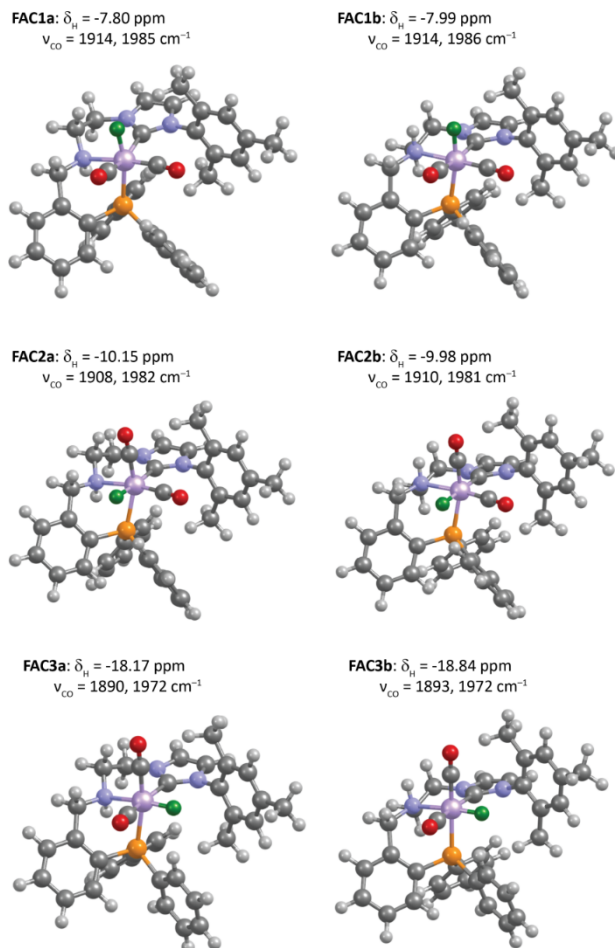


Figure 2. 5. DFT-calculated structures, CO ligand vibration frequencies and hydride resonances for fac isomers of **5**. Hydride ligand shown in green.

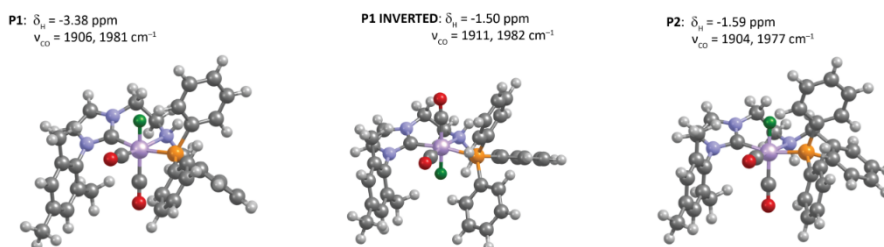


Figure 2. 6. DFT-calculated structures, CO ligand vibration frequencies and hydride resonances for mer-isomers of **5**. Hydride ligand shown in green. “O” stands for open, “P” for pincer.

From catalysis standpoint, the formation of Mn-hydride species is generally accepted as a prerequisite for entering the hydrogenation cycle. Our data, on the other hand, indicated that the Mn-H formation from **4** is slow and requires the irreversible loss of one CO ligand. Seeking for an alternative to the sluggish direct H₂ activation, we found that the reaction of pre-catalyst **3** with 2.5 equiv. of the KBHET₃ hydride donor can also generate a Mn-H species in an instant manner. In THF-*d*₈ at room temperature the reaction of **3** with KBHET₃ readily yields a reaction mixture containing 69 % of the amido complex **4** with remainder comprised of new manganese hydride species **6** (**Figure 2. 7**, a) that exist as a mixture of isomers. Unlike Mn hydride complex **5** observed in alkoxide-based activation protocol, species **6** features a free phosphine arm. The latter is evidenced by the appearance of the singlet resonances at $\delta = -16.2$ and -16.6 ppm in ³¹P NMR. In the presence of a non-bound P donor, complex **6** should be tricarbonyl species that gave two new bands at 1981, 1968 cm⁻¹ with the third one overlapped with the CO bands of complex **4** in the IR spectrum. As in the case of **5**, complex **6** exists as two isomers distinguished by ³¹P resonances and those of hydride ligands appearing as singlets at $\delta = -3.92$ and -4.40 ppm in ¹H NMR spectrum. Similar to the case of **5**, we also performed DFT analysis on the possible structures of complex **6** (**Figure 2. 8**). The good alignments of the hydride resonance and IR frequencies between the experimental observations and calculated isomers (especially **O1a** and **O2a**) suggested that complex **6** exists with meridionally bound CN ligand and hydride ligands. Species **6**, being stable in solution for several hours, slowly convert to **5** as confirmed by *in situ* solution IR studies and NMR data depicted in **Figure 2. 7 a**.

An unusual feature of the CNP ligand, responsible for the formation of complex **6** is the apparent hemilabile nature of phosphine donor arm in MnCNP precatalyst. The phenomenon of ligand hemilability is often employed to rationalize reactivity of organometallic compounds,¹⁵ especially in the context of hybrid and multidentate ligands.¹⁶ Invoked mainly for labile donor groups, e.g. oxygen or nitrogen, hemilability is scarce for phosphine donors¹⁷ in general and for manganese phosphines in particular¹⁸.

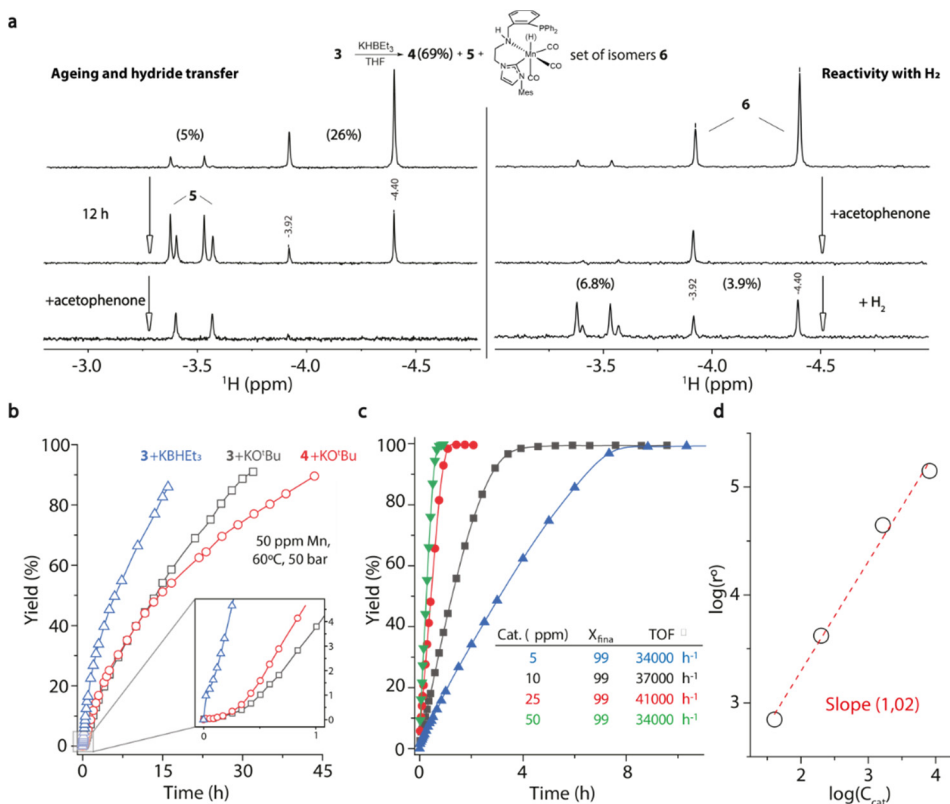


Figure 2. 7. Catalyst activation with KBHET₃ and corresponding catalytic performance. **a** ¹H NMR spectra of the hydride region for KBHET₃ activated complex **3**. Left panel shows slow conversion of **6** to complex **5** and subsequent reactivity with acetophenone; Right panel shows reactivity of species **6** with acetophenone and regeneration of reactive hydride species in H₂ atmosphere; relative content of hydride species indicated in percent units of total Mn. **b** Kinetic traces for the hydrogenation of acetophenone with complexes **3** and **4** in the presence of 1 mol% KO^tBu or 1 mol% KBHET₃ promoters at 60 °C, 50 bar H₂ and 50 ppm Mn loading. **c** Kinetic traces of acetophenone hydrogenation with **3** at different catalyst loading. Conditions: 50 bar H₂, 120 °C, 12.5 mmol substrate, 1 mol % of KBHET₃, catalyst loading indicated on the graph. **d** Double logarithmic plot for reaction order analysis with respect to catalyst concentration for the data plotted in panel **c**.

In case on MnCNP complexes, generation of hydride complex **6** presents an attractive activation protocol for **3**. Unlike the sluggish base-assisted activation with molecular H₂, the reaction with KBHET₃ proceeds instantly at room temperature and does not require CO ligand dissociation steps. The hydride species produces in such manner are catalytically competent and readily react with ketone substrates. Our stoichiometric studies indicate the higher reactivity of **6** towards ketones, compared to **5** (**Figure 2. 10**).

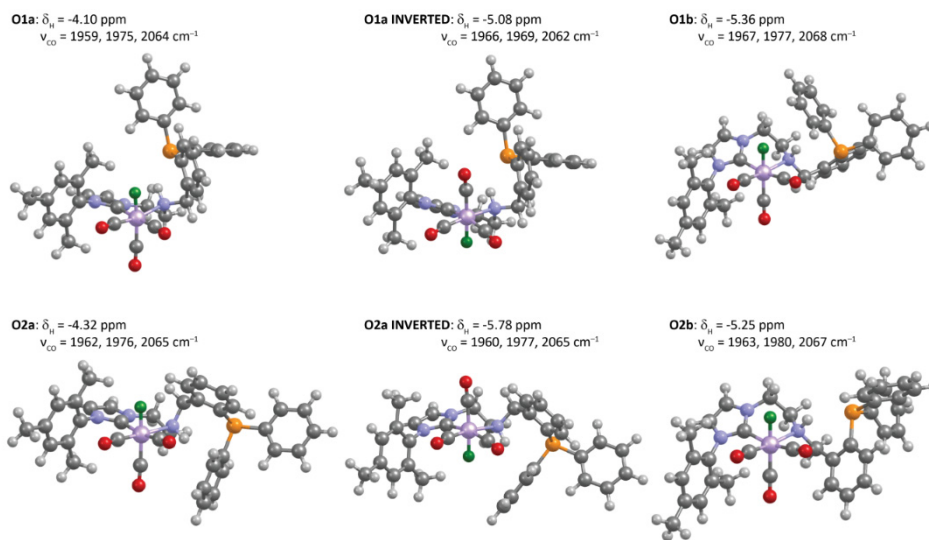


Figure 2. 8. DFT-calculated structures, CO ligand vibration frequencies and hydride resonances for mer-isomers of **6**. Hydride ligand shown in green. “O” stands for open, “P” for pincer.

We found that the improved activation protocol has a profound effect on the hydrogenation kinetics. Monitoring the hydrogenation kinetics we could confirm that the use of KHBET_3 promoter at 60°C and 50 bar H_2 pressure significantly reduces the hydrogenation onset time compared to the KO^tBu -promoted catalysis (**Figure 2. 7, b**). While the activation of the Mn-CNP pre-catalyst with the alkoxide base resulted in ca. 15 min induction period, the KHBET_3 treatment eliminated this lag time. Furthermore, the more selective pre-catalyst activation with the borohydride promoter resulted in a nearly 3-fold increase of the hydrogenation rate. We suggest this improvement to stem from an efficient catalyst activation protocol that allows for facile generation of competent hydride species **5** and **6**, thus ensuring the ability of Mn precatalyst to enter the catalytic cycle immediately. As our data depicted in **Figure 2. 7 a** suggested that both **5** and **6** are exhibiting the hydride transfer reactivity upon the contact with acetophenone, we further attempted to observe the outcome of the catalytic turnover on the relative composition of the reaction mixture using NMR spectroscopy. Results of this experiment are presented in **Figure 2. 7 a**. We observed that hydrogenation of acetophenone substrate with reaction mixtures containing predominantly hydride species **6** results in the accumulation of the dicarbonyl complex **5**. While suggesting that the catalytic turnover involving solely

species **6** and associated ligand hemilability is possible, gradual accumulation of **5** in the course of several catalytic turnovers suggests that the hydrogenation can likely proceed over the complex **5** at low catalyst loadings.

The use of the improved activation method allowed carrying out the hydrogenations at lower catalyst loadings and higher reaction temperatures (**Table 2. 3**). The borohydride activation allowed for a seven-fold reduction of reaction time compared to the best example of alkoxide-promoted hydrogenation described above (**Table 2. 3**, entry 1 vs. **Table 2. 2** entry 8). Furthermore, we could use **3** at 120 °C with the catalyst loading reduced from 50 to 5 ppm without the loss of catalytic performance (**Table 2. 3**, entries 2-5). Even at 5 ppm loading acetophenone hydrogenation was brought to completion within 9 hours at 120°C. The homogeneous nature of Mn catalysis in this reaction was confirmed by control experiments (**Table 2. 3**, entries 6, 7). Our kinetic data collected for hydrogenations at 12.5 mmol scale indicated the first order in pre-catalyst **3** (**Figure 2. 7**, d) with exceptional TOF values up to 41 000 h⁻¹ (**Figure 2. 7**, c) under these reaction conditions.

Table 2. 3. Manganese-catalyzed hydrogenation of acetophenone with KBHET₃ promotor.^a

Entry	Cat. 3 (mol%/ppm)	T (°C)	t (h) ^b	Yield (%) ^c
1	0.005/50	100	4	99
2	0.005/50	120	3	99
3	0.0025/25	120	3	99
4	0.001/10	120	6	99
5	0.0005/5	120	9	99
6	No Mn	120	12	trace
7 ^d	0.005/50	120	3	99

^a Reactions were conducted with acetophenone (5 mmol), Mn catalyst **3**, KBHET₃ (1 mol%) in 1,4-dioxane (3 mL), P = 50 bar H₂. ^b Total reaction time and that of GC analysis. ^c Yield determined by GC with dodecane as internal standard. ^d Reactions was conducted under conditions identical to Entry 2 in presence of 2 mol% Hg.

2.4 Substrate scope.

Finally, complex **3** proved to be a versatile hydrogenation catalyst (**Figure 2. 9**). With mere 50 ppm Mn loading at 120 °C, aromatic ketones **8a** to **8i** were reduced in high to quantitative yield with the exception of sterically demanding *tert*-butyl phenyl ketone **8b** that was converted with 81% yield. Milder conditions (80 °C) were used for activated ketones with heterocycles and functional groups (**8j** – **8l**), affording corresponding alcohols with 85 – 99% isolated yields. Cyclic and linear aliphatic ketones **8m** - **8q** were also hydrogenated with quantitative yields. A noteworthy exception to this set was conjugated α,β -unsaturated ketone **8q** that was not converted by our catalytic system at appreciable level. In addition to ketones, functionalized aldehydes (**8r** – **8u**) and imines (**8v** – **8x**) were converted using 50-100 ppm catalyst loading. Finally, the activity of **3** was sufficient to convert formate esters (**8y** – **8aa**) to the corresponding alcohols at 200 ppm catalyst loading.

2.5 Conclusion

In summary, moving to pincer ligands proves to be an effective strategy to strengthen the thermal stability of Mn-CN, leading to a Mn(I)-CNP complex **3** as a truly robust and versatile hydrogenation catalyst. These findings highlight the pronounced improvements of catalytic performance that can be achieved by suppressing the deactivation of catalysts. In addition, the mechanistic studies in this chapter reveal that bifunctional hydrogenation precatalyst can require further transformation, i.e. dissociation of ancillary ligand, during activation apart from the base-induced dehydrohalogenation. Changing the activation reagents from alkoxide base to hydride donors significantly accelerated this process and gave rise to much higher reaction rates. Since the activation protocol defines how fast the active catalyst species are supplied to the catalytic cycle we conclude that the overall performance of the catalytic system can be largely dependent on the efficiency, rate and selectivity of the catalyst activation step.

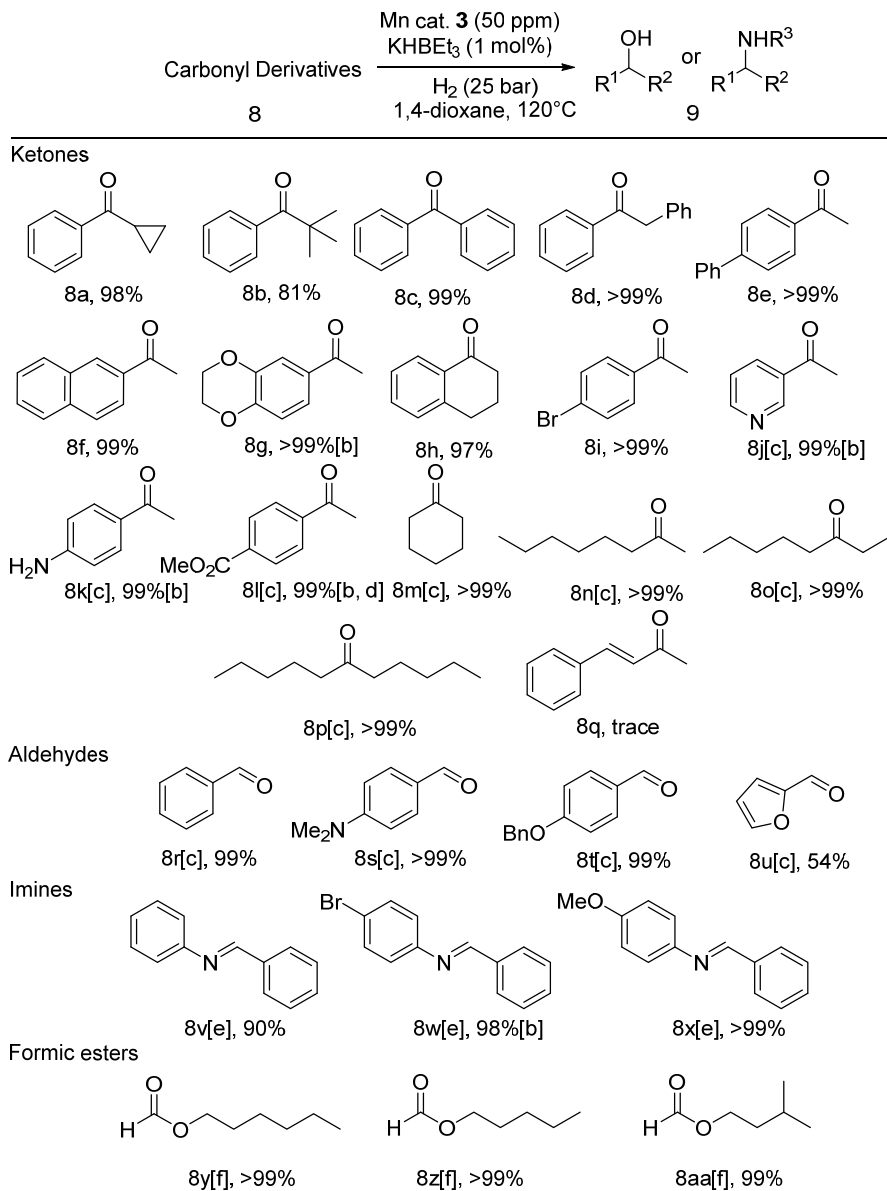
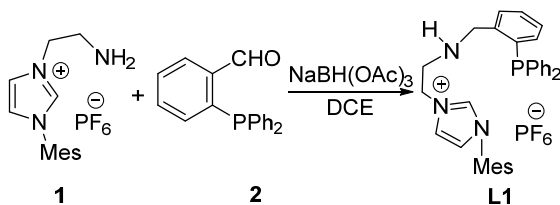


Figure 2. 9. [a] Typical conditions: 5 mmol substrate, complex **3** (50 ppm), KBHET₃ (1 mol%) in 1,4-dioxane (3 mL), 120 °C, P = 25 bar H₂, 24 h. Yields determined by GC-FID with dodecane internal standard. [b] Isolated yields. [c] Reactions carried out in isopropanol (3 mL) at 80 °C instead. [d] The product was corresponding isopropyl ester identified by NMR. [e] 100 ppm of **3** used in isopropanol (3 mL), 120 °C. [f] 200 ppm of **3** used.

2.6 Experimental details

2.6.1 Synthetic procedures

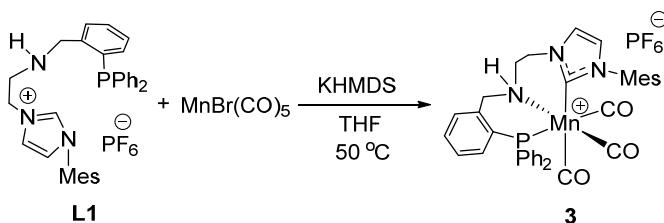
Synthesis of Ligand L1:



Under an inert atmosphere, compound **1** (3 g, 8 mmol) and **2** (2.32 g, 8 mmol) were dissolved in DCE (20 mL) and stirred overnight. Sodium triacetoxyborohydride (4.24 g, 20 mmol) was then slowly added as solid to the resulting solution. After stirring for another night, the solution was quenched by water and extracted with DCM. The combined organic phases were dried over anhydrous Na₂SO₄, concentrated and purified by column chromatography to provide the compound **L1** as white foam solid in 81% yield (4.2 g). The compound was used for pre-catalyst **3** preparation without further purification.

¹H NMR (400 MHz, CDCl₃, 297 K) δ 8.51 (s, 1H), 7.60 (s, 1H), 7.37 – 7.27 (m, 6H), 7.20 – 7.18 (m, 7H), 7.05 (s, 1H), 6.98 (s, 2H), 6.90 – 6.87 (m, 1H), 4.29 – 4.22 (m, 2H), 3.94 (s, 2H), 3.02 – 2.90 (m, 2H), 2.34 (s, 3H), 1.97 (s, 5H); ³¹P{¹H}NMR (162 MHz, CDCl₃, 297 K) δ -16.1 (s); ¹³C {¹H}NMR (101 MHz, CDCl₃, 297 K) δ 143.7, 143.4, 141.3, 136.6, 136.4, 136.3, 135.7, 135.6, 134.5, 133.9, 133.8, 133.6, 130.6, 129.8, 129.4, 129.3, 129.0, 128.9, 128.7, 128.6, 128.2, 127.8, 125.3, 123.8, 122.8, 52.0, 50.0, 47.8, 21.5, 21.1, 17.1; HRMS (m/z): [M-PF₆]⁺ Calcd. for C₃₃H₃₅N₃P₁⁺, 504.2563; found 504.2544.

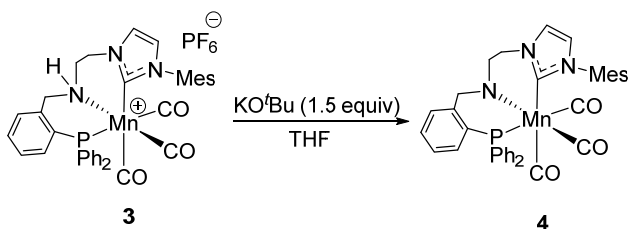
Synthesis of complex **3**:



To the orange suspension of $[\text{MnBr}(\text{CO})_5]$ (137.5 mg, 0.5 mmol) in THF (5 mL) was added ligand **L1** (325 mg, 0.5 mmol) and stirred for 3 h at 50 °C. The resulting solution was then cooled down to room temperature, potassium bis(trimethylsilyl)amide (110 mg, 0.55 mmol) in THF (2 mL) was added dropwise, stirred for another 3 h and evaporated to dryness. Residual oil was washed with pentane, re-dissolved in DCM, filtered through a Celite plug to remove inorganic salts and evaporated to dryness. The crude product was further purified by crystallization (diethyl ether vapor diffusion into solution in THF) to afford **3** as yellow solid in 51% yield (200.1 mg).

^1H NMR (400 MHz, CD_2Cl_2 , 297 K) δ 7.60 – 7.52 (m, 4H), 7.47 – 7.41 (m, 3H) 7.37 – 7.33 (m, 2H), 7.29 (s, 1H), 7.25 – 7.14 (m, 2H), 7.11 (s, 1H), 7.00 – 6.96 (m, 2H), 6.76 – 6.72 (m, 2H), 6.68 (s, 1H), 5.24 (s, 1H), 3.89 – 3.86 (m, 2H), 3.68 (s, 1H), 3.34 (s, 1H) 3.23 – 3.21 (m, 2H), 2.25 (s, 3H, CH_3 -Mes), 1.88 (s, 3H), 1.55 (s, 3H); $^{31}\text{P}\{^1\text{H}\}$ NMR (162 MHz, CD_2Cl_2 , 297 K) δ 37.6 (s), -144.4 (hep, $^1J_{\text{FP}}$ 712.8 Hz); $^{13}\text{C}\{^1\text{H}\}$ NMR (101 MHz, CD_2Cl_2 , 297 K) δ 217.7 (Mn-CO), 215.5 (Mn-CO), 213.9 (Mn-CO), 187.0 (NHC Mn-C), 140.2, 139.4 ($^1J_{\text{PC}}$ 16.2 Hz), 136.6, 135.9, 133.3, 133.2, 133.1, 133.0, 132.9, 132.8, 132.1, 131.7, 131.4, 131.3, 130.1, 130.0, 129.6, 129.5, 129.3, 129.1, 129.0, 126.5, 125.4, 56.3, 53.1, 45.8, 20.7, 18.5 and 17.6. FTIR-ATR (solid): $\bar{\nu}$ [cm^{-1}] 2021 (s, $\bar{\nu}$ CO), 1943 (s, $\bar{\nu}$ CO), 1919 (s, $\bar{\nu}$ CO); Elemental analysis: (calcd., found for $\text{C}_{36}\text{H}_{34}\text{F}_6\text{MnN}_3\text{O}_3\text{P}_2$): C (54.90, 54.80), H (4.35, 4.41), N (5.34, 5.33).

Synthesis of complex 4:

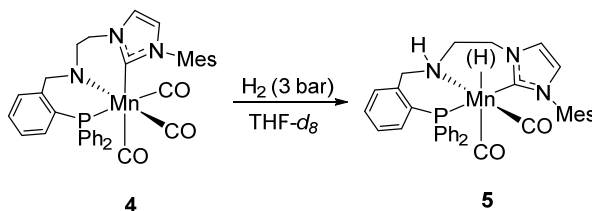


To the solution of complex **3** (52.5 mg, 0.067 mmol) in THF (2 mL) was dropwise added KO^tBu (9.4 mg, 0.08 mmol) in 0.5 mL THF. After stirring for 1 h, the resulting mixture was evaporated to dryness. Residual oil was re-dissolved in DCM, filtered through a Celite plug to remove inorganic salt and evaporated to dryness. The crude was further purified

by slow diffusion of pentane into its solution in THF to afford **6** as red crystals in 70 % yield (30.2 mg).

^1H NMR (400 MHz, THF- d_8 , 297 K) δ 7.34 – 7.19 (m, 8H), 7.12 (t, $J = 6.9$ Hz, 2H), 7.06 (s, 1H), 6.94 – 6.82 (m, 5H), 6.70 (s, 1H), 6.54 (t, $J = 8.6$ Hz, 1H), 4.82 – 4.78 (m, 1H), 4.10 – 4.04 (m, 1H), 3.64 – 3.63 (m, 1H), 3.39 – 3.35 (m, 1H), 2.79 – 2.75 (m, 1H), 2.23 (s, 3H), 1.94 – 1.87 (s, 4H), 1.74 (s, 3H); $^{31}\text{P}\{^1\text{H}\}$ NMR (162 MHz, THF- d_8 , 297 K) δ 33.6 (s); ^{13}C -NMR (101 MHz, THF- d_8 , 297 K) 223.0, 220.4, and 216.4 (Mn-CO), 192.2 (NHC Mn-C), 150.5 ($^1J_{\text{PC}} 6.1$ Hz), 142.0, 139.9, 139.5, 138.9, 138.6, 137.8, 137.1, 135.1, 134.1, 134.0, 130.2, 130.1, 130.0, 129.7, 129.2, 128.8, 128.2, 128.1, 127.7, 127.6, 125.5, 125.4, 125.3, 125.2, 72.3, 62.6, 51.3, 21.2, 19.5, and 18.1. IR (solution in THF): $\bar{\nu}$ [cm^{-1}] 1989 (s, $\bar{\nu}$ CO), 1901 (s, $\bar{\nu}$ CO), 1885 (s, $\bar{\nu}$ CO); Elemental analysis: (calcd., found for $\text{C}_{36}\text{H}_{33}\text{MnN}_3\text{O}_3\text{P}_1\cdot\text{H}_2\text{O}$): C (65.55, 65.79), H (5.35, 5.21), N (6.37, 6.37).

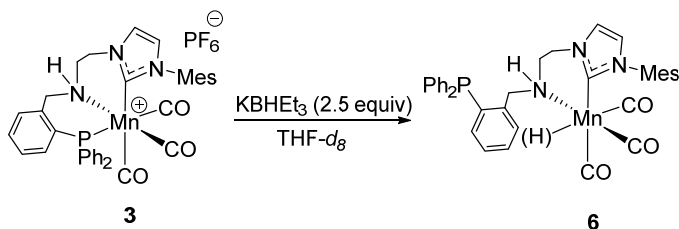
In situ-generation of Mn-H complex 5:



The solution of **4** was pressurized with 3 bar H_2 and dwelled at 25°C for 12 h. The NMR spectra were collected and the sample was heated at 50°C for another 12 h to form species **5**.

5: ^1H NMR (400 MHz, THF- d_8 , 297 K, hydride resonances): δ -3.46 (d, $^2J_{\text{PH}} 60.0$ Hz, Mn-H), -3.49 (d, $^2J_{\text{PH}} 68.0$ Hz, Mn-H); $^{31}\text{P}\{^1\text{H}\}$ NMR (162 MHz, THF- d_8 , 297 K) $\delta = 81.1$ (s). IR: (solution in THF, 297 K): $\bar{\nu}$ [cm^{-1}] 1897 (s, $\bar{\nu}$ CO, DFT estimated, overlaps with band of **4**), 1814 (s, $\bar{\nu}$ CO).

In-situ generation of hydride complex via activation with KBHET_3 :



Upon treatment of complex **3** (7.9 mg, 1 equiv.) with KBHET_3 (25 μl of 1M THF solution, 2.5 equiv.) in $\text{THF-}d_8$ (0.6 mL) an orange solution was formed immediately producing the mixture of complex **4** and hydride complexes **5** and **6**. The resulting solution was monitored by NMR immediately after borohydride addition and at 12 h time. Subsequently, three measurements after addition of 1, 0.1, and 1 equiv. of acetophenone respectively were then added sequentially to probe the reactivity of hydride species (**Figure 2. 10**). Corresponding IR analysis was performed through same procedure with protic THF as solvent.

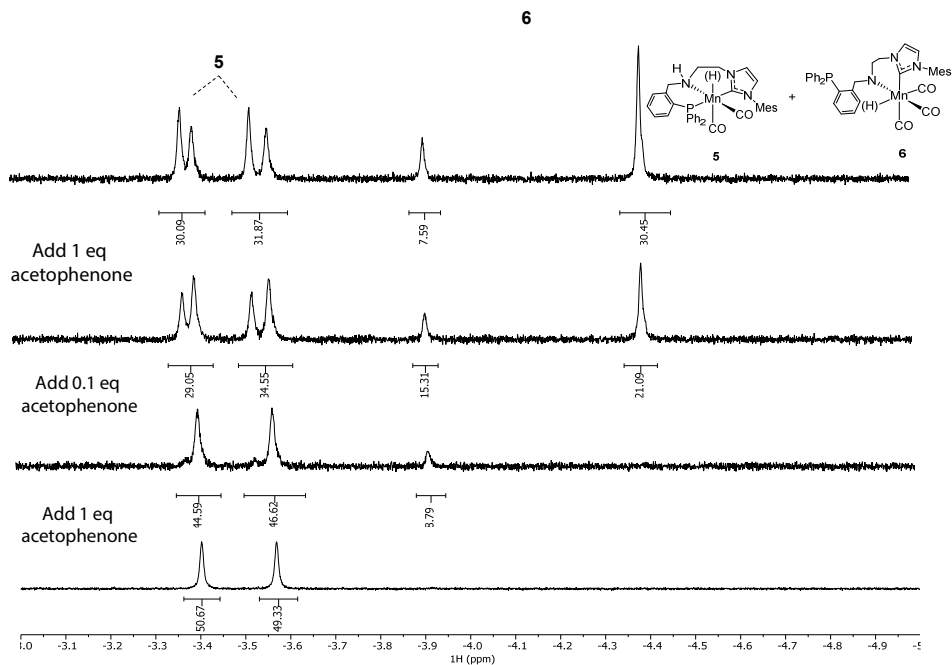


Figure 2. 10. $^1\text{H-NMR}$ spectrum (hydride region) of *in situ*-formed mixture of **5** and **6** (12 h) and its reaction with acetophenone in $\text{THF-}d_8$. The order of hydride consumption is indicating higher reactivity of **6** towards ketone substrates.

6: ^1H NMR (400 MHz, THF- d_6 , 297 K, partial, hydride resonances only): δ -3.92 (s, Mn-H, **6a**), -4.40 (s, Mn-H, **6b**); FTIR-ATR (solution in THF, 297 K): $\bar{\nu}$ [cm^{-1}] 1981 (s, $\bar{\nu}$ CO), 1891 (s, $\bar{\nu}$ CO, estimated), 1868 (s, $\bar{\nu}$ CO).

2.6.2. Catalytic experiments

General Procedure for catalytic hydrogenation. Stock solutions of **3** (0.01 M) were prepared in dioxane solvent. In a typical run, substrate (5 mmol), dioxane (3 mL), dodecane internal standard (56.8 μL , 0.25 mmol), base promoter (0.05 mmol) and complex **3** were combined in a 4 mL glass vials and transferred into a stainless steel autoclave in the glovebox. The system was purged with N_2 (3 \times 8 bar) and H_2 (1 \times 30 bar), pressurized with H_2 to specified pressure, and heated to specified temperature. The yields of products were determined by GC or GC-MS.

Kinetic study of acetophenone hydrogenation with Mn catalyst 3 on a large scale.

Inside the glovebox, a stock solution of **3** (0.0125 M) was prepared in 0.875 mL dioxane, treated with 0.125 mL of 1M KBHET_3 solution in THF and stirred for 0.5 h. A 1mL syringe was loaded with the mixture of activated catalyst solution (500, 250, 100, 50 μL), KBHET_3 (62.5, 93.8, 112.5, 118.8 μL) and dioxane (total volume 0.7 mL), and a 20 mL syringe was loaded with the mixture of acetophenone (1.460 mL, 12.5 mmol), dodecane (113.6 μL , 0.625 mmol) and 10 mL dioxane. Under N_2 flow, the substrate syringe was first injected into high pressure stainless steel reactor in which a glass liner was inserted in advance. The dissolved catalyst was then placed in an injection port and the system was purged with H_2 (3 \times 10 bar). The reactor was brought to at 120 $^\circ\text{C}$ at 50 bar H_2 pressure with stirring at 1000 rpm and reaction was initiated by injecting the catalyst solution. The samples were withdrawn at given time intervals using an autosampler apparatus and analyzed with GC. Data plotted in Figure 4 of the manuscript.

2.6.3. Computational details

All quantum chemical calculations were performed by Ivan Chernyshov using Gaussian16 software.¹⁹ Geometries and IR spectra were calculated at PBE0-D3/6-311+G(d,p) level of theory with a continuous description of the THF solvent using the SMD model. ^1H NMR shielding was computed for the optimized geometries at PBE0/6-311++G(2d,2p) level of theory, which shows good performance for the calculation of

shielding constants;^{20,21} the solvent (d_8 -THF) was taken into account with the PCM model, which works well for modeling NMR spectra in solutions.^{22,23}

The calculated IR frequencies were scaled with the factor $f = 0.9576$, which was chosen for best agreement of experimental and calculated data. It is applied to minimize the error of the harmonic approach for the vibration frequency calculation²⁴. The Half width of the plotted calculated spectra is 5 cm^{-1} .

2.6.4. Crystallographic details

X-ray diffraction studies were performed by M. Weber and prof. dr. C. Müller (Freie Universität Berlin). Crystallographic details are available in the electronic supporting information of the published work: *Nat. Commun.* **2021**, *12*, 1-8. CCDC entries 1994375 (4) contain the crystallographic data for this work.

2.7 References

1. Rylander, P. N., *Catalytic Hydrogenation in Organic Syntheses: Paul Rylander*. Academic Press: New York, 1979.
2. (a) Vries, J. G. d., *The handbook of homogeneous hydrogenation*. Wiley-Vch: Weinheim, 2007; (b) Arai, N.; Ohkuma, T., Design of molecular catalysts for achievement of high turnover number in homogeneous hydrogenation. *Chem. Rec.* **2012**, *12*, 284-289.
3. (a) Werkmeister, S.; Neumann, J.; Junge, K.; Beller, M., Pincer-Type Complexes for Catalytic (De) Hydrogenation and Transfer (De) Hydrogenation Reactions: Recent Progress. *Chem. Eur. J.* **2015**, *21*, 12226-12250; (b) Zell, T.; Milstein, D., Hydrogenation and dehydrogenation iron pincer catalysts capable of metal–ligand cooperation by aromatization/dearomatization. *Acc. Chem. Res.* **2015**, *48*, 1979-1994; (c) Filonenko, G. A.; van Putten, R.; Hensen, E. J.; Pidko, E. A., Catalytic (de) hydrogenation promoted by non-precious metals–Co, Fe and Mn: recent advances in an emerging field. *Chem. Soc. Rev.* **2018**, *47*, 1459-1483; (d) Clarke, M. L.; Widegren, M. B., Hydrogenation reactions using Group III to Group VII transition metals. *Homogeneous Hydrogenation with Non-Precious Catalysts* **2019**, 111-140.
4. (a) Snider, B. B., Manganese (III)-based oxidative free-radical cyclizations. *Chem. Rev.* **1996**, *96*, 339-364; (b) Carney, J. R.; Dillon, B. R.; Thomas, S. P., Recent advances of manganese catalysis for organic synthesis. *Eur. J. Org. Chem.* **2016**, *2016*, 3912-3929; (c) Valyaev, D. A.; Lavigne, G.; Lugan, N., Manganese organometallic compounds in homogeneous catalysis: Past, present, and prospects. *Coordination*

Chemistry Reviews **2016**, *308*, 191-235; (d) Maji, B.; Barman, M. K., Recent developments of manganese complexes for catalytic hydrogenation and dehydrogenation reactions. *Synthesis* **2017**, *49*, 3377-3393; (e) Kallmeier, F.; Kempe, R., Manganese Complexes for (De) Hydrogenation Catalysis: A Comparison to Cobalt and Iron Catalysts. *Angew. Chem. Int. Ed.* **2018**, *57*, 46-60; (f) Chandra, P.; Ghosh, T.; Choudhary, N.; Mohammad, A.; Mobin, S. M., Recent advancement in oxidation or acceptorless dehydrogenation of alcohols to valorised products using manganese based catalysts. *Coordination Chemistry Reviews* **2020**, *411*, 213241.

5. Elangovan, S.; Topf, C.; Fischer, S.; Jiao, H.; Spannenberg, A.; Baumann, W.; Ludwig, R.; Junge, K.; Beller, M., Selective catalytic hydrogenations of nitriles, ketones, and aldehydes by well-defined manganese pincer complexes. *J. Am. Chem. Soc.* **2016**, *138*, 8809-8814.

6. (a) Elangovan, S.; Garbe, M.; Jiao, H.; Spannenberg, A.; Junge, K.; Beller, M., Hydrogenation of Esters to Alcohols Catalyzed by Defined Manganese Pincer Complexes. *Angew. Chem. Int. Ed.* **2016**, *49*, 15364-15368; (b) Papa, V.; Cabrero-Antonino, J. R.; Alberico, E.; Spanneberg, A.; Junge, K.; Junge, H.; Beller, M., Efficient and selective hydrogenation of amides to alcohols and amines using a well-defined manganese-PNN pincer complex. *Chem. Sci.* **2017**, *8*, 3576-3585; (c) Glatz, M.; Stöger, B.; Himmelbauer, D.; Veiros, L. F.; Kirchner, K., Chemoselective Hydrogenation of Aldehydes under Mild, Base-Free Conditions: Manganese Outperforms Rhenium. *ACS Catal.* **2018**, *8*, 4009-4016; (d) Kaithal, A.; Hölscher, M.; Leitner, W., Catalytic Hydrogenation of Cyclic Carbonates using Manganese Complexes. *Angew. Chem. Int. Ed.* **2018**, *57*, 13449-13453; (e) Kumar, A.; Janes, T.; Espinosa-Jalapa, N. A.; Milstein, D., Manganese Catalyzed Hydrogenation of Organic Carbonates to Methanol and Alcohols. *Angew. Chem. Int. Ed.* **2018**, *57*, 12076-12080; (f) Li, H.; Wei, D.; Bruneau-Voisine, A.; Ducamp, M.; Henrion, M.; Roisnel, T.; Dorcet, V.; Darcel, C.; Carpentier, J.-F.; Soulé, J.-F. o., Rhenium and manganese complexes bearing amino-bis (phosphinite) ligands: synthesis, characterization, and catalytic activity in hydrogenation of ketones. *Organometallics* **2018**, *37*, 1271-1279; (g) Wei, D.; Bruneau-Voisine, A.; Chauvin, T.; Dorcet, V.; Roisnel, T.; Valyaev, D. A.; Lugan, N.; Sortais, J. B., Hydrogenation of Carbonyl Derivatives Catalysed by Manganese Complexes Bearing Bidentate Pyridinyl-Phosphine Ligands. *Adv. Synth. Catal.* **2018**, *360*, 676-681; (h) Zou, Y.-Q.; Chakraborty, S.; Nerush, A.; Oren, D.; Diskin-Posner, Y.; Ben-David, Y.; Milstein, D., Highly Selective, Efficient Deoxygenative Hydrogenation of Amides Catalyzed by a Manganese Pincer Complex via Metal-Ligand Cooperation. *ACS Catal.* **2018**, *8*, 8014-8019; (i) Freitag, F.; Irrgang, T.; Kempe, R., Mechanistic Studies of Hydride Transfer to Imines from a Highly Active and Chemoselective Manganate Catalyst. *J. Am. Chem. Soc.* **2019**, *141*, 11677-11685; (j) Weber, S.; Stöger, B.; Veiros, L. F.; Kirchner, K., Rethinking Basic Concepts—Hydrogenation of Alkenes Catalyzed by Bench-Stable Alkyl Mn (I) Complexes. *ACS Catal.* **2019**, *9*, 9715-9720; (k) Zhang, L.; Tang, Y.; Han, Z.; Ding, K., Lutidine-Based

Chiral Pincer Manganese Catalysts for Enantioselective Hydrogenation of Ketones. *Angew. Chem. Int. Ed.* **2019**, *58*, 4973-4977; (l) Ling, F.; Hou, H.; Chen, J.; Nian, S.; Yi, X.; Wang, Z.; Song, D.; Zhong, W., Highly enantioselective synthesis of chiral benzhydrols via manganese catalyzed asymmetric hydrogenation of unsymmetrical benzophenones using an imidazole-based chiral PNN tridentate ligand. *Org. Lett.* **2019**, *21*, 3937-3941.

7. Kallmeier, F.; Irrgang, T.; Dietel, T.; Kempe, R., Highly active and selective manganese C=O bond hydrogenation catalysts: the importance of the multidentate ligand, the ancillary ligands, and the oxidation state. *Angew. Chem. Int. Ed.* **2016**, *55*, 11806-11809.

8. Espinosa-Jalapa, N. A.; Nerush, A.; Shimon, L. J.; Leitus, G.; Avram, L.; Ben-David, Y.; Milstein, D., Manganese-Catalyzed Hydrogenation of Esters to Alcohols. *Chem. Eur. J.* **2017**, *23*, 5934-5938.

9. Van Putten, R.; Uslamin, E. A.; Garbe, M.; Liu, C.; Gonzalez-de-Castro, A.; Lutz, M.; Junge, K.; Hensen, E. J.; Beller, M.; Lefort, L., Non-Pincer-Type Manganese Complexes as Efficient Catalysts for the Hydrogenation of Esters. *Angew. Chem. Int. Ed.* **2017**, *56*, 7531-7534.

10. Weber, S.; Stöger, B.; Kirchner, K., Hydrogenation of nitriles and ketones catalyzed by an air-stable bisphosphine Mn (I) complex. *Org. Lett.* **2018**, *20*, 7212-7215.

11. Garduño, J. A.; García, J. J., Non-Pincer Mn (I) Organometallics for the Selective Catalytic Hydrogenation of Nitriles to Primary Amines. *ACS Catal.* **2018**, *9*, 392-401.

12. Buhaibeh, R.; Filippov, O. A.; Bruneau-Voisine, A.; Willot, J.; Duhayon, C.; Valyaev, D. A.; Lugan, N.; Canac, Y.; Sortais, J.-B., Phosphine-NHC Manganese Hydrogenation Catalyst Exhibiting a Non-Classical Metal-Ligand Cooperative H₂ Activation Mode. *Angew. Chem. Int. Ed.* **2019**, *58*, 6727-6731.

13. van Putten, R.; Benschop, J.; de Munck, V. J.; Weber, M.; Müller, C.; Filonenko, G. A.; Pidko, E. A., Efficient and Practical Transfer Hydrogenation of Ketones Catalyzed by a Simple Bidentate Mn–NHC Complex. *ChemCatChem* **2019**.

14. Fu, S.; Shao, Z.; Wang, Y.; Liu, Q., Manganese-catalyzed upgrading of ethanol into 1-butanol. *J. Am. Chem. Soc.* **2017**, *139*, 11941-11948.

15. (a) Foerstner, J.; Kakoschke, A.; Wartchow, R.; Butenschön, H., Reactions of cyclopropenone derivatives with a cyclopentadienylcobalt (I) chelate: formation of a cobaltacyclobutenone and a transformation of 2, 2-dimethoxycyclopropenone to methyl acrylate at cobalt. *Organometallics* **2000**, *19*, 2108-2113; (b) Müller, C.; Lachicotte, R. J.; Jones, W. D., Catalytic C–C Bond Activation in Biphenylene and Cyclotrimerization of Alkynes: Increased Reactivity of P, N-versus P, P-Substituted Nickel Complexes. *Organometallics* **2002**, *21*, 1975-1981; (c) Müller, C.; Lachicotte, R. J.; Jones, W. D.,

Chelating P, N versus P, P Ligands: Differing Reactivity of Donor-Stabilized Pt (η^2 -PhC: CPh) Complexes Toward Diphenylacetylene. *Organometallics* **2002**, *21*, 1118-1123; (d) Becker, E.; Mereiter, K.; Puchberger, M.; Schmid, R.; Kirchner, K.; Doppiu, A.; Salzer, A., Novel [2+ 2+ 1] cyclotrimerization of alkynes mediated by bidentate cyclopentadienylphosphine ruthenium complexes. *Organometallics* **2003**, *22*, 3164-3170; (e) Eliasson, S. H. H.; Jensen, V. R., Benefit of a hemilabile ligand in deoxygenation of fatty acids to 1-alkenes. *Faraday Discuss.* **2019**, *220*, 231-248; (f) Wei, C.; Han, B.; Zheng, D.; Zheng, Q.; Liu, S.; Li, Z., Aluminum Complexes Bearing Bidentate Amido-Phosphine Ligands for Ring-Opening Polymerization of ϵ -Caprolactone: Steric Effect on Coordination Chemistry and Reactivity. *Organometallics* **2019**, *38*, 3816-3823.

16. (a) Müller, C.; Vos, D.; Jutzi, P., Results and perspectives in the chemistry of side-chain-functionalized cyclopentadienyl compounds. *J Organomet Chem* **2000**, *600*, 127-143; (b) Braunstein, P.; Naud, F., Hemilability of hybrid ligands and the coordination chemistry of oxazoline-based systems. *Angew. Chem. Int. Ed.* **2001**, *40*, 680-699; (c) Grützmacher, H., Cooperating ligands in catalysis. *Angew. Chem. Int. Ed.* **2008**, *47*, 1814-1818.

17. (a) Krut'ko, D. P.; Borzov, M. V.; Veksler, E. N.; Churakov, A. V.; Mach, K., Crystal structures and solution dynamics of monocyclopentadienyl titanium (IV) complexes bearing pendant ether and phosphanyl type functionalities. *Polyhedron* **2003**, *22*, 2885-2894; (b) Yong, L.; Hofer, E.; Wartchow, R.; Butenschön, H., Oxidative addition of hydrosilanes, hydrogermane, and hydrostannane to cyclopentadienylcobalt (I) bearing a pendant phosphane ligand: Cyclopentadienylhydridocobalt (III) chelate complexes with silyl, germyl, and stannyl ligands. *Organometallics* **2003**, *22*, 5463-5467; (c) Yu, X.-J.; He, H.-Y.; Yang, L.; Fu, H.-Y.; Zheng, X.-L.; Chen, H.; Li, R.-X., Hemilabile N-heterocyclic carbene (NHC)-nitrogen-phosphine mediated Ru (II)-catalyzed N-alkylation of aromatic amine with alcohol efficiently. *Catal. Commun.* **2017**, *95*, 54-57.

18. (a) Chakraborty, S.; Gellrich, U.; Diskin-Posner, Y.; Leitus, G.; Avram, L.; Milstein, D., Manganese-Catalyzed N-Formylation of Amines by Methanol Liberating H₂: A Catalytic and Mechanistic Study. *Angew. Chem.* **2017**, *129*, 4293-4297; (b) Kumar, A.; Espinosa-Jalapa, N. A.; Leitus, G.; Diskin-Posner, Y.; Avram, L.; Milstein, D., Direct synthesis of amides by dehydrogenative coupling of amines with either alcohols or esters: manganese pincer complex as catalyst. *Angew. Chem. Int. Ed.* **2017**, *56*, 14992-14996.

19. Gaussian 16, Revision B.01, M. J. Frisch, G. W. Trucks, H. B. Schlegel, G. E. Scuseria, M. A. Robb, J. R. Cheeseman, G. Scalmani, V. Barone, G. A. Petersson, H. Nakatsuji, X. Li, M. Caricato, A. V. Marenich, J. Bloino, B. G. Janesko, R. Gomperts, B. Mennucci, H. P. Hratchian, J. V. Ortiz, A. F. Izmaylov, J. L. Sonnenberg, D. Williams-Young, F. Ding, F. Lipparini, F. Egidi, J. Goings, B. Peng, A. Petrone, T. Henderson, D. Ranasinghe, V. G. Zakrzewski, J. Gao, N. Rega, G. Zheng, W. Liang, M. Hada, M. Ehara, K. Toyota, R. Fukuda, J. Hasegawa, M. Ishida, T. Nakajima, Y. Honda, O. Kitao, H. Nakai,

T. Vreven, K. Throssell, J. A. Montgomery, Jr., J. E. Peralta, F. Ogliaro, M. J. Bearpark, J. J. Heyd, E. N. Brothers, K. N. Kudin, V. N. Staroverov, T. A. Keith, R. Kobayashi, J. Normand, K. Raghavachari, A. P. Rendell, J. C. Burant, S. S. Iyengar, J. Tomasi, M. Cossi, J. M. Millam, M. Klene, C. Adamo, R. Cammi, J. W. Ochterski, R. L. Martin, K. Morokuma, O. Farkas, J. B. Foresman, and D. J. Fox, Gaussian, Inc., Wallingford CT, 2016.

20. I. Yu. Chernyshov, M. V. Vener, I. G. Shenderovich, Local-structure effects on ^{31}P NMR chemical shift tensors in solid state. *J. Chem. Phys.* **2019**, *150*, 144706.

21. B. Maryasin, H. Zipse, Theoretical studies of ^{31}P NMR spectral properties of phosphanes and related compounds in solution. *Phys. Chem. Chem. Phys.* **2011**, *13*, 5150–5158.

22. M. Dračinský, P. Bouř, Computational Analysis of Solvent Effects in NMR Spectroscopy, *J. Chem. Theory Comput.* **2010**, *6*, 288–299.

23. V. A. Semenov, D. O. Samultsev, L. B. Krivdin, Solvent effects in the GIAO-DFT calculations of the ^{15}N NMR chemical shifts of azoles and azines. *Magn. Reson. Chem.* **2014**, *52*, 686–693.

24. A. L. Spek, Structure validation in chemical crystallography. *Acta Cryst.* **2009**, *D65*, 148–155.

**Switching Between Carbonyl
Hydrogenation and Olefin Transposition
Catalysis via Controlling Ligand
Dynamics in Mn(I) complexes**

Abstract

Managing catalyst-activation process is crucial to transition-metal-catalyzed transformations of olefins involving hydride transfer. Herein we report the first Mn(I) pincer complex that effectively promotes site-controlled transposition of olefins. This new reactivity is shown to emerge once the N-H functionality within Mn/NH bifunctional complex is suppressed by alkylation. While detrimental for carbonyl (de)hydrogenation, such a masking of the cooperative NH functionality enhances the ligand dynamics of the N donor and facilitates its reversible dissociation. The catalyst therefore can create temporary free space for substrates and enables the highly efficient conversion of a wide range of allylarenes to higher-value 1-propenybenzenes in near-quantitative yield with excellent stereoselectivities. The reactivity towards a single positional isomerization was also retained for longer-chain alkenes resulting in the highly regioselective formation of 2-alkenes, which are less thermodynamically stable compared to other possible isomerization products.

This chapter has been published as:

Wenjun Yang, Ivan Yu Chernyshov, Manuela Weber, Christian Müller, Evgeny A Pidko, Georgy A Filonenko, *ACS Catal.* **2022**, *12*, 10818-10825.

Contributions: W.Y. designed, conducted the experiments, and analyzed the data; I.Y.C. performed the DFT calculation; M.W. performed crystal structure determination and analysis; G.A.F. and E.A.P. supervised the research.

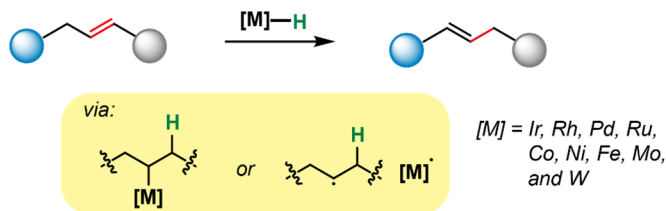
3.1 Introduction

Carbon-carbon double bonds are key skeletal units in a plethora of natural and industrial chemicals¹ as well as versatile precursors for many synthetic transformations.² Despite the availability of numerous protocols for installing olefin functional group (e.g., olefination, elimination, condensation, dehydrogenation), such transformations are frequently disadvantaged by low stereoselectivities or restrictions on functional groups.³ Alternatively, transposition of pre-existing olefins offers a powerful and atom-economical route to incorporate and manipulate C=C bonds with far-reaching applications in industrial production e.g., pharmaceuticals, cosmetics, fragrances, polymers and fuels.⁴ Various processes were developed with efficient catalysts based on transition metals: Ir,⁵ Rh,⁶ Pd,⁷ Ru,⁸ Cr,⁹ Co,¹⁰ Ni,¹¹ Fe,¹² W,¹³ among others. (**Figure 3. 1 a**). Missing in this set of examples is a highly abundant and biocompatible manganese metal that remains unknown in olefin transposition so far.

Alkene transposition catalysis is mechanistically diverse and generally proceeds via either of the three alternative paths, namely, allyl, alkyl, or radical mechanisms with the latter two governing the activity of the vast majority of catalyst systems.^{4c, 10i, 14} In both mechanisms metal hydrides are the active species, which promote the transposition reaction via an H⁻/H⁺ addition to the alkene followed by the β -H elimination/ H⁻-abstraction to furnish the isomerization product.^{4c}

The representative examples operating via the alkyl mechanism such as Pd(dba)₂ (Skrydstrup),^{7a} Co-NNP complexes (Liu),^{10f} and Fe(OAc)₂ (Koh)^{12b} typically require the *in situ* activation to form the catalytic metal hydride species by the reaction with such reagents as e.g., acyl chloride, ammonia borane, boryl reagent combined with base. Activation-free olefin transpositions catalysis was also demonstrated with isolated metal hydride or metal alkyl complexes.^{10b, 12c} With respect to the radical-type processes, the latest advances were disclosed by Shenvi and Palmer groups employing cobalt salen^{10c} and cobaloxime complexes,^{10e} respectively. Upon the reductive treatment, these complexes form Co hydrides that can act as H⁻-donors. The central role of the metal hydrides for the catalytic C=C bond suggests a potentially broader scope of catalyst systems for this chemistry.

a) Transition-metal catalyzed C=C transposition



b) Tuneable reactivity of Mn-H toward C=O and C=C (this work)

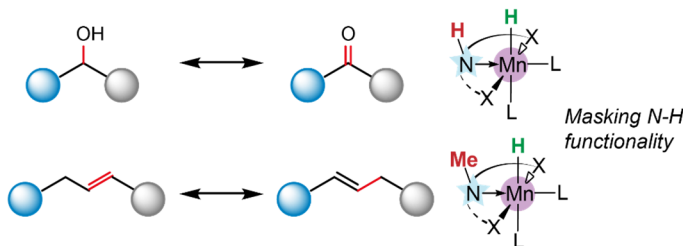


Figure 3. 1. Metal complex-mediated olefin transpositions (a) and the reactivity discussed in this work (b).

Manganese complexes emerged as potent carbonyl (de)hydrogenation catalysts in the last decade together with other two base metals: Fe and Co.¹⁵ The generation of Mn hydride species has been widely accepted as a prerequisite for the (de)hydrogenation cycle.¹⁶ However, the hydride transfer to non-polar olefins remains uncommon for Mn homogeneous catalysis. Recently a few cases of alkene hydrogenations have been reported with Mn non-pincer complexes.¹⁷ In particular, the alkyl bisphosphine Mn (I) catalyst reported by the Kirchner group forms an active 16e Mn hydride under H₂ atmosphere that can reduce a range of mono- and disubstituted alkenes to alkanes.^{17a}

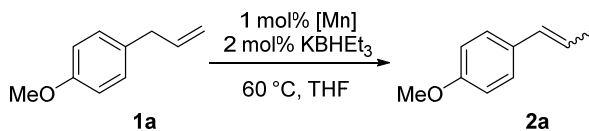
Given these results, we envisioned that the olefin transposition reactivity could be accessible by Mn-based systems. Herein we disclose that by masking the metal/NH cooperativity one can tune the reactivity of Mn hydrides from polar C=X (X = O, N) substrates to C=C bonds. With this strategy we develop the first highly selective olefin transposition reactions catalyzed by Mn(I), specifically an N-methylated Mn-CNP complex (**Figure 3. 1 b**).

3.2 Olefin transposition reactivity of Mn complexes

At the onset of investigation, we screened the activity of several well-defined Mn(I) complexes reported by our group and others (**Figure 3. 2**) towards the transposition of 4-allylanisole (**1a**) as a model substrate. The pre-catalysts **Mn-3—5**,^{16j, 18} that were reported to be efficient for carbonyl hydrogenation, surprisingly displayed no reactivity in transposition with the exception of **Mn-3** that gave 18% yield of isomerized product **2a** (**Table 3. 1**, entries 1-3).

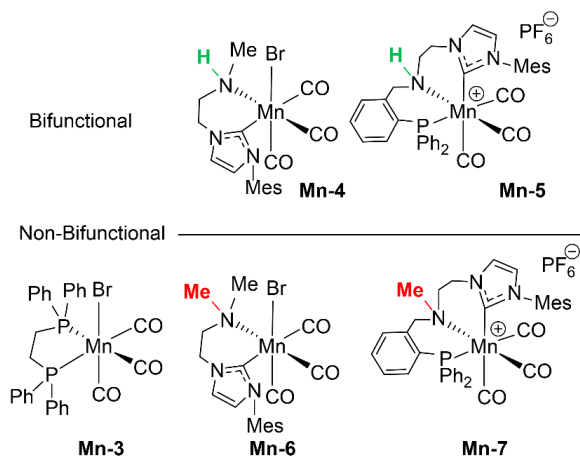
Since only non-bifunctional complex **Mn-3** was active, we assumed the N-H functionality might be detrimental to C=C transposition and synthesized the N-H methylated complexes **Mn-6** and **Mn-7** based on **Mn-4** and **Mn-5** (see chapter 2). Interestingly, once the N-H functionality is blocked, Mn complexes start exhibiting the transposition activity (entries 4, 5) with **Mn-7** giving the highest yield in the model reaction (61%). The yield and *E*-selectivity in product **2a** could be increased to 89% and 91:9 (*E*:*Z*) in a prolonged run (entry 6). Control experiments indicated the necessity of the catalyst activation with KBHET₃ that typically allows for more selective generation of Mn hydrides (entries 7, 8). Further screening of solvents and reaction temperatures confirmed the THF solvent and 60 °C temperature to be optimal for the catalytic performance of **Mn-7** (**Table 3. 2**). This catalytic process seemed to be sluggish with the reaction at low temperatures (40, 50 °C) giving low conversion of **1a** even at 48 h (entries 3 and 4). The high reaction temperature seemed to be not beneficial to the stereoselectivity of product **2a** (entries 1 and 2). Solvents with high (MeCN, IPA) and low (DCM, dioxane, toluene, hexane) polarities/dielectric constants were both found to be not beneficial for the catalysis (entries 5-10).

With the transposition reactivity established, we sought to examine the generality of this process. A broad scope of substrates can be converted with good selectivities with complex **Mn-7** (**Scheme 3. 1**). The industrially relevant anethole, isoeugenol, isosafrole, and isoelemicin (**2a-2d**) were successfully generated via the transposition reaction in excellent yields (72-99%) and *E*:*Z* ratios (>90:10). Our protocol is also efficient toward allylbenzene (**1e**) and its substituted derivatives with electron-withdrawing groups (**1f-h**), electron-donating groups (**1i-m**), and sterically hindered naphthyl (**1n**), furnishing the desired styrenyl products in ≥91% yields and ≥92% *E* selectivities.

Table 3. 1. Manganese-catalyzed transposition of 4-allylanisole model compound.^a

Entry	[Mn]	Time (h)	Yield (%)	E:Z
1	Mn-3	12	18	88:12
2	Mn-4	12	trace	-
3	Mn-5	12	trace	-
4	Mn-6	12	27	86:14
5	Mn-7	12	61	85:15
6	Mn-7	24	89 (89) ^b	91:9
7	--	24	trace	--
8 ^c	Mn-7	24	trace	--

^a Reaction conditions: **1a** (0.25 mmol), Mn catalyst (1 mol%), and 2 mol% KBHET₃ in 0.5 mL of THF at 60 °C. ^b Conversion given in parenthesis, ^c KBHET₃ not used for the activation of Mn catalyst.

**Figure 3. 2.** Mn catalysts used in this study.

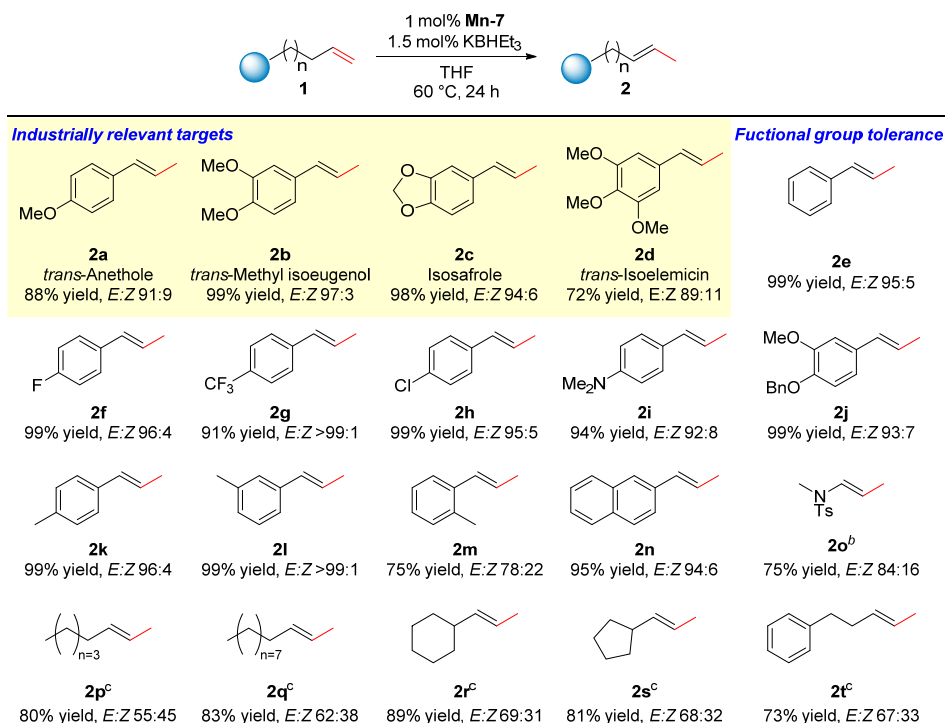
Controlling the site selectivity is a recognized challenge for migrating the C=C bonds over extended carbon skeletons, due to the thermodynamic similarities of positionally isomerized products. **Mn-7** allows for the highly regioselective monoisomerization of longer-chain alkenes, even though further migration could be thermodynamically more favourable. Both 1-octene (**1p**) and 1-dodecene (**1t**) were isomerized to corresponding 2-alkenes in excellent yield albeit with moderate *E:Z* ratios. The monoisomerization process is also compatible with functionalities (**1r-1t**), including cycloalkyl and phenyl.

Table 3. 2. Condition screening for transposition of 4-allylisoole with **Mn-7**.^a



Entries	T/°C	solvent	yield%	<i>E:Z</i>
1	70	THF	99	91:9
2	60	THF	97	92:8
3	50	THF	60	88:12
4	40	THF	8	83:17
5	60	DCM	-	
6	60	Toluene	37	86:14
7	60	dioxane	21	86:14
8	60	IPA	59	86:14
9	60	MeCN	-	
10	60	hexane	66	90:10

^aReactions were conducted with **1a** (0.25 mmol), **Mn-7** (1 mol%), KBHEt_3 (2 mol%) in solvent (0.5 mL) for 48 h.

Scheme 3. 1. Catalytic double bond transposition with **Mn-7**.^a

^a Reaction conditions: substrate **1** (0.25 mmol), **Mn-7** (1 mol%), and 2 mol% KBHET₃ in 0.5 mL of THF at 60 °C for 24 h. ^b 5 mol% **Mn-7** was used instead. ^c Reaction was performed with 4 mol% **Mn-7** at 70 °C in toluene instead.

3.3 Reactivity over C=C and C=O

The N-H functionality has been broadly reported as the key structural parameter that enables the (de)hydrogenation of polar moieties and Mn/NH bifunctional behaviour in principle.¹⁹ This was typically confirmed in the studies where alkylation of N-H functionality produced inactive (de)hydrogenation catalysts.^{16h, 16i, 18a, 20} Our catalytic data (**Table 3. 1**, entries 2-5) implies that for olefin transposition this structure-activity relationship is inverted.

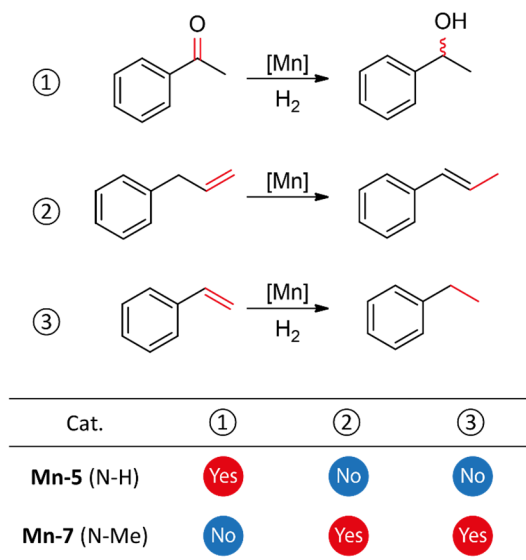
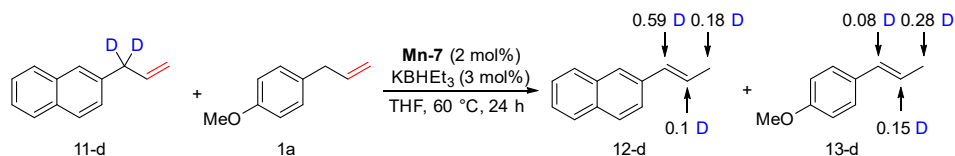


Figure 3. 3. Reactivities of Mn(I)-CNP complexes toward C=O and C=C functionalities.

To confirm this, we compared the C=O/C=C substrate preference using cooperative and non-cooperative Mn(I)-CNP counterparts: **Mn-5** and **Mn-7**, respectively. As depicted in **Figure 3. 3**, the N-H methylation in Mn-CNPs completely suppressed the ketone hydrogenation, but enabled the transposition of allylbenzene and even the hydrogenation of styrene. Notably, **Mn-5** with the cooperative N-H functionality was inactive for either of C=C bond transformation paths. The displayed selectivity prompted a further mechanistic analysis of **Mn-7** operation in the course of reaction.

Scheme 3. 2. Results of deuterium crossover experiments.



3.4 Mechanistic studies

As a first step to the mechanistic investigation we conducted cross reactivity experiments with deuterium-labelled **11-d** and non-deuterated **2a** (**Scheme 3. 2**). We observed both the intramolecular scrambling as well as the intermolecular crossover of the deuterium

label between the olefin products. This is indicative of transposition proceeding via either alkyl or hydrogen atom transfer mechanisms, because the cross reactivity between deuterated and label-free olefins should involve a Mn-H species as a transfer medium. Together with the previous observation that KBHET_3 activation was necessary for the catalytic reactivity (**Table 3. 1**, entry 8), labelling data implies that the formation of Mn hydride *must* take place in the course of reaction. To verify this we monitored the KBHET_3 activation of pre-catalysts **Mn-7** followed by the catalytic turnover using NMR and IR spectroscopies.

Mn-7 readily forms hydrides upon activation. At room temperature the reaction of **Mn-7** with KBHET_3 in $\text{THF-}d_8$ gave rise to three new doublet resonances in the ^1H NMR spectrum at -5.01, -5.65, and -6.77 ppm, with $^2J_{\text{PH}} = 40.0, 48.0, \text{ and } 88.0$ Hz, respectively (**Figure 3. 4 a, b**). We attributed these peaks to the isomers of tricarbonyl Mn-H species **8**, in total accounting for 97% of the activation products. The retention of three CO ligands upon the near-quantitative transformation of **7** during the activation step is confirmed by IR spectroscopy revealing three new bands at 1981, 1896, and 1876 cm^{-1} (**Figure 3. 4 c**). Since **8** is a tricarbonyl, monohydride complex featuring Mn-bound phosphine donor we conclude that activation of **Mn-7** leads to the dissociation of the central N-donor group rendering it hemilabile. This contrasts the case of non-methylated analogue **Mn-5**,^{16j} which dissociated the phosphine arm in a similar activation step (see chapter 2).

The dissociation of the central N-donor is the major transformation within the $\text{CN}(\text{Me})\text{P}$ ligand upon the activation and the hydride complex with dissociated P-donor (**9**) was observed in minor amounts (3% NMR yield, see **Figure 3. 8** in section 3.6.1). The difference between Mn hydrides with dissociated N or P donor was reflected in the hydride ligand shifts in the NMR spectrum. Namely, the coupling feature between hydride and P donor in complex **8** disappeared and the hydride resonances showed as singlet peaks in the ^{31}P -decoupled ^1H NMR spectrum.

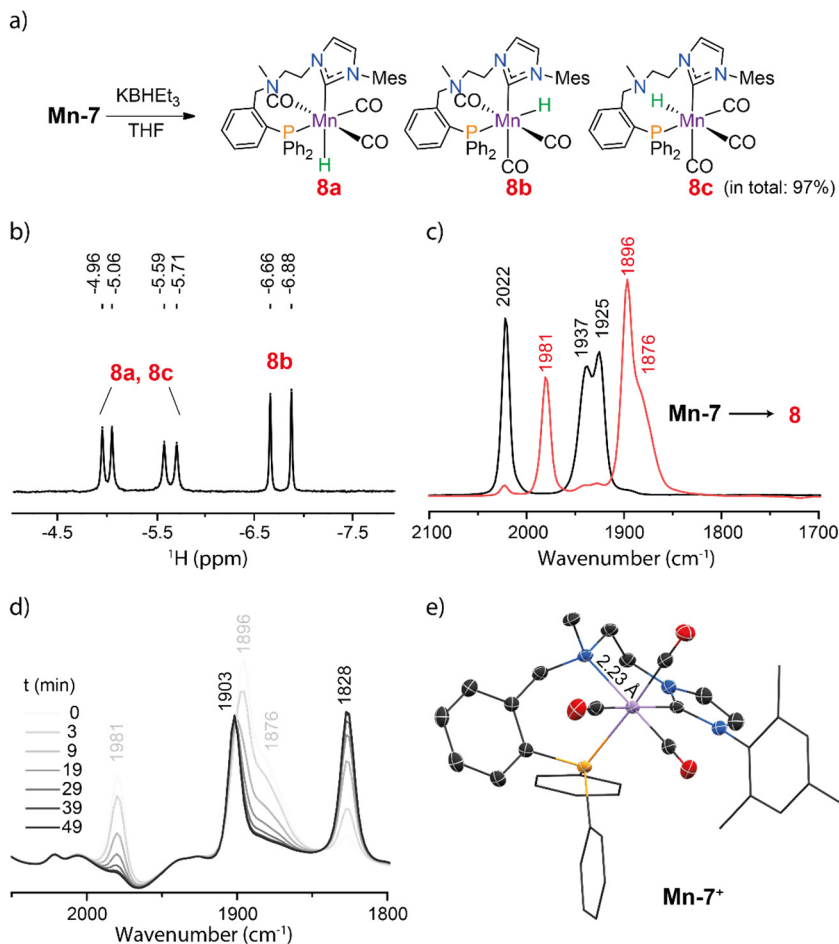


Figure 3. 4. Activation of **Mn-7** upon the reaction with KBHET_3 (a), hydride region of ^1H -NMR (THF-d_8) spectra (b) of in-situ generated complex **8** and IR spectra (c) of complex **Mn-7** (black) and in-situ generated complex **8** (red) recorded in THF. Time-dependent IR spectra evolution (d) for the reaction of complex **8** with 100 eq. of olefin (0 to 49 min, grey to black). Molecular structure (e) of complex **Mn-7** in the solid state with thermal ellipsoids drawn at 50% probability. Hydrogen atoms are omitted for clarity.

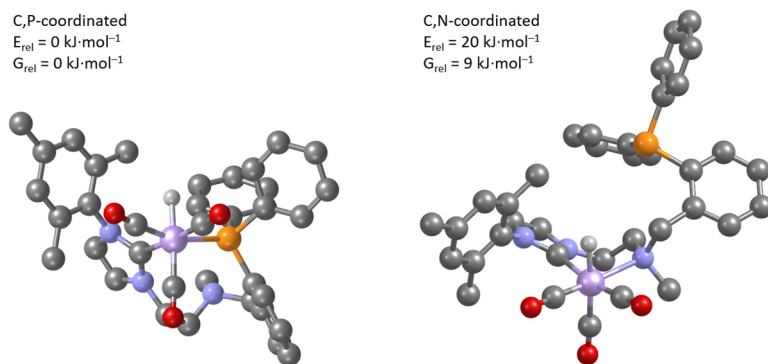


Figure 3. 5. The most stable configurations of C,N- and C,P- coordinated bidentate Mn hydride complexes.

Table 3. 3. Comparison of theoretical and experimental IR bands for CO stretching of complex **8**.

Vibration mode	IR frequency, cm^{-1}		
	DFT	norm	exp
Mn-7 , nosymm_1	2043	1936	1925
Mn-7 , nosymm_2	2049	1941	1937
Mn-7 , symm	2127	2015	2022
8 , nosymm_1	1992	1887	1876
8 , nosymm_2	1994	1889	1896
8 , symm	2080	1970	1981
Norm. coef.	0.9473		
RMSE	8.83		

Table 3. 4. Comparison of theoretical and experimental ^1H NMR (hydride) chemical shifts of complexes **8** and **9**.

Complex	Experiment hydride (ppm)	Calculated hydride (ppm)
8	-5.01, -5.65, -5.77	-5.7
9	-3.50, -3.80	-3.7

To validate the proposed structures of complexes **8**, DFT calculations were first carried out to assess the stabilities of the Mn hydrides with the dissociations of different donors.

As depicted in **Figure 3. 5**, Mn-CP hydride (with free N) forms the most stable configuration that is preferred over Mn-CN hydride (with free P) by 9 kJ·mol⁻¹. This stability difference was close to the ratio of different hydrides species observed in NMR experiments (see **Figure 3. 8** in section 3.6.1), suggesting the dominating complexes **8** were probably Mn-CP hydrides, and complexes **9** were Mn-CN hydrides. The computed and experimental spectroscopies (**Table 3. 3**, **Table 3. 4**) were subsequently compared. Since species **9** were minor products in the activation of **7** and not noticeable in the IR spectra, we only compared the bands of CO ligands of **8** and took well-characterized **Mn-7** as a reference (**Table 3. 3**). The low root-mean-square deviation (8.8 cm⁻¹) revealed an excellent alignment between the computational and experimental results. The calculated hydride resonances of both species **8** and **9** were also close to those observed in experiments (**Table 3. 4**). Taken all together, our calculations confirm **8** and **9** as the tricarbonyl Mn hydride complexes with dissociated N and P donors respectively. Because the identification of exact stereochemistry for the isomers presented a challenge, we assumed that complex **8** might exist as an octahedral complex with facially bound P and C donor groups with isomers distinguished by hydride ligand placement *trans* to either NHC, phosphine or carbonyl ligand (**8a**, **8b** and **8c** respectively, **Figure 3. 4**).

Hydride complexes **8** readily react with olefins. A clean consumption of hydrides in **8** was observed within minutes upon the addition of 4-allylanisole (**1a**). The analysis of this reaction with IR and NMR spectroscopy indicates the formation of the dicarbonyl Mn-alkyl species. Namely, the IR spectrum (**Figure 3. 4 d**) indicates the consumption of **8** and formation of two new bands at 1903, 1828 cm⁻¹ typical of dicarbonyl complexes. In the absence of the hydride resonance in the NMR spectrum, this suggests that reaction of **8** with olefin leads to the formation of metal-alkyl complexes with N donor group reattaching to the Mn center. As expected, the gradual production of **2a** was then detected in ¹H NMR upon the heating the reaction mixture to 60 °C (**Figure 3. 6 a**). This observation of hydride transfer suggests that **Mn-7** isomerizes olefins via the alkyl mechanism. Since we observe no further change in the NMR spectrum, we assume that the metal alkyl complexes likely represent the resting states in this transformation as was earlier proposed for the high-spin cobalt(II) system by Wiex, Holland and co-workers.^{10b} The following transformation of the resting state in catalysis is typically the rate-determining step. The rate of olefin

transposition reaction should then be determined by the rate of β -hydride elimination (**Figure 3. 7**, intermediate II-III), suggesting that catalysis rate should be independent of substrate concentration. Indeed our kinetic studies revealed an order of 0.14 with respect to the alkene substrate, confirming the hypothesis above (**Figure 3. 6 b**).

Based on the results above we conclude that metal-alkyl mechanism is likely manifested in the present catalytic system (**Figure 3. 7**). The activated Mn(I)-hydride precatalyst **8** enters the cycle via the reaction with alkene via the intermediate **I**. This step requires the dissociation of a CO ligand detected experimentally. Further transformation of **I** involves the hydride transfer to form Mn-alkyl species **II** aided by the reattachment of N-donor ligand. Subsequent β -hydride elimination furnishes the isomerized olefin product **2** and dicarbonyl Mn hydride **III**. The final coordination of another alkene substrate can be kinetically unfavourable due to the saturation of Mn centre with strong field ligands. However, we speculate that this step can be facilitated by the dissociation of the labile N donor within Mn-CN(Me)P complex that would liberate the vacant site for olefin coordination regenerating the species **I**.

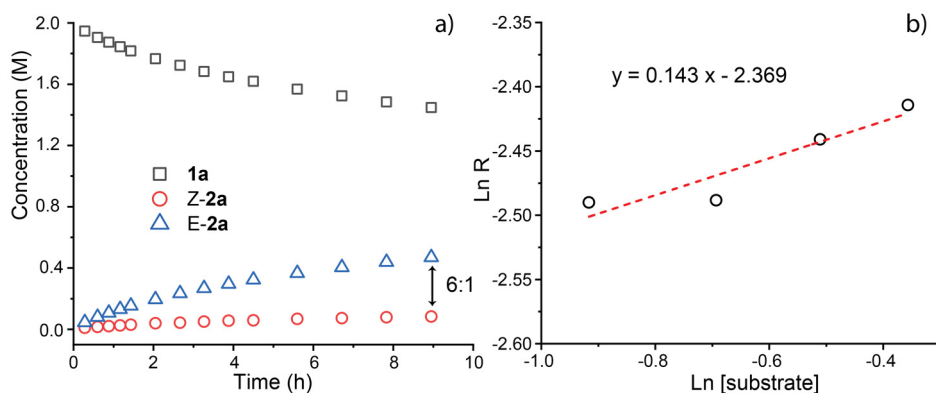


Figure 3. 6. Kinetic trace (a) of Mn alkyl-promoted isomerization of **1a** at 60 °C in THF- d_8 and the determination of reaction order (b) of olefin substrate via the plot of \ln (initial reaction rate) v.s. \ln (initial substrate concentration).

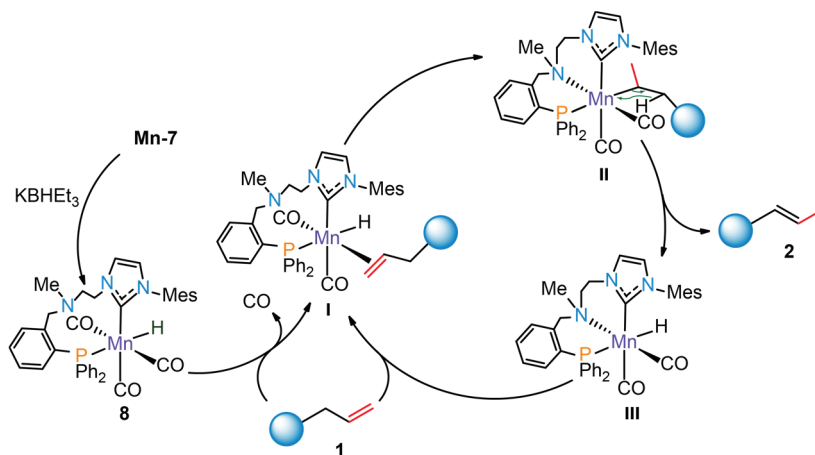


Figure 3. 7. Mechanistic proposal for Mn-catalyzed olefin transpositions.

Table 3. 5. Manganese-catalyzed transposition of 4-allylanisole **1a** in the presence of donor additives.^a

Entries	Donors	Yield (%)	E:Z
1	-	89	91:9
2	PPh ₃	7	-
3	CO (3 bar)	4	-
4	pyridine	68	85:15
5	acetonitrile	24	83:17

^a Reaction conditions: **1a** (0.25 mmol), donor additive (0.125 mmol), **Mn-7** (1 mol%), and 2 mol% KBHEt₃ in 0.5 mL of THF at 60 °C for 24 h.

Table 3. 6. Bond length of Mn-N for selected Mn complexes in the solid state calculated from X-Ray data.

Complexes	N-H		N-Me	
	Mn-4	Mn-5	Mn-6	Mn-7
Mn-N (Å)	2.14	2.14 ^a	2.24	2.23

^a The bond length for **Mn-5** was determined by DFT analysis previously. 16j

Similar to the case of NH-cooperative Mn(I) catalyst **Mn-5** our results reveal the high extent of tridentate ligand dynamics throughout the catalyst activation. The suggested

involvement of the N-donor dissociation in the catalytic cycle²¹ would rationalize the selectivity flip toward C=C for Mn complexes obtained by blocking the N-H functionality (**Table 3. 1**, **Figure 3. 3**). To investigate the occurrence of ligand dissociation, control experiments of the transposition catalysis were performed in the presence of a series of donor additives that can compete with olefin substrates for the open sites of Mn catalysts (**Table 3. 5**). The additions of strong field ligands, PPh₃ and CO, both rendered **Mn-7** nearly inactive (entries 2 and 3), while the reactions with weaker field ligands, pyridine and acetonitrile, gave much lower yields of **2a** (entries 4 and 5) compared to the additive-free experiment (entry 1). The inhibitory effects of donor additives validate the importance of generating coordination space for the catalysis. Analysing the crystal structures (**Figure 3. 4** and **Table 3. 6**) of methylated **Mn-6** and **7** we find that the Mn-N bonds lengths are significantly longer in these complexes compared to their NH counterparts **Mn-4**, **5**.^{16j, 18a} This trend further suggests that conventional pincer and tridentate ligands in Mn(I) complexes might exhibit dynamics and donor ligand lability that is not characteristic for their noble metal-based counterparts. While the catalytic functionality of this behaviour is open to debate, it clearly invites further research into ligand dissociation dynamics of catalytically relevant Mn(I) complexes.

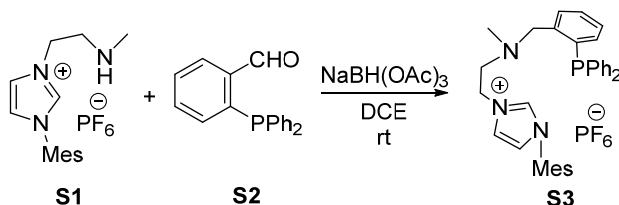
3.5 Conclusion

In conclusion, this chapter describes the first precedent of olefin transposition catalysed by complexes based on abundant and biocompatible Mn metal. This reactivity furnishes an array of 2-alkenes in good selectivities and yields. Importantly, this activity manifests upon disabling the cooperative function in related Mn catalysts that show activity in carbonyl hydrogenation. In contrast to polar substrates, catalytic hydride transfer to olefins is via a stepwise manner, which involves the coordination of olefin on metal catalyst followed by migratory insertion. Because of this, controlling the activation of precatalysts to generate vacant sites becomes the key to inducing olefin hydrogenation/transposition activity. Utilization of ligand dynamics have been shown to be an effective protocol to create space for substrates, enabling the olefin transposition catalysed by Mn complexes.

3.6 Experimental details

3.6.1 Synthetic procedures

Synthesis of Ligand S3:



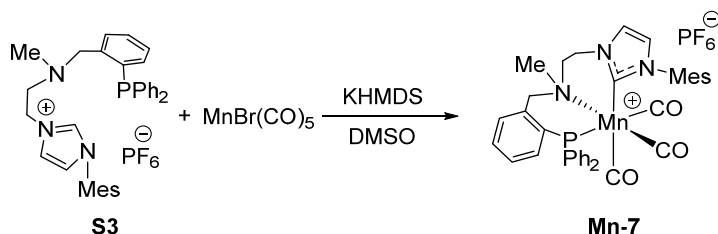
In a Schlenk tube solution of **S1** (1.556 g, 4 mmol) and **S2** (1.218 g, 4.2 mmol) was prepared in dry DCE (20 mL) and stirred overnight. Sodium triacetoxyborohydride (1.336 g, 6.3 mmol) was then slowly added as solid to the resulting solution. After stirring for another night, the solution was quenched by KHCO_3 (aq) and extracted with DCM. The combined organic phases were dried over anhydrous Na_2SO_4 , concentrated and purified by Et_2O wash to provide the compound **S3** as white foam solid in 49% yield (1.3 g).

^1H NMR (400 MHz, $\text{THF-}d_8$, 297 K) δ 8.95 (s, 1H), 7.81 (s, 1H), 7.59 (s, 1H), 7.42 – 7.03 (m, 15H), 6.93 – 6.82 (m, 1H), 4.44 (t, $J = 5.8$ Hz, 2H), 3.79 (s, 2H), 2.90 (t, $J = 5.7$ Hz, 2H), 2.34 (s, 3H), 2.19 (s, 3H), 2.05 (s, 6H);

$^{31}\text{P}\{^1\text{H}\}$ NMR (162 MHz, $\text{THF-}d_8$, 297 K) δ -14.3;

^{13}C $\{^1\text{H}\}$ NMR (101 MHz, $\text{THF-}d_8$, 297 K) δ 144.9 ($^1J_{\text{PC}}$ 23.2 Hz), 142.6, 139.1, 138.9 ($^2J_{\text{PC}}$ 11.1 Hz), 138.2 ($^1J_{\text{PC}}$ 15.1 Hz), 136.6, 135.6, 135.4, 135.3, 133.2, 131.2, 131.0 ($^2J_{\text{PC}}$ 6.1 Hz), 130.5, 130.4, 130.3, 130.2, 129.0, 125.7, 125.3, 61.8, 58.1, 49.5, 42.5, 22.0, 18.2.

Synthesis of complex Mn-7:



To the solution of ligand **S3** (663 mg, 1 mmol) in DMSO (5 mL) was slowly added KHMDS solution (209.4 mg, 1.05 mmol, in 0.5 mL DMSO) and stirred at rt for 5 min under Ar atmosphere. The MnBr(CO)₅ was then added and stirred for another 12 h. The resulting reaction mixture was then quenched by H₂O (15 mL) and extracted by DCM for 3 times. The combined organic phase was dried over MgSO₄, filtered, evaporated to dryness and further purified by crystallization (petane vapor diffusion into solution in DCM) as light yellow solid in 57 % yield (460 mg).

Complex **Mn-7**: ¹H NMR (400 MHz, CD₂Cl₂, 297 K) δ 7.79 – 7.32 (m, 11H), 7.32 – 7.03 (m, 3H), 6.98 (s, 1H), 6.72 – 6.65 (m, 3H), 4.08 (d, J = 15.2 Hz, 1H), 3.88 (d, J = 12.7 Hz, 1H), 3.48 – 3.35 (m, 2H), 3.05 – 2.87 (m, 5H), 2.22 (s, 3H), 1.95 (s, 3H), 1.73 (s, 3H);

³¹P{¹H}NMR (162 MHz, CD₂Cl₂, 297 K) δ 37.2;

¹³C {¹H}NMR (101 MHz, CD₂Cl₂, 297 K) δ 217.0, 216.6, 214.8, 185.6, 140.3, 137.3 (¹J_{PC} 16.2 Hz), 136.4, 135.7, 133.8 (³J_{PC} 8.1 Hz), 133.4, 133.3, 132.9 (²J_{PC} 11.1 Hz), 132.3, 131.8, 131.4, 130.4, 130.0, 129.8 (³J_{PC} 7.1 Hz), 129.7, 129.6, 129.37, 129.0 (²J_{PC} 10.1 Hz), 128.4, 128.0 (²J_{PC} 9.1 Hz), 126.9, 125.6, 63.9, 58.4, 45.5, 20.6, 19.1, 17.5;

IR (solution in THF): $\bar{\nu}$ [cm⁻¹] 2022 (s, $\bar{\nu}$ CO), 1937 (s, $\bar{\nu}$ CO), 1925 (s, $\bar{\nu}$ CO);

EA: Found (Calcd.) for C₃₇H₃₆F₆MnN₃O₃P₂: C: 55.07 (55.44); H: 4.51 (4.53); N: 5.19 (5.24).

***In-situ* generation of hydride complex**

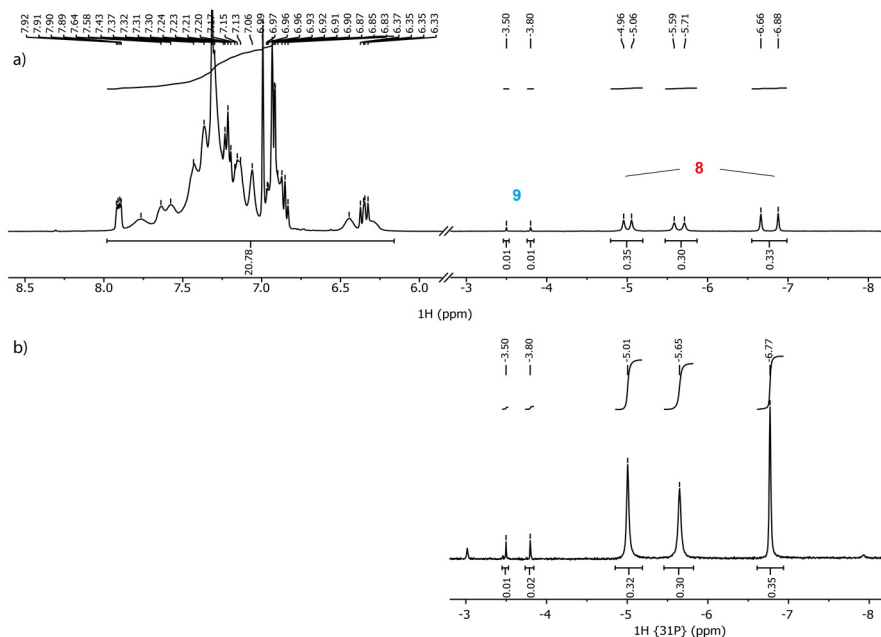
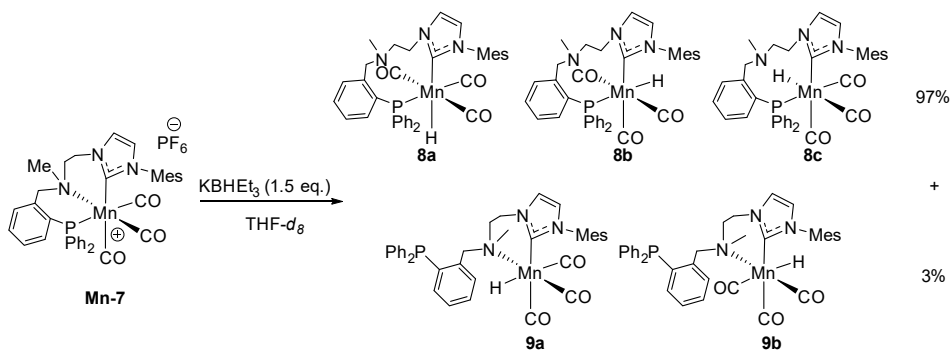


Figure 3. 8. ^1H -NMR (a), $^1\text{H}\{^{31}\text{P}\}$ -NMR (b) spectrum of KBHET_3 -activated **Mn-7** in THF-d_8 immediately after reaction. Bidentate Mn-H **8** with free nitrogen donor were formed as major products. Additionally, hydride from complex **9** with free phosphine donor was also formed in trace amount. The disappearance of phosphine-hydride coupling feature for **8** and the retention of two hydride resonances for **9** in phosphorus decoupled ^1H NMR are consistent with the bound and non-bound nature of P-arm in **8** and **9**, respectively. The hydride species were estimated the fraction of **8** at ca. 97% and **9** at ca. 3%.



Upon treatment of complex **Mn-7** (8.0 mg, 1 equiv.) with KBHET_3 (15 μL of 1M THF solution, 1.5 equiv.) in THF-d_8 (0.6 mL) an orange solution was formed immediately producing the mixture of hydride complexes **8** and **9** followed by NMR measurements. IR analysis was performed through same procedure with protic THF as solvent.

3.6.2. Catalytic experiments

General procedures for catalytic transposition of olefin. Inside the glovebox, a solution of **Mn-7** (2.0 mg, 1 mol%) was prepared in 0.3 mL THF and activated with KBHET_3 (4 μL , 1.5 mol%, 1M THF solution) for 10 min. Another solution with substrate **1** (0.25 mmol), THF (0.3 mL), and 1-methyl naphthalene (11.2 μL , 0.0789 mmol) was prepared. 10 μL of the substrate mixture was taken and dissolved in CDCl_3 as the reference for yield analysis. The catalyst and substrate solutions were combined in a vial that was subsequently dwelled at 60 °C for 24 h. After the reaction, resulting mixture was cool down to room temperature. NMR samples of products were prepared by the dilution of the reaction mixture in CDCl_3 (30 μL into 0.5 mL deuterium solvent). The products were identified and quantified by $^1\text{H-NMR}$.

Catalytic hydrogenation of acetophenone. Inside the glovebox, the solution of Mn complex (0.05 mol%) was prepared in 1 mL THF and activated with KBHET_3 (10 μL , 0.2 mol%, 1M THF solution) for 10 min. Acetophenone (5 mmol), THF (3 mL), and dodecane (56.8 μL , 0.25 mmol) were then added. The resulting mixture was transferred into a stainless steel autoclave in the glovebox. The system was purged with N_2 (3 \times 8 bar) and H_2 (1 \times 30 bar), pressurized with H_2 to 30 bar, and heated to 60 °C. After 12 h, the resulting mixture was depressurized, cooled to room temperature, and analysed on an Agilent 6890 gas chromatograph equipped with an FID detector. GC samples were prepared by dilution of the reaction mixture in THF (20 μL into 1 mL THF).

Catalytic hydrogenation of styrene: Inside the glovebox, the solution of Mn complex (1 mol%) was prepared in 0.2 mL THF and activated with KBHET_3 (5 μL , 2 mol%, 1M THF solution) for 10 min. Styrene (0.25 mmol), THF (0.3 mL), dodecane (56.8 μL , 0.25 mmol) were then added. The resulting mixture was transferred into a stainless steel autoclave in the glovebox. The system was purged with N_2 (3 \times 8 bar) and H_2 (1 \times 30 bar), pressurized with H_2 to 50 bar, and heated to 70 °C. After 12 h, resulting mixture was depressurized,

cooled to room temperature, and analysed on an Agilent 6890 gas chromatograph equipped with an FID detector. GC samples were prepared by dilution of the reaction mixture in THF (20 μ L into 1 mL THF).

3.6.3. Computational details

All quantum chemical calculations were performed by Ivan Chernyshov. The MACE protocol²² was used to generate starting geometries for all allowed configurations of C,N- and C,P-bound Mn hydride complexes. The following optimization and frequency calculations were carried out at the PBE0-D3/6-311+G(d,p)/PCM(THF) level of theory using the Gaussian16 software^{23,24}. (see section A.1 in Appendix) The calculated frequencies were scaled with the factor $f = 0.9576$, which was chosen for best agreement of experimental and calculated data. It is applied to minimize the error of the harmonic approach for the vibration frequency calculation. The Half width of the plotted calculated spectra is 5 cm^{-1} . ¹H NMR shielding was computed for the optimized geometries at PBE0/6-311++G(2d,2p) level of theory.

3.6.4. Computational details

X-ray diffraction studies were performed by M. Weber (Freie Universität Berlin). Crystallographic details of complex **Mn-7** are available in Cambridge Crystallographic Data Centre via CCDC entries 2165735 (http://www.ccdc.cam.ac.uk/data_request/cif).

3.7 References

1. (a) Panten, J.; Surburg, H., *Flavors and fragrances*, 3. aromatic and heterocyclic compounds. Wiley: Weinheim, 2015; p 1-45; (b) Larsen, C. R.; Grotjahn, D. B., *The value and application of transition metal catalyzed alkene isomerization in industry*. Wiley-VCH Verlag: Weinheim, Germany, 2017; p 1365-1378.
2. (a) Machkenzie, K., *In The Chemistry of Alkenes*. Wiley-Interscience: New York, 1964; (b) Larock, R. C., *Comprehensive Organic Transformations. A Guide to Functional Group Preparations* 2ed.; VCH: 1999; (c) Alcaide, B.; Almendros, P.; Luna, A., Grubbs' ruthenium-carbenes beyond the metathesis reaction: less conventional non-metathetic utility. *Chem. Rev.* **2009**, 109, 3817-3858; (d) Lohr, T. L.; Marks, T. J., Orthogonal tandem catalysis. *Nat. Chem.* **2015**, 7, 477-482; (e) Pollini, J.; Pankau, W. M.; Gooßen, L. J., Isomerizing Olefin Metathesis. *Chem. Eur. J.* **2019**, 25, 7416-7425.

3. Wang, J., *Stereoselective alkene synthesis*. Springer: 2012; Vol. 327.
4. (a) Donohoe, T. J.; O'Riordan, T. J.; Rosa, C. P., Ruthenium-Catalyzed Isomerization of Terminal Olefins: Applications to Synthesis. *Angew. Chem. Int. Ed.* **2009**, *48*, 1014-1017; (b) Hilt, G., Double Bond Isomerisation and Migration—New Playgrounds for Transition Metal-Catalysis. *ChemCatChem* **2014**, *6*, 2484-2485; (c) Larionov, E.; Li, H.; Mazet, C., Well-defined transition metal hydrides in catalytic isomerizations. *Chem. Commun.* **2014**, *50*, 9816-9826; (d) Vilches-Herrera, M.; Domke, L.; Börner, A., Isomerization–hydroformylation tandem reactions. *ACS Catal.* **2014**, *4*, 1706-1724; (e) Hassam, M.; Taher, A.; Arnott, G. E.; Green, I. R.; van Otterlo, W. A., Isomerization of allylbenzenes. *Chem. Rev.* **2015**, *115*, 5462-5569; (f) Vasseur, A.; Bruffaerts, J.; Marek, I., Remote functionalization through alkene isomerization. *Nat. Chem.* **2016**, *8*, 209-219; (g) Molloy, J. J.; Morack, T.; Gilmour, R., Positional and geometrical isomerisation of alkenes: the pinnacle of atom economy. *Angew. Chem. Int. Ed.* **2019**, *58*, 13654-13664.
5. (a) Biswas, S.; Huang, Z.; Choliy, Y.; Wang, D. Y.; Brookhart, M.; Krogh-Jespersen, K.; Goldman, A. S., Olefin isomerization by iridium pincer catalysts. Experimental evidence for an η^3 -allyl pathway and an unconventional mechanism predicted by DFT calculations. *J. Am. Chem. Soc.* **2012**, *134*, 13276-13295; (b) Wang, Y.; Qin, C.; Jia, X.; Leng, X.; Huang, Z., An Agostic Iridium Pincer Complex as a Highly Efficient and Selective Catalyst for Monoisomerization of 1-Alkenes to trans-2-Alkenes. *Angew. Chem. Int. Ed.* **2017**, *56*, 1614-1618; (c) Camp, A. M.; Kita, M. R.; Blackburn, P. T.; Dodge, H. M.; Chen, C.-H.; Miller, A. J., Selecting double bond positions with a single cation-responsive iridium olefin isomerization catalyst. *J. Am. Chem. Soc.* **2021**, *143*, 2792-2800; (d) Kita, M. R.; Miller, A. J., An Ion-Responsive Pincer-Crown Ether Catalyst System for Rapid and Switchable Olefin Isomerization. *Angew. Chem. Int. Ed.* **2017**, *129*, 5498-5502; (e) Massad, I.; Sommer, H.; Marek, I., Stereoselective Access to Fully Substituted Aldehyde-Derived Silyl Enol Ethers by Iridium-Catalyzed Alkene Isomerization. *Angew. Chem. Int. Ed.* **2020**, *59*, 15549-15553.
6. (a) Zhuo, L.-G.; Yao, Z.-K.; Yu, Z.-X., Synthesis of Z-alkenes from Rh (I)-catalyzed olefin isomerization of β , γ -unsaturated ketones. *Org. Lett.* **2013**, *15*, 4634-4637; (b) Yip, S. Y.; Aïssa, C., Isomerization of Olefins Triggered by Rhodium-Catalyzed $\text{C}\equiv\text{C}-\text{H}$ Bond Activation: Control of Endocyclic β -Hydrogen Elimination. *Angew. Chem.* **2015**, *127*, 6974-6977.
7. (a) Gauthier, D.; Lindhardt, A. T.; Olsen, E. P.; Overgaard, J.; Skrydstrup, T., In situ generated bulky Palladium hydride complexes as catalysts for the efficient isomerization of olefins. Selective transformation of terminal alkenes to 2-alkenes. *J. Am. Chem. Soc.* **2010**, *132*, 7998-8009; (b) Lin, L.; Romano, C.; Mazet, C., Palladium-catalyzed long-range deconjugative isomerization of highly substituted α , β -unsaturated carbonyl compounds. *J. Am. Chem. Soc.* **2016**, *138*, 10344-10350.

8. (a) Larsen, C. R.; Grotjahn, D. B., Stereoselective alkene isomerization over one position. *J. Am. Chem. Soc.* **2012**, 134, 10357-10360; (b) Larsen, C. R.; Erdogan, G.; Grotjahn, D. B., General catalyst control of the monoisomerization of 1-alkenes to trans-2-alkenes. *J. Am. Chem. Soc.* **2014**, 136, 1226-1229; (c) Engel, J.; Smit, W.; Foscatto, M.; Occhipinti, G.; Törnroos, K. W.; Jensen, V. R., Loss and reformation of ruthenium alkylidene: connecting olefin metathesis, catalyst deactivation, regeneration, and isomerization. *J. Am. Chem. Soc.* **2017**, 139, 16609-16619; (d) Paulson, E. R.; Moore, C. E.; Rheingold, A. L.; Pullman, D. P.; Sindewald, R. W.; Cooksy, A. L.; Grotjahn, D. B., Dynamic π -Bonding of Imidazolyl Substituent in a Formally 16-Electron $Cp^* Ru(\kappa^2-P, N)^+$ Catalyst Allows Dramatic Rate Increases in (E)-Selective Monoisomerization of Alkenes. *ACS Catal.* **2019**, 9, 7217-7231; (e) Scaringi, S.; Mazet, C., Kinetically controlled stereoselective access to branched 1, 3-dienes by Ru-catalyzed remote conjugative isomerization. *ACS Catal.* **2021**, 11, 7970-7977.
9. Zhao, K.; Knowles, R. R., Contra-Thermodynamic Positional Isomerization of Olefins. *J. Am. Chem. Soc.* **2021**.
10. (a) Puenner, F.; Schmidt, A.; Hilt, G., Up the Hill: Selective Double-Bond Isomerization of Terminal 1, 3-Dienes towards Z-1, 3-Dienes or 2Z, 4E-Dienes. *Angew. Chem. Int. Ed.* **2012**, 51, 1270-1273; (b) Chen, C.; Dugan, T. R.; Brennessel, W. W.; Weix, D. J.; Holland, P. L., Z-selective alkene isomerization by high-spin cobalt (II) complexes. *J. Am. Chem. Soc.* **2014**, 136, 945-955; (c) Crossley, S. W.; Barabé, F.; Shenvi, R. A., Simple, chemoselective, catalytic olefin isomerization. *J. Am. Chem. Soc.* **2014**, 136, 16788-16791; (d) Schmidt, A.; Nödling, A. R.; Hilt, G., An Alternative Mechanism for the Cobalt-Catalyzed Isomerization of Terminal Alkenes to (Z)-2-Alkenes. *Angew. Chem. Int. Ed.* **2015**, 54, 801-804; (e) Li, G.; Kuo, J. L.; Han, A.; Abuyuan, J. M.; Young, L. C.; Norton, J. R.; Palmer, J. H., Radical isomerization and cycloisomerization initiated by H• transfer. *J. Am. Chem. Soc.* **2016**, 138, 7698-7704; (f) Liu, X.; Zhang, W.; Wang, Y.; Zhang, Z.-X.; Jiao, L.; Liu, Q., Cobalt-catalyzed regioselective olefin isomerization under kinetic control. *J. Am. Chem. Soc.* **2018**, 140, 6873-6882; (g) Meng, Q. Y.; Schirmer, T. E.; Katou, K.; König, B., Controllable Isomerization of Alkenes by Dual Visible-Light-Cobalt Catalysis. *Angew. Chem. Int. Ed.* **2019**, 58, 5723-5728; (h) Zhang, S.; Bedi, D.; Cheng, L.; Unruh, D. K.; Li, G.; Findlater, M., Cobalt (II)-catalyzed stereoselective olefin isomerization: facile access to acyclic trisubstituted alkenes. *J. Am. Chem. Soc.* **2020**, 142, 8910-8917; (i) Kim, D.; Pillon, G.; DiPrimio, D. J.; Holland, P. L., Highly Z-selective double bond transposition in simple alkenes and allylarenes through a spin-accelerated allyl mechanism. *J. Am. Chem. Soc.* **2021**, 143, 3070-3074; (j) Liu, X.; Rong, X.; Liu, S.; Lan, Y.; Liu, Q., Cobalt-Catalyzed Desymmetric Isomerization of Exocyclic Olefins. *J. Am. Chem. Soc.* **2021**, 143, 20633-20639.
11. (a) Kapat, A.; Sperger, T.; Guven, S.; Schoenebeck, F., E-Olefins through intramolecular radical relocation. *Science* **2019**, 363, 391-396; (b) Iwamoto, H.; Tsuruta,

T.; Ogoshi, S., Development and Mechanistic Studies of (E)-Selective Isomerization/Tandem Hydroarylation Reactions of Alkenes with a Nickel (0)/Phosphine Catalyst. *ACS Catal.* **2021**, 11, 6741-6749; (c) Huang, L.; Lim, E. Q.; Koh, M. J., Secondary phosphine oxide-activated nickel catalysts for site-selective alkene isomerization and remote hydrophosphination. *Chem Catalysis* **2022**.

12. (a) Jennerjahn, R.; Jackstell, R.; Piras, I.; Franke, R.; Jiao, H.; Bauer, M.; Beller, M., Benign catalysis with iron: unique selectivity in catalytic isomerization reactions of olefins. *ChemSuschem* **2012**, 5, 734-739; (b) Yu, X.; Zhao, H.; Li, P.; Koh, M. J., Iron-catalyzed tunable and site-selective olefin transposition. *J. Am. Chem. Soc.* **2020**, 142, 18223-18230; (c) Garhwal, S.; Kaushansky, A.; Fridman, N.; de Ruiter, G., Part per million levels of an anionic iron hydride complex catalyzes selective alkene isomerization via two-state reactivity. *Chem Catalysis* **2021**; (d) Xu, S.; Geng, P.; Li, Y.; Liu, G.; Zhang, L.; Guo, Y.; Huang, Z., Pincer Iron Hydride Complexes for Alkene Isomerization: Catalytic Approach to Trisubstituted (Z)-Alkenyl Boronates. *ACS Catal.* **2021**, 11, 10138-10147.

13. Jankins, T.; Bell, W.; Zhang, Y.; Qin, Z.-Y.; Gembicky, M.; Liu, P.; Engle, K., Low-Valent Tungsten Redox Catalysis Enables Controlled Isomerization and Carbonylative Functionalization of Alkenes. **2021**.

14. (a) Biswas, S., Mechanistic Understanding of Transition-Metal-Catalyzed Olefin Isomerization: Metal-Hydride Insertion-Elimination vs. π -Allyl Pathways. *Comments Inorg. Chem.* **2015**, 35, 300-330; (b) Green, S. A.; Crossley, S. W.; Matos, J. L.; Vásquez-Céspedes, S.; Shevick, S. L.; Shenvi, R. A., The high chemofidelity of metal-catalyzed hydrogen atom transfer. *Acc. Chem. Res.* **2018**, 51, 2628-2640; (c) Liu, X.; Li, B.; Liu, Q., Base-metal-catalyzed olefin isomerization reactions. *Synthesis* **2019**, 51, 1293-1310.

15. (a) Maji, B.; Barman, M. K., Recent developments of manganese complexes for catalytic hydrogenation and dehydrogenation reactions. *Synthesis* **2017**, 49, 3377-3393; (b) Filonenko, G. A.; van Putten, R.; Hensen, E. J.; Pidko, E. A., Catalytic (de)hydrogenation promoted by non-precious metals—Co, Fe and Mn: recent advances in an emerging field. *Chem. Soc. Rev.* **2018**, 47, 1459-1483; (c) Irrgang, T.; Kempe, R., 3d-Metal Catalyzed N- and C-Alkylation Reactions via Borrowing Hydrogen or Hydrogen Autotransfer. *Chem. Rev.* **2018**, 119, 2524-2549; (d) Kallmeier, F.; Kempe, R., Manganese Complexes for (De) Hydrogenation Catalysis: A Comparison to Cobalt and Iron Catalysts. *Angew. Chem. Int. Ed.* **2018**, 57, 46-60; (e) Wang, Y.; Wang, M.; Li, Y.; Liu, Q., Homogeneous manganese-catalyzed hydrogenation and dehydrogenation reactions. *Chem* **2020**, 7, 1180-1223; (f) Azouzi, K.; Valyaev, D. A.; Bastin, S.; Sortais, J.-B., Manganese—new prominent actor in transfer hydrogenation catalysis. *Curr. Opin. Green Sust.* **2021**, 31, 100511.

16. (a) Elangovan, S.; Topf, C.; Fischer, S.; Jiao, H.; Spannenberg, A.; Baumann, W.; Ludwig, R.; Junge, K.; Beller, M., Selective catalytic hydrogenations of nitriles, ketones,

and aldehydes by well-defined manganese pincer complexes. *J. Am. Chem. Soc.* **2016**, 138, 8809-8814; (b) Bertini, F.; Glatz, M.; Gorgas, N.; Stöger, B.; Peruzzini, M.; Veiros, L. F.; Kirchner, K.; Gonsalvi, L., Carbon dioxide hydrogenation catalysed by well-defined Mn (I) PNP pincer hydride complexes. *Chem. Sci.* **2017**, 8, 5024-5029; (c) Glatz, M.; Stöger, B.; Himmelbauer, D.; Veiros, L. F.; Kirchner, K., Chemoselective Hydrogenation of Aldehydes under Mild, Base-Free Conditions: Manganese Outperforms Rhenium. *ACS Catal.* **2018**, 8, 4009-4016; (d) Kaithal, A.; Hölscher, M.; Leitner, W., Catalytic Hydrogenation of Cyclic Carbonates using Manganese Complexes. *Angew. Chem. Int. Ed.* **2018**, 57, 13449-13453; (e) Kumar, A.; Janes, T.; Espinosa-Jalapa, N. A.; Milstein, D., Manganese Catalyzed Hydrogenation of Organic Carbonates to Methanol and Alcohols. *Angew. Chem. Int. Ed.* **2018**, 57, 12076-12080; (f) Freitag, F.; Irrgang, T.; Kempe, R., Mechanistic Studies of Hydride Transfer to Imines from a Highly Active and Chemoselective Manganate Catalyst. *J. Am. Chem. Soc.* **2019**, 141, 11677-11685; (g) Zhang, L.; Tang, Y.; Han, Z.; Ding, K., Lutidine-Based Chiral Pincer Manganese Catalysts for Enantioselective Hydrogenation of Ketones. *Angew. Chem. Int. Ed.* **2019**, 58, 4973-4977; (h) Fu, S.; Shao, Z.; Wang, Y.; Liu, Q., Manganese-catalyzed upgrading of ethanol into 1-butanol. *J. Am. Chem. Soc.* **2017**, 139, 11941-11948; (i) Kulkarni, N. V.; Brennessel, W. W.; Jones, W. D., Catalytic upgrading of ethanol to n-butanol via manganese-mediated Guerbet reaction. *ACS Catal.* **2018**, 8, 997-1002; (j) Yang, W.; Chernyshov, I. Y.; van Schendel, R. K.; Weber, M.; Müller, C.; Filonenko, G. A.; Pidko, E. A., Robust and efficient hydrogenation of carbonyl compounds catalysed by mixed donor Mn (I) pincer complexes. *Nat. Commun.* **2021**, 12, 1-8.

17. (a) Weber, S.; Stöger, B.; Veiros, L. F.; Kirchner, K., Rethinking Basic Concepts—Hydrogenation of Alkenes Catalyzed by Bench-Stable Alkyl Mn (I) Complexes. *ACS Catal.* **2019**, 9, 9715-9720; (b) Rahaman, S. W.; Pandey, D. K.; Rivada-Wheelaghan, O.; Dubey, A.; Fayzullin, R. R.; Khusnutdinova, J. R., Hydrogenation of alkenes catalyzed by a non-pincer Mn complex. *ChemCatChem* **2020**, 12, 5912-5918.

18. (a) van Putten, R.; Benschop, J.; de Munck, V. J.; Weber, M.; Müller, C.; Filonenko, G. A.; Pidko, E. A., Efficient and Practical Transfer Hydrogenation of Ketones Catalyzed by a Simple Bidentate Mn–NHC Complex. *ChemCatChem* **2019**, 11, 5232-5235; (b) Weber, S.; Stöger, B.; Kirchner, K., Hydrogenation of nitriles and ketones catalyzed by an air-stable bisphosphine Mn (I) complex. *Org. Lett.* **2018**, 20, 7212-7215.

19. (a) Clapham, S. E.; Hadzovic, A.; Morris, R. H., Mechanisms of the H₂-hydrogenation and transfer hydrogenation of polar bonds catalyzed by ruthenium hydride complexes. *Coordination Chemistry Reviews* **2004**, 248, 2201-2237; (b) Dub, P. A.; Scott, B. L.; Gordon, J. C., Why does alkylation of the N–H functionality within M/NH bifunctional Noyori-type catalysts lead to turnover? *J. Am. Chem. Soc.* **2017**, 139, 1245-1260.

20. (a) Li, H.; Wei, D.; Bruneau-Voisine, A.; Ducamp, M.; Henrion, M.; Roisnel, T.; Dorcet, V.; Darcel, C.; Carpentier, J.-F.; Soulé, J.-F. o., Rhenium and manganese complexes bearing amino-bis (phosphinite) ligands: synthesis, characterization, and catalytic activity in hydrogenation of ketones. *Organometallics* **2018**, *37*, 1271-1279; (b) Gausas, L.; Donslund, B. S.; Kristensen, S. K.; Skrydstrup, T., Evaluation of Manganese Catalysts for the Hydrogenative Deconstruction of Commercial and End-of-Life Polyurethane Samples. *Chemsuschem* **2022**, *15*, e202101705.
21. (a) Müller, C.; Vos, D.; Jutzi, P., Results and perspectives in the chemistry of side-chain-functionalized cyclopentadienyl compounds. *J Organomet Chem* **2000**, *600*, 127-143; (b) Braunstein, P.; Naud, F., Hemilability of hybrid ligands and the coordination chemistry of oxazoline-based systems. *Angew. Chem. Int. Ed.* **2001**, *40*, 680-699; (c) Grützmacher, H., Cooperating ligands in catalysis. *Angew. Chem. Int. Ed.* **2008**, *47*, 1814-1818.
22. Chernyshov, I.V.; Pidko, E.A. in preparation.
23. Frisch, M. J.; Trucks, G. W.; Schlegel, H. B.; Scuseria, G. E.; Robb, M. A.; Cheeseman, J. R.; Scalmani, G.; Barone, V.; Petersson, G. A.; Nakatsuji, H.; Li, X.; Caricato, M.; Marenich, A. V.; Bloino, J.; Janesko, B. G.; Gomperts, R.; Mennucci, B.; Hratchian, H. P.; Ortiz, J. V.; Izmaylov, A. F.; Sonnenberg, J. L.; Williams-Young, D.; Ding, F.; Lipparini, F.; Egidi, F.; Goings, J.; Peng, B.; Petrone, A.; Henderson, T.; Ranasinghe, D.; Zakrzewski, V. G.; Gao, J.; Rega, N.; Zheng, G.; Liang, W.; Hada, M.; Ehara, M.; Toyota, K.; Fukuda, R.; Hasegawa, J.; Ishida, M.; Nakajima, T.; Honda, Y.; Kitao, O.; Nakai, H.; Vreven, T.; Throssell, K.; Montgomery Jr., J. A.; Peralta, J. E.; Ogliaro, F.; Bearpark, M. J.; Heyd, J. J.; Brothers, E. N.; Kudin, K. N.; Staroverov, V. N.; Keith, T. A.; Kobayashi, R.; Normand, J.; Raghavachari, K.; Rendell, A. P.; Burant, J. C.; Iyengar, S. S.; Tomasi, J.; Cossi, M.; Millam, J. M.; Klene, M.; Adamo, C.; Cammi, R.; Ochterski, J. W.; Martin, R. L.; Morokuma, K.; Farkas, O.; Foresman, J. B.; Fox, D. J. *Gaussian16 Revision C.01*. 2016.
24. Marenich, A. V.; Cramer, C. J.; Truhlar, D. G., Universal solvation model based on solute electron density and on a continuum model of the solvent defined by the bulk dielectric constant and atomic surface tensions. *The Journal of Physical Chemistry B* **2009**, *113*, 6378-6396.

**Composition Dynamics of Reaction
Environment in Homogeneous Ester
Hydrogenation**

Abstract

The changes of reaction mixture composition in the course of catalysis alter the reaction environment and affect the catalytic performance. Herein we describe that in a Mn-catalyzed ester hydrogenation catalytic cycle the dissociation of alcohol product from the catalyst is a reversible step sensitive to the composition of the reaction medium. The accumulation of alcohol products in the course of reaction disfavors this process, leading to catalysis inhibition. We show that this inhibitory effect can be suppressed by using basic alkoxide promoters. Although alkoxides base additives do not directly participate in the inhibitory transformations, they affect the equilibrium constants of these processes. Experimentally we confirm that by varying base promoter concentration one can control catalyst speciation and inflict substantial changes to the standard free energies of the key steps in the catalytic cycle. Despite the fact that the latter are universally assumed to be constant, we demonstrate that reaction thermodynamics and catalyst state are subject to external control.

Part of this chapter has been published as:

Wenjun Yang, Tejas Y. Kalavalapalli, Annika M. Krieger, Taras A. Khvorost, Ivan Yu. Chernyshov, Manuela Weber, Evgeny A. Uslamin, Evgeny A. Pidko and Georgy A. Filonenko, *J. Am. Chem. Soc.*, **2022**, *144*, 8129-8137.

Contributions: W.Y. designed, conducted the experiments, and analyzed the data; T.Y.K. performed part of the UV-vis measurements; A.M.K., T.A.K., and I.Y.C. performed the DFT and COSMO-RS calculations; M.W. performed crystal structure determination and analysis; E.A.U., G.A.F. and E.A.P. supervised the research.

4.1 Introduction

Comprising a vast class of reactions, catalytic hydrogenations have high industrial relevance.¹ Utilizing molecular hydrogen with appropriate catalyst, these reactions can convert unsaturated functional groups in a variety of substrates to their saturated counterparts. Out of numerous functional groups that can be reduced in this way, esters pose significant challenge for direct catalytic hydrogenation.²

Conversion of esters to alcohols via catalytic hydrogenation have been explored for several decades with the most prominent homogeneous catalysts for this transformation being bifunctional noble metal complexes of ruthenium³, iridium⁴, and osmium⁵. Recent years have seen the focus of catalytic community shifting towards utilizing early transition metal (TM) catalysts, viewed as sustainable and non-toxic alternatives for noble metals.⁶ First found for iron and cobalt, ester hydrogenation activity was recently discovered for manganese complexes that are the focus of our work. While the manganese catalysts offer high sustainability benefits, their performance rarely matches that of noble metals.⁷ The best examples of Mn catalysts for hydrogenation of esters still require high catalyst loadings >2000 ppm and often operate at temperatures and pressures up to 110 °C and 50 bar to achieve high conversion.⁸ The search for the new Mn complexes with high intrinsic reactivity continues to be the central topic during this field.

However, the reactivity alone is not sufficient to forecast catalytic performance since catalysis is complex and dynamic. A growing evidence suggests that the reactivity of catalytic species can significantly vary depending on reaction conditions. Our group, for example, demonstrated that reaction medium composition can directly impact reactivity patterns in homogeneous catalysis.⁹ Similarly in heterogeneous catalysis, Liu, Lercher and co-workers demonstrated that local solvation and ionic strength changes can alter the reactivity of zeolite catalysts.¹⁰ The change of reaction conditions in ester hydrogenation is even more dramatic with reaction medium changing from aprotic to highly protic. Whether this change can steer the catalyst reactivity remained unknown and resolving this question and its molecular origins is the aim of this work.

Using a combination of operando spectroscopy, DFT calculations and stoichiometric reactivity studies we demonstrate that composition and relative content of catalytic

species during hydrogenation is not constant but dynamic. This dynamics is largely caused by the change in reaction mixture composition during ester hydrogenation wherein the growing fraction of reaction product causes catalyst inhibition (**Figure 4. 1**). We directly demonstrate that kinetically competent catalysts species are in equilibrium with inhibited catalyst formed through a reaction with hydrogenation product. Strikingly, we found reaction conditions can directly affect this equilibrium. Specifically, addition of basic promoters could change the *standard* thermodynamic parameters of inhibitory equilibrium and make this inhibition unfavorable. Considering that standard thermodynamic potentials are universally assumed constant, our discovery of their condition dependence makes a strong case that catalytic reactions are inherently dynamic on every level: from molecules to environment fundamentals.

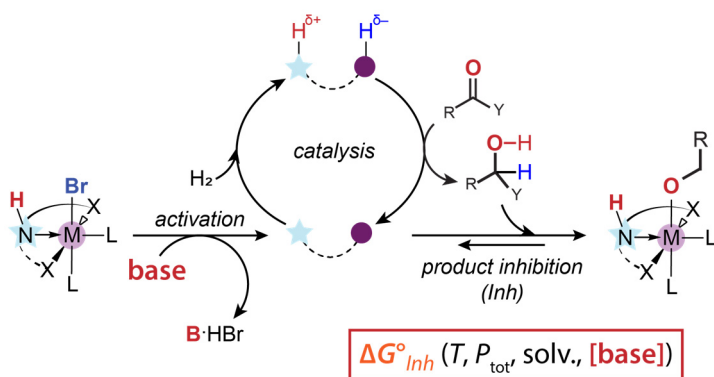


Figure 4. 1. Product inhibition of homogeneous ester hydrogenation.

4.2 Synthesis and catalytic activity of Mn-CNC pincers

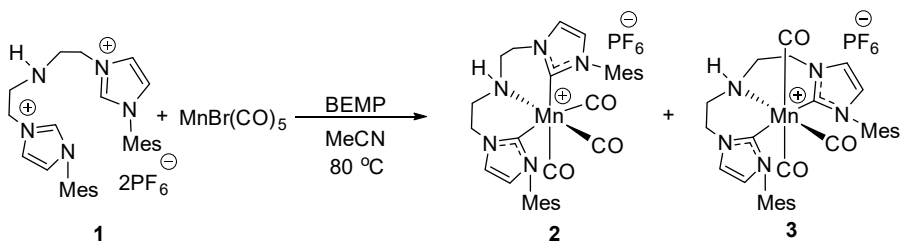


Figure 4. 2. Synthesis of Mn(I) complexes 2 and 3.

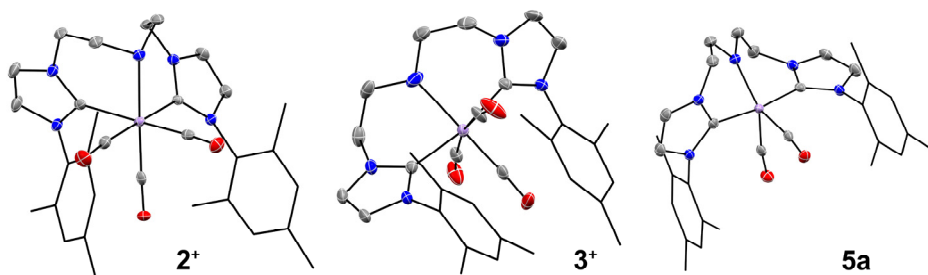


Figure 4. 3. Molecular structure of complexes **2**, **3**, and **5a** in the crystal with thermal ellipsoids drawn at 50% probability. Hydrogen atoms and PF_6^- anions in cationic **2** and **3** are omitted for clarity.

At first we developed new Mn pincer catalysts for ester hydrogenation that were both catalytically competent and easy to track using spectroscopic methods. We based our model catalyst design on bis-*N*-heterocyclic carbene amino (CNC) pincer ligands that proved to be a versatile ligand motif for transition-metal hydrogenation catalysts.^{3d, 11} The representative ligand **1** readily underwent complexation with $\text{Mn}(\text{CO})_5\text{Br}$ in the presence of the phosphazene base BEMP (2-*tert*-Butylimino-2-diethylamino-1,3-dimethylperhydro-1,3,2-diazaphosphorine) in acetonitrile at 80 °C yielding Mn complexes **2** and **3** (**Figure 4. 2**) that can be isolated individually.

As evidenced by X-ray diffraction data, the CNC ligand in these complexes adopts *facial* and *meridional* configurations for **2** and **3** respectively (**Figure 4. 3**). Exposure to ambient light slowly (about 5 days for full conversion) converted light-yellow complex **2** to orange **3** in solution implying that **2** might be a kinetic product of the complexation.^{8a} Both complexes are cationic tricarbonyl species that are readily distinguished by ^1H NMR and IR spectroscopy (**Figure 4. 3** and section 4.8). The reaction of these complexes with KO^tBu converts both **2** and **3** to the dicarbonyl Mn amido species **5a** with its base adduct **5b** (see DFT-supported assignment of molecular structure in section A.2 of Appendix) detected by IR spectroscopy in small amounts (**Figure 4. 4 B** and **C**), while complex **2** underwent a transient tricarbonyl state (**4**). Upon exposure to H_2 a mixture of **5a** and **5b** converts to pure **5a** with no detectible amounts of Mn hydride species, allowing to suggest that both **2** and **3** will exhibit similar catalytic activity (**Figure 4. 4 D**).

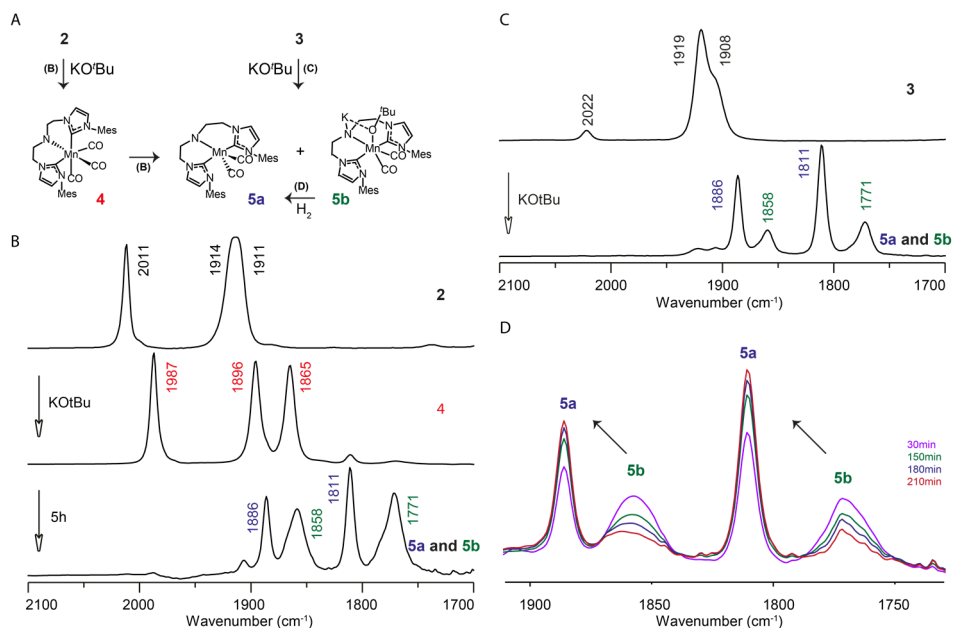
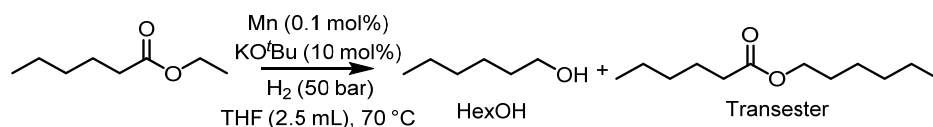


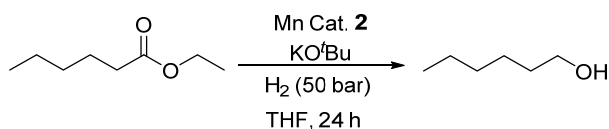
Figure 4. Activation of complex 2 and 3 with KOtBu (2 eq.) in THF (A), IR spectrum for *in situ* activation of 2 (B), IR spectrum for *in situ* activation of 3 (C), evolution of IR spectrum of mixture of 5a and 5b under H₂ for 30 min, 150 min, 180 min, and 210 min reaction times (D).

Both Mn-CNC complexes 2 and 3 are active in ester hydrogenation. As implied by their reactivity, in hydrogenation of ethyl hexanoate benchmark substrate both 2 and 3 gave nearly identical conversion confirming the catalytic equivalency of these precatalysts (**Table 4.1**) and prompting us to use complex 2 in all further studies. In addition, the low conversion (13-14 %) at 14 h reaction time indicated the sluggish reaction rates at current condition, and high substrate concentration (2.5 M) and reaction temperatures (80 °C) could be used to enhance the catalytic efficiency (**Table 4.2**). The most peculiar feature of the catalytic system with 2 is its reliance on the base promotor for remaining active. While only the trace amounts of alcohol product were obtained with 1 mol% KOtBu, increasing base amount to 10 and 20 mol% significantly increased hexanol yield to 41% and 46% respectively (**Table 4.2**, entries 1–3). An increase in the catalyst loading and temperature (**Table 4.2**, entries 4–6) proved beneficial for catalytic performance with 96% yield reached at 100 °C with 0.2 mol% complex 2. Further increase of reaction

Table 4. 1. Reactivity test of Mn complexes for ethyl hexanoate hydrogenation.^a

Entry	Cat.	t/h	HexOH/%	Transester/%	Yield/%
1	2	14	4	9	13
2	3	14	4	10	14

^aReactions were conducted with ethyl hexanoate (1.25 mmol), Mn catalyst (0.1 mol%), KOtBu (10 mol%) in solvent (2.5 mL) under 50 bar H₂. Yield of each component was determined by GC with dodecane as internal standard.

Table 4. 2. Hydrogenation of ethyl hexanoate with **2** under varied reaction conditions.^a

Entry	T (°C)	2 (mol%)	KOtBu(mol%)	Conv. (%)	Yield (%)
1	80	0.1	1	< 1	<1
2	80	0.1	10	63	41
3	80	0.1	20	67	46
4	80	0.2	20	77	65
5	90	0.2	20	92	87
6	100	0.2	20	96	96
7	110	0.2	20	93	84
8	100	0.2	10	93	75
9 ^b	100	0.2	10	99	98

^a Conditions: ethyl hexanoate (1.25 mmol), Mn catalyst **2**, KOtBu, THF (0.5 mL), P = 50 bar H₂, t = 24 h. Conversion and yield determined by GC analysis with dodecane as internal standard. ^b Reaction was run for 48 h

temperature to 110 °C however furnished hexanol in slightly lower yield (84 %), suggesting the occurrence of catalyst deactivation (entry 7). With 10 mol% KO^tBu, nearly quantitative hexanol yield could be reached in prolonged run at 100 °C (entries 8-9).

While catalyst **2** was highly efficient in converting model substrates, the dependence of its activity on the base concentration prompted a further investigation into the role of the base promoter in catalysis. Given the previously proposed interactions between alkoxide base and catalytic species,¹² we initially assumed the role of the base (**Table 4. 2**, entries 1–3) to be purely kinetic with the base concentration affecting the initial hydrogenation rate. Our kinetic data, however, refutes that assumption. The results presented in **Figure 4. 6** A-B reveal nearly identical initial rates for the hexyl hexanoate hydrogenation in the presence of **2** and 10 mol% or 2 mol % KO^tBu base, ruling out any kinetically productive interactions between the catalyst and the base promoter. On the other hand, decay of the hydrogenation rate was significantly less rapid in the increased base loading experiment, suggesting that the base can be relevant to the catalyst deactivation.

4.3 Product inhibition and effects of base promoter in hydrogenation catalysis

To probe the presence of deactivation we monitored reaction progress with simultaneous spectroscopic analysis of reaction mixture composition with IR spectroscopy. A typical dataset produced in this study is depicted in **Figure 4. 5** that presents a detailed overview of our assignments. Examining the evolution of the carbonyl ligand bands of **2** in the course of reaction we note that the reaction onset is marked by the fast conversion of base adduct **5b** to the amido complex **5a** (**Figure 4. 5**). As the hydrogenation progressed and the alcohol product was formed we observed a gradual consumption of **5a** and the formation of a new species **6** with $\nu(\text{CO}) = 1902$, and 1806 cm^{-1} suggesting that **6** is a Mn dicarbonyl complex. Performing an ex-situ test to assign the structure of **6** we found that this complex is the product of the metal-ligand cooperative alcohol addition to the amido complex **5a** (**Figure 4. 5 C**). Using methanol as a model alcohol we could obtain reference FTIR and NMR spectra for the alkoxide **6** and establish the reversibility of its formation with the alkoxide being favored at low temperature and the amido complex **5a** favored at elevated temperatures (see **Figure 4. 7 A**).

We assigned an inhibitory role to the alkoxide complex **6** based on our real-time FTIR data (**Figure 4. 5** and **Figure 4. 6**) evidenced by the drop in the overall catalytic hydrogenation rate that coincides with accumulation of **6** (**Figure 4. 5 B**). Specifically, product inhibition manifests as the increase of alcohol product concentration leads to the consumption of the kinetically competent species **5a**. We note that formation of alkoxide complexes similar to **6** is common for metal-catalyzed (Ru, Fe, Os, Mn) hydride transfer reactions, especially in acceptorless dehydrogenative coupling, although their involvement in catalysis remains under debate.^{12b, 13} Bergens and co-workers suggested that the Ru alkoxide could be the catalytically relevant intermediate formed through inner-sphere hydrogenation.^{13b} On the other hand, many authors including Gauvin, Mezzetti and Morris proposed Mn alkoxide complexes either as off-cycle intermediates or resting states that cause lower reactivity.^{12b, 13f, 12i-1} The most detailed analysis to date was reported by the Saouma's group who investigated the relevance of the alkoxide complexes to the hydrogenation catalysis.^{13g} The authors directly measured the equilibria of the formation of Ru-alkoxide and concluded the latter to compete with the H₂ addition to Ru amido complex.

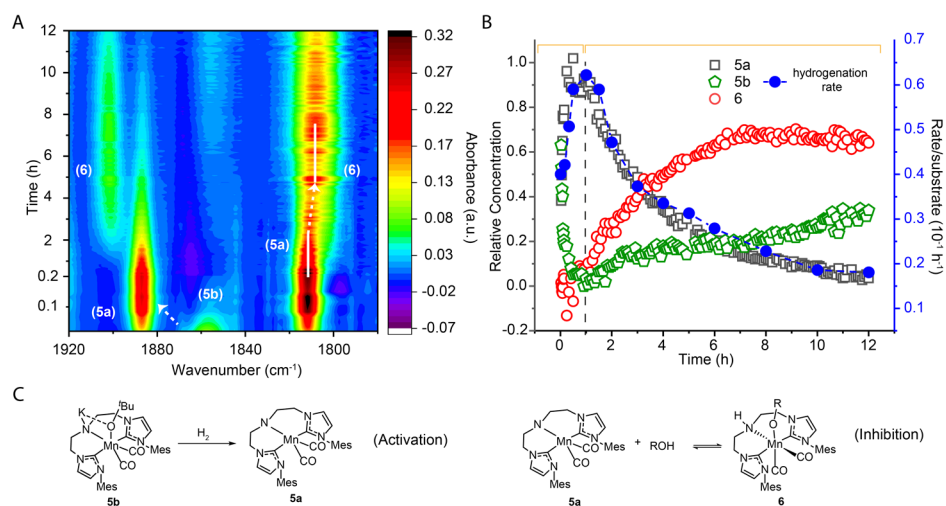


Figure 4. 5. Operando IR data for the hydrogenation of ethyl hexanoate with Mn precatalyst **2** showing the evolution of carbonyl containing species (A) and relation between hydrogenation kinetics and catalyst speciation (B). Observed catalytic intermediates shown in panel C

Performing hydrogenation in the presence of the hexanol ($[\text{HexOH}]_0 = 1.25 \text{ M}$ at $t = 0$) we confirmed the inhibitory nature of alcohol binding to **5a**. Addition of alcohol strongly impacted the catalytic performance and the reaction mixture composition (**Figure 4. 6**). Firstly, we observed Mn alkoxide **6** to become the dominant Mn species from the onset of the reaction (**Figure 4. 6 D vs. F**). Secondly, we detected a significant drop in the hydrogenation rate compared to the standard hexanol-free runs at the same substrate concentration (**Figure 4. 6 C**). These experiments confirm the detrimental impact of the product formation on catalysis and constitute a typical case of product inhibition. In line with the literature discussed above, our data for the Mn-CNC provides spectroscopic and kinetic support to the notion that the accumulation of alcohol adducts of amido complexes indeed decrease catalytic efficiency of hydrogenation. Notably, this implies that the inner-sphere hydrogenation mechanisms with Mn-CNC associated with alkoxide formation are likely less favorable due to strong product inhibition.

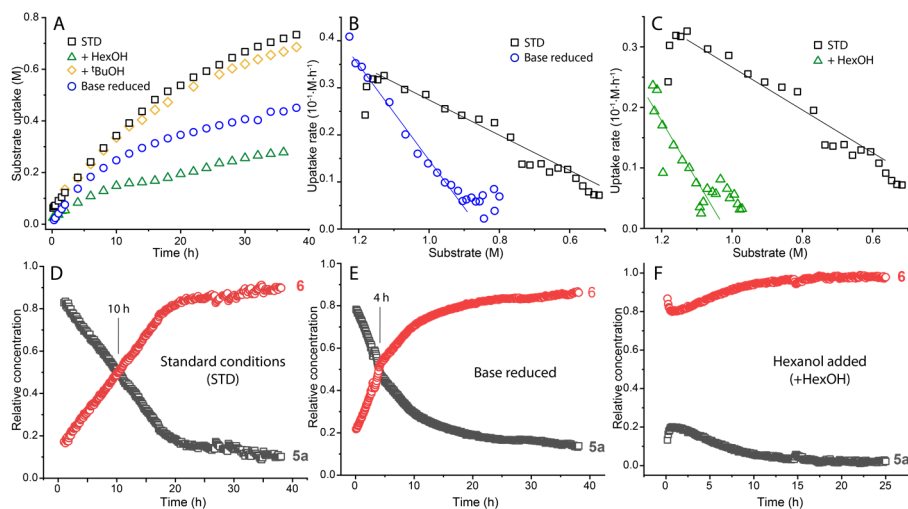
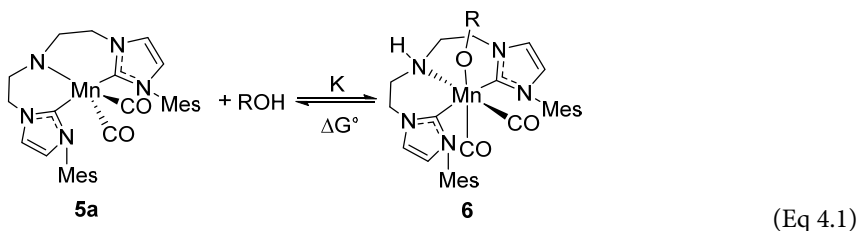


Figure 4. 6. Summary data for kinetics of hexyl hexanoate hydrogenation (A) and hydrogenation rate plots (B, C) under varying base and alcohol concentrations and the operando IR spectroscopy traces (D-F) indicating the extent of product inhibition. Conditions - standard: hexyl hexanoate (1.25 M), catalyst **2** (0.1 mol%), KO^tBu (10 mol%) in THF (8.2 mL), 70°C, 40 bar H₂; reduced base: KO^tBu loading lowered to 2 mol%; hexanol/¹BuOH added: extra alcohol added at 1.25 M. Notes: ester uptake data in A-C determined by GC analysis, relative concentrations in D-F obtained from FTIR spectroscopy.



$$K = \frac{[\text{Mn-6}]}{[\text{Mn-5a}] \times ([\text{ROH}]^\circ - [\text{Mn-6}])} \quad (\text{Eq 4.2})$$

$$\ln(K) = \frac{-\Delta H^\circ}{RT} + \frac{\Delta S^\circ}{R} \quad (\text{Eq 4.3})$$

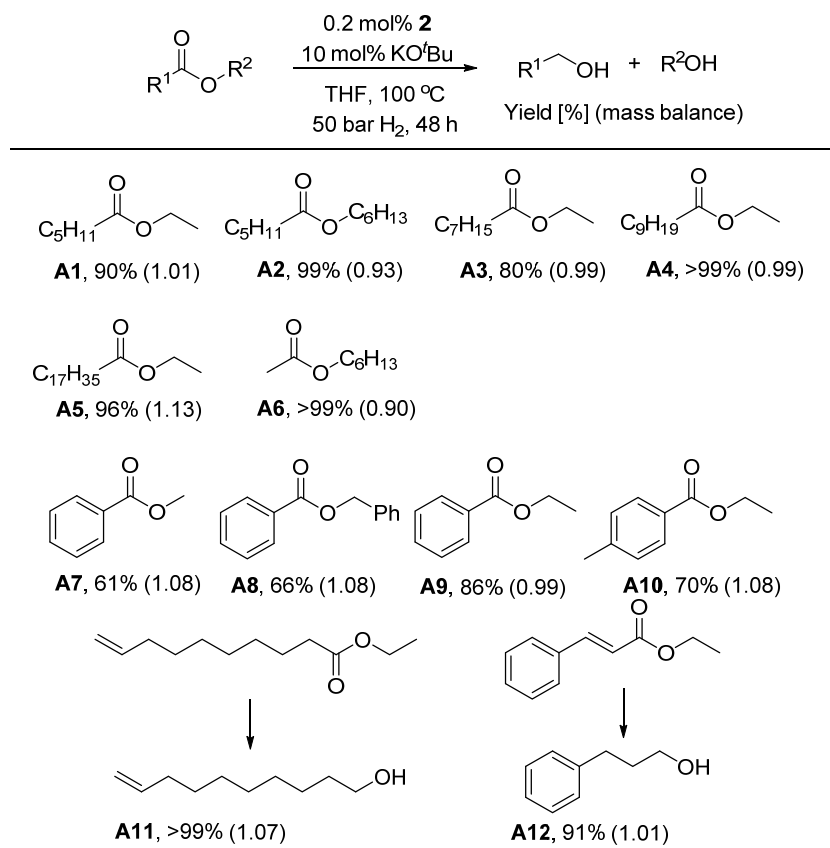
$$\Delta G^\circ = \Delta H^\circ - T\Delta S^\circ \quad (\text{Eq 4.4})$$

As the reactivity of alcohols strongly depends on their acidity we expected the magnitude of the inhibition effect to depend on the alcohol in question. Complex **5a** has blue color and a characteristic absorbance peak at 583 nm while its alcohol adduct **6** has a distinct feature at 428 nm (see **Figure 4. 7 A** for representative spectra). Monitoring the equilibrium between **5a** and **6** (Eq 4.1) with UV-Vis spectroscopy we could track the temperature dependence of the equilibrium constant (Eq 4.2) and by extension obtain the estimate of reaction free energy ΔG_{298K}° (Eqs 4.3 and 4.4) for this transformation.

Table 4. 3. Thermodynamic parameters for the addition of different alcohols to Mn amido complex **5**.^a

Alcohol	ΔG_{298K}° (kJ·mol ⁻¹)	ΔH° (kJ·mol ⁻¹)	ΔS° (J·mol ⁻¹ ·K ⁻¹)
MeOH	-13.5±0.8 ^a	-49.8±0.6	-121.6±1.9
HexOH	-4.4±1.0 ^a	-36.2±0.7	-106.9±2.5
BnOH	-11.3±0.6 ^a	-40.5±0.4	-97.9±1.3

^a Error from propagation of the error of ΔH° and ΔS° , $\sigma_{\Delta G} = \sqrt{(\sigma_{\Delta H})^2 + (T|\sigma_{\Delta S}|)^2}$. Errors in the enthalpy and entropy are from errors in the slope and intercept, respectively.

Table 4. 4. Substrate scope for esters hydrogenations with **2**.^a

^a Reactions were conducted with ethyl hexanoate (1.25 mmol), Mn catalyst (0.1 mol%), KO^tBu in solvent (0.5 mL) under 50 bar H₂. Yield of each component was determined by GC-MS and ¹HNMR with 1-methyl naphthalene as internal standard. The mass balance was given in the brackets.

We determined thermodynamic parameters of the reversible alcohol addition for three representative alcohols - *n*-hexanol, methanol and benzyl alcohol (**Table 4. 3**). The results confirmed that more acidic alcohols, Me- and BnOH bind more favorably than hexanol with the measured ΔG_{298K}° being -13.5 and -11.3 kJ/mol for MeOH and BnOH, respectively, compared to -4.4 kJ/mol for hexanol. These data mimic the trends that we observed in our substrate scope screening (**Table 4. 4**) where methyl and benzyl esters consistently provided lower hydrogenation yields compared to their long chain counterparts (substrates **A7**, **A8**, and **A9**). Similarly, hydrogenation of aromatic esters (**A7-A10**) that produce benzyl alcohol as one of the products resulted in lower yields

compared to the aliphatic esters (**A1-A6**) despite the latter being less electrophilic and less susceptible to the hydride transfer reactions often invoked as the first step in ester hydrogenation. These observations suggest that the product-induced inhibition might direct the performance of a large number of hydrogenation catalysts or at least impact their productivity. Similar trends favoring esters producing less acidic alcohols upon hydrogenation have been observed in Ru-catalyzed hydrogenations.^{3c, 3d, 5a, 14} Importantly, these findings suggest that the outcome of ester hydrogenation is not only defined by the substrate reactivity, but also the capacity of reaction products to inhibit catalysis.

4.4 Base effects on inhibitory equilibria

At this point we were met with contradiction arising from the UV-Vis data describing the equilibrium between **5a** and **6** in THF. The measured negative Gibbs free energy change implied that in the presence of hexanol, hydrogenation would be strongly inhibited at all times during catalysis that was not the case according to the operando IR data depicted in **Figure 4. 6** D-F. We assumed that the presence of the alkoxide bases might affect the catalyst inhibition and extended the catalyst lifetime. To probe this we extended the temperature dependent UV-vis spectroscopy studies to track the **5a** - **6** equilibrium in the presence of KO^tBu additive. As noted by Kempe and co-workers, superstoichiometric amount of base may promote further deprotonation of the neutral Mn alkoxide.^{7n, 14} We additionally verified that **6** cannot convert in the same manner using NMR spectroscopy where a proton resonance of N-H group of **6** can be observed even in the presence of multifold excess of KO^tBu. Strikingly, we found that the addition of substoichiometric amounts of KO^tBu with respect to alcohol significantly impacts the equilibrium and catalyst speciation in Mn/alcohol mixtures.

This translates to a substantial change of the standard Gibbs free energy for the **5a** - **6** transformation (**Figure 4. 7**) although the base promotor is not involved in this equilibrium directly. Compared to the case of pure **5a**/alcohol system showing a negative ΔG_{298K}° of $-4.4 \text{ kJ}\cdot\text{mol}^{-1}$ the addition of 0.25 equivalents of KO^tBu with respect to the alcohol elevates the Gibbs free energy by approximately $3 \text{ kJ}\cdot\text{mol}^{-1}$ to $-1.4 \text{ kJ}\cdot\text{mol}^{-1}$, which

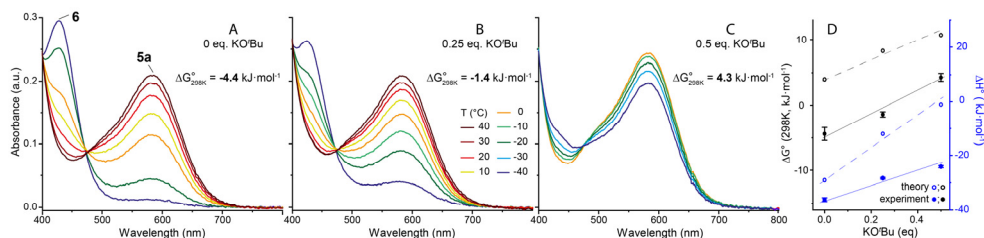


Figure 4. 7. UV-vis spectra describing the dependence of the equilibrium of **5a** – **6** (Eq 1) on the concentration of KO^tBu in THF. Comparison between mixtures of **5a** (0.567mM) and (A) hexanol (55.6 mM), (B) hexanol (113.4 mM) and KO^tBu (28.35 mM, 0.25 eq.) and (C) hexanol (113.4 mM) and KO^tBu (56.7 mM, 0.5 eq.). Reaction free energy change (ΔG) for reversible alkoxide formation given in A-C and plotted together with theoretical data in panel D (COSMO-RS//PBE0-D3(SMD_{THF})/6-311++G(d,p)).

increases further to $4.3 \text{ kJ}\cdot\text{mol}^{-1}$ upon the elevation of the base contents to 0.5 equivalents (**Figure 4. 7**). These values remain valid even when we incorporate a likely exchange reaction between tert-butoxide and free hexanol in our calculation. Such a correction affects the obtained ΔG_{298K}° values by no more than $1 \text{ kJ}\cdot\text{mol}^{-1}$ suggesting a large magnitude of the alkoxide addition effects in perturbing the equilibria responsible for the catalyst inhibition. Since the addition of alkoxide bases affects the catalyst speciation it also has a direct impact on catalysis. The operando IR follow-up of the ester hydrogenation confirmed that the inhibition onset in hydrogenations with reduced base loading (**Figure 4. 6 D vs. E**) occurs at lower alcohol concentrations, while higher base loadings allow for delaying this inhibition and extending the catalyst lifetime.

4.5 Extension to other bifunctional complexes

We expected our findings about the tunable thermodynamics of inhibitory process to be general since basic additives have been widely used in excessive amounts to promote the bifunctional hydrogenation systems. The alcohol addition to the amido pinners is a common reaction for many catalysts. We selected two Mn-MACHO complexes (Et₂, **7** and ^{*i*}Pr₂, **8**),^{7a, 8a} both demonstrated as active hydrogenation catalysts, and treated them with strong base to achieve the corresponding deprotonated amido species (**Figure 4. 8**). Notably, the reaction of **7** with KO^tBu gave rise to several minor resonances in ³¹P NMR spectrum at 45.3, 32.43, -26.8 and -27.1 ppm, apart from the major one of 90.6 ppm corresponding to the amido complex **9** (**Figure 4. 8 bottom**). Summarizing previously

reported Mn catalysts it can be noticed that the ^{31}P resonances at 40-60 ppm typically represent Mn complexes with only one phosphine donor bound to metal center, and those at -30-10 ppm belong to free phosphine ligands or Mn complexes with unbound phosphine. Give the nearly identical ratio of these two types of ^{31}P signals (5.5% for 45.3 and 32.43 ppm, 5.5% for -26.8 and -27.1 ppm), we assumed these unexpected signals observed in the activation of **7** corresponded to two isomers of deprotonated Mn species featuring dissociated phosphine arm. Similarly, the amido species **10** was the main product for the reaction of complex **8** with KO^tBu and deprotonated Mn complex with dissociated P donor was also generated in around 10%. The latter was evidenced by the appearance of the resonances at $\delta = 51.1$ and -0.11 ppm in ^{31}P NMR. The direct treatment with base is a common activation procedure of Mn precatalyst. Our observation of side products with free P donor indicated the partial degradation of Mn catalyst during activation process, which could result in the permanent decrease of catalytic activity due to the loss of active catalyst species before catalysis.

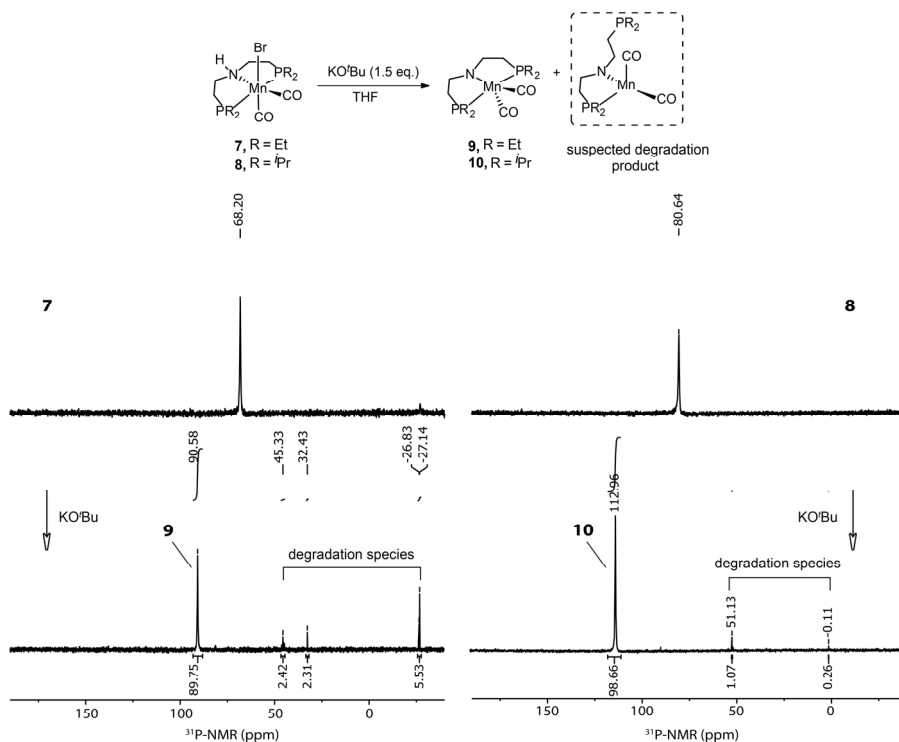


Figure 4. 8. The activation of Mn-PNP complexes with KO^tBu and corresponding ^{31}P NMR spectra.

While the catalyst activation did not process with quantitative selectivities, the amido complexes **9** and **10** could be isolated via the extraction with benzene. With **9** and **10** in hand, we set out to explore the thermodynamics for the alcohol addition to them in the presence of KO^tBu additives. Indeed, the increase of base promotor concentration strongly suppress the alkoxide formation with the standard Gibbs free energy changes ΔG_{298K}° elevating from -19.2 to -12.7 kJ·mol⁻¹ at 0.75 eq. KO^tBu (with respect to benzyl alcohol) and -4.4 to -1.1 kJ·mol⁻¹ at 0.2 eq. KO^tBu (with respect to EtOH) for **9-11** and **10-12** transformations respectively (**Figure 4. 9** A and B). Similar to the case of Mn-CNC, we found that increasing the base loading from 2 to 10 mol% could gradually improve the performance of Mn-PNP (**7**) catalyzed ethyl benzoate reduction with alcohol yields rising from <1 to 45% (**Figure 4. 9** C). The basic additives in the reaction medium tuned the free energy surface of inhibitory process unfavorable and prolonged the lifetime of Mn-MACHO catalysts in hydrogenation.

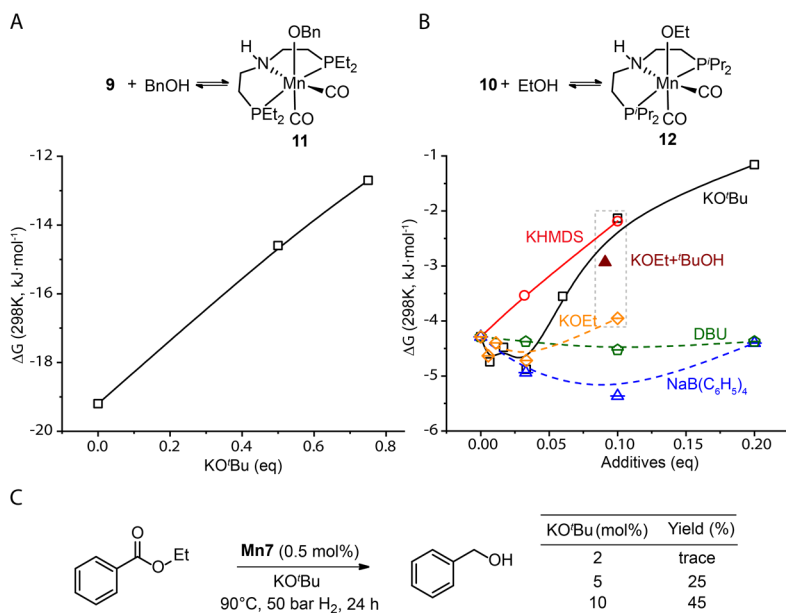


Figure 4. 9. Thermodynamic analysis for alcohol addition to amido Mn-PNP complexes (**9** and **10**) in presence of additives (A and B) and ester hydrogenation with **7** (C). Hydrogenation conditions: ethyl benzoate (1.25 mmol), **7** (0.5 mol%), KO^tBu, THF (0.5 mL), 50 bar H₂, 90 °C, 24 h.

Taking our data together, we conclude that standard thermodynamic parameters universally assumed constant are, in fact, condition dependent. Interestingly, this dependence can be reflected on the level of theory when examined using DFT calculations (see section A.2 in Appendix). Specifically, we utilized the COSMO-RS method that allows calculating chemical potentials and their concentration dependences in real solutions based on the DFT data.¹⁵ We analyzed the condition-dependencies of the thermodynamics of alkoxide formation in the presence of base and found that addition of alkoxide base can indeed affect the standard thermodynamic constant ΔG° of the reaction, which does not formally involve this base as a reactant. The magnitude of this effect is sufficient to perturb the reaction Gibbs free energy change by 4-8 kJ·mol⁻¹ in line with our experimental observations depicted in **Figure 4. 7**. We found that addition of base mainly affects the chemical potential of the alcohol component rather than the metal complexes. Indeed, in aprotic solvent, one would expect the alcohol component to be affected stronger by the interaction with ionic alkoxide bases thus making this behavior sensible from the molecular standpoint. Nevertheless, the magnitude of this effect and its impact on catalysis are novel and entirely unexpected.

4.6 Effects of different additives

To get molecular insights to the condition-dependent thermodynamics for Mn alkoxide formation, the effects of different additives on this equilibrium were investigated. Sodium tetraphenylborate, a common salt soluble in THF, was firstly tested in the equilibrium between **9** and **11**. As shown in **Figure 4. 9 B**, the addition of NaB(C₆H₅)₄ made trivial changes to the thermodynamics of this transformation with the ΔG_{298K}° ranging within -5 to -4 kJ·mol⁻¹. This results excluded the possibility that the substantial perturbation to free energy surface caused by alkoxide base stemmed from the enhancement of ionic environment. Therefore the basicity of additive seems to be the key of such effect. We then screened a highly strong base-KHMDS, the conjugate base of ethanol-KOEt, and a relatively weak organic base-DBU, the pK_a of whose conjugate acid are around 26, 16, and 14 respectively. While KOEt and DBU barely affected the **9-11** equilibrium, the presence of 0.1 eq KHMDS with respect to ethanol largely increased its ΔG_{298K}° by approximate 2 kJ·mol⁻¹. Taking this and the effect of KO^tBu together, we can envision that only the

additives that are more basic than the conjugate base of examined alcohol can effectively tune its reaction with amido complex. However, strong base like KO^tBu can readily react with the EtOH in the mixture, leading to the large conversion to ^tBuOH and KOEt. To identify which component took effect, we monitored the **9**/ethanol system in the presence of pure ^tBuOH and the ^tBuOH/KOEt mixture by variable-temperature UV-vis. Similar to KOEt, the increase of ^tBuOH concentration did not cause prominent perturbation to the free energy surface of the system. Notably, the addition of equal amount of ^tBuOH and KOEt (both 0.1 eq. to EtOH) elevated ΔG_{298K}° to around $-3 \text{ kJ}\cdot\text{mol}^{-1}$, very close to that of the system with same amount of KO^tBu. The results supported our previous assumption that the basic promotor tuned the alkoxide formation equilibrium mainly by the interaction with alcohol as suggested in COSMO-RS studies (see section A.2 in Appendix). Furthermore, this interaction should involve alcohol, KOEt, and the conjugate acid of added base.

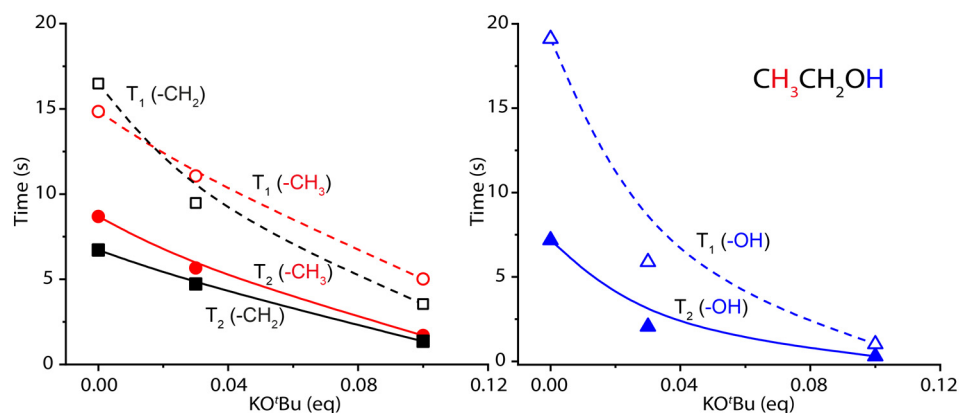


Figure 4.10. The relaxation time of ethanol in THF in presence of KO^tBu.

At last, a NMR study was conducted to monitor the spin-lattice relaxation (T_1) and spin-spin relaxation (T_2) of ethanol mixed with different amounts of KO^tBu in THF (**Figure 4.10**). The protons from CH₂ and CH₃ groups of ethanol had similar relaxation rates that showed linear dependence on base concentration. The addition of 0.1 eq. KO^tBu with respect to ethanol decreased the T_1 of protons from CH_n from around 15 to around 4 s and their T_2 from about 7 to 1 s. The O-H proton seems to be more responsive to the change of K^tBuO concentration. For instance, 0.03 eq KO^tBu dropped the T_1 of O-H

proton significantly by approximate 13 s, which further decreased to 0.3 s in the presence of 0.1 eq. KO^tBu. The T_2 of OH proton became 20 times smaller when adding same amount of KO^tBu. The substantial drop of relaxation time indicated the enlarged size of examined system. Therefore, the KO^tBu additives or derived KOEt and ^tBuOH seemed to form cluster with ethanol, which could stabilize ethanol and lower its chemical potential.

4.7 Conclusions

In summary, this chapter describes two features of early metal based catalysts that have profound influence on the outcome of the catalytic ester hydrogenation. First, is the pronounced product inhibition developing throughout catalysis, caused by the reversible binding of the alcohol product to the catalyst. Demonstrating its capacity to severely diminish the steady state concentration of the catalytically competent species we expect this inhibitory pathway to be highly relevant for the early transition metal catalysts that tend to form more stable alkoxide complexes compared to their noble metal counterparts. The case of several manganese pincers demonstrates that even at low reaction extent, these well-defined complexes largely exist in an inhibited state if no base promotor is used.

More importantly, we found that common alkoxide bases can counter this by affecting the inhibitory equilibrium and its standard thermodynamic parameters. While the latter is often assumed ironclad, we show that thermodynamic favorability of steps in a catalytic cycle is defined by reaction medium and can be tuned by promotors and additives that do not participate in any specific chemical transformation. We stress the necessity to view promotors as an integral component of the reaction medium rather than a stoichiometric reagent. In this way, one would be able to quantify such environmental effects rather than fall into the unmeasurable explicit molecular model. We also figure out that the additive need to be more basic than the conjugate base of alcohol product for weakening its inhibitory effect to hydrogenation catalysts.

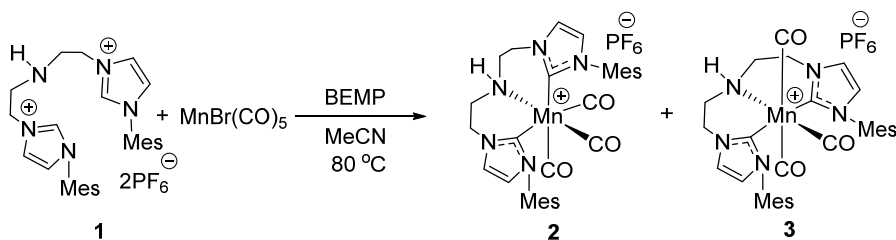
Finally, we conclude by noting that complexity uncovered in this Chapter can impact any catalytic transformation involving reversible alcohol binding. Having demonstrated the generality of our findings for Mn-catalyzed hydrogenations, we expect that the rational

use of promotors can become a powerful tool for designing catalytic reactions where the favorability of elementary steps is no longer a perceived constant, but can be tuned and manipulated at will.

4.8 Experimental details

4.8.1 Synthetic procedures

Synthesis of complex 2 and 3:



To the orange suspension of ligand **1** (733.0 mg, 1 mmol) and $[\text{MnBr}(\text{CO})_5]$ (275.0 mg, 1 mmol) in MeCN (5 mL) was added 2-tert-Butylimino-2-diethylamino-1,3-dimethylperhydro-1,3,2-diazaphosphorine solution (BEMP, 1M in hexane, 2.5 mL) and stirred at 80 °C for 24 h under Ar atmosphere and darkness. The resulting reaction mixture was then cooled down to room temperature and evaporated to dryness. The yellow solid residue was washed with MeOH to afford mixture of **2** (soluble in THF) and **3** (insoluble in THF). Complex **2** was fully extracted with 80 mL THF. The solution was filtered, evaporated to dryness and further purified by crystallization (MeOH vapor diffusion into solution in acetone) under darkness as light yellow solid in 15 % yield (108.5 mg). The remaining crude **3** was dissolved in minimal amount of DMSO, placed under light for a week, and further purified by crystallization (Et_2O vapor diffusion into solution in DMSO) as orange solid in 11 % yield (78.5 mg).

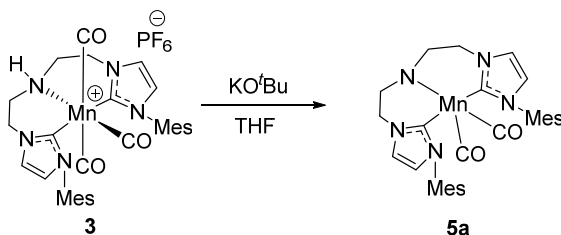
Note: Complex **2** in solution was slightly sensitive to light and could be slowly isomerized to **3**, so the above workup should be performed immediately.

Complex **2**: ^1H NMR (400 MHz, DMSO- d_6 , 297 K) δ 7.68 (d, J = 1.9 Hz, 2H), 7.26 (d, J = 1.8 Hz, 2H), 6.91 (s, 2H), 6.81 (s, 2H), 5.94 (s, 1H), 4.36 (d, J = 15.1 Hz, 2H), 3.78 (s, 2H),

3.11 (d, $J = 13.7$ Hz, 2H), 2.88 (s, 2H), 2.22 (s, 6H), 1.78 (s, 6H), 1.40 (s, 6H); $^{31}\text{P}\{^1\text{H}\}$ NMR (162 MHz, DMSO- d_6 , 297 K) δ -144.2 (hep, $^1J_{\text{FP}} 711.2$ Hz); $^{13}\text{C}\{^1\text{H}\}$ NMR (101 MHz, DMSO- d_6 , 297 K) δ 218.7 (Mn-CO), 216.1 (Mn-CO), 187.7 (NHC Mn-C), 138.8, 137.0, 136.3, 135.7, 129.4, 129.1, 125.8, 125.3, 52.6, 47.4, 21.0, 18.0, 17.2; IR (solution in THF): $\bar{\nu}$ [cm^{-1}] 2011 (s, $\bar{\nu}$ CO), 1914 (s, $\bar{\nu}$ CO), 1911 (s, $\bar{\nu}$ CO); EA: Found (Calcd.) for $\text{C}_{31}\text{H}_{35}\text{F}_6\text{MnN}_5\text{O}_3$: C: 51.34 (51.32); H: 4.84 (4.86); N: 9.63 (9.65).

Complex 3: ^1H NMR (400 MHz, DMSO- d_6 , 297 K) δ 7.66 (s, 2H), 7.18 (s, 2H), 6.91 (s, 4H), 4.95 – 4.78 (m, 1H), 4.41 – 4.26 (m, 2H), 4.22 – 4.05 (m, 2H), 3.15 – 2.96 (m, 2H), 2.62 – 2.42 (m, 2H), 2.23 (s, 6H), 1.92 – 1.84 (m, 12H); $^{31}\text{P}\{^1\text{H}\}$ NMR (162 MHz, DMSO- d_6 , 297 K) δ -144.2 (hep, $^1J_{\text{FP}} 712.8$ Hz); $^{13}\text{C}\{^1\text{H}\}$ NMR (101 MHz, DMSO- d_6 , 297 K) δ 222.3 (Mn-CO), 216.4 (Mn-CO), 214.4 (Mn-CO), 189.4 (NHC Mn-C), 138.6, 136.4, 136.2, 135.9, 129.0, 125.4, 124.9, 50.6, 47.6, 21.1, 18.3, 18.1; IR (solution in THF): $\bar{\nu}$ [cm^{-1}] 2034 (s, $\bar{\nu}$ CO), 1914 (s, $\bar{\nu}$ CO), 1904 (s, $\bar{\nu}$ CO); EA: Found (Calcd.) for $\text{C}_{31}\text{H}_{35}\text{F}_6\text{MnN}_5\text{O}_3$: C: 51.31 (51.32); H: 4.85 (4.86); N: 9.65 (9.65).

Synthesis of complex 5a:

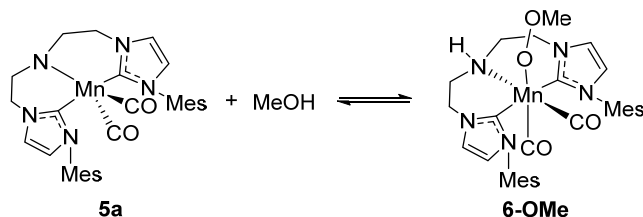


To the solution of complex 3 (72.5 mg, 0.1 mmol) in THF (0.5 mL) was dropwise added KO^tBu (11.8 mg, 0.105 mmol) in the mixture of 0.5 mL THF and 0.2 mL pentane. After stirring at rt for 1 h, the resulting mixture became dark blue and was filtered through a Celite plug to remove precipitation. The crude was further purified by slow diffusion of pentane into its solution in THF to afford 5a as blue crystals in 45 % yield (24.6 mg).

^1H NMR (400 MHz, THF- d_8 , 297 K) δ 7.19 (d, $J = 1.8$ Hz, 2H), 6.78 (s, 4H), 6.73 (d, $J = 1.8$ Hz, 2H), 3.97 – 3.94 (m, 4H), 2.88 – 2.86 (m, 4H), 2.20 (s, 6H), 1.90 (s, 12H); $^{13}\text{C}\{^1\text{H}\}$ NMR (101 MHz, THF- d_8 , 297 K) δ 236.2 (Mn-CO), 208.3 (NHC Mn-C), 137.8, 136.8, 135.9, 128.3, 120.9, 119.6, 57.3, 52.1, 20.2, 17.4; IR (solution in THF): $\bar{\nu}$ [cm^{-1}] 1886 (s, $\bar{\nu}$

CO), 1811 (s, $\bar{\nu}$ CO); EA: Found (Calcd.) for $C_{30}H_{34}MnN_5O_2$: C: 65.19 (65.33); H: 6.19 (6.21); N: 12.61 (12.70).

In situ-generation of Mn-alkoxide complex 6:



Upon treatment of complex **5a** (5.5 mg, 0.01 mmol) with MeOH (4.05 μ L, 0.1 mmol) in THF- d_8 (0.6 mL) the solution immediately turned to green from blue, partially producing complex **6-OMe**. Since the equilibrium was exothermic, the samples were cooled to -40 $^{\circ}$ C and hold for 10 min. As NMR showed, complex **5a** was nearly fully converted to **6-OMe** featured as an yellow solution. We then run the full NMR characterization at this temperature.

6-OMe (in situ): ^1H NMR (400 MHz, THF- d_8 , 233K) δ 7.25 (s, 2H), 6.81 – 6.76 (m, 6H), 4.48 – 4.32 (m, 2H), 4.32 – 4.27 (m, 2H), 3.78 (s, 1H), 3.26– 3.17 (m, 2H), 2.93 (s, 3H), 2.76– 2.68 (m, 2H), 2.22 (m, 12H), 1.88 (s, 6H); ^{13}C NMR (101 MHz, THF- d_8 , 233K) δ 232.9, 230.2, 207.8, 139.6, 138.7, 138.5, 138.3, 124.2, 123.8, 58.6, 53.0, 50.8, 49.4, 22.2, 19.8, 19.7; IR (solution in THF, 297 K): $\bar{\nu}$ [cm^{-1}] 1886 (s, $\bar{\nu}$ CO), 1811 (s, $\bar{\nu}$ CO).

4.8.2. Catalytic experiments

Catalytic hydrogenation of esters with Mn catalyst:

Into a 4 mL brown glass vial was added Mn complex (0.1 or 0.2 mol%), KOtBu (2 mg), and solvent (0.2 mL). The solution was stirred in glove box at room temperature for 10 mins followed by the addition of ethyl hexanoate (207 μ L, 1.25 mmol), KOtBu (12 mg, in total 10 mol%), solvent (0.3 mL), and dodecane (56.8 μ L, 0.25 mmol). The vial was then transferred into a stainless steel autoclave and connected to gas line. The system was purged with N_2 (3 \times 8 bar) and H_2 (1 \times 30 bar), pressurized with H_2 to specified pressure, and heated to specified temperature. After the reaction, resulting mixture was quenched

with H₂O (50 μ L) and then GC samples were prepared by dilution of the reaction mixture in THF (20 μ L into 1 mL THF).

4.8.3. Operando spectroscopy studies

Device: The high-pressure FTIR apparatus for performing the hydrogenation reactions consisted of a 20 mL stainless steel autoclave with mechanistic stirrer and an oil bath thermostat coupled with a heated transmission flow-through IR cell (Harrick Scientific, DLC-S25) and an autosampler (<https://www.cyberhydra.nl/>) for taking GC samples during the reaction. Circulation of the reaction solution through the IR cell and back to the autoclave was enabled via a micro gear pump. A 2-port valve with a 1 mL tubing was used for storing catalyst mixture. A Bruker Alpha II spectrometer was used for spectra recording. The IR cell was equipped with CaF₂ window as well as a wedged spacer, which provide a 0.15 mm optical path length. Pressurization facilities were installed for hydrogen and argon gas.

Experimental procedures: Inside glovebox, a catalyst solution of **2** (8.7 mg, 0.125 mmol) was prepared in 0.7 mL THF and activated with 10 mg KO^tBu for 10 min. The resulting solution was then loaded in a 1mL syringe. A 20 mL syringe was loaded with ester substrate (12.5 mmol) and dodecane (568 μ L, 2.5 mmol) in 7.5 mL THF (total volume 10 mL). Under N₂ flow, the substrate syringe was first injected into high pressure stainless steel reactor in which a glass beaker was inserted in advance. In an injection port the dissolved catalyst mixture was then placed and activated for 2 h under 40 bar (H₂). The reaction was started by injecting the catalyst mixture at 120 °C with stirring at 500 r.p.m, and the FTIR measurements and the sampling procedure were started.

FTIR spectra were recorded from 4000 to 400 cm⁻¹ with resolution of 2 cm⁻¹. Per spectrum were collected with 16 scans. Intervals between two measurements were 5 min (for the first 12 h) and after that 10 min.

FTIR data processing: The raw data were processed by baseline subtraction within metal-carbonyl wavenumber region (2100–1700 cm⁻¹) in OriginPro 2019. 10 anchor points snapped to the spectrum were selected (1763.7, 1767.7, 1781.8, 1789.8, 1829.9, 1835.5, 1839.9, 1867.3, 1916.6, 2020.1, 2052.2 cm⁻¹, can be modified slightly depending on the real spectrum) to fit the base line via 2nd derivative mode with 0.05 threshold. Beta spline was

used as the interpolation method. The obtained base line-subtracted data were then used directly for spectrum plotting or integral analysis for all the Mn species. In the processed IR spectrum, one of CO vibration bands of complex **5a** (1810 cm⁻¹) overlapped with that of **6** (1806 cm⁻¹), thus these two peaks should be deconvoluted for integration analysis. Therefore, the integral of the band of **5a** was directly calculated based on that of the second band (1886 cm⁻¹), as the proportion between these two bands could be assumed constant. We got the average coefficient $\beta_{5a} = \frac{Integral_{1810}}{Integral_{1886}}$ as 1.4835 based on the IR results depicted in Figures S19, S21, S22, S23, S27. Thus the integral of 1806 cm⁻¹ band of **6** was obtained by subtracting the total integral of the peaks in 1825–1775 cm⁻¹ by that of 1810 cm⁻¹ band of **5a**. Similarly, one band of complex **5b** (1771 cm⁻¹) was fully overlapped with the carbonyl of ester substrates with high concentration. The coefficient β_{5b} for this band was thus obtained as 1.334 through the same method. The total integral of all Mn species observed in the spectrum were shown to be nearly constant. Therefore we conclude the extinction coefficient for all the Mn compounds is identical and no deactivation through other pathway (e.g. decarbonylation) occurs.

4.8.4. UV-vis studies

1.6 mL of 0.567 mM solution of **Mn-5a** (0.5 mg) in THF were added to two identical cuvettes inside glovebox. The first sample was pure complex solution as reference. To the second sample was added corresponding amount of alcohol. For base effect study, base was mixed with the stock solution before adding to cuvette. The cuvettes were capped with Teflon seals, removed from glovebox, and loaded into UV-vis spectrometer and measured through transmission channel. The samples were heated or cooled to specified temperature and hold for 5 min before spectra were collected. All the transmission data were converted to absorbance for further analysis.

4.8.5. Calculation details

All quantum chemical calculations were performed by Ivan Chernyshov, Annika M. Krieger, Taras A. Khvorost. All the results can be found in section A.2 in Appendix.

4.8.6. Crystallographic details

X-ray diffraction studies were performed by M. Weber (Freie Universität Berlin). Crystallographic details are available in the electronic supporting information of the published work: *J. Am. Chem. Soc.*, **2022**, *144*, 8129-8137. CCDC entries 2099208 (2), 2099206 (3), and 2099207 (5a) contain the crystallographic data for this work.

4.9 References

1. (a) Rylander, P. N., *Catalytic Hydrogenation in Organic Syntheses: Paul Rylander*. Academic Press: New York, 1979; (b) Blaser, H. U.; Malan, C.; Pugin, B.; Spindler, F.; Steiner, H.; Studer, M., Selective hydrogenation for fine chemicals: Recent trends and new developments. *Adv. Synth. Catal.* **2003**, *345*, 103-151; (c) Vries, J. G. d., *The handbook of homogeneous hydrogenation*. Wiley-Vch: Weinheim, 2007; (d) McQuillin, F. J., *Homogeneous hydrogenation in organic chemistry*. Springer Science & Business Media: 2012; Vol. 1; (e) Chaloner, P. A.; Esteruelas, M. A.; Joó, F.; Oro, L. A., *Homogeneous hydrogenation*. Springer Science & Business Media: 2013; Vol. 15; (f) Seo, C. S.; Morris, R. H., Catalytic Homogeneous Asymmetric Hydrogenation: Successes and Opportunities. *Organometallics* **2018**, *38*, 47-65.
2. (a) Clarke, M. L., Recent developments in the homogeneous hydrogenation of carboxylic acid esters. *Catal. Sci. Technol.* **2012**, *2*, 2418-2423; (b) Werkmeister, S.; Junge, K.; Beller, M., Catalytic hydrogenation of carboxylic acid esters, amides, and nitriles with homogeneous catalysts. *Org. Process Res. Dev.* **2014**, *18*, 289-302; (c) Pritchard, J.; Filonenko, G. A.; van Putten, R.; Hensen, E. J.; Pidko, E. A., Heterogeneous and homogeneous catalysis for the hydrogenation of carboxylic acid derivatives: history, advances and future directions. *Chem. Soc. Rev.* **2015**, *44*, 3808-3833; (d) Dub, P. A.; Batrice, R. J.; Gordon, J. C.; Scott, B. L.; Minko, Y.; Schmidt, J. G.; Williams, R. F., Engineering catalysts for selective ester hydrogenation. *Org. Process Res. Dev.* **2020**, *24*, 415-442.
3. (a) Kuriyama, W.; Matsumoto, T.; Ogata, O.; Ino, Y.; Aoki, K.; Tanaka, S.; Ishida, K.; Kobayashi, T.; Sayo, N.; Saito, T., Catalytic hydrogenation of esters. Development of an efficient catalyst and processes for synthesising (R)-1, 2-propanediol and 2-(1-menthoxy) ethanol. *Org. Process Res. Dev.* **2012**, *16*, 166-171; (b) Spasyuk, D.; Smith, S.; Gusev, D. G., Replacing phosphorus with sulfur for the efficient hydrogenation of esters. *Angew. Chem. Int. Ed.* **2013**, *52*, 2538-2542; (c) Filonenko, G. A.; Cosimi, E.; Lefort, L.; Conley, M. P.; Copéret, C.; Lutz, M.; Hensen, E. J.; Pidko, E. A., Lutidine-derived Ru-CNC hydrogenation pincer catalysts with versatile coordination properties. *ACS Catal.* **2014**, *4*, 2667-2671; (d) Filonenko, G. A.; Aguila, M. J. B.; Schulpen, E. N.; van Putten, R.; Wiecko, J.; Muller, C.; Lefort, L.; Hensen, E. J. M.; Pidko, E. A., Bis-N-heterocyclic Carbene Aminopincer Ligands Enable High Activity in Ru-Catalyzed Ester

Hydrogenation. *J. Am. Chem. Soc.* **2015**, *137*, 7620-7623; (e) Tan, X.; Wang, Y.; Liu, Y.; Wang, F.; Shi, L.; Lee, K.-H.; Lin, Z.; Lv, H.; Zhang, X., Highly efficient tetradentate ruthenium catalyst for ester reduction: especially for hydrogenation of fatty acid esters. *Org. Lett.* **2015**, *17*, 454-457; (f) Wang, Z.; Chen, X.; Liu, B.; Liu, Q.-b.; Solan, G. A.; Yang, X.; Sun, W.-H., Cooperative interplay between a flexible PNN-Ru (ii) complex and a NaBH₄ additive in the efficient catalytic hydrogenation of esters. *Catal. Sci. Technol.* **2017**, *7*, 1297-1304; (g) He, T.; Buttner, J. C.; Reynolds, E. F.; Pham, J.; Malek, J. C.; Keith, J. M.; Chianese, A. R., Dehydroalkylative activation of CNN- and PNN-pincer ruthenium catalysts for ester hydrogenation. *J. Am. Chem. Soc.* **2019**, *141*, 17404-17413.

4. (a) Junge, K.; Wendt, B.; Jiao, H.; Beller, M., Iridium-Catalyzed Hydrogenation of Carboxylic Acid Esters. *ChemCatChem* **2014**, *6*, 2810-2814; (b) Brewster, T. P.; Rezayee, N. M.; Culakova, Z.; Sanford, M. S.; Goldberg, K. I., Base-free iridium-catalyzed hydrogenation of esters and lactones. *ACS Catal.* **2016**, *6*, 3113-3117.

5. (a) Spasyuk, D.; Gusev, D. G., Acceptorless dehydrogenative coupling of ethanol and hydrogenation of esters and imines. *Organometallics* **2012**, *31*, 5239-5242; (b) Spasyuk, D.; Vicent, C.; Gusev, D. G., Chemoselective hydrogenation of carbonyl compounds and acceptorless dehydrogenative coupling of alcohols. *J. Am. Chem. Soc.* **2015**, *137*, 3743-3746.

6. (a) Zell, T.; Milstein, D., Hydrogenation and dehydrogenation iron pincer catalysts capable of metal–ligand cooperation by aromatization/dearomatization. *Acc. Chem. Res.* **2015**, *48*, 1979-1994; (b) Maji, B.; Barman, M. K., Recent developments of manganese complexes for catalytic hydrogenation and dehydrogenation reactions. *Synthesis* **2017**, *49*, 3377-3393; (c) Alig, L.; Fritz, M.; Schneider, S., First-row transition metal (de) hydrogenation catalysis based on functional pincer ligands. *Chem. Rev.* **2018**, *119*, 2681-2751; (d) Filonenko, G. A.; van Putten, R.; Hensen, E. J.; Pidko, E. A., Catalytic (de) hydrogenation promoted by non-precious metals–Co, Fe and Mn: recent advances in an emerging field. *Chem. Soc. Rev.* **2018**, *47*, 1459-1483; (e) Gorgas, N.; Kirchner, K., Isoelectronic manganese and iron hydrogenation/dehydrogenation catalysts: Similarities and divergences. *Acc. Chem. Res.* **2018**, *51*, 1558-1569; (f) Irrgang, T.; Kempe, R., 3d-Metal Catalyzed N- and C-Alkylation Reactions via Borrowing Hydrogen or Hydrogen Autotransfer. *Chem. Rev.* **2018**, *119*, 2524-2549; (g) Kallmeier, F.; Kempe, R., Manganese Complexes for (De) Hydrogenation Catalysis: A Comparison to Cobalt and Iron Catalysts. *Angew. Chem. Int. Ed.* **2018**, *57*, 46-60; (h) Wang, Y.; Wang, M.; Li, Y.; Liu, Q., Homogeneous manganese-catalyzed hydrogenation and dehydrogenation reactions. *Chem* **2020**, *7*, 1180-1223.

7. (a) Elangovan, S.; Topf, C.; Fischer, S.; Jiao, H.; Spannenberg, A.; Baumann, W.; Ludwig, R.; Junge, K.; Beller, M., Selective catalytic hydrogenations of nitriles, ketones, and aldehydes by well-defined manganese pincer complexes. *J. Am. Chem. Soc.* **2016**, *138*, 8809-8814; (b) Kallmeier, F.; Irrgang, T.; Dietel, T.; Kempe, R., Highly active and selective

manganese C=O bond hydrogenation catalysts: the importance of the multidentate ligand, the ancillary ligands, and the oxidation state. *Angew. Chem. Int. Ed.* **2016**, *55*, 11806-11809; (c) Garbe, M.; Junge, K.; Walker, S.; Wei, Z.; Jiao, H.; Spannenberg, A.; Bachmann, S.; Scalone, M.; Beller, M., Manganese (I)-Catalyzed Enantioselective Hydrogenation of Ketones Using a Defined Chiral PNP Pincer Ligand. *Angew. Chem. Int. Ed.* **2017**, *56*, 11237-11241; (d) Papa, V.; Cabrero-Antonino, J. R.; Alberico, E.; Spanneberg, A.; Junge, K.; Junge, H.; Beller, M., Efficient and selective hydrogenation of amides to alcohols and amines using a well-defined manganese-PNN pincer complex. *Chem. Sci.* **2017**, *8*, 3576-3585; (e) Garduño, J. A.; García, J. J., Non-Pincer Mn (I) Organometallics for the Selective Catalytic Hydrogenation of Nitriles to Primary Amines. *ACS Catal.* **2018**, *9*, 392-401; (f) Glatz, M.; Stöger, B.; Himmelbauer, D.; Veiros, L. F.; Kirchner, K., Chemoselective Hydrogenation of Aldehydes under Mild, Base-Free Conditions: Manganese Outperforms Rhenium. *ACS Catal.* **2018**, *8*, 4009-4016; (g) Kaithal, A.; Hölscher, M.; Leitner, W., Catalytic Hydrogenation of Cyclic Carbonates using Manganese Complexes. *Angew. Chem. Int. Ed.* **2018**, *57*, 13449-13453; (h) Kumar, A.; Janes, T.; Espinosa-Jalapa, N. A.; Milstein, D., Manganese Catalyzed Hydrogenation of Organic Carbonates to Methanol and Alcohols. *Angew. Chem. Int. Ed.* **2018**, *57*, 12076-12080; (i) Weber, S.; Stöger, B.; Kirchner, K., Hydrogenation of nitriles and ketones catalyzed by an air-stable bisphosphine Mn (I) complex. *Org. Lett.* **2018**, *20*, 7212-7215; (j) Wei, D.; Bruneau-Voisine, A.; Chauvin, T.; Dorcet, V.; Roisnel, T.; Valyaev, D. A.; Lugan, N.; Sortais, J. B., Hydrogenation of Carbonyl Derivatives Catalysed by Manganese Complexes Bearing Bidentate Pyridinyl-Phosphine Ligands. *Adv. Synth. Catal.* **2018**, *360*, 676-681; (k) Zou, Y.-Q.; Chakraborty, S.; Nerush, A.; Oren, D.; Diskin-Posner, Y.; Ben-David, Y.; Milstein, D., Highly Selective, Efficient Deoxygenative Hydrogenation of Amides Catalyzed by a Manganese Pincer Complex via Metal-Ligand Cooperation. *ACS Catal.* **2018**, *8*, 8014-8019; (l) Buhaibeh, R.; Filippov, O. A.; Bruneau-Voisine, A.; Willot, J.; Duhayon, C.; Valyaev, D. A.; Lugan, N.; Canac, Y.; Sortais, J.-B., Phosphine-NHC Manganese Hydrogenation Catalyst Exhibiting a Non-Classical Metal-Ligand Cooperative H₂ Activation Mode. *Angew. Chem. Int. Ed.* **2019**, *58*, 6727-6731; (m) Freitag, F.; Irrgang, T.; Kempe, R., Mechanistic Studies of Hydride Transfer to Imines from a Highly Active and Chemoselective Manganate Catalyst. *J. Am. Chem. Soc.* **2019**, *141*, 11677-11685; (n) Wang, Y.; Zhu, L.; Shao, Z.; Li, G.; Lan, Y.; Liu, Q., Unmasking the ligand effect in manganese-catalyzed hydrogenation: mechanistic insight and catalytic application. *J. Am. Chem. Soc.* **2019**, *141*, 17337-17349; (o) Weber, S.; Stöger, B.; Veiros, L. F.; Kirchner, K., Rethinking Basic Concepts—Hydrogenation of Alkenes Catalyzed by Bench-Stable Alkyl Mn (I) Complexes. *ACS Catal.* **2019**, *9*, 9715-9720; (p) Weber, S.; Veiros, L. F.; Kirchner, K., Old Concepts, New Application—Additive-Free Hydrogenation of Nitriles Catalyzed by an Air Stable Alkyl Mn (I) Complex. *Adv. Synth. Catal.* **2019**, *361*, 5412-5420; (q) Zhang, L.; Tang, Y.; Han, Z.; Ding, K., Lutidine-Based Chiral Pincer Manganese Catalysts for Enantioselective Hydrogenation of Ketones. *Angew. Chem. Int. Ed.* **2019**, *58*, 4973-4977; (r) Garbe, M.; Budweg, S.; Papa, V.; Wei, Z.;

Hornke, H.; Bachmann, S.; Scalone, M.; Spannenberg, A.; Jiao, H.; Junge, K., Chemoselective semihydrogenation of alkynes catalyzed by manganese (i)-PNP pincer complexes. *Catal. Sci. Technol.* **2020**, *10*, 3994-4001; (s) Papa, V.; Cao, Y.; Spannenberg, A.; Junge, K.; Beller, M., Development of a practical non-noble metal catalyst for hydrogenation of N-heteroarenes. *Nat. Catal.* **2020**, *3*, 135-142; (t) Zubar, V.; Sklyaruk, J.; Brzozowska, A.; Rueping, M., Chemoselective hydrogenation of alkynes to (Z)-alkenes using an air-stable base metal catalyst. *Org. Lett.* **2020**, *22*, 5423-5428; (u) Kaithal, A.; Werlé, C.; Leitner, W., Alcohol-Assisted Hydrogenation of Carbon Monoxide to Methanol Using Molecular Manganese Catalysts. *JACS Au* **2021**, *1*, 130-136; (v) Liu, C.; Wang, M.; Liu, S.; Wang, Y.; Peng, Y.; Lan, Y.; Liu, Q., Manganese-Catalyzed Asymmetric Hydrogenation of Quinolines Enabled by π - π Interaction**. *Angew. Chem. Int. Ed.* **2021**, *60*, 5108-5113; (w) Yang, W.; Chernyshov, I. Y.; van Schendel, R. K.; Weber, M.; Müller, C.; Filonenko, G. A.; Pidko, E. A., Robust and efficient hydrogenation of carbonyl compounds catalysed by mixed donor Mn (I) pincer complexes. *Nat. Commun.* **2021**, *12*, 1-8.

8. (a) Elangovan, S.; Garbe, M.; Jiao, H.; Spannenberg, A.; Junge, K.; Beller, M., Hydrogenation of Esters to Alcohols Catalyzed by Defined Manganese Pincer Complexes. *Angew. Chem. Int. Ed.* **2016**, *49*, 15364-15368; (b) Espinosa-Jalapa, N. A.; Nerush, A.; Shimon, L. J.; Leitus, G.; Avram, L.; Ben-David, Y.; Milstein, D., Manganese-Catalyzed Hydrogenation of Esters to Alcohols. *Chem. Eur. J.* **2017**, *23*, 5934-5938; (c) Van Putten, R.; Uslamin, E. A.; Garbe, M.; Liu, C.; Gonzalez-de-Castro, A.; Lutz, M.; Junge, K.; Hensen, E. J.; Beller, M.; Lefort, L., Non-Pincer-Type Manganese Complexes as Efficient Catalysts for the Hydrogenation of Esters. *Angew. Chem. Int. Ed.* **2017**, *56*, 7531-7534; (d) Widegren, M. B.; Harkness, G. J.; Slawin, A. M.; Cordes, D. B.; Clarke, M. L., A highly active manganese catalyst for enantioselective ketone and ester hydrogenation. *Angew. Chem. Int. Ed.* **2017**, *56*, 5825-5828; (e) Widegren, M. B.; Clarke, M. L., Towards practical earth abundant reduction catalysis: design of improved catalysts for manganese catalysed hydrogenation. *Catal. Sci. Technol.* **2019**, *9*, 6047-6058.

9. (a) Krieger, A. M.; Kuliaev, P.; Armstrong Hall, F. Q.; Sun, D.; Pidko, E. A., Composition-and Condition-Dependent Kinetics of Homogeneous Ester Hydrogenation by a Mn-Based Catalyst. *J. Phys. Chem. C* **2020**, *124*, 26990-26998; (b) Kuliaev, P. O.; Pidko, E. A., Operando modeling of multicomponent reactive solutions in homogeneous catalysis: from non-standard free energies to reaction network control. *ChemCatChem* **2020**, *12*, 795.

10. Pfriem, N.; Hintermeier, P. H.; Eckstein, S.; Kim, S.; Liu, Q.; Shi, H.; Milakovic, L.; Liu, Y.; Haller, G. L.; Baráth, E., Role of the ionic environment in enhancing the activity of reacting molecules in zeolite pores. *Science* **2021**, *372*, 952-957.

11. Zhong, R.; Wei, Z.; Zhang, W.; Liu, S.; Liu, Q., A Practical and Stereoselective In Situ NHC-Cobalt Catalytic System for Hydrogenation of Ketones and Aldehydes. *Chem* **2019**, *5*, 1552-1566.
12. (a) Liu, C.; van Putten, R.; Kulyaev, P. O.; Filonenko, G. A.; Pidko, E. A., Computational insights into the catalytic role of the base promoters in ester hydrogenation with homogeneous non-pincer-based Mn-P, N catalyst. *J. Catal.* **2018**, *363*, 136-143; (b) Hamilton, R. J.; Bergens, S. H., An unexpected possible role of base in asymmetric catalytic hydrogenations of ketones. Synthesis and characterization of several key catalytic intermediates. *J. Am. Chem. Soc.* **2006**, *128*, 13700-13701.
13. (a) Abdur-Rashid, K.; Clapham, S. E.; Hadzovic, A.; Harvey, J. N.; Lough, A. J.; Morris, R. H., Mechanism of the hydrogenation of ketones catalyzed by trans-dihydrido (diamine) ruthenium (II) complexes. *J. Am. Chem. Soc.* **2002**, *124*, 15104-15118; (b) Hamilton, R. J.; Bergens, S. H., Direct Observations of the Metal– Ligand Bifunctional Addition Step in an Enantioselective Ketone Hydrogenation. *J. Am. Chem. Soc.* **2008**, *130*, 11979-11987; (c) Bertoli, M.; Choualeb, A.; Lough, A. J.; Moore, B.; Spasyuk, D.; Gusev, D. G., Osmium and ruthenium catalysts for dehydrogenation of alcohols. *Organometallics* **2011**, *30*, 3479-3482; (d) Alberico, E.; Lennox, A. J.; Vogt, L. K.; Jiao, H.; Baumann, W.; Drexler, H.-J.; Nielsen, M.; Spannenberg, A.; Checinski, M. P.; Junge, H., Unravelling the mechanism of basic aqueous methanol dehydrogenation catalyzed by Ru–PNP pincer complexes. *J. Am. Chem. Soc.* **2016**, *138*, 14890-14904; (e) Gusev, D. G., Dehydrogenative coupling of ethanol and ester hydrogenation catalyzed by pincer-type YNP complexes. *ACS Catal.* **2016**, *6*, 6967-6981; (f) Nguyen, D. H.; Trivelli, X.; Capet, F. d. r.; Paul, J.-F. o.; Dumeignil, F.; Gauvin, R. g. M., Manganese pincer complexes for the base-free, acceptorless dehydrogenative coupling of alcohols to esters: development, scope, and understanding. *ACS Catal.* **2017**, *7*, 2022-2032; (g) Mathis, C. L.; Geary, J.; Ardon, Y.; Reese, M. S.; Philliber, M. A.; VanderLinden, R. T.; Saouma, C. T., Thermodynamic Analysis of Metal–Ligand Cooperativity of PNP Ru Complexes: Implications for CO₂ Hydrogenation to Methanol and Catalyst Inhibition. *J. Am. Chem. Soc.* **2019**, *141*, 14317-14328.
14. O, W. W. N.; Morris, R. H., Ester Hydrogenation Catalyzed by a Ruthenium(II) Complex Bearing an N-Heterocyclic Carbene Tethered with an "NH₂" Group and a DFT Study of the Proposed Bifunctional Mechanism. *ACS Catal.* **2013**, *3*, 32-40.
15. (a) Freire, M. G.; Ventura, S. P.; Santos, L. M.; Marrucho, I. M.; Coutinho, J. A., Evaluation of COSMO-RS for the prediction of LLE and VLE of water and ionic liquids binary systems. *Fluid Phase Equilib.* **2008**, *268*, 74-84; (b) Marenich, A. V.; Cramer, C. J.; Truhlar, D. G., Universal solvation model based on solute electron density and on a continuum model of the solvent defined by the bulk dielectric constant and atomic surface tensions. *J. Phys. Chem. B* **2009**, *113*, 6378-6396.

**Utilizing Design of Experiments Approach
to Assess Kinetic Parameters for a Mn
Homogeneous Hydrogenation Catalyst**

Abstract

Kinetic data can provide comprehensive insights to the mechanism and behavior of catalytic reactions. Since collecting formal kinetic datasets is time-consuming and challenging, we attempt to extract kinetic information from minimal high-throughput experiments by using design of experiments and statistic modelling. In this work, we employ response surface Box-Wilson methodology and establish a set of different statistical models to obtain the detailed kinetic description of a highly active homogeneous Mn-CNP ketone hydrogenation catalyst as a representative model system. The reaction kinetics was analysed using the full second order polynomial regression model, the model with eliminated parameters and finally to the model which implements “chemical logic”. The coefficients obtained are compared with the corresponding high-quality kinetic parameters assessed using conventional kinetic experiments. We demonstrate that various kinetic effects can be well captured using the different statistical models, providing important insights into the reaction kinetics and mechanism of a complex catalytic reaction.

This chapter has been published as:

Robin K. A. van Schendel, Wenjun Yang, Evgeny A. Uslamin, Evgeny A. Pidko, *ChemCatChem*, **2021**, 13, 4886-4896.

Contributions: R.K.A.S. designed, conducted the experiments, and analyzed the data; W.Y. conducted the experiments, and analyzed the data; E.A.U., G.A.F. and E.A.P. supervised the research.

5.1 Introduction

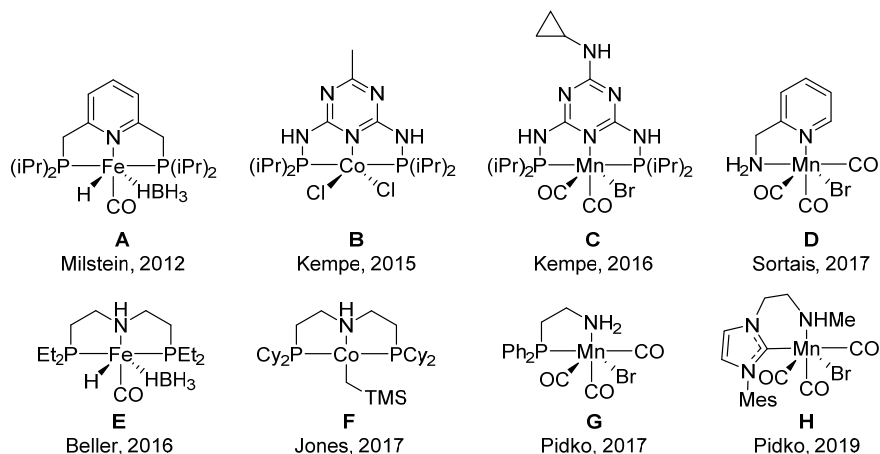


Figure 5. 1. Selected examples of 3d metal complexes active in hydrogenation reactions.

Rapidly increasing demand in chemicals and fuels puts forward new challenges for chemical industry and chemistry in general. The fast implementation of novel catalytic processes is therefore becoming crucial as it enables more sustainable and effective chemical transformations.¹ The transition from the laboratory catalytic research to the industrial application is often a limiting step. This requires deep understanding of the behaviour of the system on both molecular and reactor scale. Implementing data-driven approaches can help solving this complex problem by providing descriptive non-biased models.² Design of experiment and statistical analysis of the experimental data are the key ingredients within this approach.³

Reduction of carbonyl compounds is an important process widely applied in the fine and bulk chemical industry. In contrast to conventional stoichiometric reactions yielding vast amount of inorganic waste, catalytic hydrogenation utilizing molecular hydrogen represents an environmentally-friendly and atom-efficient alternative.⁴ This becomes especially attractive as the hydrogen market is rapidly expanding over the last few years. The hydrogenation reactions require the use of a catalyst. Over the last decades, a number of highly active homogeneous carbonyl hydrogenation catalysts based on defined transition metal complexes, e.g. ruthenium, iridium, and rhodium, were developed. Many of these catalysts enable highly selective homogeneous hydrogenation under mild

conditions.^{4b, 5} However, the possibility to use cheaper earth-abundant 3d metals complexes as an alternative to their noble metal based counterparts recently draws considerable attention.^{6,7} **Figure 5. 1** presents selected representative examples of such highly-active catalysts. Fe-A,⁸ Co-B,⁹ and Mn-C¹⁰ containing lutidine- and diamino triazine-derived pincer ligands were found to be highly active in the hydrogenation of ketones and aldehydes and can operate at 0.05–0.25 mol. % catalyst loading. Amino ligand-based complexes (**E**,¹¹ **F**,¹² and **G**¹³) represent most potent 3d metal catalysts for ester hydrogenations requiring 0.2–2 mol. % catalyst loading. Mn-based complexes (e.g. **D**¹⁴, **H**¹⁵) have also emerged as highly efficient transfer hydrogenation catalysts enabling excellent performance at metal concentration as low as 75 ppm.

Modern synthetic protocols allow obtaining well-defined catalytic complexes with nearly any given ligand environment. In contrast, the testing procedures used to evaluate the catalyst performance are less defined. The limited scope of conditions used during the initial catalyst screening phase often result in a situation when important effects including the catalyst activation, its stability under the reaction conditions and different deactivation pathways are overlooked. This may lead to a limited understanding of the intrinsic catalyst activity and therefore hamper the establishment of solid predictive structure-performance relationships. The availability of the kinetic data and its accurate

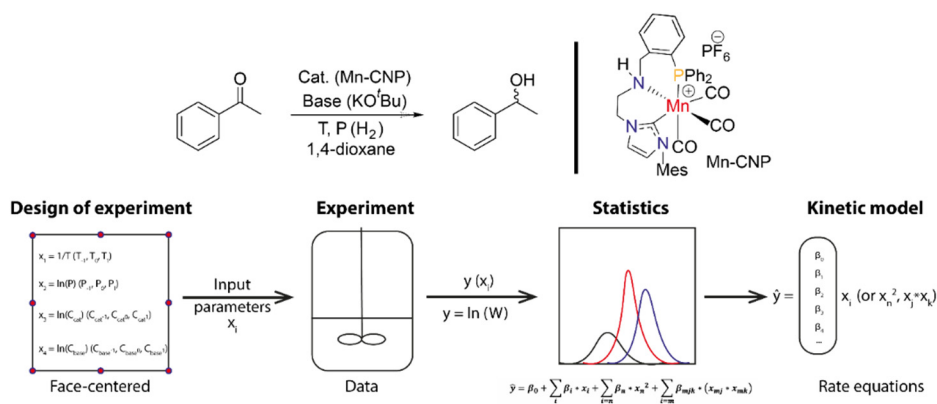


Figure 5. 2 Reaction schematics showing the hydrogenation of acetophenone in presence of MnCNP catalyst (top); the schematics of the experimental workflow (bottom).

modelling would provide a comprehensive insight in the behaviour and mechanisms of catalytic reactions and therefore facilitate the further development and optimization of high-efficient hydrogenation catalysts.¹⁶

The modelling of homogeneous catalytic reaction can be based on different approaches ranging from a purely empirical description to formal kinetics and to theory-assisted micro kinetic modelling.¹⁷ The resulting rate equations can therefore take various forms ranging from simple power laws to highly complex polynomial forms. Due to the complexity of the realistic catalytic networks, these models may not fully describe the system in many cases. In the specific case of the hydrogenation catalysis, the situation is further complicated by the experimental challenges related to the use of the high-pressure equipment. Thus, the development of the precise and rapid kinetic modelling approaches based on minimum experimental runs become indispensable. Herein we apply the response surface Box-Wilson statistical methodology¹⁸ to the kinetic analysis of ketone hydrogenation reaction catalysed by a novel Mn (I) CNP complex (**Figure 5. 2**).¹⁹ Response Surface Design (RSD) is found to not only provide a rapid access to the “classic” kinetic parameters with less experimentation, but it also indicate the hidden parameters which are not observed during the conventional kinetic experiments.

5.2 Experimental design and statistical methods

Design of experiment

Experimental setup was designed according to the Box-Wilson methodology¹⁸ also known as response surface design using the central composite face-centred type. Four continuous regressors in three levels were chosen (temperature, H₂ pressure, concentration of the catalyst and concentration of the base) and kept un-coded. Due to uncertainty in measuring initial reaction rates, the chosen regressor was the average reaction rate (measured as $product \cdot t^{-1}$). The average rate was calculated as the concentration of produced alcohol divided by the reaction time in hours. No blocks were used and all runs were randomized save for the temperature due to the home-built autoclave heating six reactions at a time in unison. With all the cube points, axial points

and replicates, a total of 30 runs were performed. The reaction loadings and conditions are summarized in **Table 5. 4**.

Response surface design

A central composite face-centred design was used to obtain a multiple polynomial regression equation that would take the same form as an adjusted Arrhenius equation describing the kinetics of the reaction.²⁰ A response surface design is a setup for an experiment where for each regressor three points are taken, namely a lower boundary, the mid-point and a higher boundary. Generally, for a face centred design, these boundaries are codified as -1, 0 and 1. In this work we were not interested in creating an abstract statistical model, but rather one with physical significance. With a polynomial fit of multiple regressors a “response surface” is created to facilitate finding an optimum. A response surface design is therefore usually performed after the initial factorial design with two-level factors and linear fits. If the optimum is not found within the bounds of the factorial design it is followed by a path of steepest ascent approach. Instead of using this methodology to find an optimum, the main focus was put on mapping the effects of each regressor and constructing a physical equation from the dependence obtained. A multiple polynomial regression analysis takes the form of a linear equation where each separate factor is included. In this sense, the *simplest first order* version with no quadratic terms and no interaction terms of such equation takes the following form:

$$\hat{y} = \beta_0 + \sum_i \beta_i * x_i \quad (\text{Eq 5.1})$$

where \hat{y} is the actual (or expected) response, β_0 is the coefficient corresponding to the intercept, β_i is the coefficient corresponding to the i -th iteration of the regressor x_i .

A physical meaning for a linear regression model can be established from the generalization of the formal reaction kinetics. Thus, in a general form for a given chemical process $\sum_i \nu_i X_i \xrightarrow{k} \sum_j \nu_j Y_j$, the reaction rate W can be defined in a differential and logarithmic form:

$$W = -\frac{d[X_i]}{\nu_i dt} = \frac{d[Y_j]}{\nu_j dt} = \prod_i k X_i^{n_i} \quad (\text{Eq 5.2})$$

$$\ln(W) = \ln(k) + \sum_i n_i \ln X_i \quad (\text{Eq 5.3})$$

The temperature dependence of the reaction rate constant is described by the Arrhenius equation:

$$\ln(k) = -\frac{E_a}{R} * \frac{1}{T} + \ln(A_k) \quad (\text{Eq 5.4})$$

Overall, the expansion of the rate constant in the rate equation leads to a full linear equation as such:

$$\ln(W) = \ln(A_k) - \frac{E_a}{R} * \frac{1}{T} + \sum_i n_i \ln X_i \quad (\text{Eq 5.5})$$

Via the comparative analysis of Eq. 5.1 and 5.5, intercept β_0 can be denoted as the frequency factor, and the rest are similar first order terms. Besides, one regressor (x_i) may be seen as $1/T$, leaving one coefficient β_i as $-E_a/R$.

A second order polynomial regression of multiple variables includes square terms and interaction terms, each with its own coefficient.²¹ With the ordinary least squares method, empirical response values are fit to approximate the actual response. The fit is assessed by analysing the *goodness of fit*. Additional values for assessing the model are the R^2 value, adjusted R^2 value, the predicted residual error sum of squares (PRESS), the predicted R^2 and the p-value assessing the statistical significance of each term in the model.²²

A potential benefit of attempting to approximate a physical equation with an abstract statistical model is with the inclusion of normally excluded factors or terms, which might have a more complex effect on the reaction kinetics. This is exemplified by our addition of pressure as a factor, or the inclusion of *quadratic* and *interaction* terms showing the joint effect of couples of parameters. If the addition of these terms is properly justified, it can be indicative to some actual physical effects. The eventual *full regression equation* will take the form of

$$\hat{y} = \beta_0 + \sum_i \beta_i * x_i + \sum_{i=n} \beta_n * x_n^2 + \sum_{i=m} \beta_{mjk} * (x_{mj} * x_{mk}) \quad (\text{Eq. 5.6})$$

Following this approach, the first step is to construct a full multiple polynomial regression with all quadratic terms and interaction terms. The resulting model is then examined and insignificant terms or factors are removed using a stepwise elimination (regression) algorithm. To further justify the resulting model, the linearity of the corresponding main effects plot should be assessed along with the p-value for the regressor.

The key process variables including temperature, hydrogen pressure, concentration of the catalyst and concentration of the base are modified into a logarithmic form to fit the physical equation (**Table 5. 1**). Additionally, the corresponding responses are shown as the logarithm of the concentration of the reaction product divided by the reaction time which represents an averaged reaction rate. It is worth noting that the average rate is different from the initial reaction rate conventionally used in kinetic experiments. The initial reaction rate is often preferred as it makes it easier to extract formal kinetic parameters. However, for fast processes and for processes with a more complex behaviour extracting the initial rates can be problematic and the resulting values can be heavily impacted by the reaction initiation procedure. Besides, it does not provide information about the overall process kinetics which can change during the process. In contrast, the average reaction rate can be a good descriptor for obtaining the formal kinetic parameters and capturing more complex behaviour. For the formal kinetic parameters, the assumption can be made that the rate throughout the reaction is either linear or in correlation with the initial reaction rate of the target process.

Table 5. 1. Overview of the main variables used in all models, their mathematical notation and the form in which they are generally used

Variable	Notation	Input form
Temperature / T	X_1	1/T
Pressure / P	X_2	P
Catalyst concentration / (Cat)	X_3	ln(Cat)
Base concentration / (Base)	X_4	ln(Base)
Average reaction rate (system response)	y	ln(Product / Time)

The full quadratic fit was done using linear regression model fir function (*fitlm*) based on a least squares methodology. The data is weighted with the *RobustOpts* function which uses an iteratively reweighted least squares methodology. The analysis of variance was done using the ANOVA procedure.²³ This analysis was done on both the components of the model, and the whole model. R-squared and adjusted R-squared values are given with each produced model. The predicted R-squared is produced by the following formula:

$$\text{pred } R^2 = 1 - \left(\frac{\text{PRESS}}{\text{SST}} \right) \quad (\text{Eq. 5.7})$$

where one is subtracted by PRESS (the prediction error sum of squares)⁴ which is calculated from all the factors in the model, divided by the SST (sum of square total).

Formulation of statistic models

The data obtained from the catalytic tests were processed using four different statistic models schematically shown in **Figure 5. 3**. First the fully linear regression model (I) was constructed featuring all possible parameters and their interaction. Subsequent elimination of the parameters based on the significance and chemical logics principles gave rise to the reduced linear regression models (II) and (III), respectively. The non-linear regression model (IV) was constructed by following the general principles of the formal kinetics. The specific details of these models and the associated mathematical equations denoted in the **Figure 5. 3** will be described in detail in the text below.

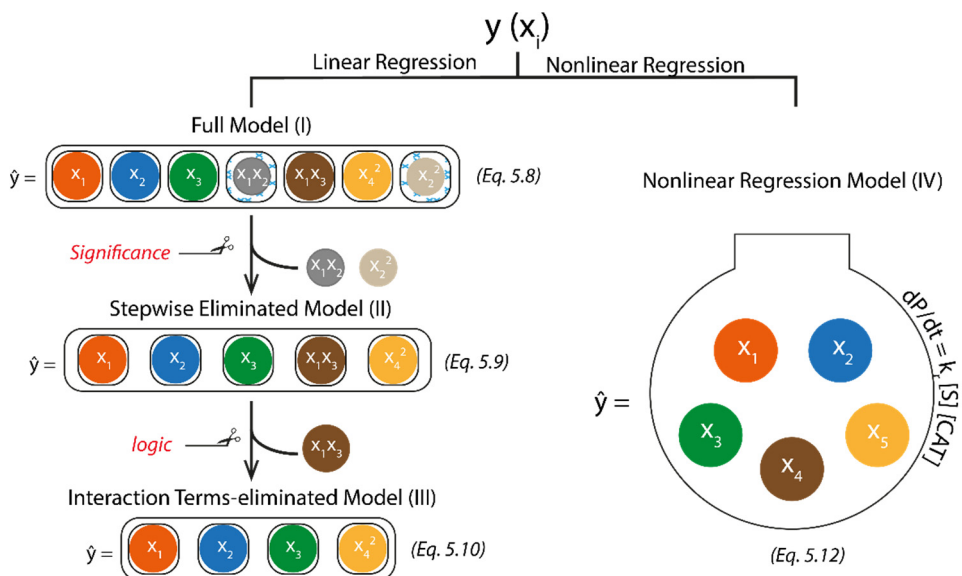


Figure 5. 3. Statistical models based on linear (I-III) and non-linear (IV) regression used in this work.

5.3 Full Model (I)

To describe the experimental kinetic dataset, we first introduce kinetic model (I) based on the full multiple polynomial regression, which includes all the quadratic terms and interaction terms (Eq. 5.2). In this model the reaction rate (system response) can be defined as follows:

$$\hat{y} = \beta_0 + \beta_1x_1 + \beta_2x_2 + \beta_3x_3 + \beta_4x_4 + \beta_5x_1x_2 + \beta_6x_1x_3 + \beta_7x_2x_3 + \beta_8x_1x_4 + \beta_9x_2x_4 + \beta_{10}x_3x_4 + \beta_{11}x_1^2 + \beta_{12}x_2^2 + \beta_{13}x_3^2 + \beta_{14}x_4^2 \quad (\text{Eq. 5.8})$$

Figure 5. 4 shows the goodness of fit of the experimental data points with the model (I). The results point to the substantial predictive power of this indiscriminately constructed multiple polynomial model as evidenced by predicted $R^2 = 0.9003$ (**Table 5. 2**). Further validation can be done via a p-value test that gives the probability of new data deviating from model prediction. The p-value of $1.29e^{-10}$ suggests a good predictability of this model based on the data provided. The F-statistic vs. constant model was 60.7 showing the significance of the model against the model consisted of only a constant term. However, the analysis of the individual p-value for each term in the model reveals many instances far larger than 0.05 indicating that many of the term effects are to be deemed insignificant, or within the “noise” (**Table 5. 5**). The only terms deemed significant are x_1 , x_2 , x_3 , x_4 , the interactions $x_1:x_3$ and $x_2:x_4$, as well as the x_4^2 quadratic term. Furthermore, the p-value for the lack of fit is 0.015 (**Table 5. 2**). These data shows that the inclusion of excess (catalysis-irrelevant) terms in model (I) renders it over-fitted.

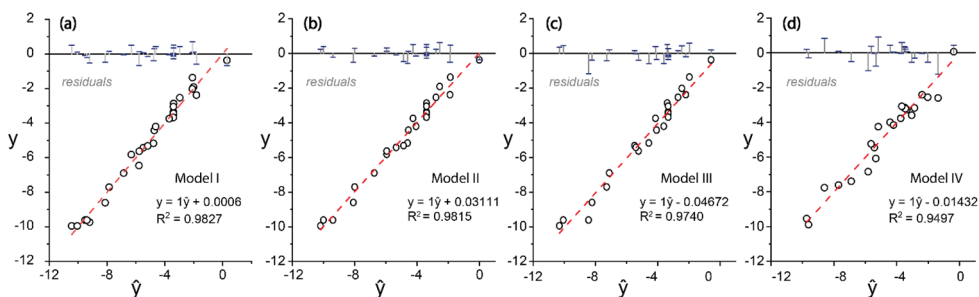


Figure 5. 4 Model fitting with residual plot incorporated: a) full statistical model (I); b) stepwise eliminated model (II); c) interaction terms-eliminated model (III); d) nonlinear regression model (IV). The y stands for the observed responses whereas the \hat{y} stands for the predicted response.

Table 5. 2. Statistical analyses for all the models comprising of statistical values including R-squared, adjusted R-squared, predicted R-squared, the p-value for the model, F-statistic versus constant model, the root mean squared error (RMSE) and the p-value for the lack of fit.

	R ²	adj R ²	pred R ²	p-value	F-statistic vs. constant model	RMS E	Lack of fit p-value
Model I	0.983	0.966	0.9003	1.29E-10	60.7	0.515	0.014863
Model II	0.984	0.978	0.9696	6.75E-15	160	0.387	0.0598
Model III	0.979	0.973	0.9572	2.24E-14	165	0.413	0.0448
Model IV	0.955	0.945	0.9221	1.79E-12	99.7	0.657	-

5.4 Stepwise eliminated model (II)

To remove the redundant factors, a new model was derived using the stepwise regression methodology. This methodology iteratively adds terms and keeps them if they meet a pre-defined criterion, or removes them otherwise. The criterion used was the p-value for the F-test of the change in the sum of squared error when a term is added or removed. Additionally, outliers were removed by assessing whether the standardized residuals were larger than 1.25 or smaller than -1.25. In our case, 4 outliers were determined, leaving a dataset of 26 observations. Accordingly, a model with actually significant terms was obtained:

$$\hat{y} = \beta_0 + \beta_1 x_1 + \beta_2 x_2 + \beta_3 x_3 + \beta_4 x_4 + \beta_5 x_1 x_3 + \beta_6 x_2 x_4 + \beta_7 x_4^2 \quad (\text{Eq. 5.9})$$

This model has a predicted R² of 0.9696 and an adjusted R² of 0.978 (as can be seen in **Table 5. 2**). The nuance between predicted and adjusted R² makes the assessing of these coefficients of determination trustworthy. The p-value for the model being so small stems from this value being susceptible to overfitting. The goodness of fit is further exemplified by the residual plot (**Figure 5. 4 b**).

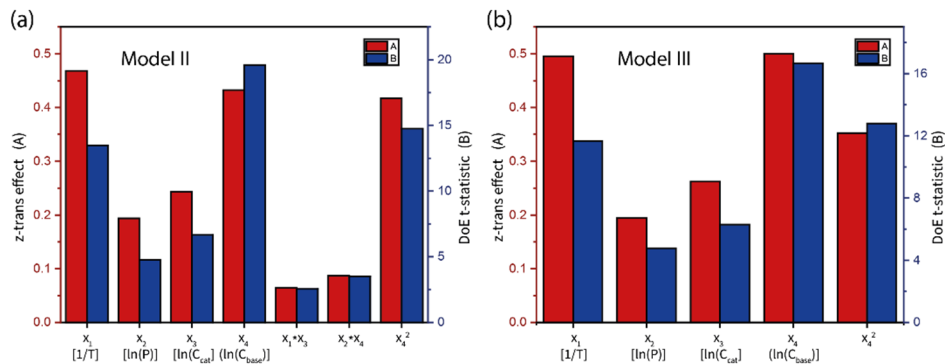


Figure 5.5. Effects of the reaction parameters: a) stepwise eliminated model (II); b) interaction terms-eliminated model (III).

To further evaluate the models, the effect of model parameters was examined using z-score and DoE t-statistics methods. Upon conversion of each term value (including the response) to a “standard score” (also known as standardising) or z-score with same unit, we are able to compare the effects of those catalysis parameters.²⁴ Besides, terms from multiple z-transformed models can be compared.²⁵ The z-trans effect results (A) in **Figure 5.5 a** show that the terms with the largest weight are the temperature, the base concentration and the 2nd order term for the base concentration.

The interaction terms have the lowest impact on the reaction rate. Next, by codifying the used factors as 1 and -1 for highest level and lowest level value respectively, the corresponding t-statistic may be interpreted as the amount of influence of the term on the response in a standardised form, though the technical definition is it being a test of the null hypothesis that the effect is zero. The added value of this method is that the significance of such a standardised effect can be verified with a two tailed test using the error degrees freedom (df) and the chosen significance level α . For a df of 20 and an α of 0.05 the significance level is 2.086. In this case the response does not require standardisation. The DoE t-statistic results (B) in **Figure 5.5a** show that all the terms are significant, with the terms for the base concentration, the 2nd order base concentration and the temperature having the most significance to the change in response being from these terms.

5.4 Interaction terms-eliminated model (III)

The stepwise eliminated model also runs the risk of overfitting. Though the predicted R^2 is excellent, the currently abstract statistical model must bear resemblance to reality. The interaction terms between temperature and the catalyst (x_1x_3 , Eq. 5.9), and the interaction term between the pressure and the base (x_2x_4 , Eq. 5.9) are not explained by the generalized rate equations. A new model was constructed by removing these interaction terms. The square term for the base however was kept due to the high weight of its effect. Whereas the first three primary parameters may be well fitted with a linear equation, the fourth parameter (the base) is undeniably second order. Constructing the same stepwise model from this hypothetical rate normalised by the concentration of catalyst used (TOF) obviously eliminates the catalyst term and produces a model featuring only the main linear terms and a quadratic base term:

$$\hat{y} = \beta_0 + \beta_1x_1 + \beta_2x_2 + \beta_3x_3 + \beta_4x_4 + \beta_5x_4^2 \quad (\text{Eq. 5.10})$$

All p-values, except for that of the base term, are sufficiently low to refute the null hypothesis (**Table 5. 7**). Next, all experiments with standardized residuals higher than 1.25 and lower than -1.25 were removed from the model. This left 24 observations as 6 observations were identified as outliers. The residual plots for the resulting model (**Figure 5. 4 c**) show a good distribution. The main effects of each parameter are presented as the prediction slice plots (**Figure 5. 8**). The prediction plot for the base concentration shows that at a high enough base concentration the corresponding effect saturates and reaches a plateau of a certain maximum rate.

Because the current model only leans on the validity of 24 remaining experiment data-points, the p-value for the lack of fit is only 0.0448 (**Table 5. 2**). This shows that the terms currently used in the model are not sufficient. The missing terms could be the eliminated interaction terms, but could also be something as of yet unknown although the p-value for the lack of fit can also be improved with more accurate additional data. Again, the results for the effects of the reaction parameters (**Figure 5. 5 b**) show that the base concentration has the most significant effect on the reaction rate. Compared to the z-score, however, we see that the quadratic term for the base concentration and the

temperature have now exchanged places in the effect weight. With a df of 21 and an α of 0.05 the significance level is 2.080 (t -test table).

5.5 Nonlinear regression model (IV)

The linear regression models presented above imply that a kinetic equation, in which a linear product of the concentrations of the catalyst and the base produce the rate of alcohol production, which makes little sense from the chemical kinetics perspective. To understand why these variables, give rise to such a good linear fit, the kinetics of the reaction were revisited. Though the exact reaction mechanism is not fully known, the basic process of catalyst activation and carbonyl compound hydrogenation can be explicitly considered. Following the prior mechanistic analysis,¹⁹ we presume certainty over an elementary reaction where the catalyst is activated by the use of a base (e.g. potassium tert-butoxide). Secondly, we assume certainty over the reaction, upon which the substrate is converted to the product with the use of the catalyst on a human time-scale. No microscopic details are assumed for the catalytic process, but the respective processes are approximated by a power law instead. Therefore, the rate of the catalyst activation is

$$\frac{d[CAT]}{dt} = k_a [CAT^-][BASE] \quad (\text{Eq. 5.11})$$

Where $[CAT^-]$ stands for the concentration of catalyst precursor and $[CAT]$ is the concentration of the activated catalyst. Catalyst activation proceeds via the base-assisted hydride formation step. Given the assumption of the semi-batch catalytic experiment ($p(H_2) = \text{constant}$ during the reaction) with the solution saturated with H_2 , this component is left out of the reaction rate equation. The rate of the catalytic hydrogenation reaction can be written as

$$\frac{dP}{dt} = k_r [S][CAT] \quad (\text{Eq. 5.12})$$

Where S and P denote the substrate (carbonyl derivative) and the product (alcohol) of the catalytic reaction. The reaction order for the catalyst and substrate will be introduced as coefficients in the statistic model. Integrating Eq. 5.11 over time we obtain the following equation:

$$[CAT] = [CAT^0][BASE^0]e^{k_a t} \quad (\text{Eq. 5.13})$$

The zero in the superscript signifies the initial concentration. Combining Eq. 5.12 and Eq. 5.13 gives:

$$\frac{dP}{dt} = k_r[S][CAT^0][BASE^0]e^{k_a t} \quad (\text{Eq. 5.14})$$

Expanding k_r as dictated by the Arrhenius equation we obtain:

$$\frac{dP}{dt} = Ae^{-E_a/RT}[S][CAT^0][BASE^0]e^{k_a t} \quad (\text{Eq. 5.15})$$

Taking the natural logarithm thereof gives:

$$\ln\left(\frac{dP}{dt}\right) = \ln[A] - \frac{E_a}{R} * \frac{1}{T} + \ln[CAT^0] + \ln[BASE^0] + \ln[S] + k_a t \quad (\text{Eq. 5.16})$$

This equation resembles closely the one obtained from the stepwise elimination procedure (Eq. 5.9), but with a few additional factors. The additional factors in this equation include $\ln[S]$ which is the natural logarithm of the substrate concentration, and $k_a t$, which is the catalyst activation rate constant times the time in seconds. The respective parameters were next estimated using a nonlinear regression model. Due to the data for rate being taken at the end of the reaction, a decision was made to use the substrate concentration at the end of the reaction (as measured by GC) and to use the reaction time in seconds that it took to finish each reaction according to the H_2 consumption data.

The nonlinear model was set up as:

$$\hat{y} = \beta_0 - \left(\frac{\beta_1}{8.314*10^{-3}}\right) * x_1 + \beta_2 x_2 + \beta_3 x_3 + \beta_4 x_4 + x_5 + \beta_5 x_6 \quad (\text{Eq. 5.17})$$

with x_2 being pressure in bar, x_3 being the natural logarithm of the catalyst concentration, x_4 being the natural logarithm of base concentration, x_5 being the natural logarithm of the substrate concentration at the end of the reaction (note there is no coefficient for this factor) and x_6 being the reaction time in seconds and the corresponding coefficient β_5 being the rate constant for catalyst activation.

This model is set up with six initial values of 1 for the coefficients, and with robust fitting options²⁶ using weighted residuals tuned using the bi-square weight function²⁷. Outliers

were identified by setting the standardized residual at ± 1.25 and removed. After removing the outliers, 24 observations are left and there are 19 error degrees of freedom. In **Table 5. 2** certain statistical values for the model can be seen, like the R-squared values for example. It must be said that R^2 values cannot be used for nonlinear regression²⁸ and should therefore be ignored. Plotting the predicted rates with the experimental rates gives a sense for the goodness of fit with a correlation coefficient of 1 (**Figure 5. 4 d**). It must be noted that the Jacobian of this model is ill-conditioned, which can be attributed to the model being described by six independent factors.

A nonlinear regression model is generally more difficult to validate. One of the possible validation methods is “leave-one-out-cross-validation” (LOOCV). Upon analysing the model using LOOCV, an RMSE of 0.732 is calculated and an R^2 of 0.9920 (**Figure 5. 6 a**).

All the p-values for the coefficients in this model were found significant (**Table 5. 8**). The expansion of the model with an added coefficient for the substrate variable results in the respective p-value of 0.24403 which is not significant. Significantly, the coefficients for most terms are comparable to the coefficients from the interaction eliminated model, saving for the obvious addition of the fifth coefficient related to the time term, and the base term which is now ~ 1 potentially due to the lack of a second order term. The residual plots show a good distribution with a slight tailing in the histogram.

Assuming that this model accurately describes the reaction kinetics explains why the prior stepwise model fits well as it is in essence the stepwise model with additional factors corresponding to the substrate concentration and the reaction time. These factors are obviously related to the response as the substrate concentration is the current concentration at any given moment of time, and the reaction time is considerably dependent on how fast the reaction proceeds, which in itself depends on other parameters.

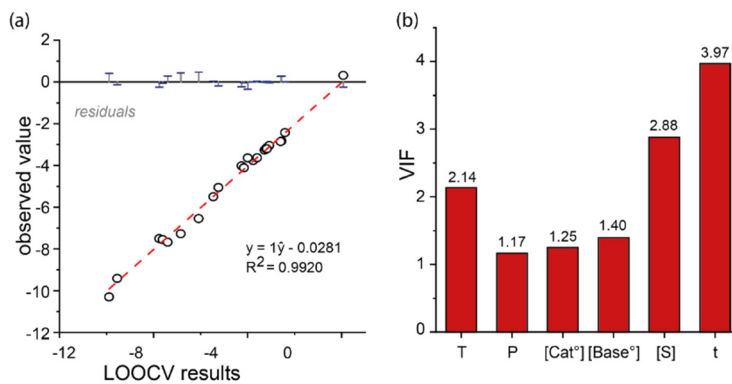


Figure 5. 6. a) Leave-One-Out-Cross-Validation fit; b) Variance Inflation Factors (VIF) for all variables used in the nonlinear regression model.

The Variance inflation factor (VIF) is a value that determines the multicollinearity of a term with other terms. Generally, a VIF of 4 would indicate strong multicollinearity, and require a term to be removed from the model. In the nonlinear model we see high VIF values for the substrate and the time terms, but low enough that one could argue they should remain (**Figure 5. 6 b**). The high multicollinearity of these terms is due to the fact that the reaction time and substrate at the end of the reaction can be considered independent variables.²⁵

5.6 Model analysis

The main statistic characteristics of the different models constructed above are listed in **Table 5. 2**. As it shows, the stepwise model (II) with the interaction terms shows a high predictability and could be considered pragmatic for predicting the results of future reactions within the model limits. Statistically, the population of observations is too low to make strong conclusions on the interaction terms as their effects are deemed small. The results in **Table 5. 2** show that the stepwise eliminated model has the lowest RMSE and the highest p-value from the models considered here. The p-value for the lack of fit is also the only one over 0.05 which indicates the model fits the data well. In contrast, the interaction terms eliminated model (III) has the best balance between overfitting, statistical accuracy and predictability possible with the current experimental data. Its lack of fit p-value is just barely insignificant with an alpha of 0.05. This however is likely due to the lack of degrees freedom, which can influence the calculation. As such, this model

will be used to compare with the kinetic data obtained via conventional protocols. Interestingly, the equation (Eq. 5.17) of nonlinear regression model (IV) shows high resemblance to those (Eq. 5.9 and 5.10) of linear stepwise multiple regression models (II, III). Accordingly, the statistical models (II, III) without incorporation of reaction mechanism should potentially be able to provide information on the kinetic nature of the reaction.

Although the exact values of the main coefficients in the three considered models vary significantly, pronounced similarities and common trends can be noted in the obtained parameters (**Table 5. 3**).²⁹ Most notably the models differ in the intercepts values due to the regression equations being markedly different in the interdependence of each parameter. The coefficients for T^{-1} are similar for the interaction-term eliminated model (III) and the nonlinear model (IV), but are distinctly different from that in the stepwise eliminated model (II). This is due to the fact that T^{-1} in the latter case is also accounted for the $\ln[\text{CAT}] \cdot T^{-1}$ interaction term. Considering the coefficient for T^{-1} can represent activation energy (Eq. 5.16 and 5.17), the above result implies that the apparent activation energy is affected by initial catalyst concentration. Similarly, $\ln[\text{CAT}]$ has a decidedly higher coefficient in model II as compared to the other models (III and IV) because of the $\ln[\text{CAT}] \cdot T^{-1}$ interaction term, suggesting effective catalyst concentration is limited by temperature. In both models II and III, the $\ln[\text{BASE}]$ is present with a negative coefficient. Model IV instead has a positive coefficient for $\ln[\text{BASE}]$, arguably due to the negative coefficient related to the reaction time t . This indicates a potentially negative coefficient for a parameter still missing in the equation IV. The coefficient for $\ln[\text{BASE}]$ thus can be interpreted as a potential catalyst deactivation path induced by base, as the reaction rate is seen to diminish at the higher $[\text{BASE}]$ (**Figure 5. 8**). It is also worth noting that interaction term $\ln[\text{P}] \cdot \ln[\text{BASE}]$ compensate for the negative effect of $\ln[\text{BASE}]$, suggesting high H_2 pressure can suppress the aforementioned deactivation. The coefficients for the $(\ln[\text{BASE}])^2$ are equivalent between the linear models I and II. Finally, the coefficients for $\ln\text{P}$ are comparable in the three models.

Table 5. 3. An overview of the parameter coefficients obtained from different statistical models.

Model parameters	Model II	Model III	Model IV
Intercept	57.28	16.705	31.554
T^{-1} ^a	162.3	41.0	39.3
lnP	0.068951	0.040648	0.035241
ln[CAT]	6.0532	1.3553	1.5982
ln[BASE]	-2.6974	-2.1133	1.0932
ln[CAT]· T^{-1}	-1601.3	-	-
$(\ln[BASE])^2$	-0.24092	-0.21516	-

^a. The coefficients for T^{-1} are normalized to the form that represent the apparent activation energy (kJ/mol).

5.7 Model validation and kinetic analysis

The statistical analysis results were then compared to the reaction parameters obtained via conventional kinetic measurements. In formal kinetic experiments, the reaction parameters are extracted from the initial reaction rates. The initial reaction rates for two different catalyst loadings were measured at varied temperature to assess the apparent activation energy, while kinetic runs at varying [BASE] and [CAT] were used to estimate the respective reaction orders. The results of the kinetic experiments are summarized in

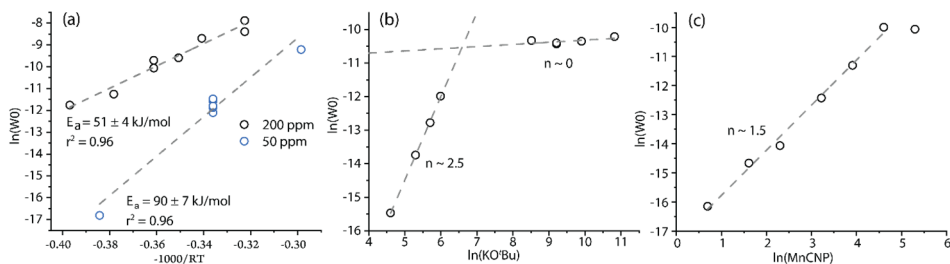
Figure 5. 7.

Figure 5. 7. Kinetic data. a) Arrhenius plot for varying catalyst loadings showing the natural log of the rate constants vs the multiplicative inverse of the temperature multiplied by the gas constant. b) The rate order plot for bases concentration showing the natural log of the rate vs the natural log of base concentration. c) The rate order plot for catalyst concentration showing the natural log of the rate vs the natural log of the catalyst concentration.

The kinetic data shown in **Figure 5. 7 a** reveal that already at the catalyst concentration of 200 ppm, the catalytic hydrogenation reaction is severely mass-transfer limited. Indeed, for the higher catalyst concentration of 200 ppm we find an activation energy of 51 kJ/mol that is approximately 2 times lower than the value obtained at a lower (50 ppm) catalyst concentration. The change in the catalyst reaction order at the higher loading also support this (**Figure 5. 7 c**). Our data strongly imply that, with mass-transfer limitations, the intrinsic activity of catalysts can be missed when screening them even at a relatively low loading amount (e.g 200 ppm). In the intrinsic kinetics regime, the reaction order in the catalyst was close to 1.5, while the reaction order for the base changes from ca. 2.5 at low base concentration to 0 at high concentrations (**Figure 5. 7 b**). The complex behaviour observed for these kinetic parameters suggest that the reaction has different regimes.

An increased reaction rate at high catalyst loading might result in diffusion limitations, while the initial reaction rate can be affected by the catalyst activation processes. It is worth noting that the exact role of the base in the homogeneous hydrogenation processes is not fully clear and might play an important role in both pre-catalyst activation and deactivation processes.¹⁹ Furthermore, previous studies have shown that the KO^tBu cation may facilitate the ketone hydrogenation by functioning as a Lewis acid.^{7e} In our previous work we have shown direct hemilability of the phosphine arm when KBHET₃ was used as an alternative activator. Similarly, the hemilability can play an important role when KO^tBu is used as the base.¹⁹

Next, the reaction parameters obtained from the direct kinetic measurements were compared to the results of the statistical analysis. The comparison of the model III and IV with the barriers obtained from the kinetic measurements (**Figure 5. 7 a**) reveal a close coherence of the T^{-1} coefficient of ~ 41 kJ/mol and ~ 39 kJ/mol with the Arrhenius barrier. Similarly, we observed the same comparableness with the base concentration, as the coefficient corresponding to the $\ln[\text{BASE}]$ in model III is -2.11. The absolute value would be comparable to the ~ 2.5 rate order found in the rate order plot for the base. However, it must be noted that the parameters have different signs. This is likely due to the completely different effects captured by the statistical and kinetic analysis.

While conventional kinetics measured under the differential conditions gives information about the initial stages of the reaction, statistical analysis is focused on the effect of the reaction parameters on the average reaction rate. Thus, the increased base concentration can have a strong positive effect on the pre-catalyst activation resulting in a higher initial reaction rate. On the other hand, it can contribute to the catalyst deactivation at the later stages of the reaction giving rise to a decreased final yield and, accordingly, lower average rate. The nonlinear regression model IV also shows resemblance between statistical coefficients and direct kinetic measurements. The activation rate from this model is ~ 39 kJ/mol which corresponds to the ~ 41 kJ/mol from model III than to the 51 kJ/mol from the experimental results. The coefficient corresponding to the catalyst concentration is 1.6 which neatly corresponds to the ~ 1.5 rate order from kinetic experiment. Other parameters however diverged. Thus, the coefficient corresponding to the base concentration is ~ 1.1 which is markedly different from the ~ 2.5 . When the stepwise model is made without quadratic term a similar coefficient (~ 0.9) was found. The coefficient of ~ 1 could be due to the lack of a quadratic term, whereas the fit remains acceptable due to the (over)abundance of terms in the form of time and substrate concentrations. This potential overabundance is indicated by an ill-conditioned Bayesian.

5.8 Conclusion

By combining a detailed kinetic analysis with statistical data analysis approaches, in this chapter we investigated the possibility of enhancing the data output from high-throughput catalyst screening / optimization procedures. The kinetics of homogeneous hydrogenation of benzophenone ketone substrate catalysed by a highly active Mn(I)-CNP catalyst described in Chapter 2 has been investigated and analysed in the framework of formal kinetics as well as by using a response surface Box-Wilson statistical methodology.

Equating the regression equations and the coefficients derived from it with statistical values has to be treated with strong scepticism and must therefore require rigorous statistics to validate this kind of method. The exact relation of the statistical models to the intrinsic reaction kinetics is often difficult to evaluate. However, having found

significant models, we are now able to speculate on the relations of certain factors to the observed reaction rate. The stepwise eliminated model (II) seems to be the most statistically significant. The critical role of the secondary effects on the performance of the homogeneous carbonyl hydrogenation catalysts were highlighted. The interaction terms between temperature and catalyst concentration and between the pressure and the base concentration indicate some complexity worth further investigation. The interaction terms eliminated model (III) retains a quadratic term for the base concentration, which may be related to the complex role that the base plays in the reaction. For both of the models II and III we consistently find that the base concentration holds the strongest effect on the reaction rate. The limited effect we observe from the pressure is explainable by the increase in molecular hydrogen availability within the reaction medium. We have clearly demonstrated the ability of the statistical model to measure the activation energy of the reaction and to capture different reaction regimes. The coefficients resulting from the stepwise model correlate with the kinetic parameters from classically obtained kinetics.

The statistical methodology described in this chapter may prove a reliable method to further understand complex and seemingly chaotic reactions. An apparent advantage of such an approach is that no initial assumption for the kinetics or the reaction mechanisms are required. This provides an opportunity to construct descriptive yet unbiased models. Once the model is made it can be used for both optimization and for the mechanistic studies.

5.9 Experimental details

Catalytic hydrogenation with Mn catalyst:

Stock solutions of the catalyst (0.01 M) were prepared. KO^tBu (5.6 mg, 1 mol%), substrate (5 mmol), solvent (3 mL), dodecane (56.8 μ L, 0.25 mmol), Mn complex (250, 500, 1000 μ L for S/Mn 20000, 10000, 5000, 4000 respectively) were mixed into a 4 mL glass vials and transferred into a stainless steel autoclave in the glovebox. The system was purged with N₂ (3 \times 8 bar) and H₂ (1 \times 30 bar), pressurized with H₂ to specified pressure, and heated to specified temperature.

After the reaction, resulting mixture was quenched with HCl aqueous (50 μL , 1 M) and then GC samples were prepared by dilution of the reaction mixture in THF (20 μL into 1 mL THF).

Experimental parameters and results.

Table 5. 4. The parameters used in experiments and their corresponding reaction time, overall reaction rate and yield

T, °C	Concentration, mmol/l		Pressure (bar)	Time (hours)	Yield (%)
	Catalyst	Base (KO ^t Bu)			
65	0.16	6.28	30	15.51	37.22
65	0.16	6.28	30	15.51	36.20
65	0.16	6.28	30	15.51	43.00
65	0.16	6.28	30	15.51	39.45
65	0.16	6.28	30	15.51	30.90
65	0.06	6.28	30	15.51	6.98
65	0.16	6.28	50	7.97	94.83
65	0.16	12.50	30	15.44	70.24
65	0.16	6.28	10	15.44	29.17
65	0.25	6.28	30	14.47	92.69
65	0.16	6.28	30	15.44	58.48
65	0.16	0.06	30	15.44	0.23
100	0.25	12.50	50	1.67	92.34
100	0.06	12.50	50	8.31	87.64
100	0.25	12.50	10	12.22	89.34
100	0.25	0.06	10	18.47	4.36
100	0.06	0.06	50	18.47	0.66
100	0.25	0.06	50	18.47	6.44
100	0.06	12.50	10	22.43	21.40
100	0.06	0.06	10	22.43	0.11
100	0.16	6.28	30	4.64	92.84
30	0.06	0.06	10	27.78	0.11
30	0.25	12.50	10	27.78	7.93
30	0.06	12.50	50	27.78	10.78
30	0.06	0.06	50	27.78	0.11
30	0.25	12.50	50	27.78	33.18
30	0.06	12.50	10	27.78	2.24
30	0.25	0.06	50	19.80	0.11
30	0.25	0.06	10	19.80	0.11
30	0.16	6.28	30	19.80	2.48

Statistic results.**Table 5. 5.** Estimated Coefficients for regression model I and corresponding statistical values like the square error, t-statistic and the p-value.

	Estimate	SE	tStat	pValue
(Intercept)	12.92	60.033	0.21522	0.83249
x ₁	-2933.4	21213	-0.13828	0.89186
x ₂	0.022821	0.11496	0.19851	0.84531
x ₃	0.4413	13.664	0.032296	0.97466
x ₄	-1.122	1.7074	-0.65712	0.52106
x ₁ :x ₂	-39.281	20.924	-1.8773	0.080063
x ₁ :x ₃	-2156.1	600.48	-3.5906	0.0026766
x ₁ :x ₄	-271.31	153.41	-1.7685	0.097296
x ₂ :x ₃	-0.00953	0.0092376	-1.0319	0.31847
x ₂ :x ₄	0.006024	0.0023601	2.5522	0.022102
x ₃ :x ₄	0.004032	0.06768	0.059569	0.95329
x ₁ ²	-3.72E+06	3.42E+06	-1.0872	0.29413
x ₂ ²	0.00137	0.00080019	1.712	0.10749
x ₃ ²	-0.41955	0.74968	-0.55964	0.58399
x ₄ ²	-0.19002	0.10492	-1.811	0.090208

Table 5. 6. Estimated Coefficients for regression model II and corresponding statistical values like the square error, t-statistic and the p-value .

	Estimate	SE	tStat	pValue
(Intercept)	57.28	14.22	4.0283	0.00078861
x1	-19523	4674	-4.177	0.00056646
x2	0.068951	0.014934	4.6171	0.00021405
x3	6.0532	1.6052	3.771	0.001399
x4	-2.6974	7.76E-01	-3.4744	0.002706
x1:x3	-1601.3	529.76	-3.0226	0.0073158
x2:x4	0.0057967	0.00217	2.6712	0.015574
x4 ²	-0.24092	0.054258	-4.4402	0.00031611

Table 5. 7. Estimated Coefficients for regression model III and corresponding statistical values like the square error, t-statistic and the p-value.

	Estimate	SE	tStat	pValue
(Intercept)	16.705	3.40E+00	4.9143	0.000112
x1	-4936.9	382.09	-12.921	1.52E-10
x2	0.040648	0.0061137	6.65E+00	3.07E-06
x3	1.3553	1.60E-01	8.48	1.06E-07
x4	-2.1133	0.82233	-2.57E+00	1.93E-02
x4^2	-0.21516	0.057568	-3.74E+00	0.001507

Table 5. 8. Estimated Coefficients for regression model IV and corresponding statistical values like the square error, t-statistic and the p-value.

	Estimate	SE	tStat	pValue
Intercept	31.554	4.0357	7.8187	3.39E-07
x ₁	39.307	7.5597	5.1995	6.04E-05
x ₂	0.035241	0.0092655	3.8035	0.0013012
x ₃	1.5982	0.27672	5.7755	1.79E-05
x ₄	1.0932	0.07059	15.487	7.54E-12
x ₆	-3.70E-05	8.84E-06	-4.19E+00	0.00055007

Prediction slice plots

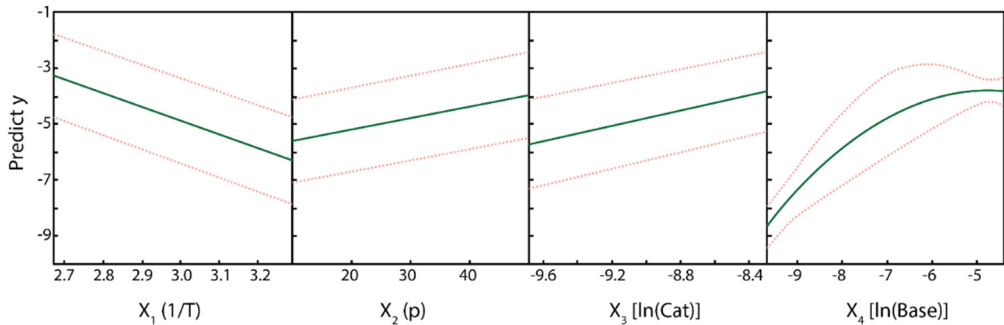


Figure 5. 8. Prediction slice plots made using the interaction terms eliminated regression model. The interactive plot was made using plotSlice mdl and shows the predicted response for each variable as each other variable is kept constant. 95% confidence bounds are also shown

5.10 References

1. (a) Delidovich, I.; Palkovits, R., Catalytic versus stoichiometric reagents as a key concept for Green Chemistry. *Green Chem.* **2016**, *18*, 590-593; (b) Van Leeuwen, P. W., *Homogeneous catalysis: understanding the art*. Springer Science & Business Media: 2006; (c) Mortreux, A.; Petit, F., *Industrial applications of homogeneous catalysis*. Springer Science & Business Media: 1987; Vol. 10.
2. (a) Maldonado, A. G.; Rothenberg, G., Predictive modeling in homogeneous catalysis: a tutorial. *Chem. Soc. Rev.* **2010**, *39*, 1891-1902; (b) Wulf, C.; Beller, M.; Boenisch, T.; Deutschmann, O.; Hanf, S.; Kockmann, N.; Kraehnert, R.; Oezaslan, M.; Palkovits, S.; Schimmler, S., A Unified Research Data Infrastructure for Catalysis Research—Challenges and Concepts. *ChemCatChem* **2021**.
3. Savara, A.; Walker, E. A., CheKiPEUQ Intro 1: Bayesian parameter estimation considering uncertainty or error from both experiments and theory. *ChemCatChem* **2020**, *12*, 5385-5400.
4. (a) Rylander, P. N., *Catalytic Hydrogenation in Organic Syntheses: Paul Rylander*. Academic Press: New York, 1979; (b) Vries, J. G. d., *The handbook of homogeneous hydrogenation*. Wiley-Vch: Weinheim, 2007; (c) Magano, J.; Dunetz, J. R., Large-scale carbonyl reductions in the pharmaceutical industry. *Org. Process Res. Dev.* **2012**, *16*, 1156-1184; (d) McQuillin, F. J., *Homogeneous hydrogenation in organic chemistry*. Springer Science & Business Media: 2012; Vol. 1; (e) Chaloner, P. A.; Esteruelas, M. A.; Joó, F.; Oro, L. A., *Homogeneous hydrogenation*. Springer Science & Business Media: 2013; Vol. 15; (f) Gunanathan, C.; Milstein, D., Applications of acceptorless dehydrogenation and related transformations in chemical synthesis. *Science* **2013**, *341*; (g) Pritchard, J.; Filonenko, G. A.; Van Putten, R.; Hensen, E. J.; Pidko, E. A., Heterogeneous and homogeneous catalysis for the hydrogenation of carboxylic acid derivatives: history, advances and future directions. *Chem. Soc. Rev.* **2015**, *44*, 3808-3833; (h) Dub, P. A.; Gordon, J. C., The role of the metal-bound N-H functionality in Noyori-type molecular catalysts. *Nat. Rev. Chem.* **2018**, *2*, 396-408; (i) Seo, C. S.; Morris, R. H., Catalytic Homogeneous Asymmetric Hydrogenation: Successes and Opportunities. *Organometallics* **2018**, *38*, 47-65.
5. Arai, N.; Ohkuma, T., Design of molecular catalysts for achievement of high turnover number in homogeneous hydrogenation. *Chem. Rec.* **2012**, *12*, 284-289.
6. (a) Chakraborty, S.; Bhattacharya, P.; Dai, H.; Guan, H., Nickel and iron pincer complexes as catalysts for the reduction of carbonyl compounds. *Acc. Chem. Res.* **2015**, *48*, 1995-2003; (b) Werkmeister, S.; Neumann, J.; Junge, K.; Beller, M., Pincer-Type Complexes for Catalytic (De) Hydrogenation and Transfer (De) Hydrogenation Reactions: Recent Progress. *Chem. Eur. J.* **2015**, *21*, 12226-12250; (c) Zell, T.; Milstein, D.,

Hydrogenation and dehydrogenation iron pincer catalysts capable of metal–ligand cooperation by aromatization/dearomatization. *Acc. Chem. Res.* **2015**, *48*, 1979-1994; (d) Garbe, M.; Junge, K.; Beller, M., Homogeneous catalysis by manganese-based pincer complexes. *Eur. J. Org. Chem.* **2017**, *2017*, 4344-4362; (e) Maji, B.; Barman, M. K., Recent developments of manganese complexes for catalytic hydrogenation and dehydrogenation reactions. *Synthesis* **2017**, *49*, 3377-3393; (f) Alig, L.; Fritz, M.; Schneider, S., First-row transition metal (de) hydrogenation catalysis based on functional pincer ligands. *Chem. Rev.* **2018**, *119*, 2681-2751; (g) Filonenko, G. A.; van Putten, R.; Hensen, E. J.; Pidko, E. A., Catalytic (de) hydrogenation promoted by non-precious metals–Co, Fe and Mn: recent advances in an emerging field. *Chem. Soc. Rev.* **2018**, *47*, 1459-1483; (h) Gorgas, N.; Kirchner, K., Isoelectronic manganese and iron hydrogenation/dehydrogenation catalysts: Similarities and divergences. *Acc. Chem. Res.* **2018**, *51*, 1558-1569; (i) Kallmeier, F.; Kempe, R., Manganese Complexes for (De) Hydrogenation Catalysis: A Comparison to Cobalt and Iron Catalysts. *Angew. Chem. Int. Ed.* **2018**, *57*, 46-60; (j) Clarke, M. L.; Widegren, M. B., Hydrogenation reactions using Group III to Group VII transition metals. *Homogeneous Hydrogenation with Non-Precious Catalysts* **2019**, 111-140; (k) Wang, Y.; Wang, M.; Li, Y.; Liu, Q., Homogeneous manganese-catalyzed hydrogenation and dehydrogenation reactions. *Chem* **2020**, *7*, 1180-1223; (l) Azouzi, K.; Valyaev, D. A.; Bastin, S.; Sortais, J.-B., Manganese—new prominent actor in transfer hydrogenation catalysis. *Curr. Opin. Green Sust.* **2021**, *31*, 100511.

7. (a) Liu, C.; Wang, M.; Liu, S.; Wang, Y.; Peng, Y.; Lan, Y.; Liu, Q., Manganese-Catalyzed Asymmetric Hydrogenation of Quinolines Enabled by π - π Interaction**. *Angew. Chem. Int. Ed.* **2021**, *60*, 5108-5113; (b) Papa, V.; Cao, Y.; Spannenberg, A.; Junge, K.; Beller, M., Development of a practical non-noble metal catalyst for hydrogenation of N-heteroarenes. *Nat. Catal.* **2020**, *3*, 135-142; (c) Zhang, L.; Tang, Y.; Han, Z.; Ding, K., Lutidine-Based Chiral Pincer Manganese Catalysts for Enantioselective Hydrogenation of Ketones. *Angew. Chem. Int. Ed.* **2019**, *58*, 4973-4977; (d) Weber, S.; Stöger, B.; Veiros, L. F.; Kirchner, K., Rethinking Basic Concepts—Hydrogenation of Alkenes Catalyzed by Bench-Stable Alkyl Mn (I) Complexes. *ACS Catal.* **2019**, *9*, 9715-9720; (e) Freitag, F.; Irrgang, T.; Kempe, R., Mechanistic Studies of Hydride Transfer to Imines from a Highly Active and Chemoselective Manganate Catalyst. *J. Am. Chem. Soc.* **2019**, *141*, 11677-11685; (f) Buhaibeh, R.; Filippov, O. A.; Bruneau-Voisine, A.; Willot, J.; Duhayon, C.; Valyaev, D. A.; Lukan, N.; Canac, Y.; Sortais, J.-B., Phosphine-NHC Manganese Hydrogenation Catalyst Exhibiting a Non-Classical Metal-Ligand Cooperative H₂ Activation Mode. *Angew. Chem. Int. Ed.* **2019**, *58*, 6727-6731; (g) Zou, Y.-Q.; Chakraborty, S.; Nerush, A.; Oren, D.; Diskin-Posner, Y.; Ben-David, Y.; Milstein, D., Highly Selective, Efficient Deoxygenative Hydrogenation of Amides Catalyzed by a Manganese Pincer Complex via Metal–Ligand Cooperation. *ACS Catal.* **2018**, *8*, 8014-8019; (h) Wei, D.; Bruneau-Voisine, A.; Chauvin, T.; Dorcet, V.; Roisnel, T.; Valyaev, D. A.; Lukan, N.; Sortais, J. B., Hydrogenation of Carbonyl Derivatives Catalysed by

Manganese Complexes Bearing Bidentate Pyridinyl-Phosphine Ligands. *Adv. Synth. Catal.* **2018**, *360*, 676-681; (i) Kumar, A.; Janes, T.; Espinosa-Jalapa, N. A.; Milstein, D., Manganese Catalyzed Hydrogenation of Organic Carbonates to Methanol and Alcohols. *Angew. Chem. Int. Ed.* **2018**, *57*, 12076-12080; (j) Kaithal, A.; Hölscher, M.; Leitner, W., Catalytic Hydrogenation of Cyclic Carbonates using Manganese Complexes. *Angew. Chem. Int. Ed.* **2018**, *57*, 13449-13453; (k) Glatz, M.; Stöger, B.; Himmelbauer, D.; Veiros, L. F.; Kirchner, K., Chemoselective Hydrogenation of Aldehydes under Mild, Base-Free Conditions: Manganese Outperforms Rhenium. *ACS Catal.* **2018**, *8*, 4009-4016; (l) Garduño, J. A.; García, J. J., Non-Pincer Mn (I) Organometallics for the Selective Catalytic Hydrogenation of Nitriles to Primary Amines. *ACS Catal.* **2018**, *9*, 392-401; (m) Widegren, M. B.; Harkness, G. J.; Slawin, A. M.; Cordes, D. B.; Clarke, M. L., A highly active manganese catalyst for enantioselective ketone and ester hydrogenation. *Angew. Chem. Int. Ed.* **2017**, *56*, 5825-5828; (n) Papa, V.; Cabrero-Antonino, J. R.; Alberico, E.; Spanneberg, A.; Junge, K.; Junge, H.; Beller, M., Efficient and selective hydrogenation of amides to alcohols and amines using a well-defined manganese-PNN pincer complex. *Chem. Sci.* **2017**, *8*, 3576-3585; (o) Nguyen, D. H.; Trivelli, X.; Capet, F. d. r.; Paul, J.-F. o.; Dumeignil, F.; Gauvin, R. g. M., Manganese pincer complexes for the base-free, acceptorless dehydrogenative coupling of alcohols to esters: development, scope, and understanding. *ACS Catal.* **2017**, *7*, 2022-2032; (p) Garbe, M.; Junge, K.; Walker, S.; Wei, Z.; Jiao, H.; Spanneberg, A.; Bachmann, S.; Scalone, M.; Beller, M., Manganese (I)-Catalyzed Enantioselective Hydrogenation of Ketones Using a Defined Chiral PNP Pincer Ligand. *Angew. Chem. Int. Ed.* **2017**, *56*, 11237-11241; (q) Deibl, N.; Kempe, R., Manganese-Catalyzed Multicomponent Synthesis of Pyrimidines from Alcohols and Amidines. *Angew. Chem. Int. Ed.* **2017**, *56*, 1663-1666; (r) Mukherjee, A.; Nerush, A.; Leitus, G.; Shimon, L. J.; Ben David, Y.; Espinosa Jalapa, N. A.; Milstein, D., Manganese-catalyzed environmentally benign dehydrogenative coupling of alcohols and amines to form aldimines and H₂: a catalytic and mechanistic study. *J. Am. Chem. Soc.* **2016**, *138*, 4298-4301; (s) Mastalir, M.; Glatz, M.; Pittenauer, E.; Allmaier, G. n.; Kirchner, K., Sustainable synthesis of quinolines and pyrimidines catalyzed by manganese PNP pincer complexes. *J. Am. Chem. Soc.* **2016**, *138*, 15543-15546; (t) Elangovan, S.; Topf, C.; Fischer, S.; Jiao, H.; Spanneberg, A.; Baumann, W.; Ludwig, R.; Junge, K.; Beller, M., Selective catalytic hydrogenations of nitriles, ketones, and aldehydes by well-defined manganese pincer complexes. *J. Am. Chem. Soc.* **2016**, *138*, 8809-8814; (u) Elangovan, S.; Garbe, M.; Jiao, H.; Spanneberg, A.; Junge, K.; Beller, M., Hydrogenation of Esters to Alcohols Catalyzed by Defined Manganese Pincer Complexes. *Angew. Chem. Int. Ed.* **2016**, *49*, 15364-15368.

8. Langer, R.; Leitus, G.; Ben-David, Y.; Milstein, D., Efficient hydrogenation of ketones catalyzed by an iron pincer complex. *Angew. Chem. Int. Ed.* **2011**, *50*, 2120-2124.

9. Rösler, S.; Obenauf, J.; Kempe, R., A Highly Active and Easily Accessible Cobalt Catalyst for Selective Hydrogenation of C=O Bonds. *J. Am. Chem. Soc.* **2015**, *137*, 7998-8001.
10. Kallmeier, F.; Irrgang, T.; Dietel, T.; Kempe, R., Highly active and selective manganese C=O bond hydrogenation catalysts: the importance of the multidentate ligand, the ancillary ligands, and the oxidation state. *Angew. Chem. Int. Ed.* **2016**, *55*, 11806-11809.
11. Werkmeister, S.; Junge, K.; Wendt, B.; Alberico, E.; Jiao, H.; Baumann, W.; Junge, H.; Gallou, F.; Beller, M., Hydrogenation of esters to alcohols with a well-defined iron complex. *Angew. Chem. Int. Ed.* **2014**, *53*, 8722-8726.
12. Zhang, G.; Scott, B. L.; Hanson, S. K., Mild and homogeneous cobalt-catalyzed hydrogenation of C=C, C=O, and C=N bonds. *Angew. Chem.* **2012**, *124*, 12268-12272.
13. Van Putten, R.; Uslamin, E. A.; Garbe, M.; Liu, C.; Gonzalez-de-Castro, A.; Lutz, M.; Junge, K.; Hensen, E. J.; Beller, M.; Lefort, L., Non-Pincer-Type Manganese Complexes as Efficient Catalysts for the Hydrogenation of Esters. *Angew. Chem. Int. Ed.* **2017**, *56*, 7531-7534.
14. Bruneau-Voisine, A.; Wang, D.; Dorcet, V.; Roisnel, T.; Darcel, C.; Sortais, J.-B., Transfer hydrogenation of carbonyl derivatives catalyzed by an inexpensive phosphine-free manganese precatalyst. *Org. Lett.* **2017**, *19*, 3656-3659.
15. Putten, R. v.; Benschop, J.; Munck, V. J. d.; Weber, M.; Müller, C.; Filonenko, G. A.; Pidko, E. A., Efficient and Practical Transfer Hydrogenation of Ketones Catalyzed by a Simple Bidentate Mn–NHC Complex. *ChemCatChem* **2019**, *11*, 1-5.
16. (a) Villadsen, J., Recent Advances in the Engineering Analysis of Chemically Reacting Systems.: Edited by LK Doraiswamy. Wiley Eastern, New Delhi, 1984, 611 pp. Pergamon: 1987; (b) Smith, J. M., *Chemical engineering kinetics*. 1981; (c) James, B. R., *Homogeneous hydrogenation*. Wiley: 1973.
17. Chaudhari, R.; Seayad, A.; Jayasree, S., Kinetic modeling of homogeneous catalytic processes. *Catal. Today* **2001**, *66*, 371-380.
18. Box, G. E.; Wilson, K. B., On the experimental attainment of optimum conditions. *Journal of the royal statistical society: Series b (Methodological)* **1951**, *13*, 1-38.
19. Yang, W.; Chernyshov, I. Y.; van Schendel, R. K.; Weber, M.; Müller, C.; Filonenko, G. A.; Pidko, E. A., Robust and efficient hydrogenation of carbonyl compounds catalysed by mixed donor Mn (I) pincer complexes. *Nat. Commun.* **2021**, *12*, 1-8.

20. Sibanda, W.; Pretorius, P., Comparative study of the application of central composite face-centred (CCF) and Box–Behnken designs (BBD) to study the effect of demographic characteristics on HIV risk in South Africa. *Netw. Model. Anal. Health Inform. Bioinform.* **2013**, *2*, 137-146.
21. Karl HRardle, W.; Simar, L., Applied multivariate statistical analysis. Springer-Verlag Berlin Heidelberg: 2015.
22. Korkmaz, M., A study over the general formula of regression sum of squares in multiple linear regression. *Numerical Methods for Partial Differential Equations* **2021**, *37*, 406-421.
23. St, L.; Wold, S., Analysis of variance (ANOVA). *Chemometrics and intelligent laboratory systems* **1989**, *6*, 259-272.
24. Fayazbakhsh, K.; Abedian, A.; Manshadi, B. D.; Khabbaz, R. S., Introducing a novel method for materials selection in mechanical design using Z-transformation in statistics for normalization of material properties. *Materials & Design* **2009**, *30*, 4396-4404.
25. Kampenes, V. B.; Dybå, T.; Hannay, J. E.; Sjøberg, D. I., A systematic review of effect size in software engineering experiments. *Inf. Softw. Technol.* **2007**, *49*, 1073-1086.
26. Holland, P. W.; Welsch, R. E., Robust regression using iteratively reweighted least-squares. *Communications in Statistics-theory and Methods* **1977**, *6*, 813-827.
27. Beaton, A. E.; Tukey, J. W., The fitting of power series, meaning polynomials, illustrated on band-spectroscopic data. *Technometrics* **1974**, *16*, 147-185.
28. Spiess, A.-N.; Neumeyer, N., An evaluation of R² as an inadequate measure for nonlinear models in pharmacological and biochemical research: a Monte Carlo approach. *BMC pharmacology* **2010**, *10*, 1-11.
29. Watts, D. G., Estimating parameters in nonlinear rate equations. *Can. J. Chem. Eng.* **1994**, *72*, 701-710.

Appendix

A.1 Geometry generations and stability calculations of chapter 3

MACE Protocol

The workflow starts with reading the ChemAxon¹ SMILES string of the octahedral complex and then generates all possible configurations of the system, considering both the stereochemistry of the octahedral center and the ligands. The next step is the filtration of the identical configurations, enantiomers, and impossible structures. For the selected stereoisomers 3D coordinates are generated using the distance geometry approach followed by an MM relaxation. For each configuration of the given complex a number of conformers are generated with the following pruning of similar conformers using a 0.5 RMSD threshold. MACE algorithm produced several distinct coordination geometries at the Mn center .

The resulting configurations were further fully relaxed following by frequency calculations using Gaussian 16 revision C01 program package. Some of the starting configurations were converged upon the geometry optimization to identical isomers as confirmed by negligible RMSD and identical spectroscopic characteristics for the respective optimized structures. To confirm the exhaustive nature of the configurational search by MACE, additional configurations were manually constructed based on the optimized geometries, which all converged to the structures identified by the automated algorithm.

Stability calculations

The MACE protocol automatically constructs all allowed configurations for the hypothetical 6-coordinated Mn-CN(CO)₃H and Mn-CP(CO)₃H complexes without using any *a priori* information. Relative stabilities of complexes were calculated as energies normalized to the most stable configuration (**Table A. 1**). Conformational entropies were calculated using two approaches. Firstly, the MACE protocol was used to generate 200 conformations for the most stable C,N- and C,P-bi-bound Mn hydride complexes. The set of unique conformers was obtained based on the values of dihedral

angles of all rotatable bonds. After DFT computations, obtained free energies were used to find conformational entropy S_{conf} using the formula:

$$S_{conf} = -R \cdot \sum p_i \cdot \ln p_i,$$

where p_i is the probability of a complex being in i^{th} conformation, which was found from the Boltzmann distribution. Secondly, the CREST software² was used. Several tests showed that semi-empirical GFN2-xTB and molecular mechanical GFN-FF levels of theory poorly reproduce the geometry of the studied complexes. To partially solve this problem, several modifications were applied to the GFN-FF force field for both C,N- and C,P- complexes. The resulting conformational entropy was found as an interval of obtained values (**Table A. 1**). Computed system MnCNmeP_biN_3 (conf5) and MnCNmeP_biP_1 were found to be the most stable configurations for Mn tricarbonyl hydride species with dissociated P donor and dissociated N donor respectively. Therefore they are used to assess the preference of donor dissociation during the activation of complex **Mn-7** and assign the structures of hydride species **8** and **9** in chapter 3.

A.2 Computational studies of chapter 4

All quantum chemical calculations were performed using Gaussian16 software.³ Geometries, relative stabilities and IR spectra were calculated at PBE0-D3/6-311+G(d,p) level of theory with a continuous description of the THF solvent using the SMD model.⁴ The calculated IR frequencies were scaled with the factor $f = 0.9576$, which was chosen for best agreement of experimental and calculated data. It is applied to minimize the error of the harmonic approach for the vibration frequency calculation. The Half width of the plotted calculated spectra is 5 cm^{-1} . Time-dependent DFT calculations at the same level of theory (60 excitations) were carried out to simulate UV-vis spectra of selected complexes.

Table A. 1. Relative electronic and free energies of representative bidentate stereoisomers of Mn hydride complexes.

Free donor group	System ^a	Geometry	Relative energy ^b kJ·mol ⁻¹		Conformational entropy -TΔS _{conf}	
			ΔE	ΔG	Q M	CREST
Free P	MnCNmeP_biN_0	N-Mn-H anti	51.0	38.8		
	MnCNmeP_biN_1	NMe/MnH syn	45.2	33.6		
	MnCNmeP_biN_2	C-Mn-H anti	45.8	29.7		
	MnCNmeP_biN_3 (conf5)	NMe/MnH anti	20.3	8.8	1. 2	[-9.4 ... - 13.6]
Free N	MnCNmeP_biP_0	C-Mn-H anti	20.6	18.1		
	MnCNmeP_biP_1	CO-Mn-H anti	0.0	0.0	1. 7	[-12.7 ... - 19.2]
	MnCNmeP_biP_2	P-Mn-H anti	11.5	7.8		
	MnCNmeP_biP_3	P-Mn-C anti	37.7	34.4		

^a) Names of metal complexes correspond to the names in the comment line of XYZ-files. ^b) QM energies normalized to the the most stable configuration.

MACE protocol

The MACE protocol automatically constructs all allowed configurations for the hypothetical 5-coordinated complexes without using any *a priori* information. The workflow starts with reading the ChemAxon¹ SMILES string of the octahedral complex and then generates all possible configurations of the system, considering both the stereochemistry of the octahedral center and the ligands. The next step is the filtration of the identical configurations, enantiomers, and impossible structures. For the selected stereoisomers 3D coordinates are generated using the distance geometry approach followed

by an MM relaxation. For each configuration of the given complex 50 conformers are generated with the following pruning of similar conformers using a 0.5 RMSD threshold. MACE algorithm produced 4 distinct coordination geometries at the Mn center (2 *facial* and 2 *meridional*) and for each coordination environment 5 isomers with different conformations of the ligand backbone and, accordingly, relative conformation of the imidazole and amino-ligand moieties giving it total 20 distinct configurations.

The resulting configurations were further fully relaxed following by frequency calculations using Gaussian 16 revision C01 program package. Some of the starting configurations were converged upon the geometry optimization to identical isomers as confirmed by negligible RMSD and identical spectroscopic characteristics for the respective optimized structures. To confirm the exhaustive nature of the configurational search by MACE, additional configurations were manually constructed based on the optimized geometries, which all converged to the structures identified by the automated algorithm.

Structural assignments of species 5b (chapter 4)

We initially assume that the species **5a** and **5b** are isomers of the deprotonated Mn-CNC complexes. A conformational screening was thus performed by the in-house MACE workflow followed by DFT calculations at the PBE1PBE-D3/6-311+G(d,p)/SMD(THF) level of theory. The distinct configurations along with their relative stabilities (in terms of ZPE-corrected energies (ΔE_{ZPE}) and Gibbs free energies ($\Delta G^{\circ}_{298\text{K},\text{SMD(THF)}}$) as well as the computed harmonic frequencies for the symmetric and asymmetric stretching vibration of the carbonyl moieties (scaling factor 0.9516 was uniformly applied) are summarized in **Figure A. 1** and **Figure A. 2** for the *facial* and *meridional* Mn(CO)₂CNC complexes, respectively. Both (distorted) trigonal bipyramidal and square pyramidal configurations of the Mn center were identified.

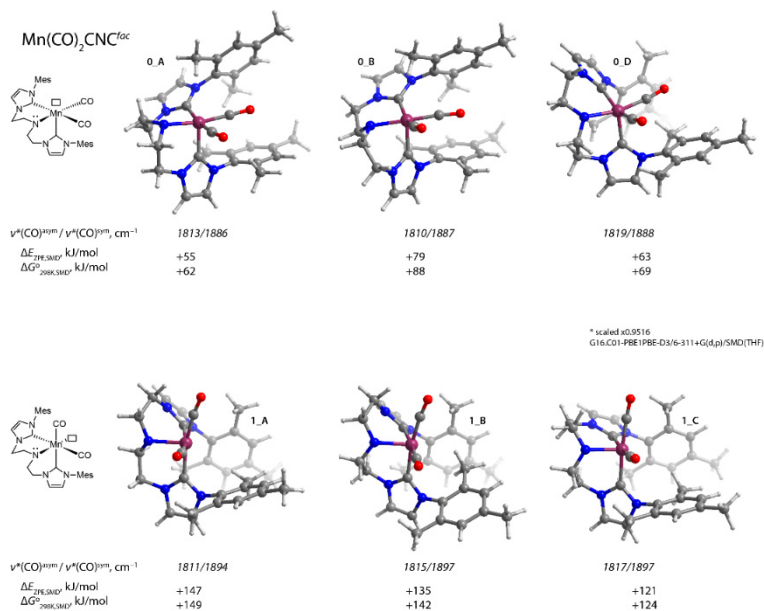


Figure A. 1. DFT-calculated structures, CO ligand vibration frequencies and relative stabilities for fac isomers of deprotonated Mn(CO)₂CNC.

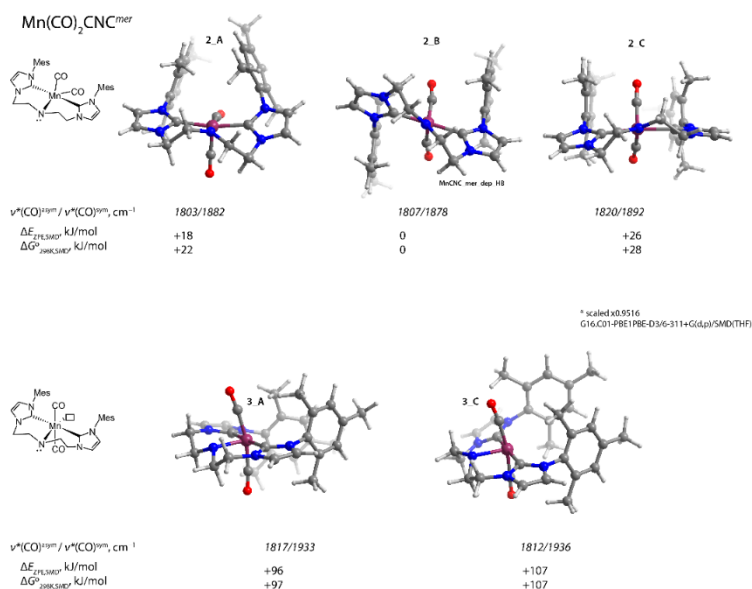


Figure A. 2. DFT-calculated structures, CO ligand vibration frequencies and relative stabilities for mer isomers of deprotonated Mn(CO)₂CNC. Conformer **2_B** is assigned to complex **5a** based on the agreements of ligand configurations (see Figure 4.3 in Chapter 4) and $\nu(\text{CO})$ (**Figure A. 4**).

The results show a strong preference for the formation of the *mer*-configuration for Mn(CO)₂CNC complexes with higher stabilities. Complex **2_B**, being the most stable conformer, with fully symmetric anti configuration of the ligand backbone is assigned to **5a** based on the agreements of configurations (see XRD details) and $\nu(\text{CO})$. However, none of the conformers considered herein exhibited the red-shifted $\nu(\text{CO})$ observed for **5b** in the experiment.

We then hypothesized that **5b** could be a metastable product of the KOR alkoxide base interaction with complex deprotonated Mn(CO)₂CNC. Therefore, the influence of the interaction with the alkoxide base on the vibrational characteristics of Mn(CO)₂CNC were further analysed by considering a variety of coordination modes of a model KOMe alkoxide base with different (meta)stable conformers of Mn(CO)₂CNC. The direct coordination of K with the N of the deprotonated ligand as well as the stabilization of the resulting cationic complex by the methoxide anion in the second coordination sphere of Mn were considered. The most stable configurations, their relative stabilities and computed $\nu(\text{CO})$ frequencies are summarized in **Figure A. 3**. Indeed, the deprotonation of reaction of **2⁺** and **3⁺** with excess alkoxide base can transiently produce either pure *fac*-configuration (**Figure A. 1**) or a distorted meridional (**Figure A. 2**) Mn(CO)₂CNC featuring basic tetrahedral N center of the amido group, which could potentially coordinate K⁺ species to the N center with the simultaneous coordination of the OR⁻ moiety to Mn. Such coordination is not allowed for the most stable fully symmetric trigonal bipyramidal complex **2_B** (also assigned to **5a**, see **Figure A. 2**), confirmed by the nearly identical $\nu(\text{CO})$ of its adduct complex **KOMe...5^{2-B}** to those of the parent complex **5a**. The other coordination modes considered resulted in a successful coordination of the KOMe moiety across the Mn-N bond resulting in slightly less thermodynamically stable adducts **KOMe...5^{0-A}**, **KOMe...5^{0-D}** and **KOMe...5^{2-A}**, among which the interconversion is expected to be kinetically hampered in the absence of proton donors or H₂ molecule, which could facilitate the pseudo-rotation of the N center of the backbone, giving rise to the substantial metastability of these configurations. These KOMe adducts of deprotonated Mn(CO)₂CNC are the only Mn carbonyl complexes considered here featuring the red-shifted $\nu(\text{CO})$, suggesting they are **5b** observed in the experiment. This

assignment is further supported by the higher apparent yield of these species upon the deprotonation of the facially-coordinated complex **2** than in the case of mer-complex **3**.

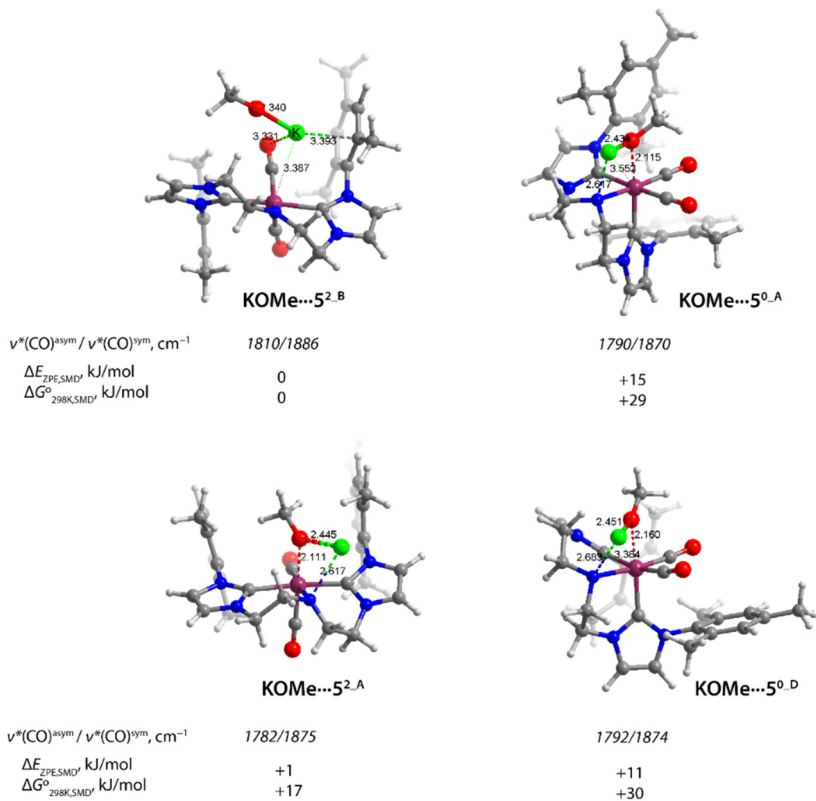


Figure A. 3. Relative stabilities and computed IR frequencies in the carbonyl region of KOMe adducts with $\text{Mn}(\text{CO})_2\text{CNC}$.

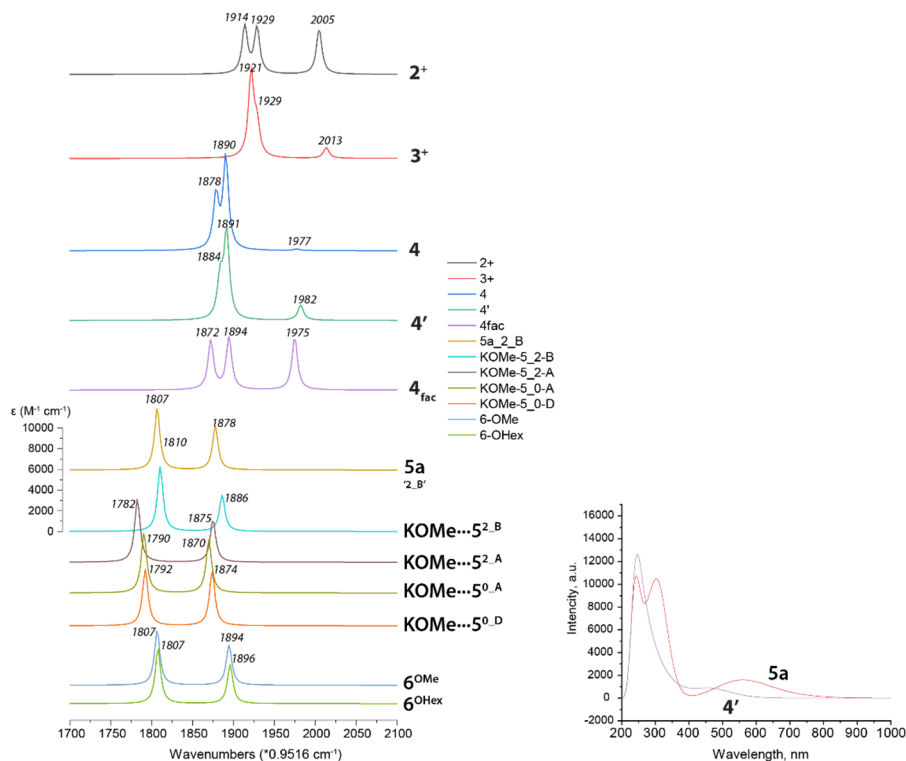


Figure A. 4 Summary of calculated FTIR spectra in CO stretching region for various MnCNC carbonyl complexes (left) and the DFT computed UV-vis spectra for complexes 4' and 5a.

COSMO-RS calculations of condition-dependent reaction free energies

COSMO-RS⁵ protocol

Methodology and terms: This is a hybrid statistical solvation model which is used to calculate the chemical potentials of molecular liquids of any composition. It describes intermolecular interactions as interaction of molecular surfaces based on COSMO polarization charge densities. A key part of the method is an empirical formula for the interaction energy between two surface segments, which considers electrostatic interactions, hydrogen bonding, and dispersion. Combination of this formula and the statistical thermodynamics gives a possibility to calculate condition-dependent chemical potentials in a few seconds and thus to easily model condition-dependent free energies of liquid-phase chemical processes.

The algorithm for calculating the condition-dependent free energy based on DFT computations consists of five steps:

1. Compute free energy of the considered molecule at DFT level of theory with any implicit solvation model (PCM, COSMO, SMD, CPCM), ΔG_{solv}^{QM} .
2. Compute free energy of the considered molecule at DFT level of theory in a gas phase, ΔG_{gas}^{QM} .
3. Optimize the geometry of all particles forming the solution (frequency computations are not required).
4. For the optimized geometries calculate COSMO-files (one SCF cycle with solvent described using the COSMO model). Obtained COSMO-files contain all information about surface segments that are required for COSMO-RS calculations.
5. Compute COSMO-RS free energy of solvation, $\Delta G_{solv}^{COSMO-RS}$, for the required solution composition which is given by COSMO-files and the corresponding mole fractions.
6. Compute resulting condition-dependent free energy of the considered molecule as:

$$\Delta G = \Delta G_{solv}^{QM} - \Delta G_{gas}^{QM} + \Delta G_{solv}^{COSMO-RS}.$$

Calculations: Gas-phase single-point energies which are necessary to get the SMD solvation energies were calculated with Gaussian16 at the PBE1PBE-D3/6-311+G(d,p) level of theory. COSMO files were generated for the optimized geometries with the Turbomole suite⁶ using standard BP_TZVP parametrization. Free energies of solvation were computed in the COSMOtherm package⁷ using BP_TZVP parametrization in the molar frame. It should be noted that when calculating $\Delta G_{solv}^{COSMO-RS}$, the COSMO-RS solvation energy of reagents and products was obtained for solutions corresponding to 0% and 100% conversion, into amide or alkoxide complexes respectively. Three experimental conditions were considered, including pure THF (#1) and two KO^tBu/THF solutions (#2 and 3) (**Table A. 2**). Due to the statistical nature of the method, it is more reliable to

represent KO^tBu as two separate ions instead of an ion pair so that the individual solvation effects can be taken into account. Using predefined ion pairs, tetramers etc would place limitations on the calculation that COSMO-RS is specifically designed to avert.

Table A. 2. Composition of model solutions employed to analyze condition-dependencies of Mn-alkoxide formations represented by molar fractions of all compounds in THF as the primary solvent; identical to those used in UV-Vis study.

Solution	Conversion	Mn(CO) ₂ CNC	ROH	MnOR(CO) ₂ CN ^H C	K ⁺	^t BuO ⁻	THF
#1	0%	0.000046	0.0045 00	0	0	0	0.9954 54
	100%	0	0.0044 54	0.000046	0	0	0.9955 00
#2	0%	0.000045	0.0089 19	0	0.0022 38	0.0022 38	0.9865 60
	100%	0	0.0088 74	0.000045	0.0022 38	0.0022 38	0.9866 05
#3	0%	0.000045	0.0088 79	0	0.0044 56	0.0044 56	0.9821 64
	100%	0	0.0088 74	0.000045	0.0044 56	0.0044 56	0.9866 05

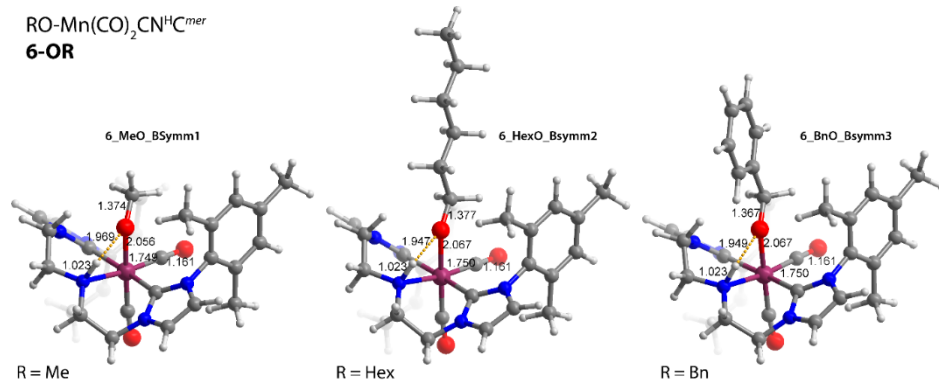


Figure A. 5. The most stable conformers of Mn(CO)₂CNC alkoxide adducts (MnOR(CO)₂CNHC) with (a) methanol, (b) hexanol, and (c) benzyl alcohol.

Table A. 3. Results of conformational analysis - the relative free energy ($\text{kJ}\cdot\text{mol}^{-1}$) of Mn alkoxide conformers.^a

Alcohol	Conformer	$\Delta G^{\text{SMD a)}$	$\Delta G^{\text{s1 b)}$	$\Delta G^{\text{s2 b)}$	$\Delta G^{\text{s3 b)}$
MeOH	Bsymm1	0.0	0.0	0.0	0.0
	A5	10.8	17.4	17.8	17.9
	A1	14.2	22.7	23.0	23.0
	A3	33.6	42.0	43.5	43.9
HexOH	Bsymm2	0.0	0.0	0.0	0.0
	Bsymm1	3.5	4.2	4.2	4.2
	A2	9.9	15.1	15.3	15.3
	A5	11.0	15.2	15.2	15.2
	Bsymm3	15.4	14.3	14.3	14.3
	A1	17.6	24.5	24.6	24.6
	A4	20.1	21.0	21.5	21.6
	A3	21.1	22.2	22.2	22.2
BnOH	Bsymm3	0.0	0.0	0.0	0.0
	Bsymm2	0.0	0.0	0.0	0.0
	A3	30.1	27.1	27.2	27.2
	A4	30.8	38.2	38.2	38.2

a) ΔG^{SMD} is a free energy for the ideal THF solution, obtained with the SMD solvation model. b) ΔG^{s1} , ΔG^{s2} , and ΔG^{s3} are free energies for the real solutions #1-3 (**Table S13**), obtained with the COSMO-RS solvation model. All values are relative to that of the most stable conformer which is taken as zero.

Additional calculations on alcohol binding to **5a** were performed to confirm the effect of base promotion on the free energies of the reaction between complex **5a** (most stable isomer **2_B** as identified earlier, **Figure A. 2**) and several alcohols, namely methanol, hexanol, and benzyl alcohol. For each manganese alkoxide ($\text{MnOR}(\text{CO})_2\text{CN}^{\text{H}}\text{C}$), several conformers were generated and their relative stability was analyzed with SMD and COSMO-RS free energies. Optimized structures for most stable conformations are shown in **Figure A. 5**. The relative stability for all optimized structures was analyzed with SMD

and COSMO-RS free energies (**Table A. 3**). The relative stabilities of low-energy conformers are similar for both solvation models, and some differences appear from the 15 kJ/mol cut-off. Thermodynamic parameters of the reaction were calculated for these most stable conformers of the initial and final manganese complexes (**Table A. 4**). The substantial mismatch between the experimental and calculated thermodynamic parameters for the methoxide is attributed by a systematic error in the theoretical solvation energies for short-chain alcohols. For example, earlier studies reported two-fold higher errors in predicted energy of solvation of ethanol compared to butanol with the SMD and COSMO-RS models.⁸ This is due to the imperfect description of hydrogen bonding interactions, of which the importance increases with decreasing alcohol size and increasing solute hydrophilicity¹⁰, which is the case for the polar manganese alkoxide.

Specifically, the COSMO-RS analysis was performed for reaction " $\mathbf{r1} + \mathbf{r2} = \mathbf{p}$ " where $\mathbf{r1}$ and $\mathbf{r2}$ are reagents and \mathbf{p} is an Mn alkoxide product. We find that alcohol reagent ($\mathbf{r2}$) is largely affected by varying base concentrations. Both enthalpy and entropy for $\mathbf{r2}$ change significantly, while these changes for Mn complexes ($\mathbf{r1}$ and \mathbf{p}) are negligible. The data for the whole reaction and individual reagents and products shown below in **Table A. 4**:

Table A. 4. Impact of COSMO-RS solvation to theoretical thermodynamic parameters of Mn alkoxide formation.^a

Alcohol	MeOH			HexOH			BnOH		
Solution	#1	#2	#3	#1	#2	#3	#1	#2	#3
Overall reaction: $r1 + r2 = p$									
ΔG	-0.2	4.2	6.9	4.0	8.3	10.7	-12.0	-7.5	-4.6
ΔH	-32.9	-15.5	-3.8	-29.1	-12.0	-1.1	-45.4	-28.5	-15.3
ΔS	-113	-68	-37	-	-70.1	-41.0	-	-72.6	-36.9
				114.5			115.4		
Solvation contributions for overall reaction and individual components: Mn amide (r1), alcohol (r2) and Mn alkoxide (p)									
ΔG_{solv}	9.2	13.6	16.2	16.0	20.3	22.7	21.2	25.7	28.6
$G_{\text{solv}}(r1)$	-	-	-	-	-	-	-	-	-
	102.7	102.5	102.3	102.6	102.4	102.2	102.6	102.4	102.2
$G_{\text{solv}}(r2)$	-19.3	-23.8	-26.4	-33.0	-37.2	-39.6	-41.2	-45.6	-48.5
$G_{\text{solv}}(p)$	-	-	-	-	-	-	-	-	-
	112.8	112.6	112.5	119.6	119.3	119.1	122.6	122.3	122.2
ΔH_{solv}	35.3	52.7	64.3	45.0	62.0	72.9	52.2	69.0	82.3
$H_{\text{solv}}(r1)$	-	-	-	-	-	-	-	-	-
	143.7	143.3	143.2	143.6	143.2	143.1	143.6	143.2	143.0
$H_{\text{solv}}(r2)$	-48.7	-66.0	-77.6	-68.6	-85.6	-96.4	-78.7	-95.5	-
									108.6
$H_{\text{solv}}(p)$	-	-	-	-	-	-	-	-	-
	157.0	156.6	156.5	167.3	166.8	166.6	170.1	169.6	169.4
ΔS_{solv}	87.7	131.2	161.3	97.0	140.1	168.4	104.0	145.6	180.2
$S_{\text{solv}}(r1)$	-	-	-	-	-	-	-	-	-
	137.6	136.9	137.0	137.7	137.1	137.2	137.6	136.9	137.0
$S_{\text{solv}}(r2)$	-98.4	-	-	-	-	-	-	-	-
		141.8	171.9	119.5	162.5	190.6	125.9	167.3	201.8
$S_{\text{solv}}(p)$	-	-	-	-	-	-	-	-	-
	148.3	147.5	147.5	160.1	159.4	159.4	159.5	158.6	158.6

Free energies and enthalpies are given in $\text{kJ}\cdot\text{mol}^{-1}$, and entropies in $\text{J}\cdot\text{mol}^{-1}\cdot\text{K}^{-1}$. (r1), (r2), and (p) indexes correspond to $\text{Mn}(\text{CO})_2\text{CNC}$, alcohol, and manganese alkoxide complex.

ΔG , ΔH , and ΔS are the total thermodynamic parameters of the reaction obtained by a combination of DFT and COSMO-RS, and other quantities with the "solv" subscript are the thermodynamic parameters of solvation obtained with the COSMO-RS model. Bold text indicates the solvation parameters which significantly depend on the solution composition.

A.3 References

1. <http://www.chemaxon.com/>
2. Pracht, P., Bohle, F., Grimme S. Automated exploration of the low-energy chemical space with fast quantum chemical methods *Phys. Chem. Chem. Phys.*, 2020, 22, 7169-7192
3. Frisch, M. J.; Trucks, G. W.; Schlegel, H. B.; Scuseria, G. E.; Robb, M. A.; Cheeseman, J. R.; Scalmani, G.; Barone, V.; Petersson, G. A.; Nakatsuji, H.; Li, X.; Caricato, M.; Marenich, A. V.; Bloino, J.; Janesko, B. G.; Gomperts, R.; Mennucci, B.; Hratchian, H. P.; Ortiz, J. V.; Izmaylov, A. F.; Sonnenberg, J. L.; Williams-Young, D.; Ding, F.; Lipparini, F.; Egidi, F.; Goings, J.; Peng, B.; Petrone, A.; Henderson, T.; Ranasinghe, D.; Zakrzewski, V. G.; Gao, J.; Rega, N.; Zheng, G.; Liang, W.; Hada, M.; Ehara, M.; Toyota, K.; Fukuda, R.; Hasegawa, J.; Ishida, M.; Nakajima, T.; Honda, Y.; Kitao, O.; Nakai, H.; Vreven, T.; Throssell, K.; Montgomery Jr., J. A.; Peralta, J. E.; Ogliaro, F.; Bearpark, M. J.; Heyd, J. J.; Brothers, E. N.; Kudin, K. N.; Staroverov, V. N.; Keith, T. A.; Kobayashi, R.; Normand, J.; Raghavachari, K.; Rendell, A. P.; Burant, J. C.; Iyengar, S. S.; Tomasi, J.; Cossi, M.; Millam, J. M.; Klene, M.; Adamo, C.; Cammi, R.; Ochterski, J. W.; Martin, R. L.; Morokuma, K.; Farkas, O.; Foresman, J. B.; Fox, D. J. Gaussian16 Revision C.01. 2016.
4. Marenich, A. V.; Cramer, C. J.; Truhlar, D. G., Universal solvation model based on solute electron density and on a continuum model of the solvent defined by the bulk dielectric constant and atomic surface tensions. *The Journal of Physical Chemistry B* **2009**, 113, 6378-6396.
5. (a) Freire, M. G.; Ventura, S. P.; Santos, L. M.; Marrucho, I. M.; Coutinho, J. A., Evaluation of COSMO-RS for the prediction of LLE and VLE of water and ionic liquids binary systems. *Fluid Phase Equilib.* **2008**, 268, 74-84; (b) Marenich, A. V.; Cramer, C. J.; Truhlar, D. G., Universal solvation model based on solute electron density and on a continuum model of the solvent defined by the bulk dielectric constant and atomic surface tensions. *J. Phys. Chem. B* **2009**, 113, 6378-6396.
6. TURBOMOLE V7.3 2018, a development of University of Karlsruhe and Forschungszentrum Karlsruhe GmbH, 1989-2007, TURBOMOLE GmbH, since 2007; available from <http://www.turbomole.com/>
7. COSMOtherm, Version C3.0, Release 17.01; COSMOlogic GmbH & Co. KG, <http://www.cosmologic.de/>
8. Marenich, A. V.; Cramer, C. J.; Truhlar, D. G., Universal solvation model based on solute electron density and on a continuum model of the solvent defined by the bulk

dielectric constant and atomic surface tensions. *The Journal of Physical Chemistry B* **2009**, *113*, 6378-6396.

Summary

The growing demands for sustainable chemical technologies have prompted a wave of searching new catalysts based on earth-abundant metals. In the field of (de)hydrogenation catalysis, however, the huge performance gap is commonly seen between the 3d-metal-based catalysts and their noble metal counterparts, which largely hamper their practical applications. In particular, while the Mn-catalyzed (de)hydrogenation has witnessed significant progress since the pioneering work by Beller and co-workers in 2016, most of the reported systems still require relatively high catalyst loadings. Apart from developing new synthetic methodologies based on the hydrogen transfer reactivity of Mn, searching highly active catalysts for (de)hydrogenation reactions therefore remains one of the central topics in Mn chemistry. The current approach to catalyst development is mainly based on the screening of the ligand backbones that proved to be effective for noble metal-based catalysts. However, the screening assessments with the reaction yields as the sole performance metrics do not probe the intrinsic reactivities of the catalysts and can easily result in the overlook of the potential ones due to suboptimal condition choice. In this thesis, we demonstrate that the catalyst performance is defined by a complex reaction network comprised of multiple stages of catalyst operation, that is catalyst activation, deactivation, and catalytic turnover. The reactivity of the catalyst itself and the reaction environment of each process determine synergistically the catalytic performance. As a result, the catalytic transformation should be viewed from the system perspective with the performance being a dynamic and highly condition-dependent characteristic.

In **chapter 2** we showed how understanding the chemistry of catalyst activation and deactivation steps helps pushing the performance of a Mn-catalyzed carbonyl hydrogenation system to unprecedentedly high levels. A previous work from our group disclosed a bidendate Mn(I)-NHC complex as a highly competent hydride transfer catalyst, the performance of which is however limited by rapid deactivation at relatively high temperature or catalyst loading beyond 100 ppm. The expansion of the ligand to a

tridentate pincer platform was found to be effective to counter the catalyst deactivation. We extended the ligand with an additional phosphine arm to come up with a new Mn(I)-CNP catalyst. This catalyst displayed enhanced thermal stability in the initial performance screening and could endure high reaction temperature up to 120 °C. Further kinetic and reactivity studies revealed that the *in situ* activation process of Mn-CNP precatalyst was so sluggish that part of its intrinsic activity was obscured. The instant activation protocol with hydride donor promoters could however eliminate the induction time associated with the catalysts activation and dramatically improve the catalytic performance. With this protocol we eventually established a powerful Mn-CNP-catalyzed hydrogenation system that gave rise to the unprecedented stability (TON up to 200 000) and productivity (TOF up to 41 000 h⁻¹). This system enabled the efficient hydrogenations of ketones, imines, aldehydes and formate esters at low catalyst loadings of 5-200 ppm.

Chapter 3 revealed the crucial role of controlling ligand dissociation during the activation of transition-metal catalysts for olefin hydrogenations/transpositions. While Mn complexes emerge as competent carbonyl hydrogenation catalysts, the Mn-catalyzed hydride transfer toward non-polar C=C bonds remains challenging. For example, the powerful carbonyl hydrogenation catalyst Mn-CNP described in **chapter 2** was completely inactive for the conversion of olefins. We proposed that the main mechanistic difference between C=C and C=O activation is that the hydride transfer to olefin can only be done via the inner-sphere migratory insertion, which firstly requires the coordinately saturated Mn hydride complex to provide an extra open site for the olefin coordination. This activation step can be particularly challenging for the Mn complex, as the dissociation of the strong-field donors or ancillary CO ligands is kinetically unfavorable. We found that the alkylation of the central NH group of CNP ligand blocked the metal-ligand cooperative function, but opened a special ligand dynamics of the N donor in the Mn-CNP complex. The alkylated N donor could reversibly dissociate from the metal center and furnish a vacant site ready to bind the substrate. Therefore such a masking of the cooperative NH functionality completely switched the reactivity of the Mn hydrides from carbonyl compounds to olefins. The first Mn-catalyzed olefin transposition system was developed with a N-methylated Mn-CNP complex. Various 1-alkenes were efficiently converted to 2-alkenes with exceptional stereoselectivities or regioselectivities.

Chapter 4 discussed the impact of the reaction environment on the performance of Mn-catalyzed ester hydrogenation. The carbonyl compounds become more inert along with the decrease of their polarity. Hydrogenation of carboxylic acid derivatives, such as esters, is therefore much more challenging than those of ketones, imines, aldehydes and so on. The Mn-catalyzed hydrogenation of esters was faced with a severe bottleneck with most of the reported systems requiring catalyst loadings higher than 1 mol%. The only one that promoted effective ester hydrogenation at 0.1 mol% catalyst loading was a Mn-PN complex, which however needed large amount of basic additive (as high as 70 mol% with respect to substrate) to achieve full conversion. We applied combined operando-IR spectroscopy, detailed kinetic analysis and operando DFT calculations to unravel the mechanistic details of ester hydrogenation catalyzed by a new Mn-CNC complex. Our study revealed the dynamic evolution of catalyst speciation intimately linked to the kinetic behavior of the catalyst system. During the reaction, the formation of the target alcohol products resulted in the conversion of the catalytic species to their inhibited Mn alkoxide form. The profound drop of the steady state concentration of the catalytically competent species due to the product inhibition largely limited the catalytic efficiency. Since early metal-based complexes tend to form more stable alkoxide complexes, this inhibitory effect seem to be the key for rationalizing the activity gap between Mn catalysts and their noble metal counterparts in ester hydrogenations. We also found that the strong alkali alkoxide base additives can suppress the inhibitory process and prolong the lifetime of the active catalyst species. Notably, the basic promotor was not chemically involved in the inhibitory equilibrium, but was able to elevate its standard free energy and render it unfavorable via the perturbation to reaction medium. Reaction thermodynamics, universally assumed ironclad, turned out to be defined by the reaction environment and subject to external control by a substance, which does not appear to take any part in the reaction, but can cause or accelerate it. The latter is the definition of catalysis by Pail Sabatier. We envision that manipulating the favourability of the elementary step via the rational use of additives or promotors can become a powerful tool for designing efficient catalytic system.

As demonstrated in many reports and in this thesis, kinetic data is necessary to obtain a comprehensive insight into the mechanism and behavior of catalytic reactions. The important effects related to catalyst activation, its stability and deactivation pathways are

also possible to be captured based on such information. However, collecting massive kinetic datasets is time-consuming and challenging, especially for hydrogenation catalysis that require high-pressure setup. Implementing data-driven approaches can potentially solve this problem. In **chapter 5**, we applied the response surface Box-Wilson methodology that combined the design of experiment and statistic modelling to the kinetic analysis of ketone hydrogenation reaction catalyzed by the Mn-CNP developed in **chapter 2**. This method allowed for the rapid construction of a set of statistical models based on the data obtained from minimum screening experiments. Moreover, kinetic parameters were well extracted from these models by rigorously equating the regression equations and related coefficients, providing important insights to the mechanism of complex catalytic system. This work revealed the possibility of enhancing the data output from high-throughput screening/optimization procedures.

In conclusion, to describe the catalytic performance, insights to reaction kinetics and the time-dependent molecular behavior of catalytic systems are required. Techniques combining operando spectroscopy, DFT calculations, kinetic and reactivity studies are found to be particularly effective for such investigations. Based on the comprehensive understandings of catalytic system, excellent catalytic efficiency has been achieved in this thesis by rationally tuning the structures of catalysts or the reaction environment.

Samenvatting

De groeiende vraag naar duurzame chemische technologieën heeft geleid tot een golf van zoektochten naar nieuwe katalysatoren op basis van aardmetalen. Op het gebied van (de)hydrogeneringskatalyse wordt echter meestal een enorme prestatiekloof gezien tussen de katalysatoren op basis van 3D-metalen en hun edel metalen tegenhangers, wat hun praktische toepassingen grotendeels belemmert. Hoewel de Mn-gekatalyseerde (de)hydrogenering aanzienlijke vooruitgang heeft geboekt sinds het pionierswerk van Beller en collega's in 2016, vereisen de meeste gerapporteerde systemen nog steeds relatief hoge hoeveelheden katalysator. Naast het ontwikkelen van nieuwe synthese methodologieën gebaseerd op de waterstofoverdrachtsreactiviteit van Mn, blijft het zoeken naar zeer actieve katalysatoren voor (de)hydrogeneringsreacties daarom een van de centrale onderwerpen in de Mn-chemie. De huidige benadering van katalysatorontwikkeling is voornamelijk gebaseerd op de screening van de ligand-backbones die effectief bleken te zijn voor edelmetaal-gebaseerde katalysatoren. De screening met de reactieopbrengsten als enige prestatie maatstaf peilt echter niet naar de intrinsieke reactiviteit van de katalysatoren en kan gemakkelijk leiden tot het missen van potentiële katalysatoren door een suboptimale keuze van de condities. In dit proefschrift tonen wij aan dat de katalysatorprestaties worden bepaald door een complex reactienetwerk dat bestaat uit meerdere stadia van katalysatorwerking, namelijk katalytische activering, deactivering en de katalytisch cyclus. De reactiviteit van de katalysator zelf en de reactieomgeving van elk proces bepalen synergetisch de katalytische prestatie. Als gevolg, moet de katalytische omzetting vanuit een systeem perspectief worden bekeken, waarbij de prestaties een dynamische en sterk van de omstandigheden afhankelijke eigenschap zijn.

In **hoofdstuk 2** lieten we zien hoe inzicht in de chemie van katalysatoractiverings- en -deactiveringsstappen de prestaties van een Mn-gekatalyseerd carbonylhydrogeneringssysteem tot ongekend hoge niveaus helpt opvoeren. Eerder werk van onze groep onthulde een bidendaat Mn(I)-NHC-complex als een zeer competente

katalysator voor hydride overdracht, waarvan de prestaties echter beperkt worden door snelle deactivering bij relatief hoge temperatuur of katalysator hoeveelheden boven 100 ppm. De uitbreiding van het ligand tot een tridentaat pincer platform bleek effectief om de katalysatordeactivatie tegen te gaan. We breidden het ligand uit met een extra fosfine-arm om tot een nieuwe Mn(I)-CNP-katalysator te komen. Deze katalysator vertoonde een grotere thermische stabiliteit bij de eerste screening van de prestaties en kon een hoge reactietemperatuur tot 120 °C verdragen. Uit verdere kinetische en reactiviteitsstudies bleek dat het in situ activeringsproces van de Mn-CNP-precatalysator zo traag verliep dat een deel van zijn intrinsieke activiteit verloren ging. Het instantane activeringsprotocol met hydridedonorpromotoren kon echter de inductietijd in verband met de katalysatoractivering elimineren en de katalytische prestaties drastisch verbeteren. Met dit protocol hebben wij uiteindelijk een krachtig Mn-CNP gekatalyseerd hydrogeneringssysteem tot stand gebracht dat ongekeerde stabiliteit (TON tot 200 000) en productiviteit (TOF^o tot 41 000 h⁻¹) opleverde. Dit systeem maakte efficiënte hydrogeneringen mogelijk van ketonen, imines, aldehyden en formateesters bij lage katalysator hoeveelheden van 5-200 ppm

Hoofdstuk 3 onthulde de cruciale rol van het beheersen van de liganddissociatie tijdens de activering van overgangsmetaalkatalysatoren voor olefinhydrogeneringen/transposities. Hoewel Mn-complexen naar voren komen als competente katalysatoren voor carbonyl hydrogenering, blijft de Mn-gekatalyseerde hydrideoverdracht naar apolaire C=C-bindingen een uitdaging. Zo was de krachtige katalysatoren voor carbonyl hydrogenering Mn-CNP, beschreven in **hoofdstuk 2**, volledig inactief voor de omzetting van olefinen. Wij stelden voor dat het belangrijkste mechanistische verschil tussen C=C- en C=O-activering is dat de hydrideoverdracht naar alkeen alleen kan plaatsvinden via de inner-sphere migratory insertion, waarvoor eerst het Mn-hydridecomplex met verzadigde coördinatie een extra open plaats moet bieden voor de alkeencoördinatie. Deze activeringsstap kan een bijzondere uitdaging zijn voor het Mn-complex, omdat de dissociatie van de sterke-velddonoren of de bijkomende CO-liganden kinetisch ongunstig is. Wij ontdekten dat de alkylering van de centrale NH-groep van het CNP-ligand de metaal-ligand coöperatieve functie blokkeerde, maar een speciale liganddynamiek van de N-donor in het Mn-CNP-complex opende. De gealkyleerde N-donor kon zich reversibel losmaken van het metaalcentrum en een vrije

plaats opleveren, klaar om het substraat te binden. Daarom schakelde een dergelijke maskering van de coöperatieve NH-functionaliteit de reactiviteit van de Mn-hydriden volledig om van carbonylverbindingen naar olefinen. Het eerste Mn-gekatalyseerde omzettingssysteem voor alkenen werd ontwikkeld met een N-gemethyleerd Mn-CNP-complex. Verschillende 1-alkenen werden efficiënt omgezet in 2-alkenen met uitzonderlijke stereoselectiviteit of regioselectiviteit.

Hoofdstuk 4 besprak de invloed van de reactieomgeving op de intrinsieke reactiviteit en prestaties van de Mn-gekatalyseerde esterhydrogenering. De carbonylverbindingen worden meer inert naarmate hun polariteit afneemt. Hydrogenering van derivaten van carboxzuren, zoals esters, is daarom veel uitdagender dan die van ketonen, imines, aldehyden enz. De Mn-gekatalyseerde hydrogenering van esters werd geconfronteerd met een ernstig knelpunt: de meeste gerapporteerde systemen vereisten een katalysatorhoeveelheid van meer dan 1 mol%. De enige die een effectieve esterhydrogenering bij 0,1 mol% katalysatorbelasting bevorderde was een Mn-PN complex, dat echter een grote hoeveelheid basisch additief nodig heeft (70 mol% ten opzichte van het substraat) om volledige conversie te bereiken. We pasten gecombineerd operando-IR spectroscopie, gedetailleerde kinetische analyse en operando-DFT berekeningen toe om de mechanistische details te ontrafelen van esterhydrogenering gekatalyseerd door een nieuw Mn-CNC complex. Onze studie onthulde de dynamische evolutie van de katalysatorspeciatie die nauw verbonden is met het kinetisch gedrag van het katalysatorsysteem. Tijdens de reactie resulteerde de vorming van de bedoelde alcoholproducten in de omzetting van de katalysatorspecies in hun geremde Mn-alkoxide vorm. De sterke daling van de stationaire concentratie van de katalytisch competente soorten als gevolg van productinhibitie beperkte de katalytische efficiëntie aanzienlijk. Aangezien early-metaalcomplexen de neiging hebben stabielere alkoxidecomplexen te vormen, lijkt dit remmende effect de sleutel te zijn voor het rationaliseren van de activiteitskloof tussen Mn-katalysatoren voor hydrogenering en hun edelmetalen tegenhangers. Wij vonden ook dat de sterke alkali alkoxide base toevoegingen het remmende proces kunnen onderdrukken en de levensduur van de actieve katalysatorsoorten kunnen verlengen. Met name de base promotor was niet chemisch betrokken bij het remmende evenwicht, maar kon de standaard vrije energie verhogen en deze ongunstig maken via de verstoring van het reactiemedium. De

reactiethermodynamica, waarvan algemeen werd aangenomen dat zij rigide was, bleek te worden bepaald door de reactieomgeving en onderhevig aan externe controle door een stof, die geen deel lijkt te nemen aan de reactie, maar deze kan veroorzaken of versnellen. Dit laatste is de definitie van katalyse door Pail Sabatier. Wij denken dat het manipuleren van de gunstigheid van de elementaire stap via het rationele gebruik van additieven of promotoren een krachtig instrument kan worden voor het ontwerpen van efficiënte katalytische systemen.

Zoals aangetoond in vele rapporten en in dit proefschrift, zijn kinetische gegevens noodzakelijk om een volledig inzicht te krijgen in het mechanisme en het gedrag van katalytische reacties. De belangrijke effecten in verband met katalytische activering, stabiliteit en deactiveringsroutes kunnen ook worden vastgelegd op basis van dergelijke informatie. Het verzamelen van massale kinetische datasets is echter tijdrovend en een uitdaging, vooral voor hydrogeneringskatalyse waarvoor hogedrukopstellingen nodig zijn. Het implementeren van datagestuurde benaderingen kan dit probleem mogelijk oplossen. In **hoofdstuk 5** pasten wij de response surface Box-Wilson methodologie toe die het Design of Experiment en statistische modellering combineerde op de kinetische analyse van de ketonhydrogenatiereactie gekatalyseerd door het in **hoofdstuk 2** ontwikkelde Mn-CNP. Deze methode maakte de snelle constructie mogelijk van een reeks statistische modellen op basis van de gegevens verkregen uit minimale screeningsexperimenten. Bovendien konden uit deze modellen goed kinetische parameters worden afgeleid door de regressievergelijkingen en bijbehorende coëfficiënten rigoureus gelijk te stellen, wat belangrijke inzichten verschafte in het mechanisme van complexe katalytische systemen. Dit werk onthulde de mogelijkheid om de gegevens van high-throughput screening-/optimalisatieprocedures te verbeteren.

Tot slot, om de katalytische prestaties te beschrijven is dus inzicht nodig in de reactiekinetiek en het tijdsafhankelijke moleculaire gedrag van katalytische systemen. Technieken die operando-spectroscopie, DFT-berekeningen, kinetische en reactiviteitsstudies combineren blijken bijzonder effectief te zijn voor dergelijke onderzoeken. Op basis van het uitgebreide begrip van katalytische systemen is in dit proefschrift een uitstekende katalytische efficiëntie bereikt door de structuren van katalysatoren of de reactieomgeving rationeel af te stemmen.

Acknowledgements

I would like to thank my supervisor Evgeny who keeps on providing guidance and support during my whole PhD study. Thank you for letting me join this lovely group, giving me adequate freedom to pursue fascinating research, advising me to step out of comfort zones and learn new things, and supporting me communicate with external researchers. I really enjoy our regular discussions on the project, as you always give different views and interesting perspectives that inspire me a lot. Your passion for science never ceases to impress me, and that will be a big encouragement for my future academic work. I also want to thank my second promotor and daily supervisor Georgy. When I started PhD, it was you who helped me go through the adaptation period by teaching me all kinds of techniques of experiments, paper writing, and presentation. I am a noisy person and always bother you with numerous questions. Thank you for being patient and brainstorming science with me. You are not only a responsible, knowledgeable promotor but also a nice friend. Thanks for kicking me to take break, sharing amazing food with me, and fighting together in the lab day and night. To Evgeny Jr., thank you for helping me build the operando FTIR apparatus, taking me to the hall of kinetic modelling, letting me survive in Novosibirsk. Your colourful humors brought me many fun memories. My students, Robin, Tejas, and Erik, thanks for your work. Your intense curiosity always let me reflect on my project and get some new understanding. To Ivan, thank you for all the calculation supports. You are indeed a genius for developing those amazing computational methodologies. It is a big pity that we do not have a chance to meet each other. Hope to see you in the near future. Mauela and Christian, thanks for analysing the crystal structures of our catalysts. To Karin and Els, thank you for taking care of all the administrative matters. I thank all the ISE members, Bob, Robert, Annika, Christophe, Liliana, Elena, Chuncheng, Ali, Jittima, Guanna, Dapeng, Chong, and Adarsh for all your helps.

I thank my parents, sister and brother for their unconditional support, love and concern. Sorry that I could not come back and get together with you very often in the last four

years. And sorry for letting you worry about my health and work all the time. These are also what I want to say to my fiancée Jin. The long distance between China and Netherland has separated us for three years. Thank you for always being there and waiting for me. Thanks for taking a visiting study in German in the first year of my PhD. During that year, we took 8-hours train to meet each other every month. It was really the happiest time of my PhD. Thank you for calling me everyday and listening to my struggles, complaints, delights, success, and failures. No matter how stubborn I am, you are always patient, tolerant and try to persuade me to do the right things. Your supports helped me went through all the difficulties in the PhD.

Curriculum Vitae

Wenjun Yang was born on September 14th, 1992 in Shangrao, China. In 2010 he went to Beijing and started his bachelor study in Chemistry. He graduated from China Agricultural University in 2014 and continued his master study in the same university under the supervision of prof. dr. Hongchao Guo. His master project was about developing new annulation methodologies for synthesizing biologically important cyclocompounds. After receiving his Master degree of Science in 2017, he worked as a research assistant in Nanjing Tech University. In 2018 he moved to the Netherlands and started his PhD study under the supervision of prof. dr. Evgeny A. Pidko in Delft University of Technology. The research is about designing efficient hydrogenation catalysts based on earth-abundant metals, and results are described in this thesis.

List of Publications

1. **Wenjun Yang**, Ivan Yu Chernyshov, Robin KA van Schendel, Manuela Weber, Christian Müller, Georgy A Filonenko, Evgeny A Pidko, Robust and efficient hydrogenation of carbonyl compounds catalyzed by mixed donor Mn (I) pincer complexes, *Nat. Commun.* **2021**, *12*, 1-8.
2. **Robin K. A. van Schendel, Wenjun Yang**, Evgeny A. Uslamin, Evgeny A. Pidko, *ChemCatChem*, **2021**, *13*, 4886-4896.
3. **Wenjun Yang**, Tejas Y. Kalavalapalli, Annika M. Krieger, Taras A. Khvorost, Ivan Yu. Chernyshov, Manuela Weber, Evgeny A. Uslamin, Evgeny A. Pidko and Georgy A. Filonenko, Basic Promotors Impact Thermodynamics and Catalyst Speciation in Homogeneous Carbonyl Hydrogenation. *J. Am. Chem. Soc.*, **2022**, *144*, 8129-8137.
4. **Wenjun Yang**, Ivan Yu. Chernyshov, Manuela Weber, Evgeny A. Pidko, Georgy A. Filonenko, Switching Between Carbonyl Hydrogenation and Olefin Transposition Catalysis via Controlling Ligand Dynamics in Mn(I) complexes, *ACS Catal.* **2022**, *12*, 10818-10825.
5. **Wenjun Yang**, Erik Nieuwlands, Georgy A. Filonenko, Evgeny A. Pidko, Reshaping the thermodynamics of homogeneous hydrogenation with base additives, in preparation.
6. **Wenjun Yang**, Georgy A. Filonenko, Evgeny A. Pidko, Rethinking the Performance of Hydrogenation Catalysts, in preparation.

